Observations of stellar occultation : applications to study of the structure and evolution of Pluto's atmosphere

Erick Gregorio Meza Quispe

THÈSE DE DOCTORAT DE
l'UNIVERSITÉ PIERRE ET MARIE CURIE

Spécialité

Astronomie

École doctorale d'Astronomie et d'Astrophysique d'Ile de France (Paris)

Présentée par

Erick G. Meza Quispe

Pour obtenir le grade de
DOCTEUR de l'UNIVERSITÉ PIERRE ET MARIE CURIE

Sujet de la thèse :

Observations d'occultations stellaires, applications à l'étude de la structure et l'évolution de l'atmosphère de Pluton

soutenue le 28 Septembre 2018

devant le jury composé de :

Dr. François FORGET	Président du jury
Dr. Michel DOBRIJEVIC	Rapporteur
Dr. Sébastien LEBONNOIS	Rapporteur
Dr. Marc BUIE	Examinateur
Pr. Pascal RANNOU	Examinateur
Pr. Darrell STROBEL	Examinateur
Pr. Bruno SICARDY	Directeur de thèse

Contents

List of Figures

List of Tables

Acknowledgement

First, I would like to thank my PhD supervisor, Bruno Sicardy, for his guidance, patience, advice, availability and his kindness and his hard work in trying to make me better.

Besides my advisor, I would like to thank the rest of my thesis committee: Dr. François Forget, Dr. Michel Dobrijevic, Dr. Sébastien Lebonnois, Dr. Marc Buie, Pr. Pascal Rannou, and Pr. Darrell Strobel for their insightful suggestions, comments, and hard questions.

I would also like to thank the members of the LESIA team (Diane, Joana, Josselin, Rodrigo, Jean Lecacheux, François Colas, and collaborators) for their support, especially when I asked obvious questions and for providing helpful comments on many issues along the thesis.

Thank you to all observers around the world to share their passion of the observations of stellar occultations.

Last but not the least, I would like to thank my family for supporting and inspiring me throughout my life.

This work was supported by CONCYTEC-Peru and the European Research Council Advanced Grant "Lucky Star" n. 669416.

GRACIAS A TODOS ! SULPAY ! MERCI À TOUS ! THANK YOU VERY MUCH !

Abstract

Summary

Ground-based stellar occultations are a very efficient method to probe Pluto's tenuous nitrogen (N_2) atmosphere from a few kilometers above the surface (pressure $\sim$10 μbar) up to 380 km altitude ($\sim$10 nbar). This atmosphere is strongly coupled with Pluto's surface properties (distribution of ices, thermal inertia and surface temperature), as the gaseous N_2 is in vapor pressure equilibrium with the nitrogen ice. This induces strong seasonal effects, due to the large obliquity (120 deg) and high orbital eccentricity (0.25) that takes the dwarf planet from 30 to 50 au during half of its 248-year orbital period.

The main topic of my thesis is an overview of twenty ground-based stellar occultations by the dwarf planet Pluto, that have been organized between 2002 and 2016 by the LESIA occultation group at Paris Observatory.

My analysis of eleven campaigns of occultations with high S/N ratio has been used to:

(1) derive Pluto's atmospheric pressure changes on decadal time scales (1988-2016), and provide constraints on the current seasonal models of the dwarf planet, putting them in perspective with the NASA New Horizons flyby of July 2015;

(2) compare our ground-based derived results with the New Horizons findings, and in particular with the results of the radio science (REX) experiment below the altitude 115 km;

(3) use the reconstructed geometries of the occultations and the newly released Gaia DR2 catalog to improve Pluto's orbital elements and provide a new ephemeris for the dwarf planet.

Résumé

Les occultations stellaires au sol sont une méthode très efficace pour sonder l'atmosphère (N_2) d'azote de Pluton à quelques kilomètres de la surface (pression $\sim$10 μbar) jusqu'à 380 km altitude ($\sim$10 nbar). Cette atmosphère est fortement couplée aux propriétés de surface de Pluton (distribution des glaces, inertie thermique et température de surface), car le N_2 gazeux est en équilibre de pression de vapeur saturante avec la glace d'azote. Cela induit de forts effets saisonniers, dus à la grande obliquité (120 degrés) et à l'excentricité orbitale élevée (0,25) qui amène la planète naine de 30 à 50 ua pendant la moitié de sa période orbitale de 248 ans.

Le sujet principal de ma thèse est une vue d'ensemble de vingt occultations d'étoiles (observées du sol) par la planète naine Pluton, organisées entre 2002 et 2016 par le groupe d'occultation du LESIA à l'Observatoire de Paris.

Mon analyse de onze campagnes d'occultations avec un rapport S/N élevé a été utilisée pour:

(1) déduire les changements de pression atmosphérique de Pluton sur des échelles de temps décennales (1988-2016) et créer des contraintes sur les modèles saisonniers actuels de la planète naine, les mettant en perspective avec le survol de la sonde NASA New Horizons en juillet 2015;

(2) comparer nous résultats obtenus au sol avec les résultats de New Horizons, en particulier avec les résultats du radio science experiment (REX) au-dessous de 115 km d'altitude;

(3) utiliser les géométries reconstruites des occultations et le nouveau catalogue Gaia DR2 pour améliorer les éléments orbitaux de Pluton et créer une nouvelle éphéméride pour la planète naine.

Chapter 1

Introduction

1.1 Pluto: from discovery to New Horizons flyby

On 1930 February 18, Clyde Tombaugh observed a faint starry image “jumping", while he was using a blink comparator. He was examining pairs of photographic plates taken at a 13-inch telescope during the search of so-called “Planet X". That hypothetical planet was suggested to explain small perturbations on Neptune's orbit claimed by certain astronomers.

This discovery was official on 1930 March 13, but it appeared that the body was not the Planet X. Indeed, Pluto's mass turned out to be far too small to create significant perturbations on Neptune's orbit. The observed deviations were actually mere artifacts due to observational errors. This was fully fully confirmed after the discovery of Charon (Christy and Harrington, 1978), which provided a small Pluto's mass of about 0.002 Earth mass, see (Duncombe and Seidelmann 1980 for a review).

From Pluto's rotational light curves obtained in 1953-1955, Walker and Hardie (1955) estimated a rotation period of 6.3 days for Pluto (Fig. 1.1).

Charon, also known as Pluto I was the first Plutonian satellite discovered in 1978 on photographic plates (Christy and Harrington, 1978). This finding played an important role to better constrain Pluto and Charon's physical parameters, using the so-called mutual events during the period 1985-1990 (see Figure 1.2). The system was then observed edge-on, causing mutual occultations and eclipses between the two bodies. The shapes and timings of those events constrained Pluto and Charon's sizes and densities (Binzel, 1989), Charon's orbital elements, as well as albedo features on both surfaces, see e.g. Marcialis (1988) and Tholen and Buie (1988). Those models suggested that Pluto has two high-albedo polar caps and a dark equatorial region with an nonuniform longitudinal albedo distribution. A comparison is shown in Fig. 1.3, where the two models of Pluto's albedo are based on two different methods and data (Buie et al., 1992; Young and Binzel, 1993).

In the early 2000's, images from the Hubble Space Telescope (HST) revealed four more moons, Nix and Hydra in 2005 (Weaver et al., 2006), Kerberos in 2011 (Showalter et al., 2011) and Styx in 2012 (Showalter et al., 2012). In 2006, Pluto was classified as a dwarf planet, i.e. a body large enough to be in hydrostatic equilibrium but not massive enough to perturb nearby objects. The NASA mission New Horizons (NH) was launched to Pluto's system, for a flyby in July 2015 provided high resolution images (up

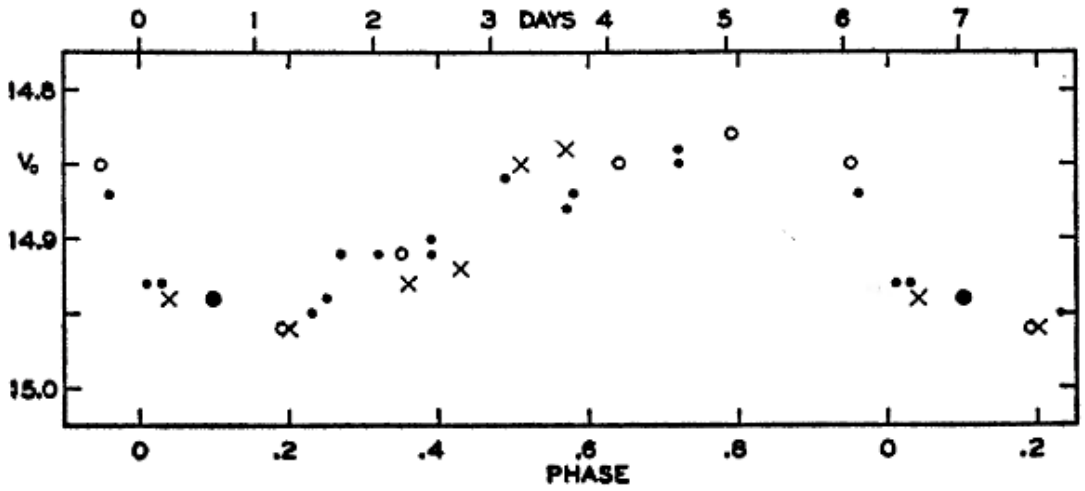

Figure 1.1: Rotational light curve of Pluto as a function of rotation phase (with a period of 6.390 days). Crosses, circles and dots are from observations made in 1953, 1954 and 1955, respectively (Walker and Hardie, 1955).

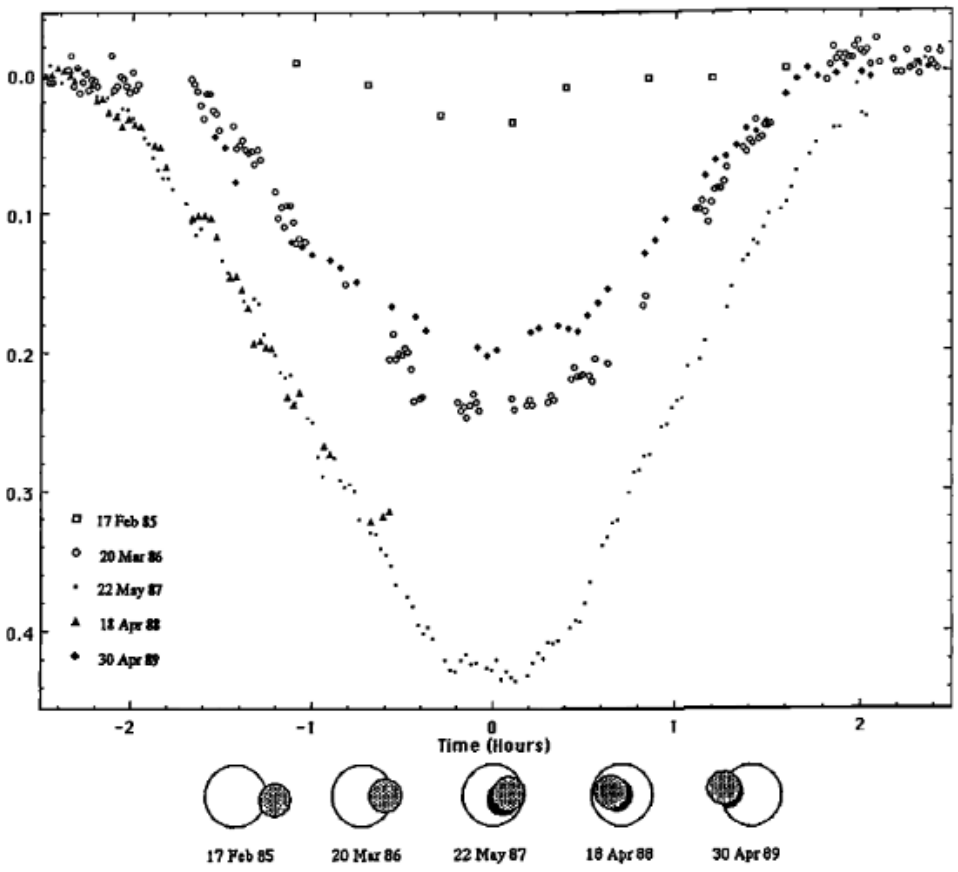

Figure 1.2: A composite of event mutual light curves from 1985 to 1989 and diagrams of the approximate geometry for each event. From Binzel (1989).

to 80 meters/pixel) of Pluto and Charon and the small satellites, resulting in accurate size and shapes for Pluto and Charon (Nimmo et al., 2017), and resolved images of Nix, Hydra, Kerberos and Styx, see Weaver et al. (2016) and Fig. 1.4.

Additionally, New Horizons images revealed significant topographic features on Pluto and Charon's surfaces, with valleys, mountains and impact craters of typical heights and depths reaching ±5 km (Nimmo et al., 2017). Global albedo maps are available from Buratti et al. (2017), see Fig. 1.5. This is an important step forward to better constrain Pluto's seasonal models, as explained later.

Finally, Fig. 1.6 displays a summary of the various discoveries and progresses brought by direct imaging over time. Note that we give at the end of this chapter a more detail account of the NH findings.

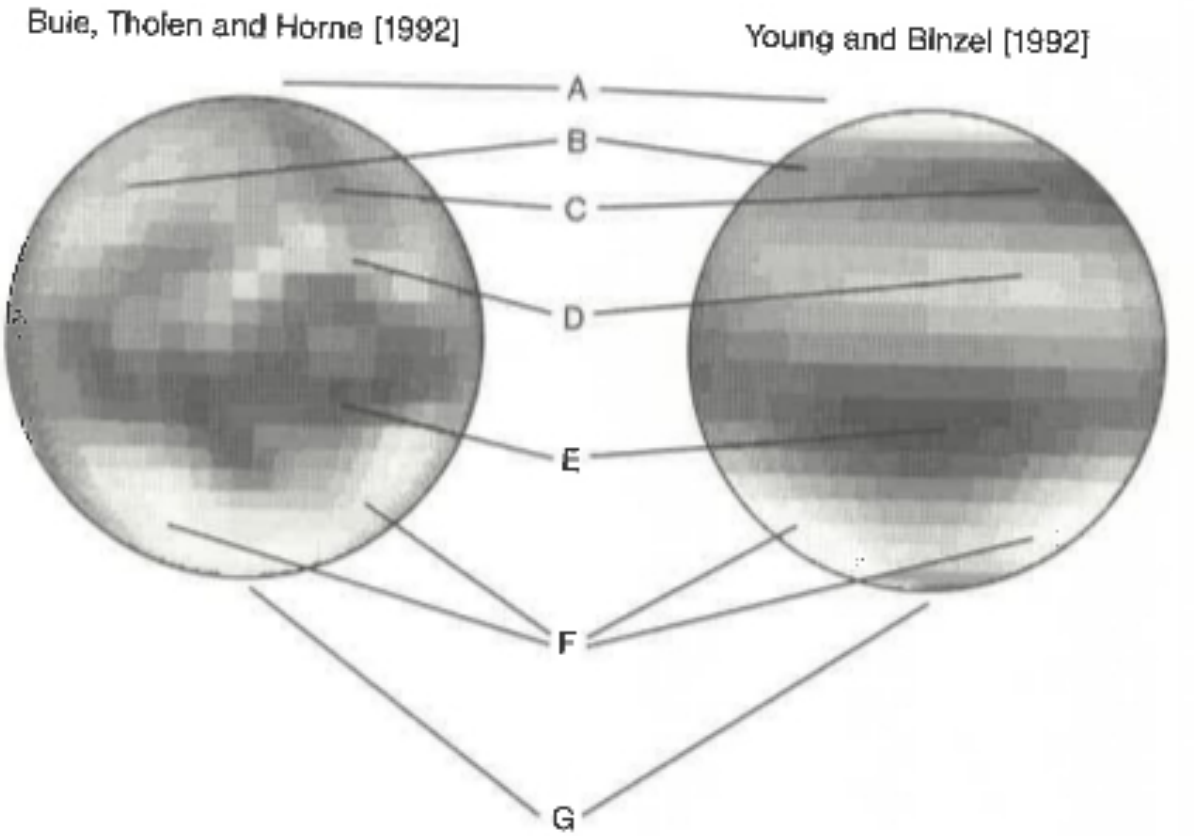

Figure 1.3: Two Pluto's albedo maps. They are based on two difference methods and data. Clear differences are observed in the area B, however area F shows similarities on the south polar cap. From Stern and Mitton (2005).

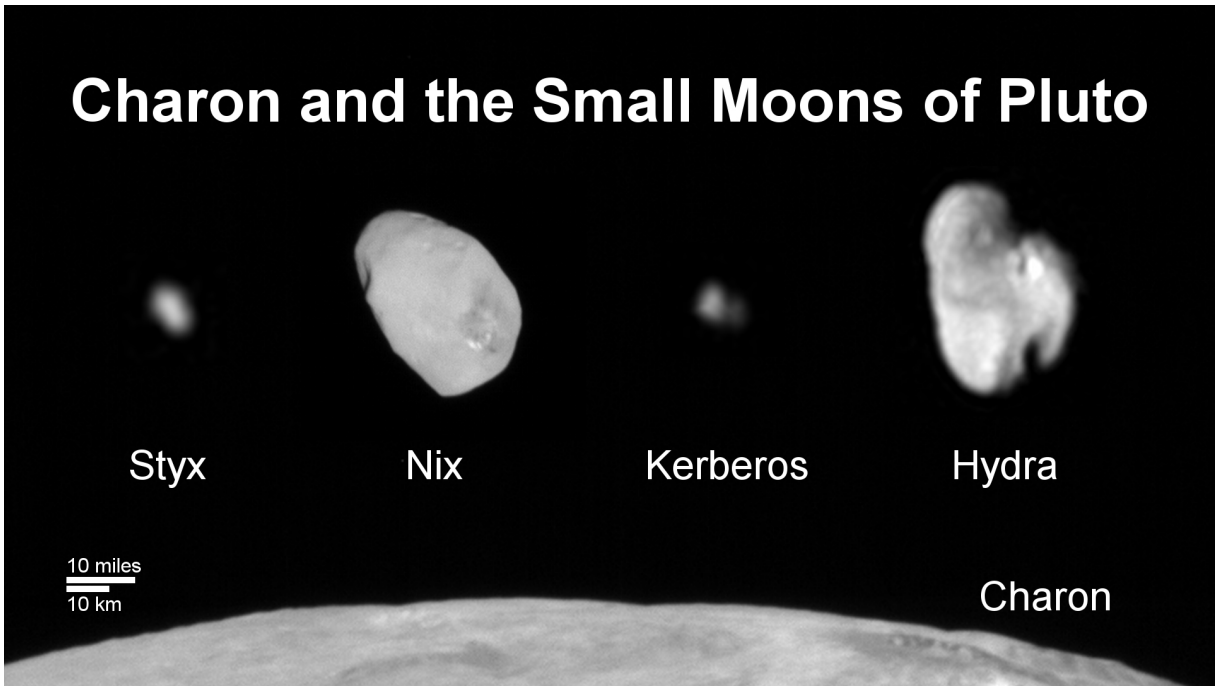

Figure 1.4: Comparison Pluto's largest moon, Charon with all four smaller moons, as resolved by the Long Range Reconnaissance Imager (LORRI) on board New Horizons. Charon has a diameter of 1,212 kilometers, while Nix and Hydra have comparable sizes, approximately 40 kilometers. Kerberos and Styx are smaller, with comparable sizes of 10-12 kilometers. Note that all four small moons have highly elongated shapes http://pluto.jhuapl.edu/.

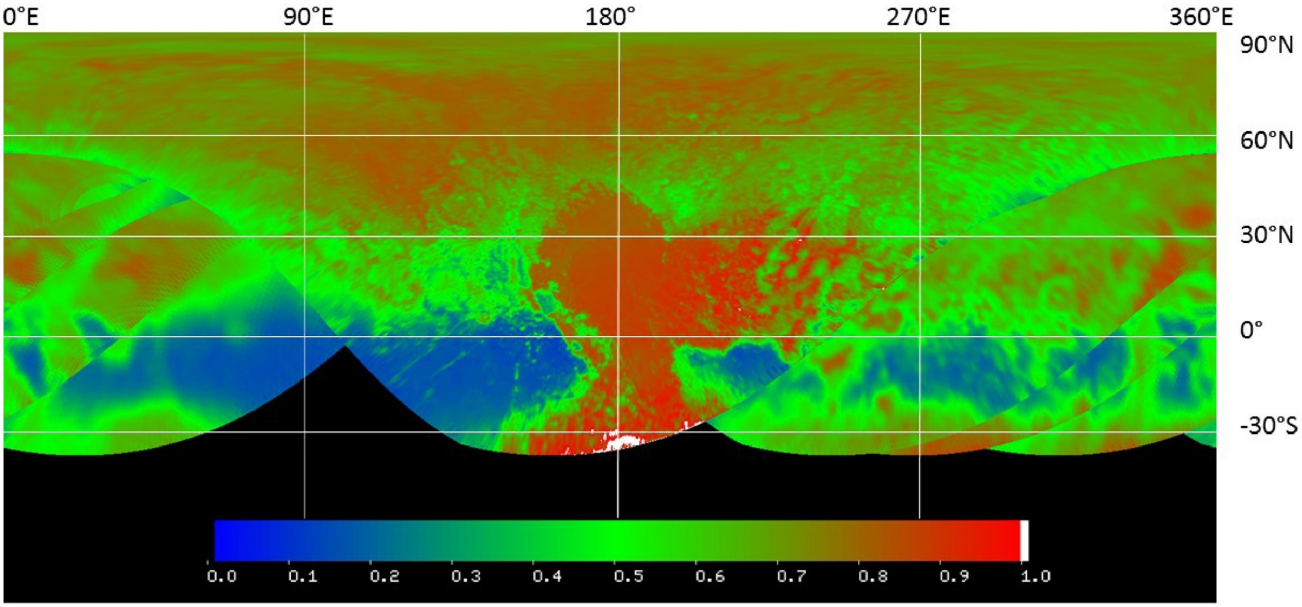

Figure 1.5: Pluto's albedo maps from New Horizons Buratti et al. (2017) .

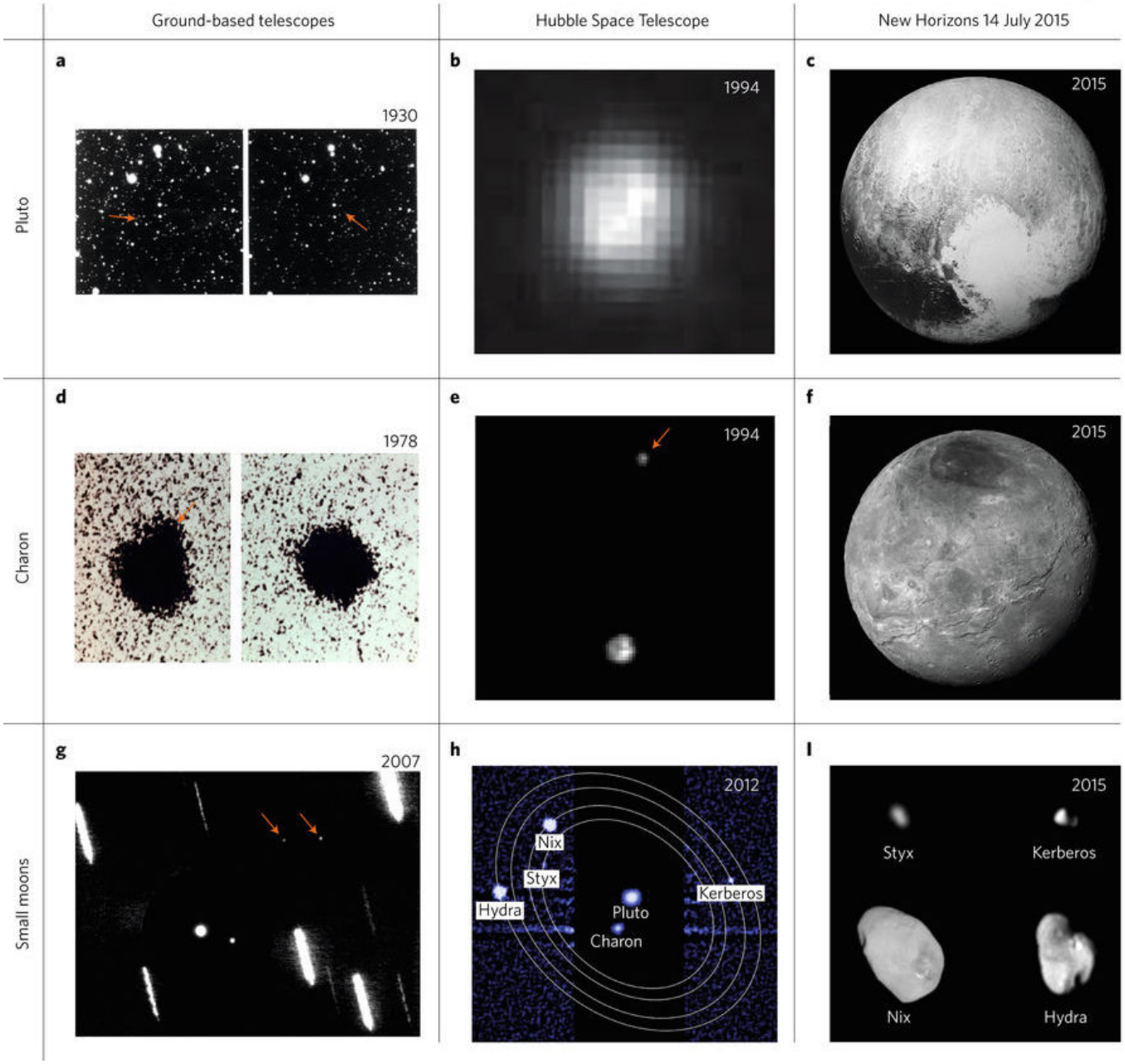

Figure 1.6: Pluto's system as seen through direct imaging at various epochs (from Olkin et al., 2017). (a) Discovery (Lowell Observatory Archives). (b) Pluto from HST (NASA/JHUAPL/SwRI). (c) Charon discovery image (NASA/JHUAPL/SwRI). (d) Charon imaged by New Horizons (NASA/JHUAPL/SwRI). (e) Charon (top) and Pluto (bottom) as observed by the HST (ESA). (f) Charon imaged by New Horizons (NASA). (g) Nix (left arrow) and Hydra (right arrow), as observed by Keck using adaptive optics (David Tholen). (h) Pluto's system as imaged by the HST (STScI). (i) New Horizons images of the four smaller moons (see Fig.1.4).

1.2 Pluto's atmosphere

During an attempt to observe a stellar occultation by Pluto in 1985, Brosch (1995) reported a gradual stellar drop that could be interpreted as the detection of a Pluto's atmosphere. Due to adverse observing conditions, though, this point remained debated and it remained unclear whether an atmosphere was indeed detected. In 1988, a higher-quality, multi-chord occultation actually revealed without ambiguity such atmosphere (Hubbard et al., 1988; Elliot et al., 1989; Yelle and Elliot, 1997).

However, our analysis of Pluto occultations over the period 1988-2016 (see Desmars et al. 2018, preprint attached in the Appendix) provides accurate astrometric measurements of Pluto, see Chapter 5. This in turn, combined with the Gaia DR2 release (Gaia Collaboration et al., 2018), allowed us to improve Pluto's ephemeris and derive a good post-diction for the 1985 event, see Fig. 4 of Desmars et al. (2018). It then appears that the event reported in Brosch (1995) matches both in time and shape what is expected from our post-diction, strongly suggesting that the Brosch (1995) report is actually a pre-discovery observation of Pluto's atmosphere.

The occultation light curves could be best explained by an atmosphere mainly composed of molecular nitrogen N_2 with traces of methane CH_4 (Yelle and Lunine, 1989). Pluto's overall temperature structure can be estimated from thermal emission in the far-infrared. Data obtained with the Infrared Space Observatory (ISO) in 1997 indicate that Pluto's surface is not isothermal, with dayside surface temperatures as high as 54-63 K (Lellouch et al., 2000), but remembering that some pure N_2 terrains have to remain near 40 K to keep a surface pressure of some 10-15 μbar through vapor pressure equilibrium.

More recent thermal measurements using date from the *Spitzer* observatory in 2004 (Lellouch et al., 2011) and 2012 (Lellouch et al., 2016) confirm those contrasted temperatures, but also provide more constrains on longitudinal and latitudinal variations.

In that context, it will be interesting to compare those results with the yet-to-be-published numbers obtained by the REX experiment on boars New Horizons spacecraft. In that context, Pluto's atmosphere has a temperature of about 35-40 K at the surface (the temperature of the free nitrogen ice patches), and then warms up along a stratospheric branch, reaching about 100 K at an altitude of about 20 km due to strong CH_4 IR absorption at 3.3 μm, see Fig. 1.7.

The global atmospheric pressure is then controlled by its major constituent, N_2, through the vapor pressure equilibrium at the contact of the surface. This basic view was confirmed in 2015 during the New Horizons flyby (Gladstone et al., 2016).

Near-infrared spectroscopy (Young et al., 1997; Lellouch et al., 2009, 2015) revealed CH_4 as the second most abundant atmospheric species (about 0.5 % relative to N_2). Fig. 1.8 shows ground-based Pluto's atmospheric spectra observed by CRIRES/VLT (Lellouch et al., 2011), while ALMA sub-millimeter spectra revealed even smaller abundances for carbon monoxide CO (about 500 ppm) and hydrogen cyanide HCN (10^{-8}-10^{-7}), see Lellouch et al. (2017) and Fig. 1.9.

In 2015, New Horizons confirmed the nitrogen-dominated composition of the atmosphere and additionally detected acetylene (C_2H_2), ethylene (C_2H_4), ethane (C_2H_6), see Fig. 1.10. The atmosphere also produces hazes. The size of the haze particles is unclear. Its blue color points to particle radii near 10 nm, but the ratio of brightnesses

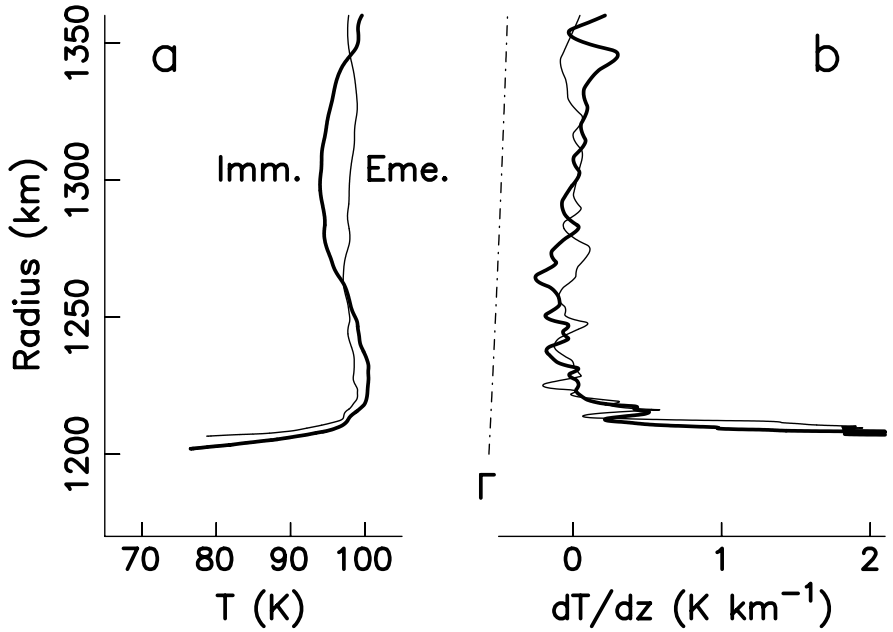

Figure 1.7: Left - The temperature profile $T(r)$ of Pluto's as a function of radius r (distance to Pluto's center). It shows the stratosphere that connects the surface estimated, at about 40 K, to an isothermal branch at about 100 K, above $r \sim 1215$ km (altitude ∼25 km). Right - The vertical temperature gradient derived from the left panel. The dash-dotted line gives the dry adiabat Γ for N_2, showing that the atmosphere is everywhere convectively stable (from Sicardy et al. 2003). We will see in Chapter 5 that more accurate profiles have been obtained from ground-based stellar occultations, and subsequently, from New Horizons.

at different phase angles indicates a radii exceeding 100 nm.

This may be explained by aggregation of small (tens of nm) particles into larger (hundreds of nm) clusters (Cheng et al., 2017).

The initial ground-based occultation results obtained in 1988 suggested the possible presence of hazes, possibly explaining a sudden drop of stellar flux (or "kink") as deeper layers were probed by the star (Yelle and Elliot, 1997).

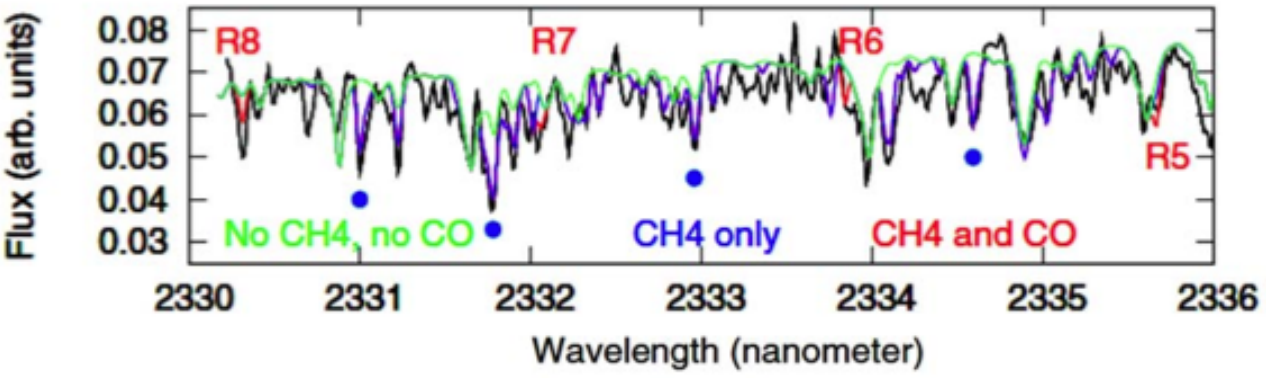

Figure 1.8: Pluto's atmosphere spectra by CRIRES/VLT. The black line are the data. Colored lines indicate models for methane, nitrogen and CO (Lellouch et al., 2011).

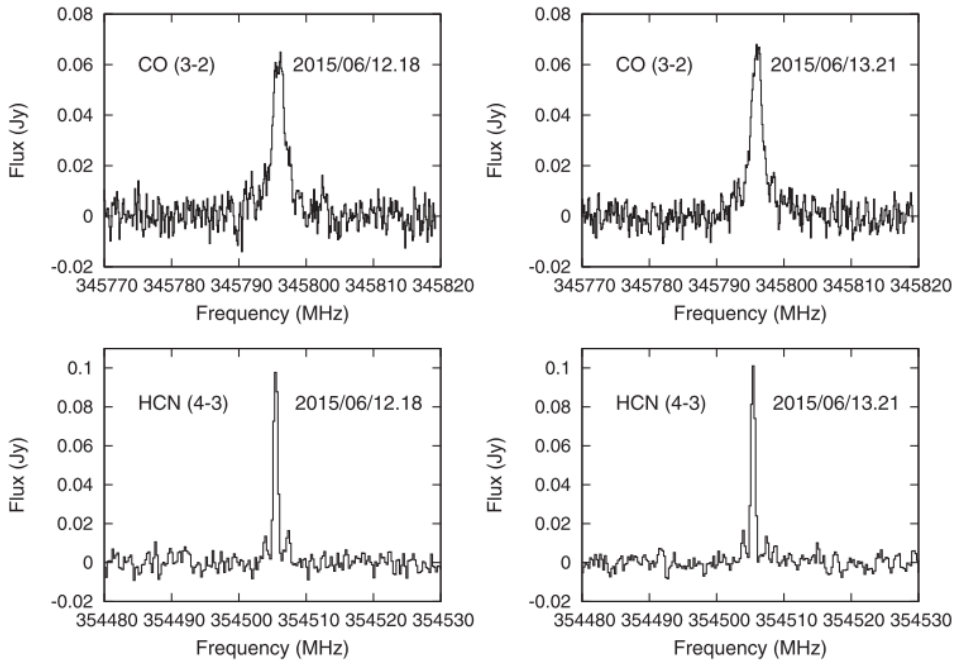

Figure 1.9: Pluto spectra in the vicinity of the CO (top) and HCN (bottom) lines during two observed days (Lellouch et al., 2017).

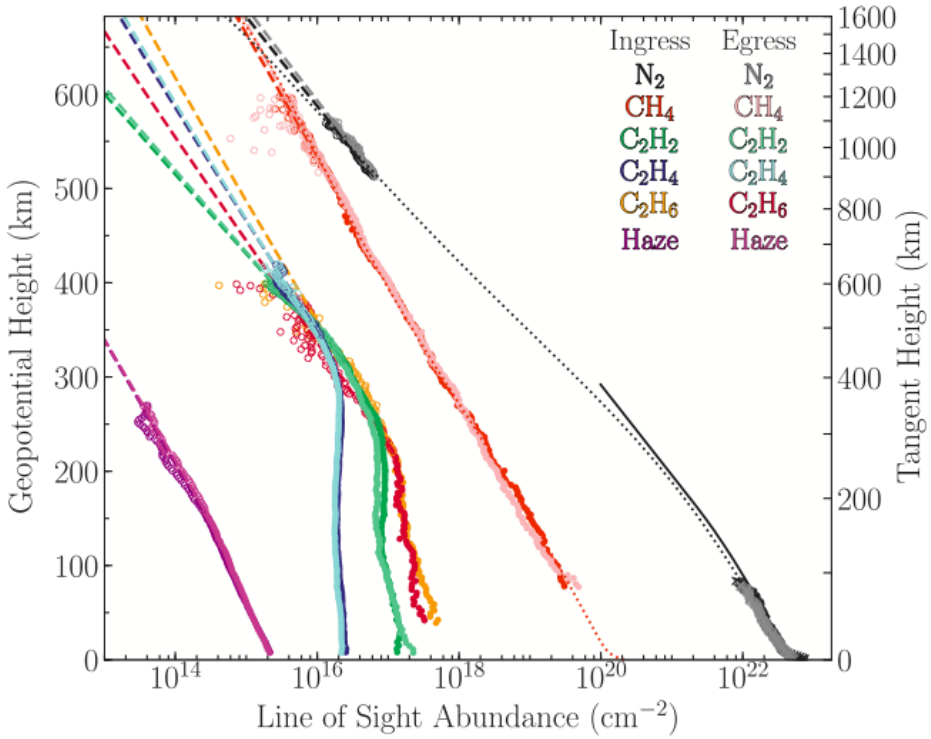

Figure 1.10: Line-of-sigth column density profiles retrieved from the observed transmission data of Alice occultation instrument (Young et al., 2018). Atmospheric profiles derived from REX instruments are shown in Chapter 5. They concern lower altitude levels, between 0 and 100 km, and are more relevant to our work, as discussed later.

However, as more occultations were observed during the 2002-2016 period, it became clear that this kink was best interpreted by an essentially transparent inversion layer that connects the surface at $\sim$ 40 K to a stratopause at $\sim$ 100 K at 25 km altitude (Sicardy et al., 2003; Dias-Oliveira et al., 2015).

This was confirmed by the LORRI visible imager (bandpass of 350-850 nm) of New Norizons, that revealed haze layers near the surface, but with a modest vertical optical depth of only 0.013 (Gladstone et al., 2016). This has refined by Cheng et al. (2017), who derived a scattering optical depth along the light of sight of about 0.24, a vertical optical depth of 0.018, and scale height of about 50 km. In that context, the ground-based stellar occultations mostly probe altitudes above 100 km, and are thus scanning essentially transparent regions of the atmosphere.

As detailed in Chapter 5 and in the preprint Meza et al. 2018 (see Appendix), the REX experiment provides density, pressure and temperature profiles between the surface and an altitude of about 100 km. As such, it is more relevant to our work and deserves a study of its own.

Pluto's atmosphere exhibits drastic seasonal effects due to it high obliquity and orbital eccentricity. In particular, a large expansion of a factor or more than two between 1988 and 2002 was revealed during a stellar occultation (Elliot et al., 2003; Sicardy et al., 2003). It was interpreted as being due to the sublimation of N_2 ice that was illuminated by the sun in the spring and then summer hemisphere of the dwarf planet, causing significant sublimation in spite of Pluto's increasing heliocentric distance, see Chapter 4.

In that context, it is important to better know Pluto's surface composition so that to better understand its atmosphere. Spectroscopy made in the 1980's (review by Stern and Mitton 2005) did reveal methane and ethane ices on Pluto's surface, from near IR spectra (Cruikshank et al., 1976; DeMeo et al., 2010). Owen et al. (1992) identified two features as the 2.15 μm absorption of N_2 ice and the 2.35 μm band of CO ice, respectively, consistent with the view that Pluto is covered by ices dominated by nitrogen. Because the shape of the N_2 spectral feature is very sensitive to temperature, it allows to estimate the average surface temperature, ranging according to authors between 55-60 K (Sykes et al., 1987; Aumann and Walker, 1987), near 40 K (Tryka et al., 1994), 35 K (Stern et al., 1993; Jewitt, 1994), or between 35-53 K (Lellouch et al., 2016).

Spectroscopy by New Horizons reveals Pluto ices composed of nitrogen, methane and water (the latter being non volatile at those temperatures). Fig. 1.11 shows the ice composition of Pluto's surface taken from Grundy et al. (2016).

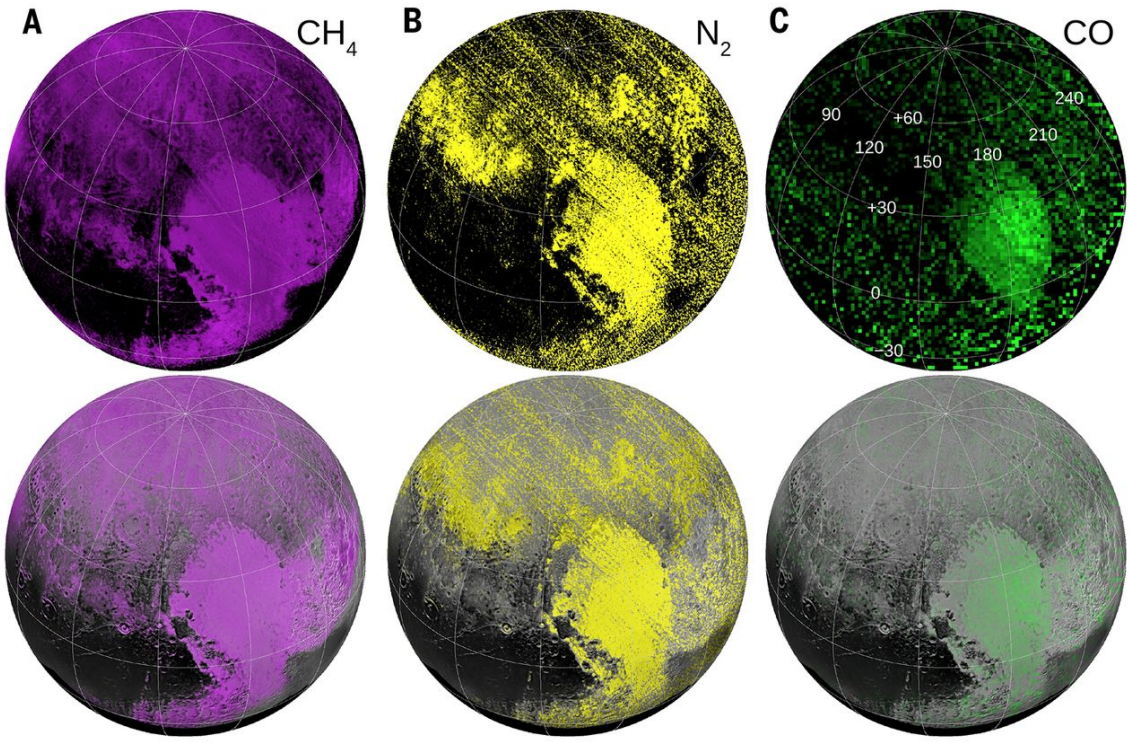

Figure 1.11: Maps of Pluto's volatile ices CH4, N2, and CO obtained by the Linear Etalon Imaging Spectral Array (LEISA) on board New Horizons (Grundy et al., 2016). For each species, the top panel shows the LEISA map, with brighter colors corresponding to greater absorption; the bottom panel shows the same data overlaid on a base map made from LORRI images reprojected to the geometry of the LEISA observation. (A) The CH_4 absorption map shows the equivalent width of the 1.3-1.4 μm band complex. (B) The N_2 absorption map is a ratio of the average over the band center (2.14-2.16 μm) to that of adjacent wavelengths (2.12-2.14 μm and 2.16-2.18 μm). (C) The CO absorption map is a ratio of the average over the band center (1.56-1.58 μm) to that of adjacent wavelengths (1.55-1.56 μm and 1.58-1.59 μm). Latitude and longitude grids at 30 deg. intervals (shown in C) apply to all maps. Note the large icy patch at the lower-right part of Pluto's disk. It is a large extension of N_2 ice accumulated in a general depression (called Sputnik Planitia) which is about 4-km-deep and 1000-km-wide. As shown by Bertrand and Forget (2016), this region is the main driver for the large changes in pressure observed during a Pluto seasonal cycle. Meanwhile, the distribution of CH_4 and CO ices are also important to constrain better Pluto climatic models (Bertrand et al., 2018).

1.3 Pluto's seasonal models

Pluto has a large obliquity (∼120 deg) and high orbital eccentricty (0.25) that takes the dwarf planet from 30 to 50 au during half of its 248-year orbital period. Equinox occurred in January 1988 and perihelion occurred soon after, in September 1989. Consequently, between 1988 (the first stellar occultation with detailed results) and July 2016 (the most recent occultation considered here), Pluto receded from the Sun, while exposing more and more its northern hemisphere to solar rays.

More precisely, in July 2016, Pluto's heliocentric distance has increased by a factor of 1.12 since perihelion, corresponding to a decrease of about 25% of the average insola-

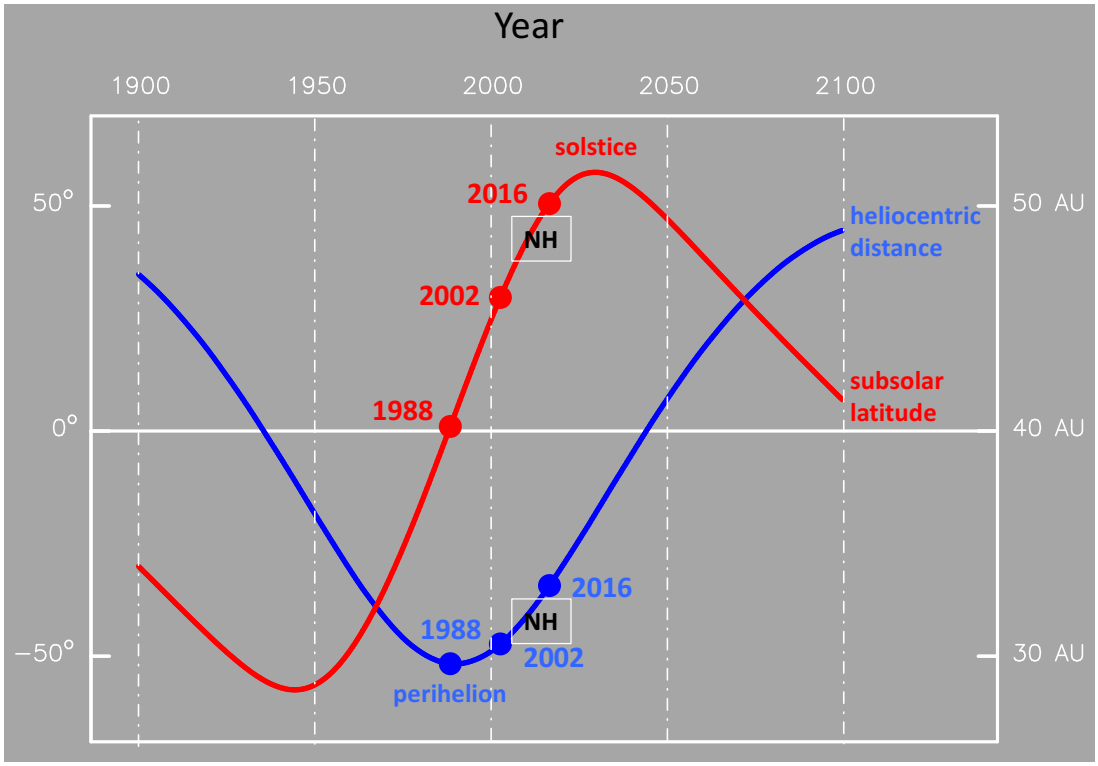

Figure 1.12: The sub-solar latitude (red) and heliocentric Pluto distance (blue) vs. time. Equinox occurred in January 1988 and perihelion occurred in September 1989. The dots mark the occultation observed in June 1988 (Yelle and Elliot, 1997), and the extreme dates of our campaigns (2002–2016). The label "NH" indicates the date of the NASA New Horizons flyby.

tion. Meanwhile, the subsolar latitude has gone from zero degree at equinox to 54 deg north in July 2016, see Fig. 1.12. In this context, drastic seasonal effects are expected, and in fact observed, with an expansion in pressure by a factor of about 2.8 between 1988 and 2016. This strongly suggests that the change in sub-solar latitude is the dominant driver of the atmospheric change. However, the paradoxical anti-correlation between pressure and insolation calls for more studies, and is discussed in more details in Chapter 5.

Pluton's seasonal models can be tackled numerically. The first studies were focused on methane (Stern et al., 1988; Binzel, 1990) and nitrogen (Hansen and Paige, 1996) cycles. Those models predicted that the north and south poles or equatorial region should become reservoirs of methane and nitrogen. Meanwhile, other models were developed to explain the 0.5% methane abundance observed in Pluto's atmosphere (Stansberry et al., 1996). Radiative and conductive models were also developed to study the vertical lower structure of the Pluto's atmosphere (Strobel et al., 1996; Lellouch et al., 2009). The goal of these models is to compare and/or explain spectroscopic and stellar occultation observations of Pluto. In recent years, more models were developed and improved to anticipate the New Horizons Pluto flyby (Hansen and Paige, 1996; Young, 2012, 2013).

After the New Horizons flyby, the Laboratoire de Météorologie Dynamique (LMD) team improved its volatile transport model. Its objective was to simulate the volatile

cycles over seasonal and astronomical timescales on the whole planetary sphere, see details in Bertrand and Forget (2016).

Those authors use a realistic version of the model, taking into account Pluto's topography maps. In particular, they use a permanent reservoir of nitrogen ice in the so-called Sputnik Planitia basin as detected by New Horizons (Schmitt et al., 2017). Bertrand and Forget (2016) use stellar occultations to constrain the parameters of their model.

Those authors predict a significant drop of Pluto's atmospheric pressure in the forthcoming years. Fig. 1.13 shows the surface pressure versus time, compared with the estimated pressure of Sicardy et al. (2016). In Chapter 5, I will present our latest findings, based on both ground-based stellar occultations estimates and Bertrand and Forget (2016); Forget et al. (2017); Bertrand et al. (2018)'s model.

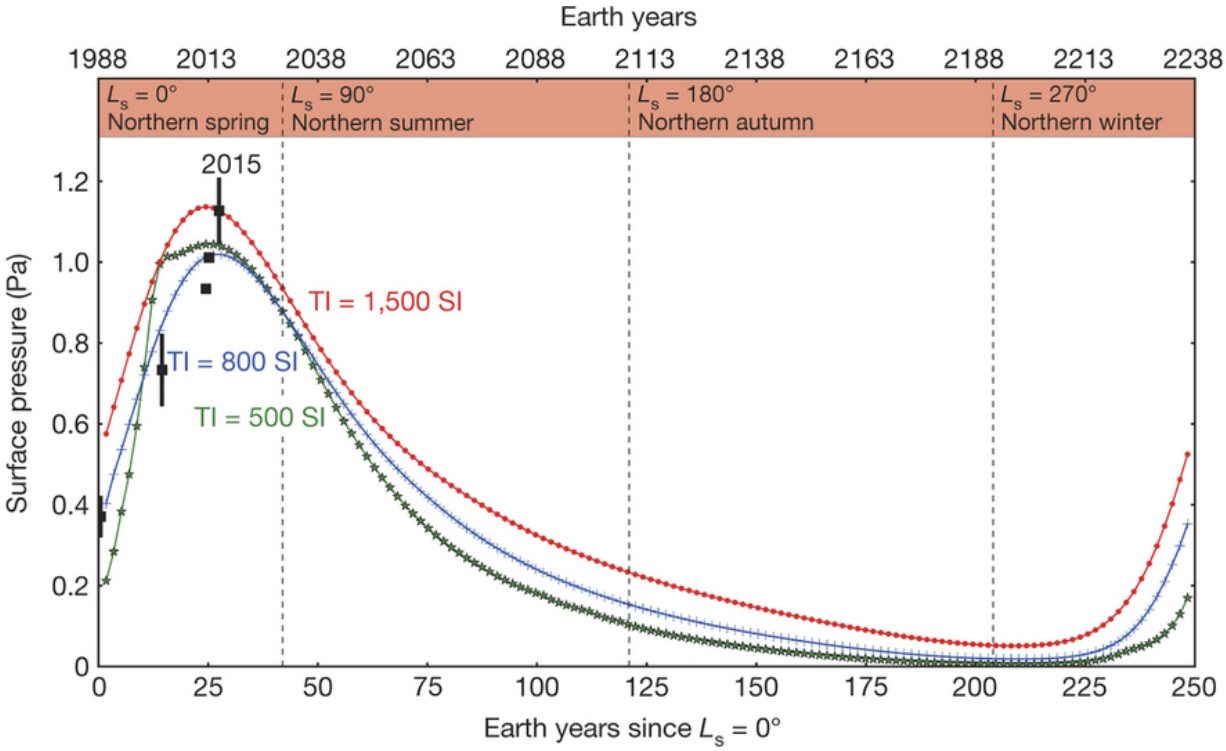

Figure 1.13: Pluto's surface pressure vs time from Bertrand and Forget (2016)

1.4 Results of the New Horizons flyby, a summary

Before entering in the main work of my thesis , I summarize here the main New Horizons findings. The instruments onboard of the New Horizons spacecraft (Fig. 1.14) were aimed at exploring the entire Pluto's system, i.e. the main body, its atmosphere, its largest satellite Charon and smaller companions Nix, Hydra, Kerberos and Styx. Those instruments are:

ALICE: Ultraviolet imaging spectrometer; analyzes composition and structure of Pluto's atmosphere.

REX: (Radio Science EXperiment) Measures atmospheric density, pressure and temperature (down to the surface); passive radiometer.

RALPH: Visible and infrared imager/spectrometer; provides color,composition and thermal maps. Ralph has two separate channels: MVIC (Multispectral Visible Imaging Camera), a visible-light CCD imager with broadband and color channels; and LEISA (Linear Etalon Imaging Spectral Array), a near-infrared imaging spectrometer.

LORRI: (Long Range Reconnaissance Imager) telescopic camera; obtains encounter data at long distances, maps at high resolution, geologic data.

SWAP: (Solar Wind Around Pluto) Solar wind and plasma spectrometer; measures atmospheric escape rate and observes Pluto's interaction with solar wind.

PEPSSI: (Pluto Energetic Particle Spectrometer Science Investigation) Energetic particle spectrometer; measures the composition and density of plasma (ions) escaping from Pluto's atmosphere.

SDC: (Student Dust Counter) Built and operated by students; measures the space dust impacting New Horizons during its voyage across the solar system.

Pluto's size was determined using LORRI data, providing a radius 1188.3 ± 1.6 km (Nimmo et al., 2017)) that is consistent with the value derived from REX, 1189.9 ± 0.2 km (Hinson et al., 2017), and consistent with ground-based occultation estimations of 1190 ± 5 km (Dias-Oliveira et al., 2015). Charon's radius was derived from the LORRI instrument, and the result 606 ± 1.0 km (2-σ, Nimmo et al. 2017), is fully consistent with the values obtained through ground-based observations, 606 ± 8 km (Gulbis et al., 2006) and 604 ± 1.4 km (Sicardy et al. 2006, 1-σ), illustrating the efficiency of this technique. Meanwhile, the small satellites yielded surprises, including unexpected rapid rotations and high obliquity and albedos, and diversity of densities (Showalter and Hamilton, 2015; Weaver et al., 2016).

New Horizons revealed new interesting characteristics on Pluto, such as previously unknown geologic features, surface composition, as well as the thermal structure and composition of its tenuous atmosphere at altitude levels unaccessible to ground-based stellar occultations.

Topography and surface composition

The high-resolution LORRI imager revealed previously unknown geological features like craters, water ice mountains glaciers and bladed terrains. The LEISA instrument provided composition and revealed a mix of nitrogen, methane, carbon monoxide and water ices (Grundy et al., 2016). For instance, Fig. 1.11 shows Pluto's volatiles ice maps obtained by LEISA, overlaid on a LORRI map. Fig. 1.15 shows a topography and morphology Pluto's map (see details in Schenk et al. 2018), while Fig. 1.5 shows Pluto's surface albedo map obtained by LORRI (Buratti et al., 2017). In general, Pluto's surface is reddish in color, due to the tholins which are solid organic complex molecules formed by cosmic rays or UV rays coming from the Sun. Note that tholins are also formed in the atmosphere and rain out to the surface. The temperature variations on Pluto's surface are expected to be about 20 K between the different terrains illuminated by the Sun (Buratti et al., 2017).

An important geological feature of Pluto's surface is the bright Sputnik Planitia (SP herein), see details in Stern et al. (2015); Moore et al. (2016); Schenk et al. (2018). This is a bright region (albedo 0.8-0.9) which contrasts with other dark regions like Cthulhu, that has albedo of only 0.1. The SP basin is a ∼1000-km depression, with typical depth of 4 km relative to the surrounding terrains (Fig. 1.15). It is centered at latitude ∼25 deg north and longitude 175 deg east, thus essentially opposite to Charon. It could be an impact crater formed by objet collision of about 200 km (Moore et al., 2016).

This region is in fact a huge nitrogen glacier that is eventually the main "engine" that controls the seasonal evolution an meteorology of the N_2 atmosphere, through the sublimation of N_2 under the effect of solar rays, see Bertrand and Forget (2016); Forget et al. (2017). A important ingredient of the N_2 cycle developped by the aforementioned authors is that the Sputnik basin being at lower altitude, it has a higher atmospheric pressure, hence a higher condensation temperature, and thus a stronger thermal infrared cooling leading to a higher condensation rate. All together, this explains the location of this N_2 ice reservoir.

The seasonal evolution of Pluto's atmosphere is discussed further in Chapter 5 and Meza et al. (2018), see Appendix, based on my analysis of stellar occultations over the period 2002-2016.

Atmosphere

We now turn to some highlights of the New Horizons results concerning Pluto's atmosphere. A general presentation of NH's atmospheric main results is found in Gladstone et al. (2016), while more specific details are given in other papers quoted below. Those works point out the consistency of the NH results with ground-based observations in general, and stellar occultations in particular, every time a comparison was possible. This confirms the importance and complementarity of ground-based data gathering and space exploration.

The REX experiment (and its connection with my work) is discussed more thoroughly in Chapter 5 and in Meza et al. (2018). Here we note that REX provided density, pressure and temperature profiles of Pluto's atmosphere between the surface (pressures up to 13 μbar) and an altitude of about 115 km, with pressure ∼1.2 μbar

(Hinson et al., 2017). REX is thus complementary to ground-based occultations that can probe atmospheric levels from 380 km altitudes (∼10 nbar) down to about 4 km (pressure ∼10 μbar), below which refraction of stellar rays creates a "blind zone" where no information can be gathered from Earth (Sicardy et al., 2016).

A noteworthy, and new result of REX is the difference of the temperature profiles obtained at entry at local sunset and above the Sputnik Planitia depression, and at exit, obtained over the higher, opposite terrains at sunrise. The deepest (entry) NH REX profile shows a 3.5-km thick troposphere close to N_2 saturation, just above the surface of SP. This is to be expected from the sublimation of nitrogen ice over SP in the afternoon hours.

Turning to the other, upper part of the atmosphere, the ALICE instrument scanned the density profiles of N_2 above an altitude ∼550 km that is unreachable with ground-based occultations (Young et al., 2018). Moreover, the density profiles of minor species, CH_4, C_2H_2, C_2H_4 and C_2H_6 were also detected by Alice down to the surface and described in the same publication.

One interesting finding of the ALICE instrument, together with PEPSSI, is that the the escape rate of nitrogen into space is only $\sim 10^{23}$ molecules per second for N_2 and $\sim 10^{25}$ molecules per second for CH_4 (Bagenal et al., 2016; Young et al., 2018), a small fraction (0.01%) of the pre-New Horizon predictions. Note that the pre-NH estimations predicted that escape was dominated by N_2, not CH_4. As a consequence, the atmosphere appears to be more stable over geological times than previously thought.

This low escape rate stems from the fact that Pluto's upper atmosphere appears to be colder than expected, roughly 70 K instead of the anticipated 100 K. The presence of a mesosphere was in fact already pointed out previous to New Horizons, based on ground-based occultations, see e.g. Dias-Oliveira et al. 2015. The reasons for the unexpectedly cold upper atmosphere are still debated. A possibility is that some minor species compound are radiating away heat to space, hydrogen cyanide (HCN) and acetylene (C_2H_2) being plausible candidates. However, observations with the ALMA radio-telescope array in Chile in 2015 suggest that there is not quite enough HCN present in the atmosphere to explain that cooling (Lellouch et al., 2017).

Another possibility is that heat is radiated away in the mesosphere by the hazes revealed by LORRI (see below), as discussed by Zhang et al. (2017). This still has to be tested against new observations, such as a mid-infrared flux predicted by those authors much higher than previously thought.

The LORRI camera clearly showed the long-searched hazes, as the spacecraft turned its instruments back to the Sun to observe the atmosphere at high phase angle (Gladstone et al., 2016). The highly layered structure of the haze layers is probably associated with gravity waves that force small temperature contrasts that are then responsible for differential saturation of minor species that compose the hazes. Such waves were already detected in ground-based occultations (Sicardy et al., 2003; Person et al., 2008; Hubbard et al., 2009). There were best explained by diurnal sublimation forcing (Toigo et al., 2010), and may have a long-term seasonal dependence that may be tested in future occultation observations (French et al., 2015).

Thus, an appealing new area of study is now the detailed analysis of the haze structure revealed by LORRI, so that to test the sublimation forcing model of Toigo et al. (2010) and Forget et al. (2017). Moreover, it is now worthwhile to investigate

the possible orographic origin of these waves, caused by winds blowing over mountains (Gladstone et al., 2016). In other words, Pluto's hazes may be the tracer of an interesting dynamical activity of this atmosphere.

The estimation of the line-of-sight optical depth of those hazes in the visible bandpass is still preliminary. Based on LORRI data, Cheng et al. (2017) estimates a vertical optical depth of ∼0.018, and a line-of-sight (scattering) optical depth of ∼0.24, with typical scale height of 50 km. This implies that ground-based stellar occultations are little affected by those hazes, except in the deepest part of the occultation light curves, especially during central flash detections. This is discussed further in Chapter 5 and in Meza et al. (2018).

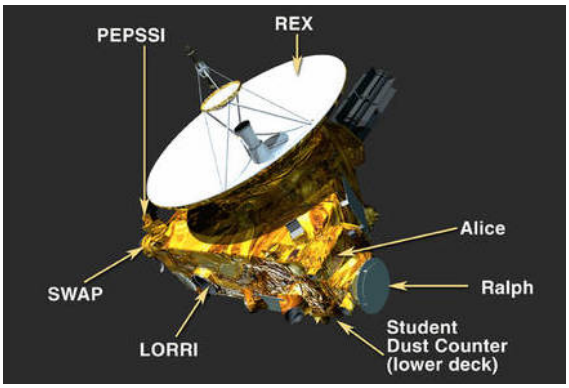

Figure 1.14: Spacecraft instruments on New Horizons: ALICE, REX, RALPH, LORRI, SWAP, PEPSSI and SDC (http://pluto.jhuapl.edu/).

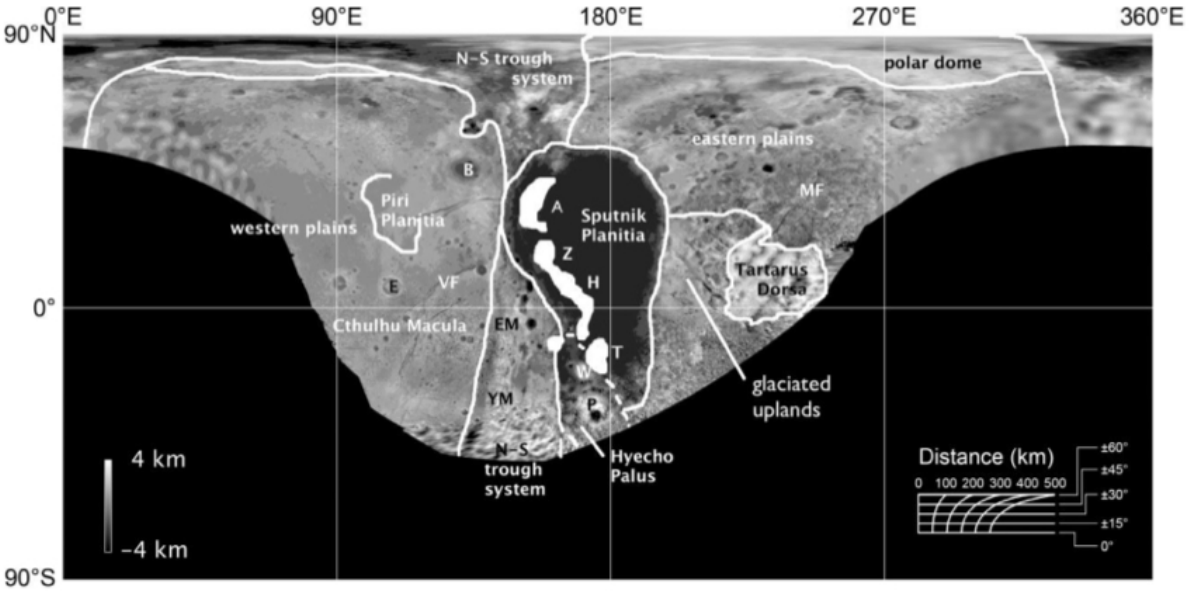

Figure 1.15: Topography map of Pluto outlining major topographic and morphologic features (from Schenk et al. 2018).

1.5 Main goals of this thesis

My thesis work was first mainly focused on instrumentation, observations and data analysis. This entire chain connects the technology of cameras (sensitivity estimations, validation of the timing accuracy and acquisition softwares) to the final product, i.e. an occultation light curve that provides the flux of the star versus time as it is occulted by an airless body or by an atmosphere.

In the meantime, an important aspect of my work has been to organize occultation campaigns (logistics, coordination), to travel to various countries worldwide, and to install fast acquisition cameras on fixed or portable camera, see Fig. 1.16.

This is the “hidden part" of the iceberg (and the most time-consuming!), but obviously an essential part of the scientific projects I worked on. I participated to various campaigns, in particular stellar occultation by an asteroid (117 Irma), Chariklo and its rings and Triton. I also reduced occultation data on other objects, that I did not personally observe. Those works are not presented here, but some of them have been already published (and co-authored by me), see for Pluto: Dias-Oliveira et al. (2015); Sicardy et al. (2016), Chariklo’s rings: Bérard et al. (2017); Leiva et al. (2017) and Haumea ring discovery: Ortiz et al. (2017).

Here I will focus on the following aspects of my work:

- Chapter 2, presents a global view of the occultation technique and how it is used in various contexts, in particular for bodies with an atmosphere.
- Chapter 3 and Chapter 4, present the derivation of the occultation light curves and analysis of eleven ground-based stellar occultations by Pluto between 2002 and 2016, and fit them consistently with a Pluto’s atmospheric model.
- Chapter 5 shows:
  - Derive the evolution of Pluto’s atmospheric pressure, and interpret it in the framework of a seasonal model.
  - Compare ground-based-derived atmospheric profiles with the New Horizons REX results, in the lower part of Pluto’s atmosphere (altitude $<\sim$ 115 km) and
  - Observed occultations are used to improve Pluto’s ephemeris, implementing the Gaia DR2 catalog, released in April 2018.
- Chapter 6 presents conclusions and perspectives of this work.

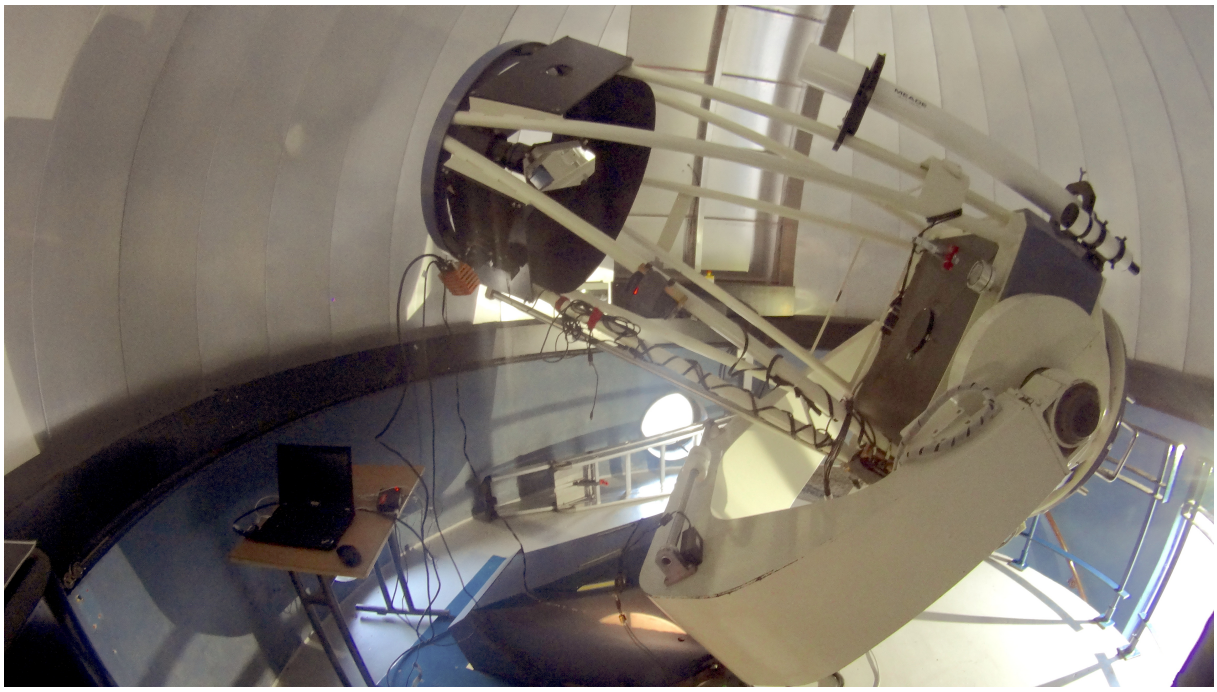

(a)Stellar occultation by Triton on 2017 October 05, at the Saint-Michel observatory in France.

(b)Stellar occultation by Chariklo and its rings on 22 May 2015, at the Pierre Auger observatory in Argentina.

(c)Stellar occultation by Chariklo and its rings on 2017 June 22, at the Cuno Hoffmeister Memorial observatory in Namibia.

Figure 1.16: Installation of a fast camera to observe stellar occultations.

Chapter 2

The stellar occultation technique

Contents

In this chapter, I present various theoretical bases of ground-based stellar occultations that have been used in this work. I also describe more technological aspects of my work, with a brief description of the instrumentation required to observe such events, and comments on the protocols that have to be followed when deriving occultation light curves.

2.1 Refractive occultations

Ground-based stellar occultations probe the tenuous parts of planetary atmospheres, typically from 10 nbar to some tens of μbar levels. Usually, but not always, hazes are absent at those levels and the dimming of the stellar flux is mainly caused the refraction that bends the stellar rays.

Let us consider a luminous ray that propagates in a refractive medium of refraction index $n_{\rm r}$ and let us define the refractivity as $\nu = n_{\rm r} - 1$. We define the vector $\vec{\tau}$ borne by the unit vector $\hat{u}$ along that ray as:

$$\vec{\tau} = (1 + \nu)\hat{u}. \tag{2.1}$$

The Snell-Descartes' refraction law then states that the luminous ray is deviated according to

$$\frac{d\vec{\tau}}{ds} = \nabla\nu, \tag{2.2}$$

where ds is elementary displacement along the ray, where ∇ denotes the gradient. Let us now consider the case of a planetary atmosphere that refracts stellar rays coming from a star at infinity, and going to Earth, also considered at infinity (because its distance D to the body is very large compared to the size of that body), as sketched in Fig. 2.1.

Outside the atmosphere, we have $\nu = 0$, so that $\vec{\tau} = \hat{u}$, and the total variation of the unit vector $\hat{u}$ is

$$\Delta\hat{u} = \int_{-\infty}^{+\infty} \nabla\nu \cdot ds, \tag{2.3}$$

which provides the total deviation of the ray, measured by $||\Delta\hat{u}||$. As noted below, this is a very small quantity for ground-based occultations. More precisely, the deviation ω is given by the projection along the vertical axis $0r$ of $\Delta\hat{u}$, i.e. $\omega = \Delta u = \Delta\hat{u} \cdot \hat{r}$, where $\hat{r}$ is the unit vector along $0r$. Note that with this definition the deviation angle ω is negative (Fig. 2.2).

The deviation of rays in a refractive medium redistributes the initial stellar flux ϕ_0 (as observed outside the occultation) from a surface element dS at the planet level to a surface element $dS' = [1 + D \cdot \partial\omega/\partial r][1 + D \cdot \partial\omega/\partial x]$ in the observer plane, at the distance D from the body.

If the medium is transparent, energy is conserved and the stellar flux ϕ observed in the observer plane is such that $\phi_0/\phi = dS'/dS$, i.e.:

$$\frac{1}{\phi} = \left[1 + D \cdot \frac{\partial\omega}{\partial r}\right]\left[1 + D \cdot \frac{\partial\omega}{\partial x}\right], \tag{2.4}$$

where we arbitrarily take here $\phi_0 = 1$, i.e. we assume that the unocculted stellar flux is normalized to unity. The first term in the equation above describes the *defocusing* of

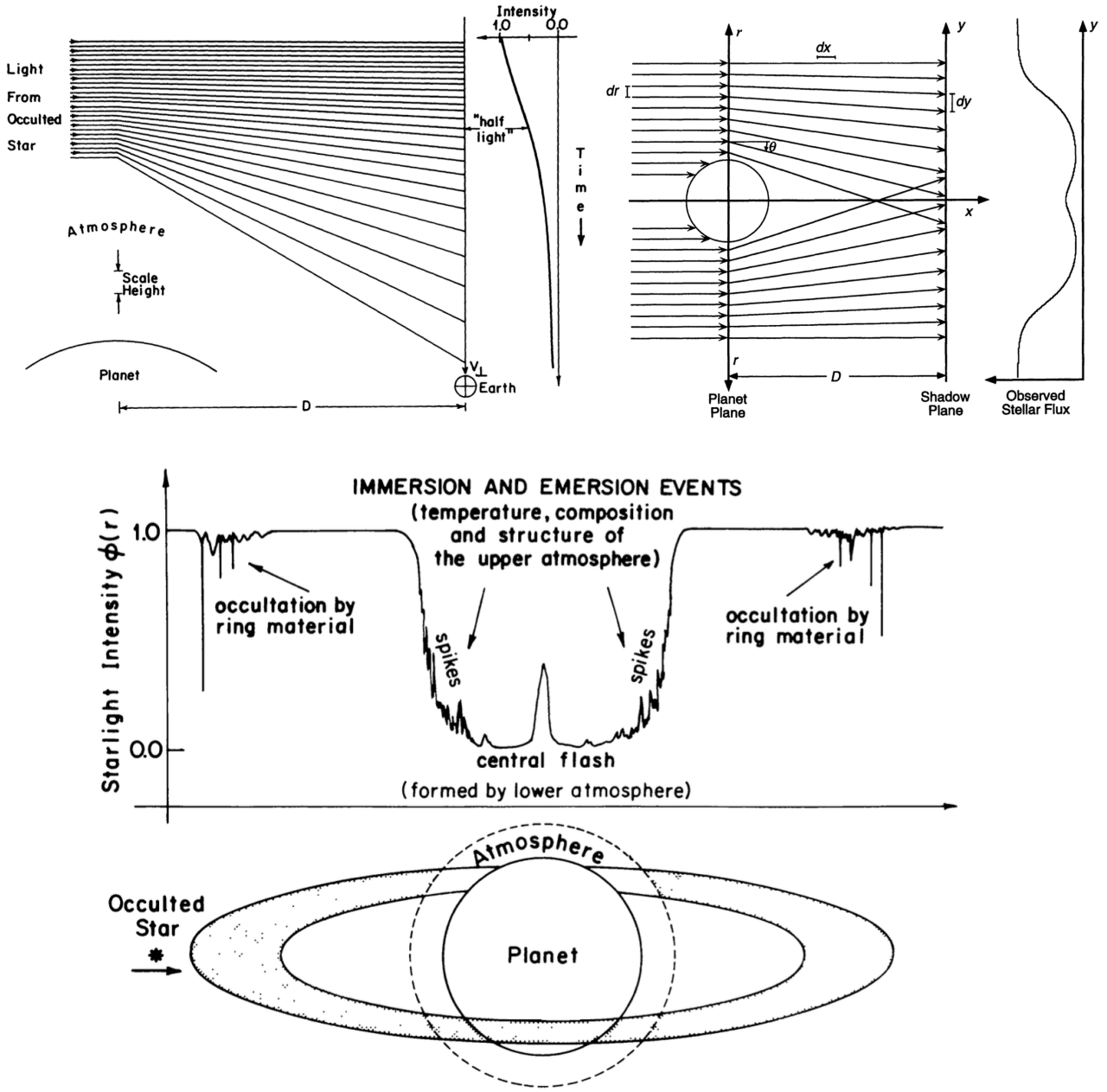

Figure 2.1: Top Left - The basic geometry of a refractive occultation. The stellar rays coming parallel from infinity at left are differentially refracted as deeper (thus denser) atmospheric layers are encountered. Note that the size of the planet and the ray deviations have been greatly enhanced for a better viewing. The observer (on Earth) observes a decay of stellar flux with time as it moves in the observer plane due to the *divergence* of the stellar rays, see also Fig. 2.2. The half-light level is then defined as the moment when the stellar flux has dropped by a factor of two. Top Right - For dense enough atmospheres, rays may cross the center line and cause a central flash, see text. Bottom - The effect on a occultation light curve. The gradual drop is caused by the differential effect depicted at left, with possible "spikes" due to local density fluctuations. Note the presence of a central flash when the star, the planet and the observer are aligned (see text), as well as partial drops caused by potential rings surrounding the planetary body. From Elliot (1979) and Elliot and Olkin (1996).

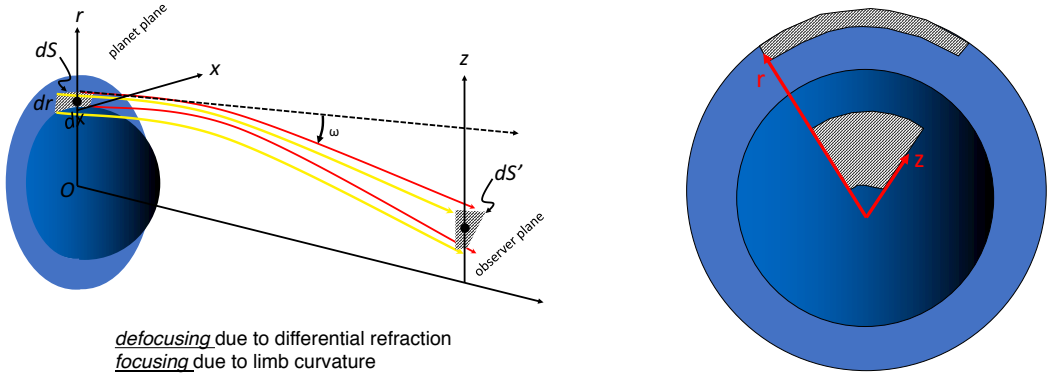

Figure 2.2: Geometry of a refractive occultation, with the competing actions of differential refraction and limb curvature.

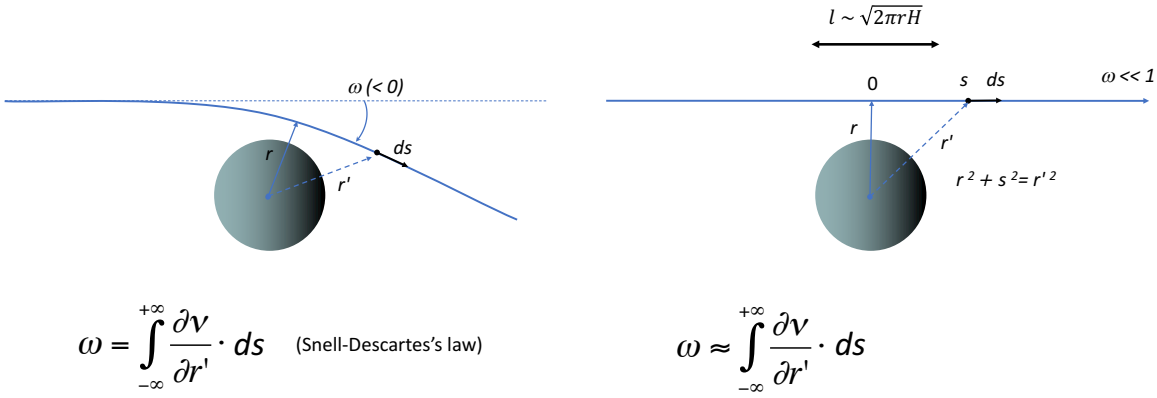

Figure 2.3: The actual ray trajectory (left) can be considered as a straight line for practical purpose (right) when calculating the ray deviation ω, see text. The length l indicates the zone where most of the ray deviation occurs, where r is the typical radius of the probed atmosphere and H its scale height, see text.

the stellar rays due to the locally vertical differential refraction, while the second term describes the *focusing* caused by the limb curvature. Assuming a spherical atmosphere, elementary geometrical considerations show that $1 + D \cdot \partial(\omega)/\partial x = z/r$, where $z = r + D \cdot \omega$ (Fig. 2.2).

Besides differential refraction, absorbing material (e.g. hazes) may decrease the incoming flux by a factor $\exp(-\tau)$, where τ is the optical depth of that material along the line of sight. Thus, the flux ϕ is finally given, for a spherical atmosphere, by:

$$\phi = \left(\frac{1}{1 + D \cdot \dfrac{\partial \omega}{\partial r}} \right) \left(\frac{r}{z} \right) \exp(-\tau). \tag{2.5}$$

Let us now look more closely at the purely refractive factor $1/[1 + D \cdot \partial\omega/\partial r]$, using the geometries depicted in Fig. 2.3.

Note first that the deviation angle ω is very small for ground-based occultations. In

effect, the planet subtends a few arcsec in general, so that $\omega \lesssim 10^{-5}$ rad (from Fig. 2.1). It is in fact much less in the case of Pluto and Triton, which subtend ~ 0.1 arcsec, i.e. a few times 10^{-7} rad. Consequently, the stellar ray shown in Fig. 2.3 (left panel) suffers a very small linear shift in the atmosphere. Most of the ray deviation stems from a length l of a few hundred kilometers traveled in such atmospheres (see below and Fig. 2.3). The deviation in the atmosphere is thus $\sim (l/D)\omega$, i.e. a fraction of meter only. This justifies the straight line approximation shown in the right panel of Fig. 2.3. This does *not* mean that we assume that $\omega = 0$, but instead that we use the straight line approximation to estimate the integral in Eq. 2.3. This said, due to the largeness of D, the deviation of the ray in the observer plane may reach tens of kilometers.

Elementary geometric considerations, combined with the Snell-Descartes' law and the symmetry of the problem (again for a spherical atmosphere) then provides:

$$\omega = 2\int_r^\infty \frac{r}{\sqrt{r'^2 - r^2}} \frac{d\nu}{dr'} dr'. \tag{2.6}$$

Moreover, $\nu = K \cdot n$, where K is the molecular refractivity of the gas. Thus, the refractivity profile $\nu(r)$ is directly linked to the density profile $n(r)$.

A simple, but illustrative, case considers an atmosphere with constant scale height H in molecular density n, for instance an isothermal atmosphere with temperature T and constant gravity acceleration g, in which case:

$$H = \frac{k_B T}{\mu g}, \tag{2.7}$$

where k_B is Boltzmann's constant and μ is the molecular mass. Even if the atmosphere is not isothermal, the calculations below are useful, as planetary atmospheres have basically (and locally) an exponential behavior in density, with a scale height defined as $H = -n/(\partial n/\partial r)$.

Thus, $d\nu/dr' \sim -(\nu/H)\exp[-(r'-r)/H]$, and

$$\omega \sim -2r\nu \int_r^\infty \frac{\exp[-(r'-r)/H]}{\sqrt{r'^2 - r^2}} dr'. \tag{2.8}$$

We now assume that $H \ll r$, i.e. that the atmospheric scale height is much smaller than the size of the body. This condition is safely met for Pluto and Triton, which have $H \lesssim 50$ km and $r \sim 1000$ km. Using $r'^2 - r^2 \sim 2r(r'-r)$, we eventually obtain, after posing $v = \sqrt{(r'-r)/H}$:

$$\omega \sim -2\nu\sqrt{\frac{2r}{H}} \int_0^{+\infty} \exp(-v^2) dv = -\nu\sqrt{\frac{2\pi r}{H}} \tag{2.9}$$

This equation shows that most of the contribution to the region where $v =$ a few times unity. In fact, it can be shown from the equations above that the column density traversed by the ray with closest approach r is:

$$\sigma_n(r) = \int_{-\infty}^{+\infty} n(r') \cdot ds = n(r)\sqrt{2\pi r H}. \tag{2.10}$$

This means that most of the contribution to the deviation (and to absorption, in case of hazes) comes from a length along the $0s$ axis (Fig. 2.3) of:

$$l \sim \sqrt{2\pi r H}. \tag{2.11}$$

With typical $r \sim 1500$ km and $H \sim 20 - 50$ km for Pluto or Triton, we obtain $l \sim 400 - 700$ km, as announced earlier. Ignoring for the moment limb curvature and haze absorption, Eq. 2.5 then provides

$$\frac{1}{\phi} = 1 - \frac{D\omega}{H} = 1 + \nu\sqrt{\frac{2\pi r D^2}{H^3}}. \tag{2.12}$$

This shows that the stellar flux reaches half of its unocculted value ("half light level") for

$$\omega_{1/2} = -H/D. \tag{2.13}$$

So, a useful rule of thumb is that the half light ray is deviated by one scale height H when it arrives at the observer (here, on Earth). This occurs for

$$\nu_{1/2} = \sqrt{\frac{H^3}{2\pi r D^2}}, \tag{2.14}$$

corresponding to a molecular density $n_{1/2} = \nu_{1/2}/K$. So, the larger the scale height H, the denser the half light level probed in the atmosphere. Conversely, the larger the distance D, the smaller $n_{1/2}$. This explains why ground-based observations, for which D is very large (billions of kilometers for Pluto and Triton), can probe very tenuous pressure levels ($\sim \mu$bar) and still cause significant stellar drops.

Remembering that the point of arrival z of the stellar ray in the observer plane is $z = r + D\omega$ (Fig. 2.2), and from the definition of the half-light level (denoted with subscript 1/2), we have

$$\begin{aligned} \frac{1}{\phi} &= 1 + \frac{r - z}{H} \\ 2 &= 1 + \frac{r_{1/2} - z_{1/2}}{H}, \end{aligned} \tag{2.15}$$

Thus

$$\frac{1}{\phi} - 2 = \frac{r - r_{1/2}}{H} - \frac{\Delta z}{H}, \tag{2.16}$$

where $\Delta z = z - z_{1/2}$. Moreover, $\omega = \nu\sqrt{2\pi r/H}$ and $\omega_{1/2} = \nu_{1/2}\sqrt{2\pi r_{1/2}/H}$. The rapidly varying variable being $\nu(r)$ (when compared with r), we obtain $\omega/\omega_{1/2} = \nu/\nu_{1/2} = \exp[-(r - r_{1/2})/H]$. Using Eq. 2.12 for ω and $\omega_{1/2}$, we finally get

$$\frac{1}{\phi} - 1 = \frac{\omega}{\omega_{1/2}} = \exp\left[-\left(\frac{r - r_{1/2}}{H}\right)\right] \tag{2.17}$$

Introducing this relation in Eq. 2.16 finally provides:

$$\frac{1}{\phi} + \log\left(\frac{1}{\phi} - 1\right) - 2 = -\frac{\Delta z}{H}, \tag{2.18}$$

called the Baum and Code equation (Baum and Code, 1953). Because Δz is the distance traveled by the observer in the occultation shadow (Fig. 2.1), it is directly related to time t through $\Delta z = v \cdot (t - t_{1/2})$, where v is the velocity of the observer in the shadow plane. Thus, the Baum and Code formula is an implicit equation that provides the light curve $\phi(t)$, Classical numerical methods then give $\phi(t)$, see examples in Fig. 2.4.

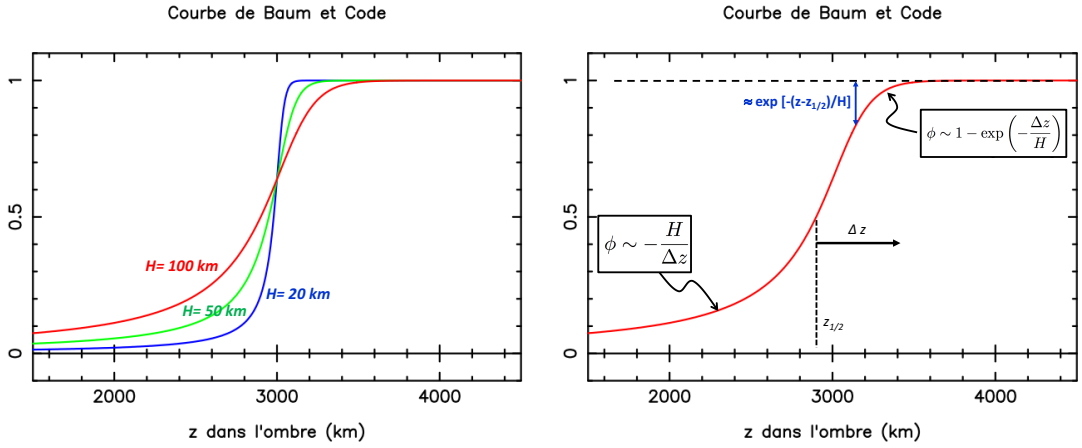

Figure 2.4: Left: typical Baum and Code occultation light curves (Eq. 2.18) for geocentric distances typical of Pluto or Triton. Note that the drop becomes steeper as the scale height H decreases, i.e. for colder atmospheres. Right: Behavior of the Baum and Code function for the limiting cases discussed in the text.

As expected, $\phi = 1/2$ for $\Delta z = 0$. Another limiting case occurs for $\Delta z \gg H$, i.e. at the edge of the occultation shadow, for which:

$$\phi \sim 1 - \exp\left(-\frac{\Delta z}{H}\right) \tag{2.19}$$

This means that a few scale heights above the half light level, the occultation light curve rapidly tends towards unity. At some point, the stellar drop $\exp(-\Delta z/H)$ is lost in the noise of the light curve, and no useful information about the atmosphere is available anymore.

More precisely, let us denote n_σ and r_σ the molecular density and corresponding radius where the stellar drop is equal to the standard deviation of the flux, σ_Φ. From Eq. 2.12, this happens for

$$n_\sigma \sim \frac{\sigma_\Phi}{K}\sqrt{\frac{H^3}{2\pi r D^2}}. \tag{2.20}$$

This equation allows us to estimate the highest level where information is available, considering the noise in the data, the distance of the body, the nature of the gas and the properties of the atmosphere.

Conversely, when Δz is negative with large absolute value, we have:

$$\phi \sim -\frac{H}{\Delta z}, \tag{2.21}$$

showing that the stellar drop proceeds rather mildly deep into the occultation shadow. However, this does not account for the limb curvature, which increases the signal near the shadow center (Eq. 2.5).

2.2 Stellar images

2.2.1 Stellar diameters

We now turn to the behavior of the stellar image as it gets refracted by a planetary atmosphere. Stellar diameters have typical apparent *angular* sizes of

$$\theta_* \sim 4.7 \times 10^{-0.2V} \times 10^{+0.223(V-K)} \text{ mas}, \tag{2.22}$$

in milli-arcsec (mas), where V and K are the apparent magnitudes in the respective colors (see van Belle 1999, and Kervella et al. 2004 for more details). Note that red stars (with large $V-K$) have larger angular diameter for a given visual magnitude V. This stems from Stefan's law that states that cooler, and thus redder, black bodies have lower surface emissivity. The angle θ_* can be projected at the planet geocentric distance D_{au} (in astronomical units) and re-expressed as a *linear* diameter:

$$D_* \sim 3.4 \times D_{au} \times 10^{-0.2V} \times 10^{+0.223(V-K)} \text{ km}. \tag{2.23}$$

The redness $V-K$ assumes a large range of values according to the stellar type and interstellar reddening, but a value $V-K \sim 2$ is typical. For Pluto or Triton, $D \sim 30$ au, while the occulted stars have typical magnitude ranges $V \sim$ 12-16. This provides typical $D_* \sim 0.1-1$ km. This is the *apparent* size of the stellar diameter projected at the planet distance. Thus, it sets the spatial resolution reached by this technique, which is almost three orders of magnitude better that provided by any current ground-based imaging systems. This said, note in passing that the Gaia catalogs (Gaia Collaboration et al., 2018) will provide interesting constraints on the star distances, reddening, and spectral type that can be useful for better planning future stellar occultations (optimum choice of filters, stellar diameter estimation for choosing the time sampling, etc).

The ultimate resolution is in fact imposed by the Fresnel diffraction, which corresponds to a characterictics scale $\lambda_F = \sqrt{\lambda D/2}$, where λ is the wavelength of observation. It can re-written as $\lambda_F \sim \sqrt{\lambda_{\mu m} D_{au}/2} \sim 1$ km for visible or near-IR observations, using $D \sim 30$ au. Consequently, the smoothing of the light curve caused by stellar diameter and diffraction in the case of ground-based stellar occultations by Pluto and Triton are of same order of magnitude, and must be examined on a case by case basis.

2.2.2 Refracted images

The differential refraction causes the shrinking of the stellar image perpendicular to the local gradient of refractivity, i.e. essentially the local vertical direction (Fig. 2.5). If the planetary atmosphere is transparent, the surface brighness per unit solid angle of the refracted stellar image is conserved. Consequently, the stellar flux is proportional to the area of the refracted stellar image. To our knowledge, the first realization of this effect was discussed by Fabry (1929) in his considerations on "Le rôle des Atmosphères dans les Occultations par les planètes", see Fig. 2.5.

This is a dual but equivalent interpretation of the ray divergence displayed in Fig. 2.1. Note that as the stellar image shrinks, the vertical spatial resolution of the occultation increases, revealing finer details in the atmosphere.

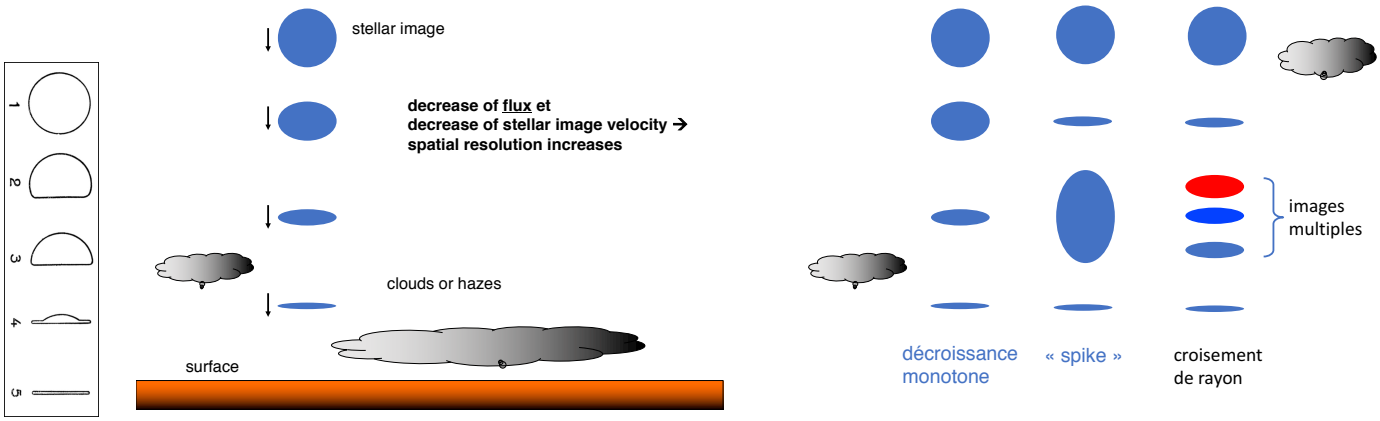

Figure 2.5: Left - The shrinking of a stellar image during an occultation by a planetary atmosphere at successive times 1,...5, as described by Fabry (1929). In this panel, the planet limb is at the bottom of the stellar image. Center - The smooth shrinking of the refracted stellar image as it gets deeper in the atmosphere. The stellar flux is proportional to the area of the image, corresponding to a decrease in the example shown here. This is equivalent to the divergence of rays displayed in Fig. 2.1. Right - Due to small local density fluctuations, the stellar rays may converge (instead of diverging), causing an expansion of the image, and thus a local increase of stellar flux, or "spike". If the fluctuation reaches a critical value, ray crossing may occur, causing multiple images, see more details in Fig. 2.6.

Complications arise due to the fact that the density profile $n(r)$ may have local fluctuations. Due to the largeness of the distance D, those fluctuations need not to be large to cause a focusing of the stellar rays that counteracts locally the general flux drop. In fact, it may occur that the differential bending shown in Fig. 2.1) is more than compensated by local fluctuations, creating ray crossings, and multiple images. Because those images cannot be resolved by current imaging systems, an observer does not know if ray crossing occurs, causing a net loss of information (Sicardy et al., 1999).

2.2.3 Primary and secondary images

If the atmosphere is dense enough, the rays that go deep into the atmosphere may be so deviated that they cross the center line that connects the star, the planet and the observer (Figs. 2.1 and 2.2). Then, the ray intersects the observer plane at negative z's . This creates (1) the appearance of two stellar images along the limb and (2) the possibility to observe a central flash.

An example is given in Fig. 2.7. Note that the refracted stellar images graze Pluto' limb at an altitude of a few kilometers. Therefore, they serve as probes of the atmosphere close to the surface, with potential detection of hazes or even topographic features that could block momentarily the stellar flux. Another example is provided in Fig. 2.8, where adaptive optics permits to resolve the body, and the two refracted images.

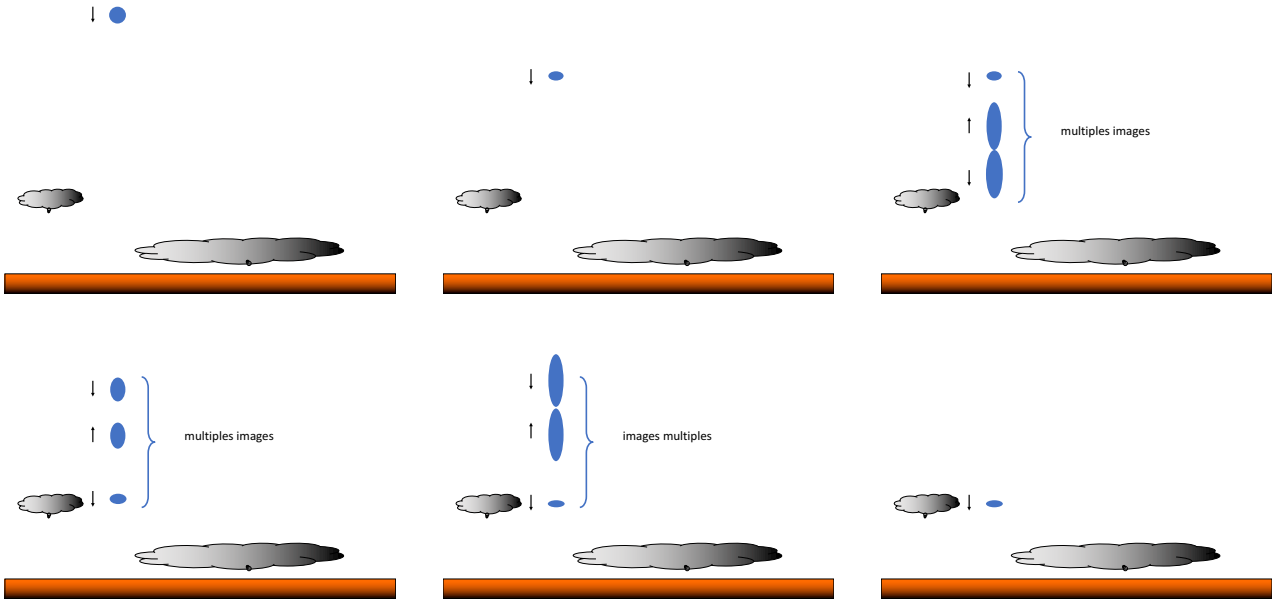

Figure 2.6: A cartoon showing the sequence of images appearing in case of ray crossing (see also fig. 2.5). For a brief interval of time, three images may appear, all contributing to the increase of stellar flux. The images being unresolved, this ray crossing cannot be documented, causing a loss of information.

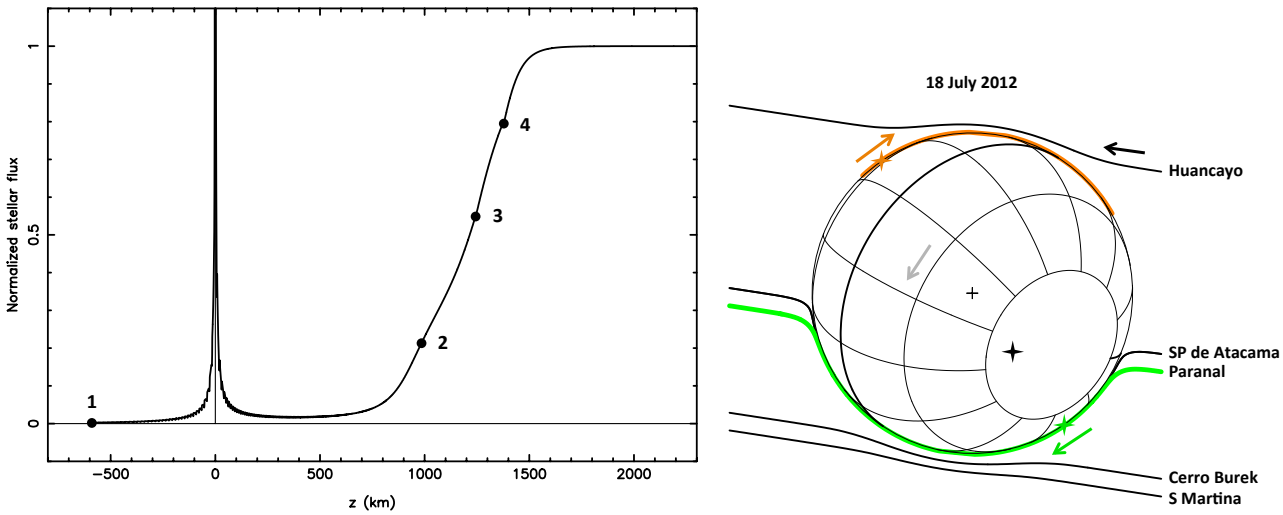

Figure 2.7: Left - The stellar flux caused by Pluto's atmosphere along the z-axis in the observer plane (Fig. 2.2), for the July 18, 2012 stellar occultation. At any position z, an observer detects the flux $\phi_1(z)$ of the primary image that corresponds to the value of the function drawn in black, plus the flux $\phi_2(z) = \phi_1(-z)$ from the secondary image. In other words, the total flux is the sum of the function $\phi_1(z)$ and its mirror value after swapping ϕ_1 with respect to the $z = 0$ vertical axis. Right - The trajectory of the primary (or near-limb) stellar image is shown in green, while the motion of the secondary (or far-limb) image is shown in orange, as seen from the Paranal site in Chile. At any moment, and for a spherical atmosphere, the primary images (green star symbol), the position of the star behind Pluto (black star symbol), Pluto's center (cross) and the secondary images (orange star symbol) are aligned. The light-gray arrow indicates the direction of Pluto's rotation, and the other arrows indicate the motions of the various stellar images. Note that the primary and secondary images move in opposite directions. Taken from Dias-Oliveira et al. (2015).

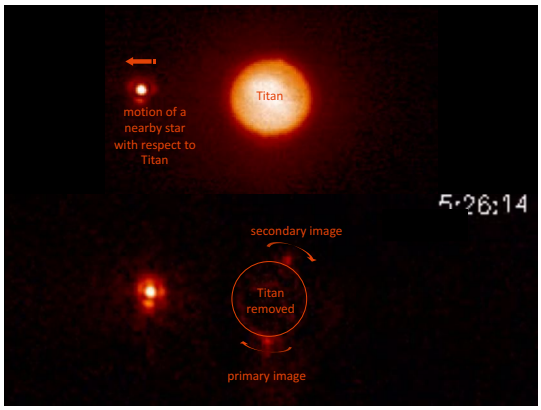

Figure 2.8: An observation where the primary and secondary images are resolved thanks to adaptive optics during an occultation by Titan on December 20, 2001, observed from the 5-m Palomar Hale telescope. The occulted star (behind Titan) has two images that are clearly visible once Titan's resolved disk image has been subtracted. Taken from Bouchez (2004).

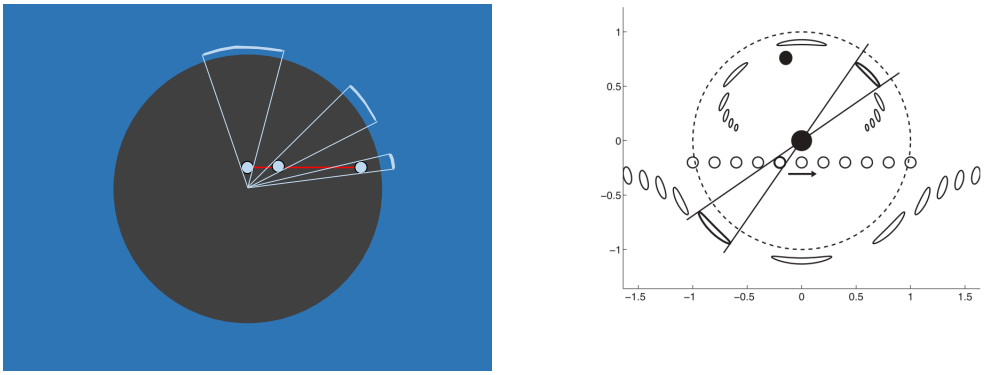

Figure 2.9: Left - The stretching of the stellar images (light blue “filaments" along the limb) as the star get closer to Right - The same process occurs during a microlensig event. Here a background star (open dots) has a elongated image due to the bending caused by the mass of a foreground star (larger black dot) and its planet (smaller black dot). From Abe et al. (2013).

2.3 Central flash

The term r/z in Eq. 2.5 stems from the focusing of stellar rays by the limb of a *spherical* planet. The stellar image then is stretched along the planet limb as depicted in Fig. 2.9. Thus, if the medium is transparent, the stellar flux increases as the shadow center is approached, as expected from the r/z factor. This is akin to what happens during lensing or microlensing events caused the ray bending of remote sources by an intervening galaxy or star. The only difference then is that the bending stems from general relativity (thus, the mass of the lens) rather that refraction, see Fig. 2.9.

The maximum value of the flash intensity is reached when the observer, the body and the star are perfectly aligned. Then the stellar image is a ring surrounding the planet (equivalent to the Einstein ring in the lensing process) with circumference $2\pi r$ and width ϕ_c, where ϕ_c is the stellar flux ϕ at the shadow center without the focusing term (and $\tau = 0$) in Eq. 2.5. The surface of such ring is thus $2\pi r\phi_c D_*$, while the surface of the stellar image outside the occultation is $\pi D_*^2/4$. Accounting for the fact that two images (primary and secondary) are present, the ratio gives the maximum flash intensity caused by a star of diameter D_*, assuming a spherical, transparent atmosphere:

$$\phi_{\text{flash max}} = 16\frac{r}{D_*}\phi_c. \tag{2.24}$$

Considering that $\phi_c \sim$ a few percent for occultations by Pluto or Triton, $r \sim 1500$ km and $D_* \sim 1$ km, we see that even accounting for the finite stellar diameter, the theoretical flash can reach several hundred times the unocculted stellar flux.

Again, complications arise as the atmosphere is usually not spherical. The centers of curvature of the limb are not collapsed at the center of a circle, but follow a locus called evolute of the limb. An example is given in Fig. 2.10 in the case of an oblate atmosphere with elliptical shape. The evolute is then a diamond-shaped curve, where observers see a discontinuous rise of signal caused by a caustics.

Flashs are interesting because they are very sensitive to the shape of the atmosphere, which is turn is supported by possible winds present in the atmosphere. In the simplified

case of zonal winds, the wind velocity $\vec{v}$ is directed along a parallel at constant latitude ϕ (not to be confounded with the stellar flux used in the previous sections). This creates centrifugal forces that must be balanced by a local pressure gradient, which in turns defines an isobaric level $r(\phi)$. In the simple case where the temperature is considered as constant along the isobar, the level $r(\phi)$ also defines an isopycnic (constant density) level.

The hydrostatic equilibrium requires that the gravity, centrifugal acceleration and pressure gradient balance (Sicardy et al., 2006):

$$\nabla p = -\rho \left\{ \vec{g} - \left[v^2(r,\phi)/r_\perp \right] \cdot \hat{u}_\perp \right\}, \tag{2.25}$$

where p is the pressure, ρ is the mass density, $\vec{g}$ is the acceleration of gravity, $v(r,\phi)$ is the zonal wind velocity at distance r from the planet center and at latitude ϕ, $r_\perp$ is the distance to the planet spin axis, and $\hat{u}_\perp$ is the unit radial vector perpendicular to the planet spin axis,

The shape $r(\phi)$ of the isobar is obtained from Eq. 2.25, implying that the isobaric surface is always perpendicular to the vector $\vec{g} - [v^2(r,\phi)/r_\perp] \cdot \vec{u}_\perp$, yielding:

$$\frac{1}{r}\frac{dr}{d\phi} = -\frac{f \cos\phi \sin\phi}{1 - f\cos^2\phi}, \tag{2.26}$$

where $f = r^3\Omega^2/GM = rv^2/(GM\cos^2\phi) \ll 1$ is the rotation parameter, Ω is the angular velocity of the atmosphere, G is the gravitational constant and M is the planetary mass. Note that Eq. 2.26 can be inverted, yielding the zonal wind velocity (r,ϕ), once the shape $r(\phi)$ of the isobaric level has been derived from the central flash:

$$v^2 = -gr\frac{(dr/d\phi)}{\tan(\phi) - (dr/d\phi)/r}. \tag{2.27}$$

Another application of interest obtained from central flashes is the detection and study of hazes. Corresponding to the rays going the deepest in the atmosphere, the flash is the most sensitive part of the light curve to detect such hazes. The amplification of the stellar flux due to the limb curvature further helps to detect haze effects.

An example is given in Fig. 2.11, where the central flash observed during a stellar occultation by Titan is detected at the same place but with different filters. The conspicuous differences between the light curves in I and K bands reveals a strong chromatic effect, which in turns can constrains the optical properties of the aerosols, see Sicardy et al. (2006).

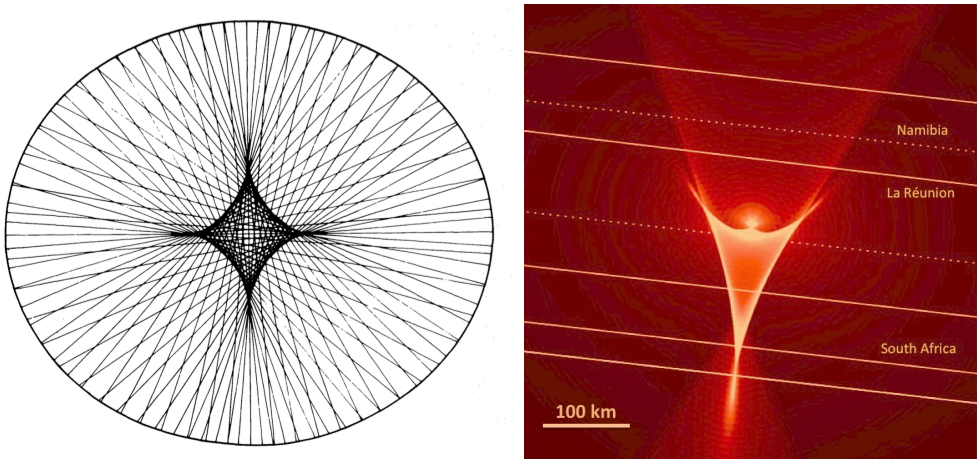

Figure 2.10: Left - A sketch showing the ray propagation perpendicular to the limb in the shadow of an oblate (here elliptical) atmosphere. The convergence of the rays near the center creates an evolute which in turn causes caustics where the flux suffers sudden increases. The oblateness of atmosphere has been greatly exagerated for a better viewing of the evolute. Taken from Elliot et al. (1977). Right - More complex evolutes may appear if the atmosphere is not elliptical, here in the case of a central flash observed during a stellar occultation by Titan on November 14, 2003. Taken from Sicardy et al. (2006).

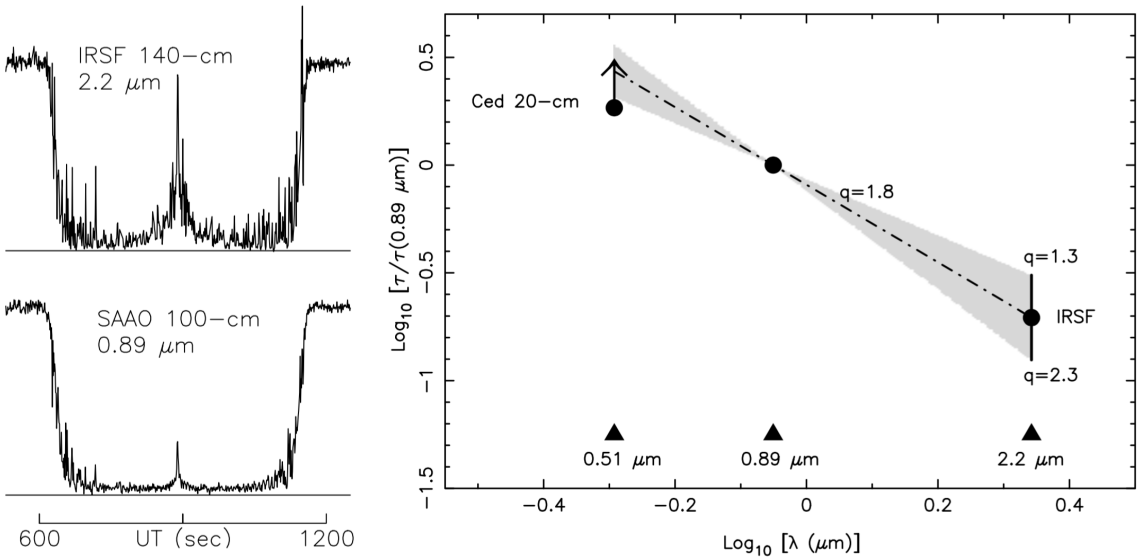

Figure 2.11: Left - The Titan central flash of November 14, 2003, observed at the same station (Sutherland, South Africa) in two different bands. Note the strong absorption of the flash in the visible (0.89 μm), when compared to near IR (2.2 μm). Right - The derived chromatic dependence of the light-of-sight optical depth after the comparison of the various flashs observed during the November 14, 2003 occultation. The index q describes here the variation of the line of sight optical depth as a function of wavelength, as $\tau \propto \lambda^{-q}$. From Sicardy et al. (2006). Note that central flash observed during stellar occultation by Pluto on 2017 July 31 in two channels (0.51 and 0.76 μm) does not show differential extinction (Olkin et al., 2014), indicating that Titan hazes extinction model cannot be applied to Pluto.

2.4 Inversion method

This technique refers to the retrieval of the atmospheric structure (density, pressure and temperature profiles) from the occultation light curve. Several works have been published on that topic. Here we refer to Vapillon et al. (1973), from whom most of the equations have been used.

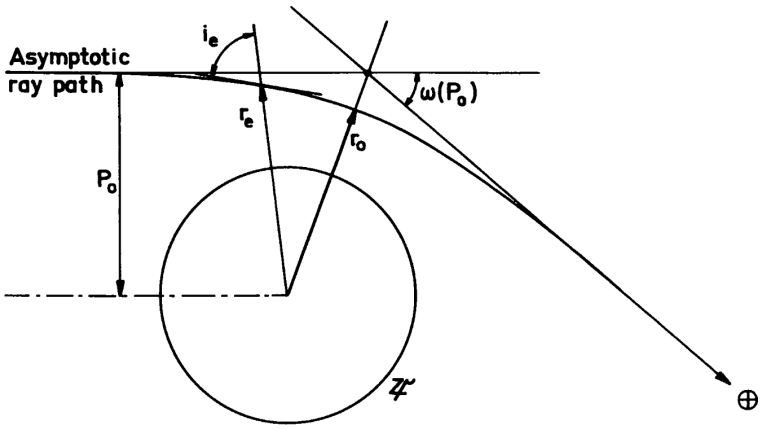

Figure 2.12: The geometry and nomenclature of the ray bending for describing the inversion method, see text. From Vapillon et al. (1973).

The basic geometry and nomenclature used by those authors are displayed in Fig. 2.12. In all the procedure described below, the atmosphere is assumed to have spherical symmetry and to be transparent. A ray coming from infinity has its closest approach to the planet at r_0. We denote $p_0 = p(r_0)$ the incoming impact parameter of the ray and $\omega(r_0)$ its overall deviation before being re-directed to Earth. As a consequence of the Snell-Descartes' law, the following quantity

$$n_{\rm r}(r) \cdot r \cdot \sin(i) = n_{\rm r}(r_0) \cdot r_0 = p_0 \tag{2.28}$$

is conserved (a result referred to as Bouguer's rule), where we recall that $n_{\rm r}$ is the index of refraction at radius r (not to be confounded with the molecular density n). The variations of the angle i during the ray propagation can then be related to the variations of ω, yielding

$$\omega(r_0) = \int_{r_0}^{\infty} \frac{2p(r)}{n_{\rm r}(r)} \frac{dn_{\rm r}(r)}{dr} \frac{dr}{\sqrt{[n_{\rm r}(r) \cdot r]^2 - [n_{\rm r}(r_0) \cdot r_0]^2}}. \tag{2.29}$$

This Abelian integral can be inverted to yield the index of refraction $n_{\rm r}(r_0)$ at the point of closest approach r_0, for which the total deviation is ω_0 (see details in Phinney and Anderson 1968; Fjeldbo et al. 1971):

$$n_{\rm r}(r_0) = \exp\left\{ \frac{1}{\pi} \int_0^{\omega_0} \log\left[\frac{p(\omega)}{p_0} + \sqrt{\left(\frac{p(\omega)}{p_0}\right)^2 - 1} \right] \cdot d\omega \right\}. \tag{2.30}$$

At this point, we need the deviation angle ω and the corresponding impact parameter $p(\omega)$ for all the rays that have been intercepted before the current ray deviated by ω_0.

The observation provides the stellar flux ϕ vs. time (and thus z), from which $\partial\omega/\partial r$ can be extracted using Eq. 2.5, where we assume that the medium is transparent, i.e. $\tau = 0$. Recalling that $z = p + D\omega$ (Fig. 2.12) and $z/r = 1 + D \cdot \partial(\omega)/\partial x$, we have:

$$\omega(t) = \frac{1}{D} \int_{-\infty}^{z(t)} \left(1 - \frac{z}{r}\phi\right) \cdot dz \tag{2.31}$$

This integral provides the deviation angle $\omega(t)$ that the ray, received at time t (and thus $z(t)$), has suffered during the refraction process. Then $p = z - D\omega$ gives the initial impact parameter of that ray, which finally allows to perform the integral in Eq. 2.30.

Once this is done, the molecular density profile $n(r)$ is immediately derived from $n(r) = \nu(r)/K$, where $\nu = n_{\rm r} - 1$ and K is the molecular refractivity defined earlier. The value of K in visible bandpass is given by $K = 1.091 \times 10^{-23} + (6.282 \times 10^{-26}/\lambda_{\mu m}^2)$ cm^3 molecule^{-1} (Washburn, 1930). The relevant value of the REX experiment 4.2 cm is $K = 1.095 \times 10^{-23}$ cm^3 molecule^{-1} (Hinson et al., 2017).

Using the hydrostatic equation

$$\frac{dp}{dr} = -\mu n(r) g(r), \text{ with } g(r) = \frac{GM}{r^2} \tag{2.32}$$

(where μ is the molecular mass and g the local gravity) and the ideal gas equation $p = nk_BT$, one obtain the following differential equation for $T(r)$:

$$\frac{dT}{T} = -\left[\frac{\mu g(r)}{k_B T} + \frac{1}{n}\frac{dn}{dr}\right] \cdot dr \tag{2.33}$$

Note that the primary (and more robust) result of the inversion is the density profile $n(r)$. Meanwhile, the temperature profile $T(r)$ suffers an unavoidable mathematical uncertainty due to the fact that it is derived from a first-order differential equation, and thus requires an initial condition $T_0 = T(r_0)$. In other words, an infinity of profiles $T(r)$ can explain the same observable (here, the occultation light curve). The choice of $T_0 = T(r_0)$ thus requires an independent information, e.g. the temperature derived from a spacecraft at some radius r_0 or a physical discussion that restricts the range of values for $T(r_0)$.

2.5 Ray tracing method

Several difficulties may hamper the inversion method. First, that method becomes unstable if the signal-to-noise ratio is not sufficient, or if the sampling of the light curve is too coarse. Second, as the observer gets close to the centrality, the two stellar images have comparable fluxes, an effect which is not accounted for in Eq. 2.31 since the observed flux ϕ is assumed to stem from only one image. Third, hazes may absorb part of the signal, biasing the retrieved profiles $n(r)$, $p(r)$ and $T(r)$.

In frequent cases, we need more global and less detailed parameters than provided by the inversion technique. For instance, one may be interested mainly at the pressure at some prescribed radius (e.g. at the surface), or some gross features of the temperature profile: thickness of the stratosphere, average temperature gradient in the mesosphere, etc...

In those cases, a *direct* method is more appropriate. We define first some a priori temperature profile $T(r)$, set the pressure at some prescribed radius r_0, use the ideal gas equation to obtain the corresponding density $n(r_0)$, and use Eq. 2.33 to obtain $n(r)$. Once this is done, the refractivity profile $\nu(r) = n(r)/K$ and its gradient $d\nu(r)/dr$ are also obtained. Finally, the integral in Eq. 2.3 can be performed numerically (this is the core of the ray-tracing code) to provide the deviation of each ray, and then the synthetic flux through Eq. 2.5.

Least-square fits to the observed light curves then determine the best-fitting parameters like the pressure at some level r_0, and their associated error domains, through a χ^2 minimization scheme. This method has the advantage of having a small number of free parameters, and account for the quality of each light curve (i.e. weighing them according to their respective noise level) using a unique, consistent model.

Moreover, as it is easy to include both the primary and secondary images in the ray tracing code, a useful feature when it comes to reproduce central flashes. This is discussed in more details in the Chapter 5.

Chapter 3

Sensitive test of fast cameras and deriving occultation light curves

Contents

3.1 Sensitive test of fast cameras

To reconstruct the sizes and shapes of distant solar system bodies (Braga-Ribas et al., 2014; Bérard et al., 2017; Leiva et al., 2017; Ortiz et al., 2017) and probe tenuous atmospheres (Sicardy et al., 2006; Dias-Oliveira et al., 2015; Sicardy et al., 2016) from ground-based occultations, an observational system and light-curve derivation need to meet the following requirements:

1. Sensitive fast cameras with no dead time between images;
2. A reliable time registration system and an adapted acquisition software, see details in (Leiva, 2017);
3. The best photometric protocol as possible.

The Lucky Star project acquired two kinds of fast cameras, the EMCCD Kite based on an Electro-Multiplied CCD[1], and the CMOS ZWO ASI178MM-Cool[2]. Both cameras are controlled with the Genika software[3] and use a TimeBox[4] as a time registration system. Table 3.1 summarizes the main features of the Kite and ZWO cameras.

In order to assess the sensitivity in real sky conditions, I performed two observational tests, one at Pic du Midi observatory (T1m) and one at the Observatorio Astronomico de la Universidad Nacional de Ingenieria, Peru, OA-UNI (T0.5m) on 2016 November 04 and 2016 August 18 respectively. Targets are well known photometric fields of view NGC2158 (T1m) and M25 (T0.5m), where the stars have a large range of magnitudes.

The photometric reduction of those fields is presented in Fig. 3.1, more exactly, it shows the SNR estimate on each star versus its G magnitude (Gaia Collaboration et al., 2016), noting that this band is a good proxy for the spectral responses of both cameras. At Pic du Midi, both cameras were tested with the same sky conditions and maximum allowed gains. The result is that the EMCCD detection limit is roughly one magnitude fainter than for the CMOS. However at OA-UNI, the EMCCD was not set at its maximum EM gain, which explains why both cameras exhibit almost identical sensitivities.

Those results explains why we eventually bought 7 Cmos, vs. 3 EMCCD's, due to the factor of four between the cost of the latters vs. the formers (10,000 euros apiece vs. 2,500 euros apiece, respectively) . So, the EMCCD's are used in those extreme case where the star is beyond the capacity of the Cmos. For brighter stars, it is important to note that SNR is, in most of the cases, dominated by scintillation ("seeing") rather than by photon noise, so that the cameras are equivalent.

[1] http://www.raptorphotonics.com/
[2] https://astronomy-imaging-camera.com/
[3] http://airylab.fr/solution-dimagerie/introduction-de-genika/
[4] http://www.timeboxutc.com/

Table 3.1: Camera comparison review

Features/cameras	**ZWO**	**Kite**
Sensor type	Cmos	EMCCD
Sensor model	IMX178	KI247-CL
Analog-to-digital converter(bits)	14	16
Active dimension (pixels)	3096x2080	568x496
Pixel dimension (μm)	2.4x2.4	10x10
Binning	up to 4x4 (but digital)	up to 2x2
Full well capacity(electrons)	15000	24000
Dark current(electrons/pixel/secons)	(not provided)	<1
Readout noise (electrons)	1.4 -2.2	<1 (EMGain=ON)
Spectral response(νm)	400-1000	350-1100
Quantum efficiency	(not provided)	53% (530nm)
Cooling (°C)	-40	-20
External trigger	no	yes
ROI	yes	yes
Interface	USB 2.0 and 3.0	CameraLink
Weight(g)	410	550

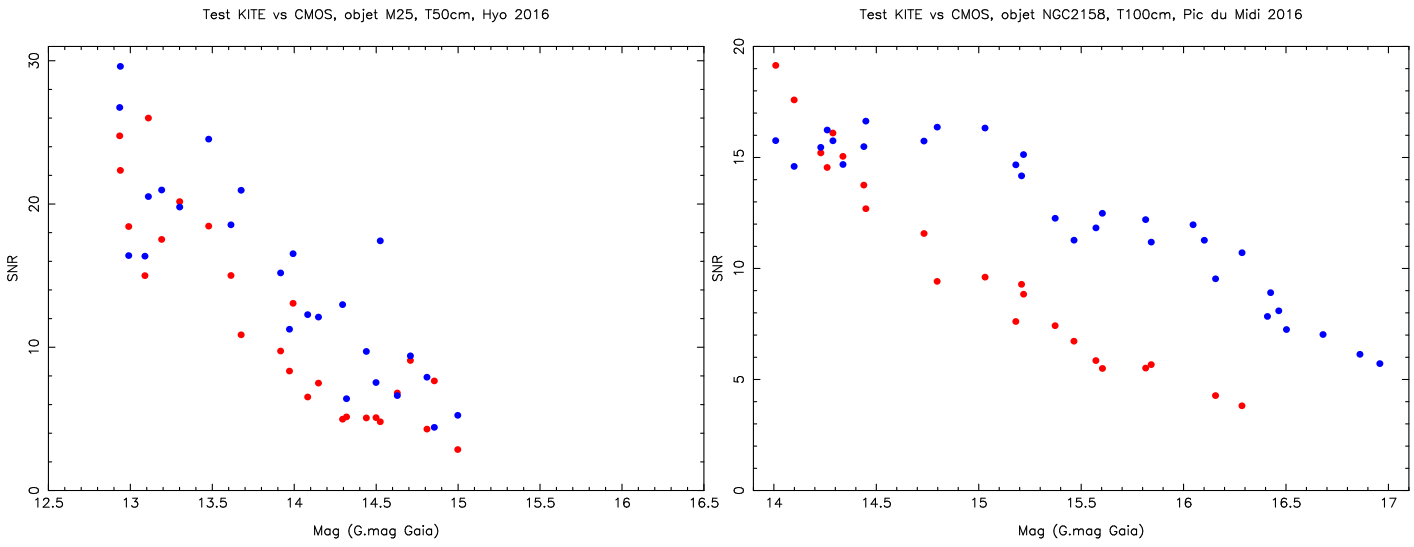

Figure 3.1: SNR measures with cmos and emccd. Blue and red dots correspond to emccd and cmos (respectively) at Pic du Midi and the contrary at OA-UNI. Right: Data observed at Pic du Midi. Left: Data observed at OA-UNI. The exposure time was 200 ms in both observations.

3.2 Deriving occultation light curves

All observations that I did in the framework were obtained with very different telescopes, from 20 cm to 8.2 m in diameter. Moreover, I observed and analyzed data from very different sites and different weather conditions. Table 3.2 summarizes my observations and data reductions. Note that besides actual observing and data analysis, those campaigns represented a time consuming aspect of my work, linked to various logistics tasks (contacts with people, transportation of equipment, coordination with other groups, etc...).

Once data are obtained, there is no unique and automatic procedure to make the photometric analysis. In general, the best light curves are obtained by ratioing the flux from the target to the flux of nearby reference star(s). This corrects slow sky transparency fluctuations. However, the correlation between the target and the reference depends on parameters that largely vary from one observation to the other: angular distance between the two objects in the sky plane, photometric quality of the sky at that moment, exposure time and wavelength of observation. In general, the target flux was ratioed by a running average of the reference, the size of the averaging box being adjusted empirically to maximize SNR. The flow diagram of our photometric protocol is displayed in Figure 3.2.

The accuracy of *absolute* time in observations works is of paramount importance, because we have to compare data obtained in different countries, or even different continents. So, reconstructing for instance, the size of Pluto's atmosphere projected in the sky plane requires that all the stations use a correct, common time basis. I have worked on that technical aspect of occultation works, see details in (Leiva, 2017). The following occultations show some examples of my data reduction along the flow chart of Figure 3.2:

3.2.1 Pluto occultation

On 2012 July 18, the Pluto occultation was successfully monitored from various sites in Chile, Argentina and Peru. It was in particular observed at the Cerro Paranal, with the 8.2-m VLT Yepun telescope, using the infrared NACO camera in H band (1.65 $\mu\ m$). Figure 3.3 shows results of a carefully photometry of this observation. This light curve has the best quality of all ground-based stellar occultation by Pluto.

3.2.2 Triton occultation

On 5 October 2017, Neptune's moon Triton occulted a star, providing an opportunity to probe Triton's atmosphere. This event was successfully recorded by many observatories, mainly in Europe,and provides more than 80 positive detections. 26 observatories record the central flash, which is big success. Figure 3.4 is an example of the reduction protocol applied to occultation by Triton observed at the C2PU 1.04m telescope of the Côte d'Azur Observatory (France) and at Constancia (Portugal, Rui Goncalves).

Table 3.2

Objet	Category	Date	Publication
Triton	Satellite	2017 October 5 [1],	
2002MS4	TNO	2017 July 28[1]	
Chariklo	Centaur	2017 July 23 [1]	
Chariklo	Centaur	2017 June 22 [1]	
Pluto	TNO	2016 July 19[1],	
Pluto	TNO	2015 June 29[2]	Sicardy et al. (2016)
Chariklo	Centaur	2015 May 22 [1]	
Chariklo	Centaur	2015 May 05[3]	
(216) Kleopatra	Asteroid	2015 Mars 12[3]	Hanuš et al. (2017); Shepard et al. (2018)
Bienor	Centaur	2014 December 30 [1]	
Chariklo	Centaur	2014 June 28 [1]	Bérard et al. (2017); Leiva et al. (2017)
Pluto	TNO	2013 May 04 [1],	Dias-Oliveira et al. (2015)
Pluto	TNO	2012 July 18 [1],	Dias-Oliveira et al. (2015)
Pluto	TNO	2010 February 14[2]	
Pluto	TNO	2008 June 24[2]	
Pluto	TNO	2008 June 22[2]	
Pluto	TNO	2007 June 14[2]	
Pluto	TNO	2002 August 21[2]	Sicardy et al. (2003)

[1] I observed and process the data.
[2] I reduced data but did not observe.
[3] I observed but did not process the data.

3.2.3 (10199) Chariklo occultation

On 2017 June 22, a occultation by Chariklo was observed from 6 sites in Namibia. We observed with two telescopes at same site in order to the compare the new kit (CMOS+timebox) with the old kit (Raptor Merlin). See Bérard et al. (2017) for circumstances of this occultation. On 2017 July 23, I observed another occultation by Chariklo in Argentina. In spite of poor weather conditions, I get a positive occultation just by the body and a light curve useful for a fit. Figure 3.5 show the light curves both occultations.

3.2.4 (177) Irma occultations

On 2011 September 17 and October 03, in Paris, the target was Irma. Figure 3.6 shows the sites which recorded the event. This time, we used a 100cm telescope in Meudon. In the first date we had a positive detection but in the second date we had a negative detection. Figure 3.7 shows the lightcurve for the September 17th event and Figure 3.8 shows the chords during these two recorded occultations. These were the start of my preparation for other occultations in the forthcoming years. In fact, one year after, I observed my first positive occultation in Peru with a small 20cm telescope mounted on

an old astrograph used as tracking system. The target was Pluto. The occulted star was faint (15.1), but the large exposure time (5.12s and 10.28s) makes the observation of the Pluto's occultation possible, as will be seen in Figure 3.3

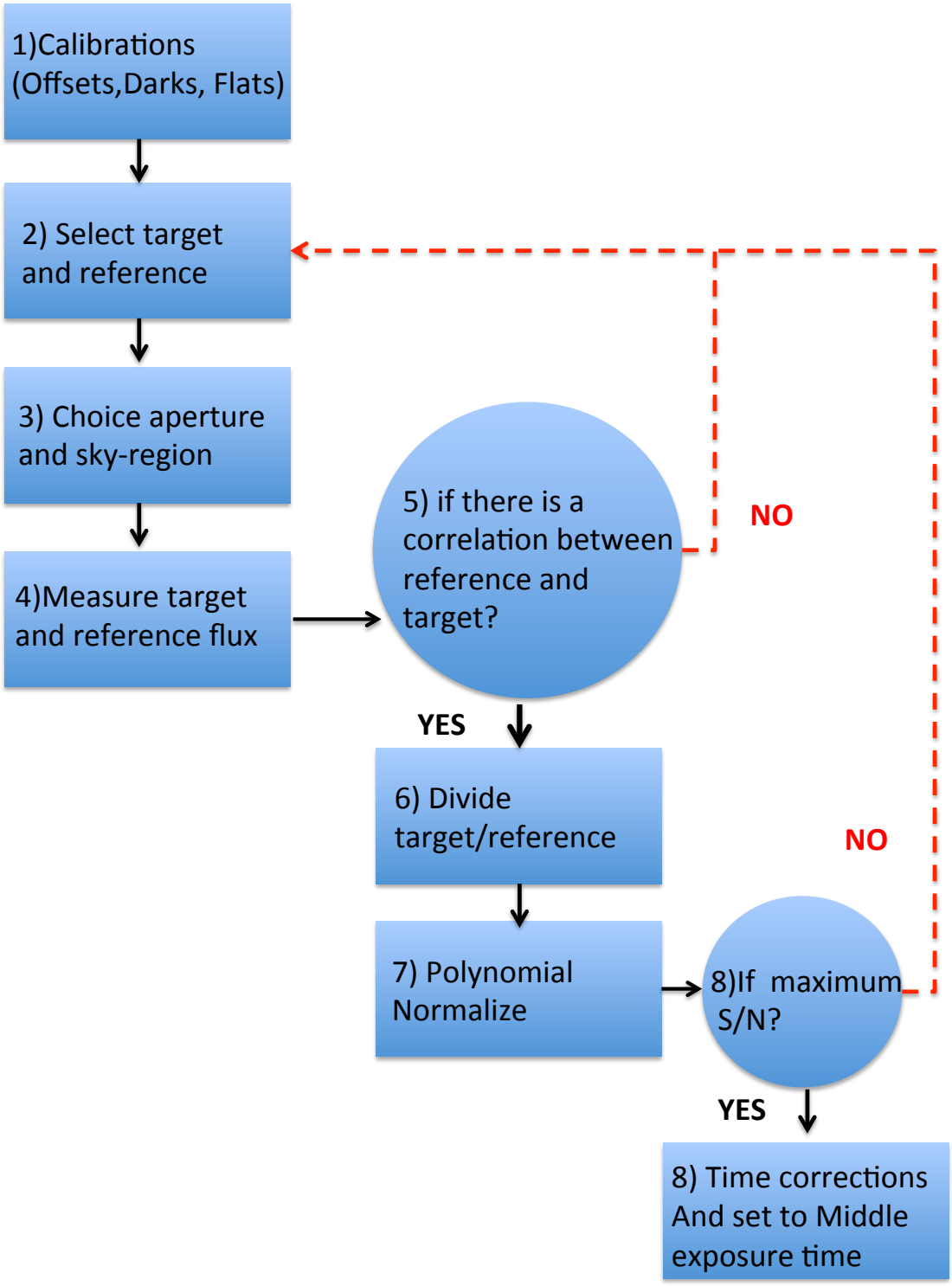

Figure 3.2: Flow chart describing my photometric reduction protocol.

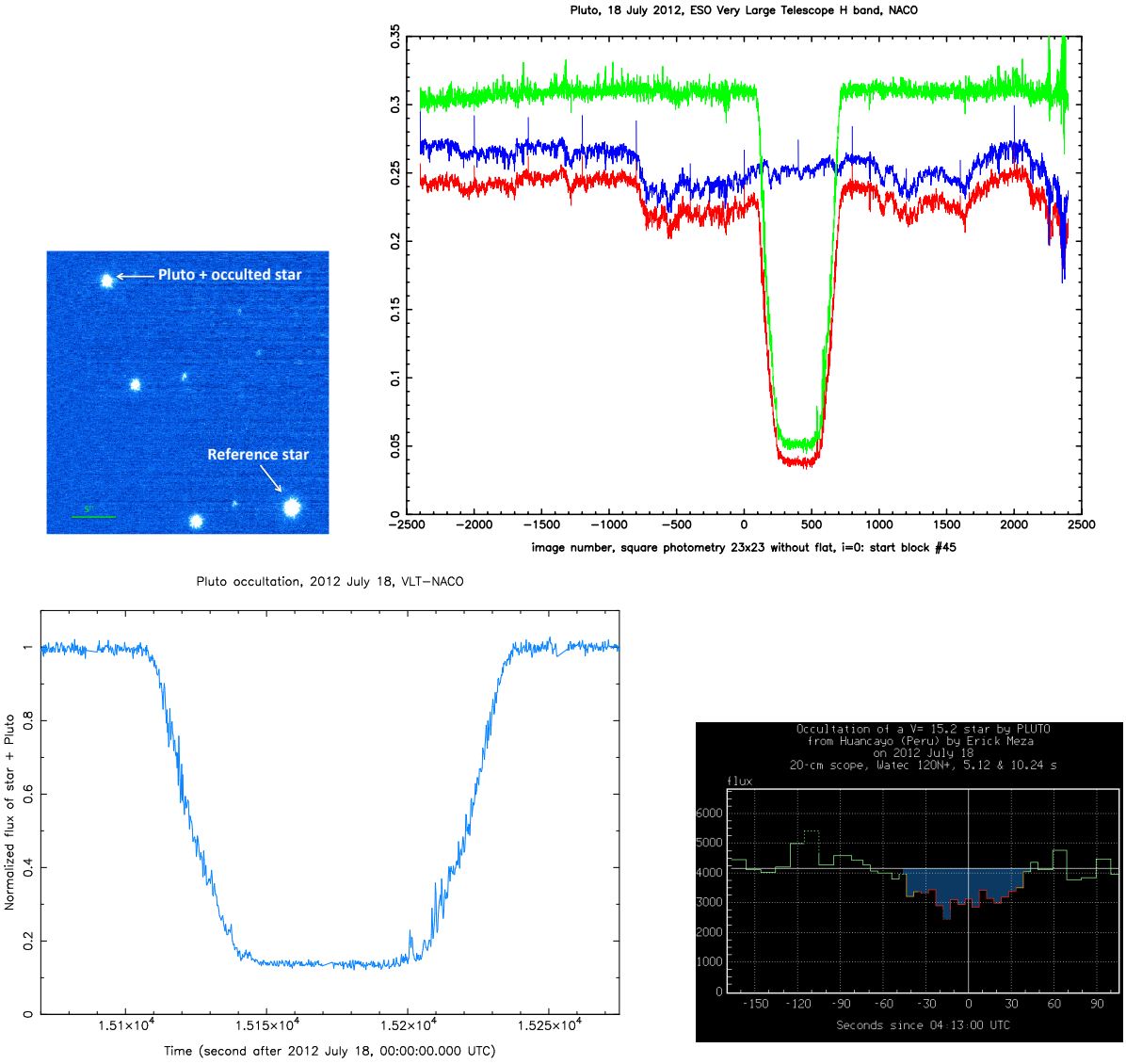

Figure 3.3: Pluto occultation on 2012 July 18. Upper left - Field of view during a stellar occultation by Pluto, at Paranal, 8m VLT, NACO. Upper right - Blue and red curves represent the light curves of the reference star and the occulted star+Pluto respectively without a classical calibration. Green curve is a ratio between target and reference star. A clear correlation is observed between the reference star and the target. Lower left - This is my best light curve derived from the Pluto occultation of 2012 July 18, using the NACO instrument attached to the Very Large Telescope (VLT) of the European Southern Observatory (ESO). The images were taken in the near IR (Ks band, 2.2 um) at a rate of five images per second, corresponding to a sampling about 4.6 km per data point along the occultation chord. Note the gradual drop of stellar flux caused by Pluto's atmosphere and presence of "spikes" due to gravity waves in that atmosphere, see Chapter 4. Lower right - Pluto light curve observed, at Huancayo (Peru) with a 20cm telescope.

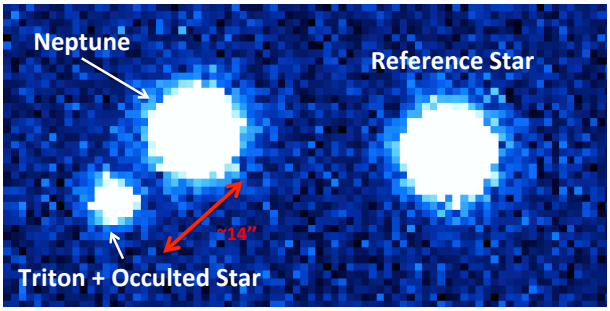

(a)Left : Field of view during a stellar occultation by Triton, at Côte d'Azur Observatory. The angular distance between the center of Neptune and Triton was less than 14". Right : Reference star used to photometric analysis.

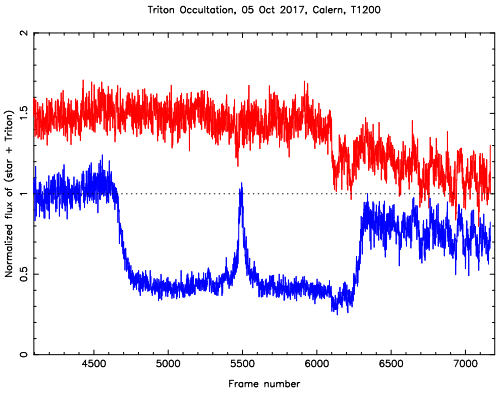

(b)Red and blue curves represent the light curves of the reference star and the occulted star+Triton respectively. After a classical calibration. A clear correlation is observed between the reference star and the target.

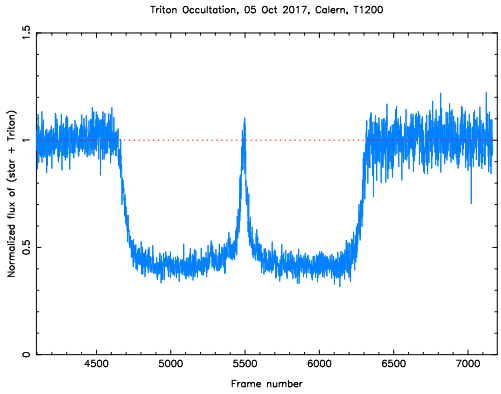

(c)Light curve after correction and ready to be use.

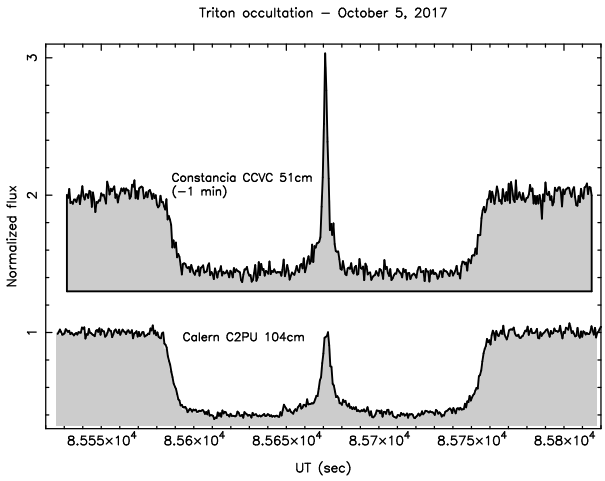

(d)The central flash observed, at Constancia (Portugal, Rui Goncalves) and at the C2PU 1.04m telescope of the Côte d'Azur Observatory (France). I processed both data sets and derived both light curves shown here, along the flow chart of Figure 3.2.

Figure 3.4: The central flash observed during the Triton occultation on 2017 October 05.

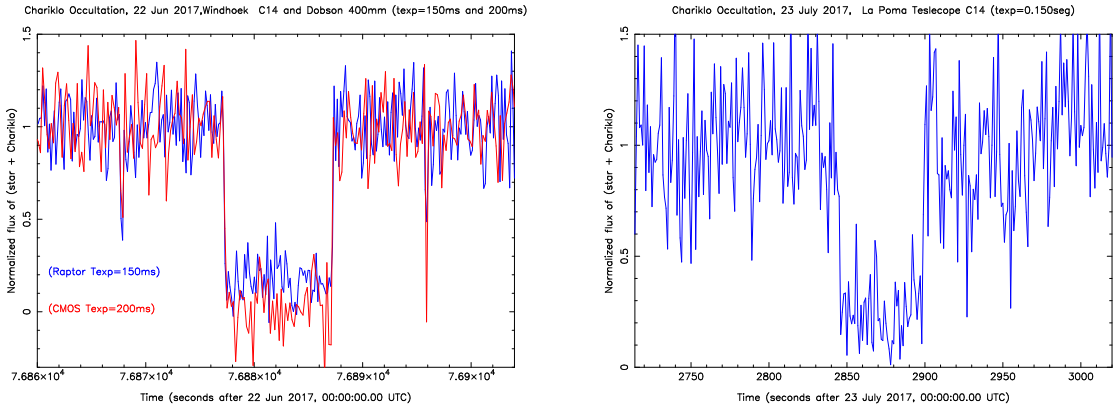

Figure 3.5: Chariklo light curves observed during 2017. Note the abrupt drops of stellar flux in the case of an airless body like Chariklo. Left: Chariklo occultation light curves observed simultaneously on 2017 June 22 at Windhoek, Namibia. The blue and red light curves correspond to the Raptor Merlin and ZWO Cmos, respectively. It shows the consistency between the absolute time recording systems, down to the 0.1 second level. Right: Light curve from the occultation by Chariklo of 2017 July 23 at La Poma, Argentina, using the EMCCD Kite camera attached to a small amateur telescope (35 cm), under poor weather conditions. Note, however, that the timing of the event can be retrieved with an accuracy of a fraction of a second, corresponding to a few kilometers projected in the sky plane, and the normalized flux is not zero during the occultation, due to Chariklo's contribution. We see that a modest instrument placed at the right site may provide an important constraint on Chariklo's shape see Berard (2017) for more details about Chariklo occultations.

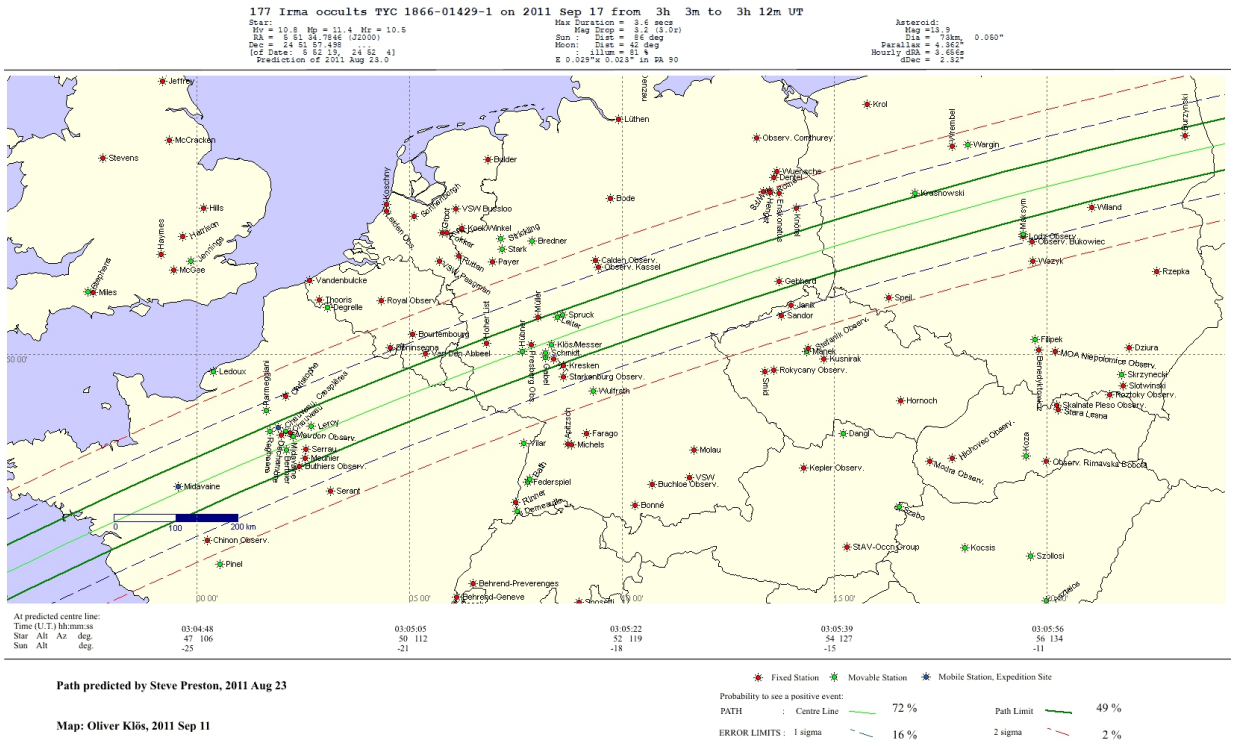

Figure 3.6: Green lines show the sites where positives occultations were reported.

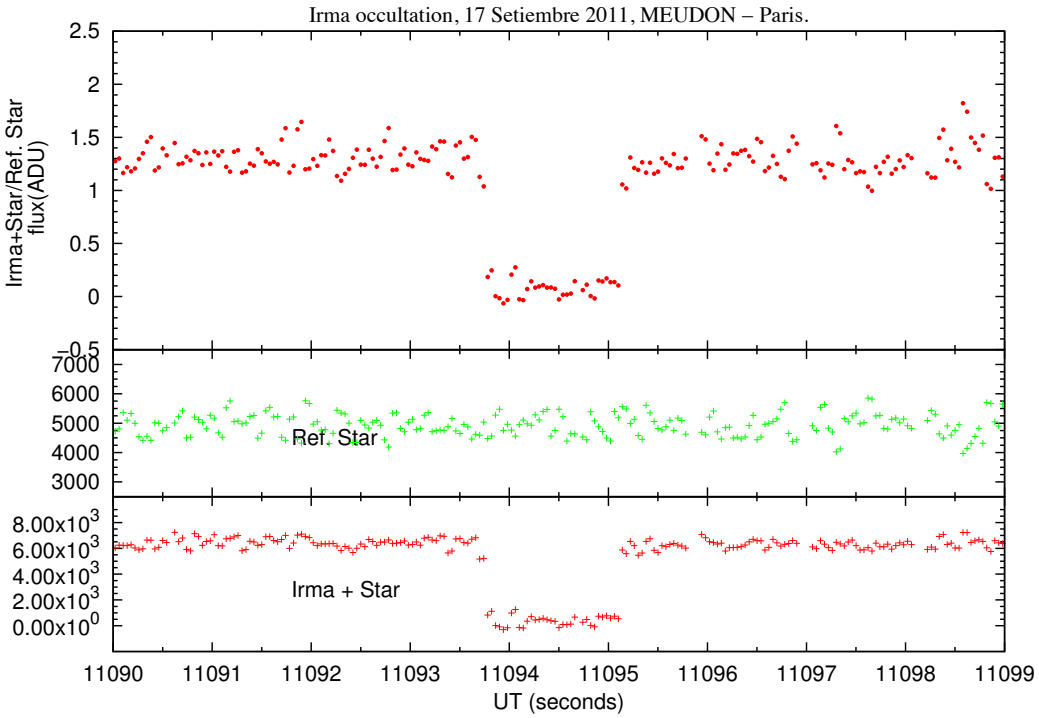

Figure 3.7: Irma occultation light curve. Top: Red points are the normalized light curve. Center: Green plus marker are the reference light curve. Bottom: Red plus markers are the Irma + occulted star flux.

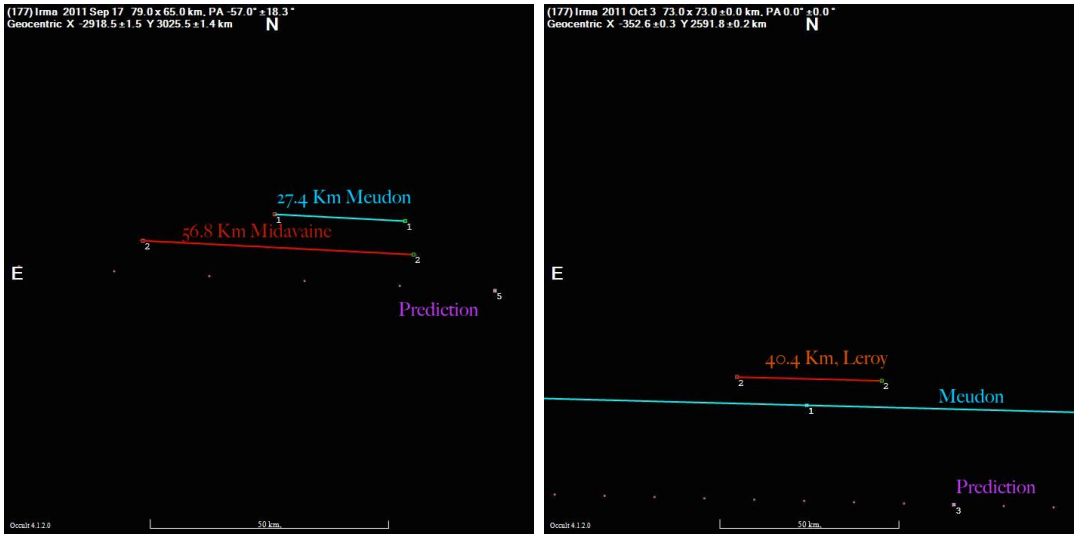

Figure 3.8: Color lines show sites where positives occultations were reported. The green squared are the ingress and egress error bars at 1σ level

Chapter 4

Pluto's ground-based stellar occultations: 2002 to 2016

Contents

4.1 Introduction

Here I present the Pluto stellar occultation campaigns that our group has organized between 2002 and 2016. Observation circumstances and analysis is also described. This period was a golden age for professional and amateur “plutonists" as the dwarf planet was crossing the Galactic Plane as seen from Earth (Fig. 4.1). This increased the rate of events to a few per year, vs. one every several years for Pluto moving against more typical stellar fields.

This allowed a monitoring of Pluto's atmosphere at a special moment, as Pluto went through equinox in 1988 and through perihelion in 1989 (Fig. 4.2). As discussed in Chapter 5, Pluto's atmospheric pressured increased by a factor of about 2.8 between 1988 and 2016, in spite of a decrease of 24 % in insolation during the same period.

Fig. 4.3 lists the campaigns that our team and collaborators have organized. We have selected in this list the events that resulted in sufficient signal-to-noise ratio (SNR) to provide a constraining pressure estimation. Among those campaigns, the 2012 and 2013 events observed from South America provided our best SNR light curves, together with a good latitudinal coverage of the dwarf planet, from which a template model of Pluto's atmospheric structure was obtained. The 2015 event resulted in the detection of a central flash in New Zealand, see Chapter 5.

Classical bias, dark, flat-field and sky subtraction (using synthetic aperture photometry) provided the occultation light curves displayed for each campaign. In all cases, a reference star brighter than the target was used to correct for low-frequency sky-transparency variations.

When possible, calibration images were taken just before or after the event (or on another night) to image the target star and the reference star without Pluto. This permits in principle to retrieve Pluto's contribution during the occultation. It is called Φ_P because it corresponds to Pluto's contribution to the total flux, and thus to the level at which the stellar flux would completely vanishes. Note that we cannot use the observed flux in the flat, middle part of the occultation to retrieve this contribution, because some residual stellar flux is still detected, due to refraction effects of the densest atmospheric layers just above the surface, see Chapter 5.

Several complications prevented us to obtain a satisfactory calibration in all cases,

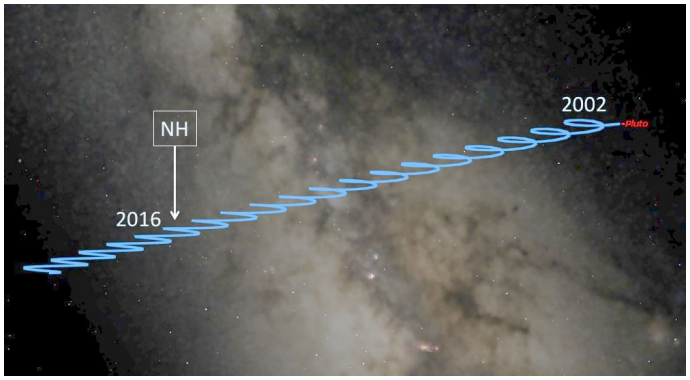

Figure 4.1: Pluto's motion in the latest two decades. The dwarf planet moved in front of the Galactic Center, an unique opportunity to observe stellar occultation at increased yearly rate. The label “NH" indicates the date of the NASA New Horizons flyby.

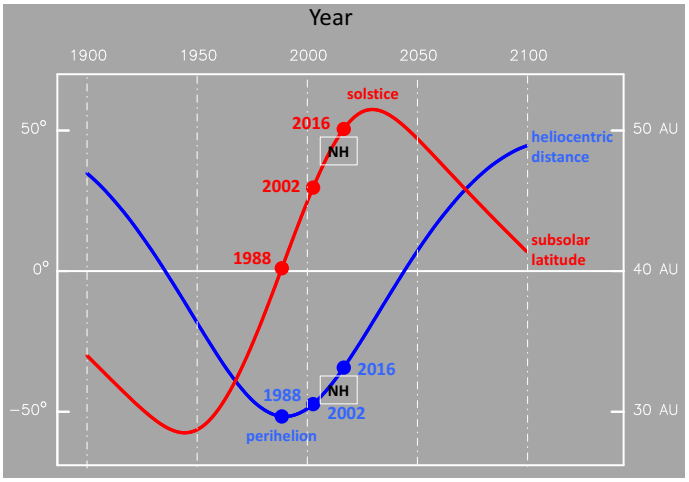

Figure 4.2: The same as Figure 1.12, repeated here to put in perspective Figure 4.1.

except for the one of July 18, 2012 observed from Paranal/VLT (Dias-Oliveira et al., 2015), see Fig. 4.4. Those complications are (1) the stellar residual flux is small, typically 2%, compared to its unocculted value, so that a photometric accuracy better than that must be reached, which is challenging by itself. See Fig. 4.5 and (Dias-Oliveira et al., 2015), (2) for broadband observations (no filter), the calibration must be done at the same elevation as for the occultation, to reproduce the same differential chromatic effects. As the target star and reference star may be of different colors, the flux ratio between the two may change from night to night, even if they are observed at same elevation, (3) Pluto cannot be measured the night before or after the event, as its flux varies by several percents over 24 hours due to its rotation and albedo features on its surface.

As a result, only the VLT observations of July 18, 2012 provided a satisfactory zero stellar flux baseline, because data were obtained in a specific band (K_s, 2.2 μm), with

Date	Sites	
2002 August 21	Hawaii	Two-fold pressure increase from 1988
2007 June 14	Chile, Namibia, Brazil	
2008 June 22	Australia, Namibia, Republic of South Africa, France(Les Makes)	
2008 June 24	Hawaii	
2010 February 14	France, Switzerland	
2010 June 04	Australia, New Zealand	
2011 June 04	Brasil, Chile	
2012 July 18	Chile, Argentina, Peru	The best S/N LC
2013 May 04	Chile, Brazil, Argentina	
2015 June 29	Australia, New Zealand	Central Flash
2016 July 19	France, Italy, Spain, Germany, Austria, Czech Republic, Poland, Israel	

Figure 4.3: Dates and geographical zone of the stellar occultations by Pluto analyzed here. The “two-fold pressure increase" noted in the first line is with respect to the pressure measured during the June 1988 stellar occultations (Elliot et al., 2003; Sicardy et al., 2003).

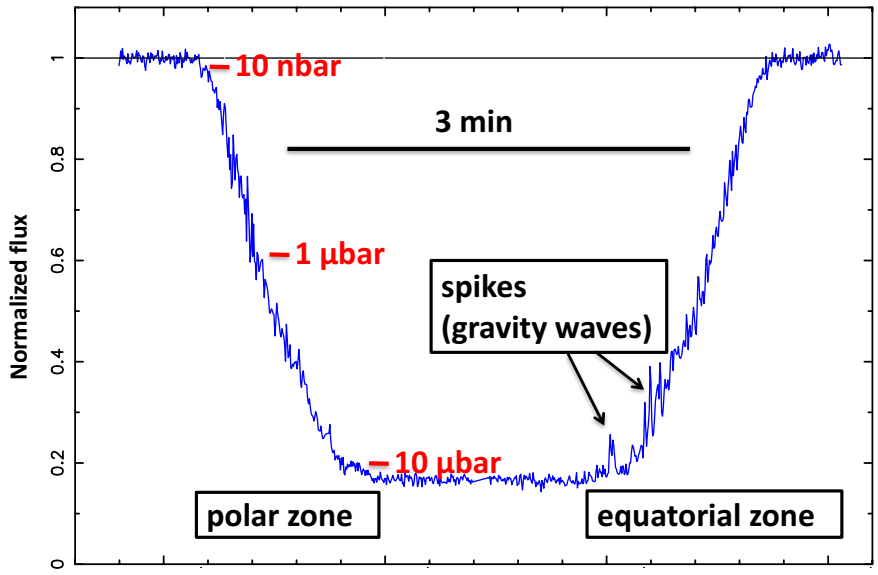

Figure 4.4: The occultation light curve obtained during the 2012 July 18 stellar occultation, using the NACO instrument attached to the Very Large Telescope (VLT) of the European Southern Observatory (ESO). The images (see Fig. 4.5) were taken in the near IR (K_s band, 2.2 μm) at a rate of five images per second, corresponding to a sampling about 4.6 km per data point along the occultation chord. The event lasted for more than 3 minutes (see horizontal bar) and probed pressure levels from about 10 nbar down to more than 10 μbar, from the polar (summer) to the equatorial (winter) limbs, see Fig. 4.37. Note the conspicuous presence of spikes, associated with gravity waves, that are better seen once a smooth synthetic light curve has been subtracted, see Fig. 4.5. Note the presence of a "kink" at exit (near the upper black arrow) that is not visible at entry. However, this is a mere effect of spikes, and does not correspond any notable feature in the resulting temperature profile, see Fig. 4.6, right panel.

a large telescope that permitted to clearly separate Pluto from the target star about 30 minutes after the event (Fig. 4.5).

The occultations are used to determine Pluto's position offsets with respect to the adopted ephemeris, so that to satisfactorily fit the observed light curves. Note that this offset *depends on the adopted stellar position* but is *independent* of the ephemeris used. In effect, using another ephemeris will shift the calculated Pluto's position, but will also change in the opposite sense the offset to apply to that ephemeris in order to fit the observations. Stated more simply, the occultation provides an accurate measurement of Pluto's position *relative to the star* at a given moment, a quantity independent of the ephemeris. As the star positions are improved, e.g. with Gaia catalogs, Pluto's position is improved accordingly, and so is its ephemeris. The typical errors on Pluto's center with respect to the star are of the order of 20-40 km, see the χ^2 maps plotted hereafter. This means that at the moment of the occultation, a relative Pluto position is obtained with a typical accuracy of 1-2 mas. As the Gaia DR2 catalog is accurate at the sub-mas level, it means that the 1-2 mas accuracy mentioned above is now entirely due to our occultation fitting procedure. Classical imaging cannot reach that accuracy, as it barely goes below the $\sim$ 30 mas level.

In several instances, I will mention the notion "Pluto's center position" (f_c, g_c),

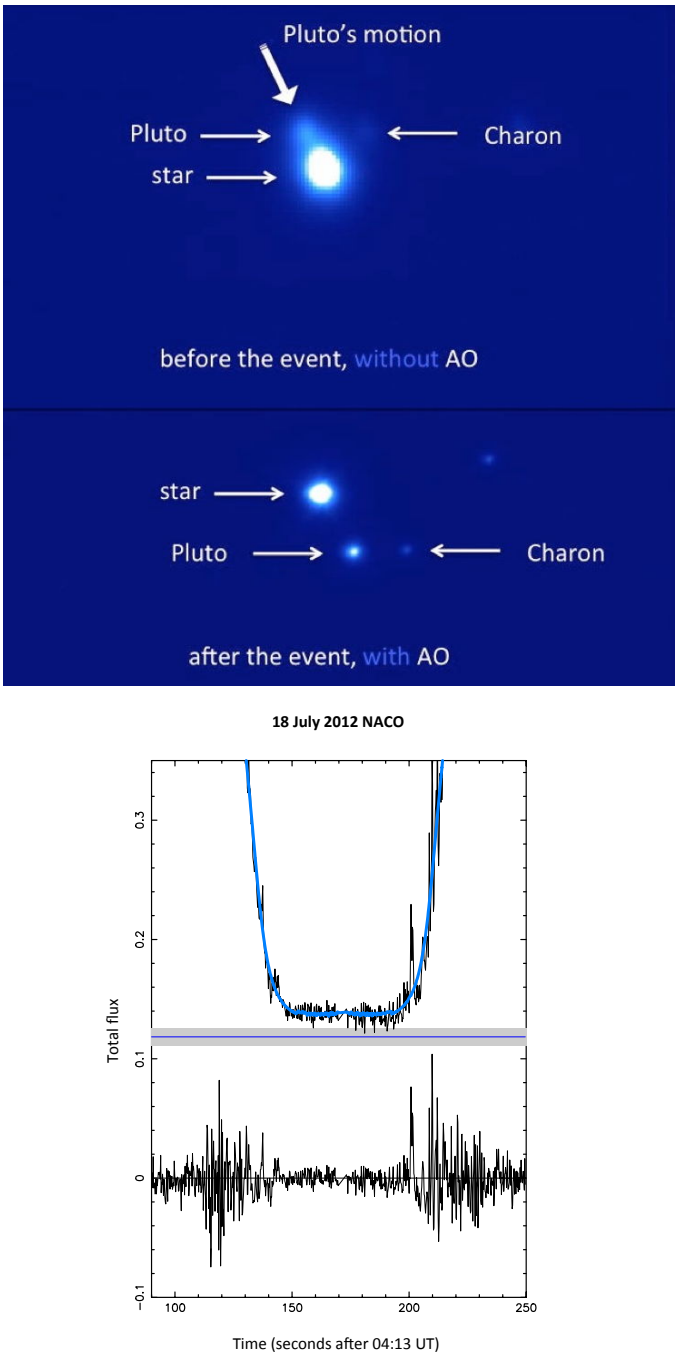

Figure 4.5: Up - Pluto and Charon's motions relative to the star during the 2012 July 18 stellar occultation, before and after the event. The images taken after the occultation were used to measure the star alone against a brighter reference star (not visible here) and derive Pluto's contribution to the flux during the event. Bottom - An expanded view of the bottom of the light light curve shown in Fig. 4.4. The bottom signal is the residual between the observations and the model (blue line in the upper panel), clearly showing Pluto's atmospheric activity (gravity waves) through the presence of rapid spikes. The horizontal line is the results of the calibration (see text) and correspond to a residual stellar flux of $2 \pm 0.8\%$, compared to its unocculted value (from Dias-Oliveira et al. 2015).

expressed in kilometers (Chapter 5). It should be understood as Pluto's position offset (in the plane of the sky) that has to be applied to the current ephemeris in order to fit the data. The quantities f_c and g_c are counted positively towards the local celestial east and north directions, respectively. They are readily translated into ephemeris offsets $[\Delta\alpha\cos(\delta), \Delta\delta]$ as Pluto's geocentric distance is known, where $\Delta\alpha$ and $\Delta\delta$ are the differences in right ascension and declination, respectively, between the observed and ephemeris values.

During an occultation by Pluto's atmosphere, there are no sharp disappearances and reappearances of the star during the event, which requires a specific technique to reconstruct the geometry of the event, i.e. pin down (f_c, g_c).

4.2 DO15 Model

To derive synthetic light curves, I used a ray tracing code (see Chapter 2) based on a template temperature profile $T(r)$ as a function of radius r (the distance to Pluto's center). This model assumes a pure molecular nitrogen N_2 atmosphere and is taken from "DO model" (see Dias-Oliveira et al. (2015) and Figure 4.6).

In order to reconstruct the geometry of all of the the occultations, we need to know at any moment the position of the star relative to Pluto's center, projected in the sky plane. This position is given by (f, g) (in kilometers) of the star in this plane, counted

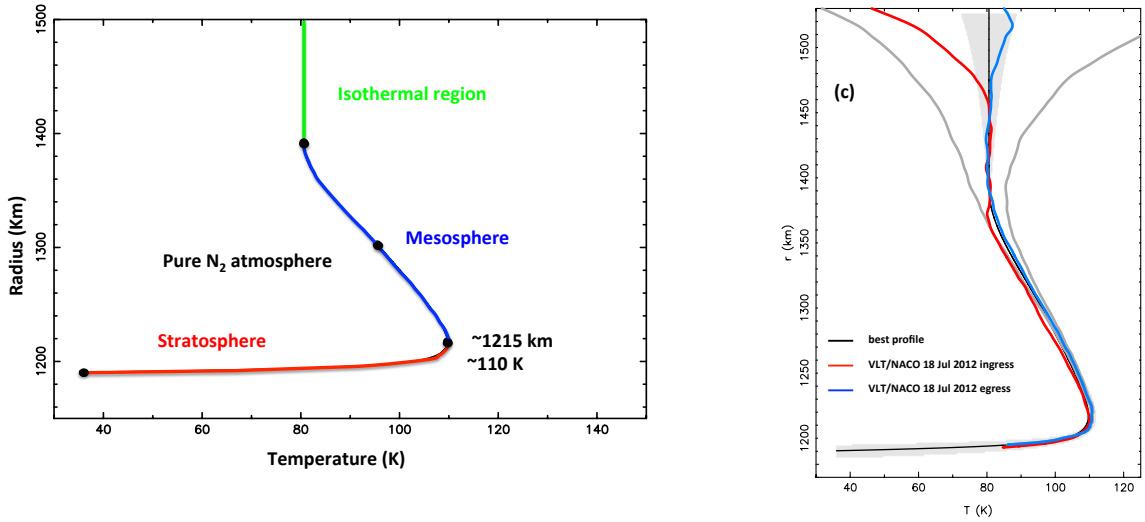

Figure 4.6: Left: Temperature profile T(r) that best fits our 2012 and 2013 light curves, DO15 model. Right:Black solid line is the DO15 model that best fits all of the 2012 July 18 NACO light curves. The red (resp. blue) lines are the particular profiles obtained from the inversion of the NACO 2012 July 18 light curve at ingress/summer (resp. egress/winter). The shaded areas at the top of the profiles indicate the expected $\pm$ 1 σ fluctuations caused by the photometric noise. The shaded areas at the bottom of the profiles are the ± 1 σ uncertainty domain caused by the uncertainty on the Pluto + Charon contribution to the 2012 July 18 NACO light curve. Rigth: Temperature vs. radius.

again positively eastward and northward, respectively, and is extracted from Pluto's ephemeris. Note that the origin is taken at Pluto's expected center, which is different from Pluto's retrieved center (f_c, g_c).

Once a fixed temperature profile $T(r)$ is adopted (here the DO model), there are four free parameters to adjust: (f_c, g_c), the pressure boundary condition p_0 at some prescribed radius r_0, and the zero stellar flux Φ_P mentioned above. In practice, we used as boundary condition p_0 the surface pressure $p_{\rm surf}$ of the DO model.

The latter parameter is determined through a linear least-square fitting of the synthetic light curves to the observed data.

Assuming a spherically symmetric Pluto's atmosphere, Pluto's offset (f_c, g_c) can be split in two parts. One part is along Pluto's motion, Δl (counted positively eastward), and is mainly determined by the timing of the event at the various stations. The other part is perpendicular to Pluto's motion, $\Delta\rho$ (counted positively northward), and controls the distance of closest approach of each station to Pluto's shadow center. An appropriate transformation that takes into account of Pluto's motion orientation in the sky plane finally relates $(\Delta l, \Delta\rho)$ to (f_c, g_c).

This procedure separates Δl, which is largely independent of the adopted Pluto's atmospheric model, from $\Delta\rho$, which may be strongly correlated to that model, especially if only grazing chords on one side of the planet are available. For such ill-configured situations, a denser atmosphere may be accomodated by increasing the distance of closest approach of the star to Pluto's center. In other words, there may be in some instances a strong correlation between $\Delta\rho$ and p_0.

Those two parameters are explored in a grid that provides the χ^2 function:

$$\chi^2(\Delta\rho, p_0) = \sum_i \left(\Phi_{\rm i,obs} - \Phi_{\rm i,the}\right)^2 / \sigma_i^2, \tag{4.1}$$

where $\Phi_{\rm i,obs}$ is the observed flux at the ith point, $\Phi_{\rm i,the}$ is the corresponding theoretical flux calculated through the ray tracing code, and σ_i is the uncertainty on data estimated from the r.m.s. scatter outside the occultation.

The best-fitting parameters (plus associated error bars) and the quality of the fit are eventually estimated through the $\chi^2(\Delta\rho, p_0)$ maps, using the classical approach described for instance in Press et al. (1992). In particular, all our fits provide minimum values $\chi^2_{\rm min}$ that are close to $N - M$, where N is the number of data points, and M the number of adjusted parameters. Here $M = 4$, as explained above, so that $N - M \sim N$ since the number of data points is always several hundreds. In practice, the marginal 1σ and 3σ error bars on p_0 and $\Delta\rho$ have been estimated by tracing the $\chi^2_{\rm min} + 1$ and $\chi^2_{\rm min} + 9$ level curves, as shown in the $\chi^2(\Delta\rho, p_0)$ maps plotted below.

4.3 2002 August 21

This occultation was observed at the Canada-France-Hawaii Telescope (CFHT) in Hawaii, using a narrow-band red I filter. Figure 4.7 shows the reconstructed Pluto's shadow path on Earth and the circumstances of observations are summarized in Table 4.1. Figure 4.8 shows the reconstructed occultation geometry and Fig. 4.9 displays the occultation light curve, one of the best that we obtained in our various campaigns.

Table 4.1: Circumstances of Observations, 2002 August 21

Site	**Coordinates altitude (m)**	**Telescope Instrument/filter**	**Exp. Time/Cycle (s)**	**Observers**
CFHT Hawaii	19 49 30.88 N 155 28 07.52 W 4200	3.6m I (0.83 ± 0.1 μm)	1/1.583	C. Veillet

Only one chord is available for this event. Thus, there is a relatively large error bar on the closest approach of the CFHT station to Pluto's shadow center, $\rho_{\rm min} = 610 \pm 250$ km (Sicardy et al., 2003). As there is a degeneracy between $\rho_{\rm min}$ and the derived surface pressure $p_{\rm surf}$, the latter has a relatively large error bar. Consequently, I have used an additional information in the fitting procedure, namely the value $\rho_{\rm min} = 597 \pm 20$ km derived independently by another team that obtained chords from continental USA and Hawaii (Elliot et al., 2003). But this does not reduce the error bar on $p_{\rm surf}$ see Fig. 4.10.

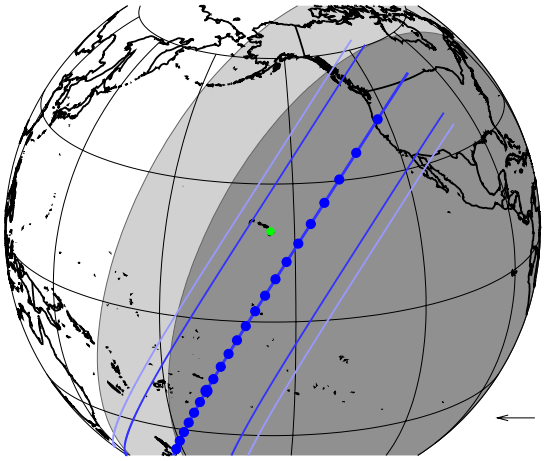

Figure 4.7: Reconstruction of Pluto's shadow track on Earth for the 2002 August 21 occultation. The dots on the central thick line are plotted every minute, and the shadow is moving from right to left (see arrow at lower right corner). The dark and light blue thinner lines are the shadow limits corresponding the stellar half-light level and 1% stellar drop level (the practical detection limit), respectively. The green dot corresponds to the site with positive occultation used in the fit. Areas in dark grey correspond to full night (Sun elevation below -18 degrees) and areas in light grey correspond to twilight (Sun elevation between -18 and 0 degrees), while daytime is in white.

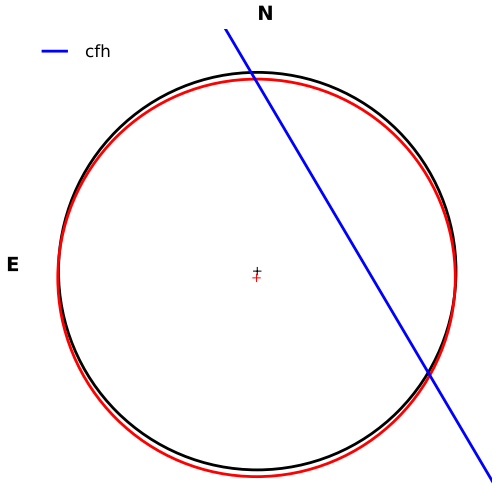

Figure 4.8: Reconstructed geometry of the 2002 August 21 Pluto stellar occultation. Labels N and E show the J2000 celestial north and east directions, respectively. Pluto's position is derived from a fit to the CFHT lightcurve, using the Dias-Oliveira et al. (2015) model, see text. The gray circle (with black center) corresponds to the fit using the CFHT observation only, using the results of Sicardy et al. (2003). The red circle (and associated center) uses the geometry constrained by Elliot et al. (2003). Both circles have a radius of 1187 km (Stern et al., 2015), the value derived by the REX New Horizons results (Hinson et al., 2017). The blue line is the stellar trajectory relative to Pluto, as observed from CFHT.

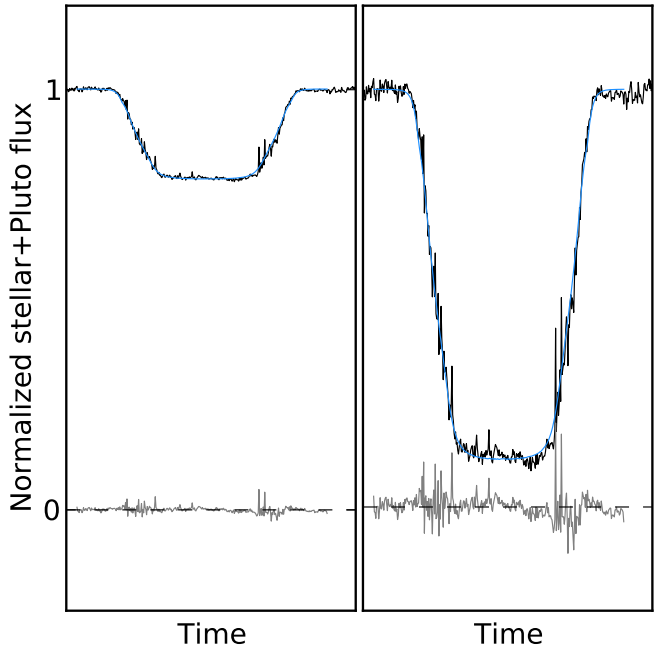

Figure 4.9: Positive Occultation light curves obtained in Hawai. Blue curve is a fit to the Dias-Oliveira et al. (2015) model, and the residuals are in gray. Left: Normal view. Right: A zoom of Left part.

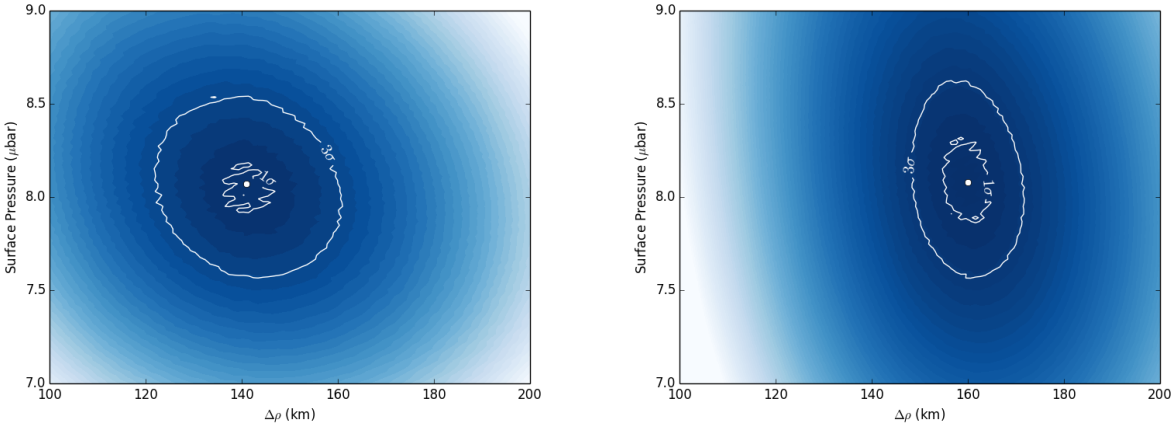

Figure 4.10: The χ^2 maps obtained from the fit to the CFHT light curve. Darker zones correspond to lower values χ^2. The 1σ level is delineated by the inner closed curve ($\chi^2_{\rm min}+1$ level). The outer closed curve corresponds to the 3σ level ($\chi^2_{\rm min}+9$ level). Left: χ^2-map for the fit to CFHT Pluto light curve with no center contrains. The white dot shows the best fit, with a surface pressure of the Dias-Oliveira et al. (2015) model (see text) of $p_{\rm surf} = 8.07 \pm 0.16$ μbar. It corresponds to $\chi^2 = 524.91$ and uses 346 data points. Right: The same using the constraints from Elliot et al. (2003), see text. The white dot shows the best fit, at $p_{\rm surf} = 8.08 \pm 0.18$ μbar,

Table 4.2: Circumstances of Observations, 2007 June 14

Site	**Coordinates altitude (m)**	**Telescope Instrument/filter**	**Exp. Time/Cycle (s)**	**Observers**
LNA	22 32 7.80 S	1.6m	0.4/0.4	Dario Silva Neto
Brazil	45 34 57.70 W	CCD301/clear		
	1864			
Hakos	23 14 50.4 S	IAS 0.5m	1.373/1.373	M. Kretlow
Namibia	16 21 41.5 E	TC245 IOC/clear		
	1825.			
Paranal	24 37 39.44 S	UT1 8.2m	0.1/0.1	V. Dhillon
Chili	70 24 18.27 W	Ultracam/g',r',i'		S. Littlefair
	2635			A. Doressoundiram
Paranal	29 15 16.59 S	UT4 8.2m	1/1	N. Ageorges,
Chili	70 44 21.82 W	NACO/Ks		B. Sicardy
	2315.			

4.4 2007 June 14

This occultation was successful recorded in Brazil, Namibia and Chili, Table 4.2 lists the circumstances of observations, Figure 4.11 shows the reconstructed Pluto's shadow path, and Figure 4.12 shows the reconstructed occultation geometry. During this campaign I have used four light curves (see Fig. 4.13) to fit the Dias-Oliveira et al. (2015) model, resulting in the χ^2-map of Figure 4.14.

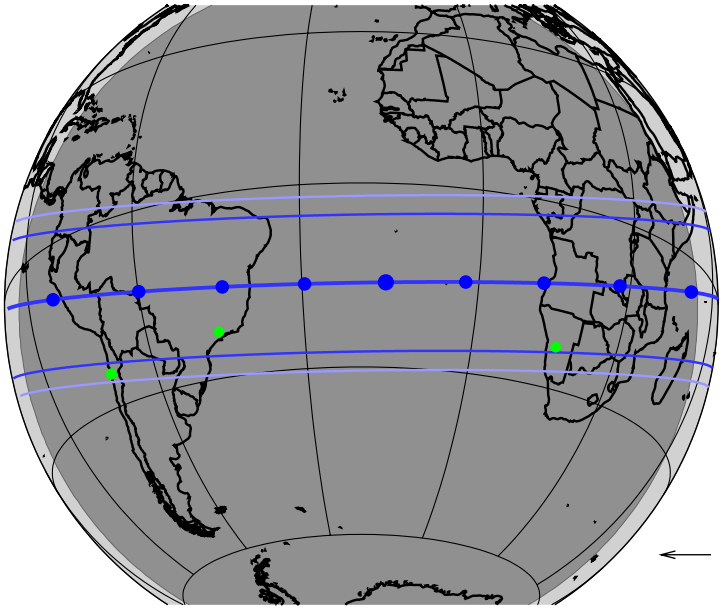

Figure 4.11: Same as Fig. 4.7 for the 2007 June 14 event.

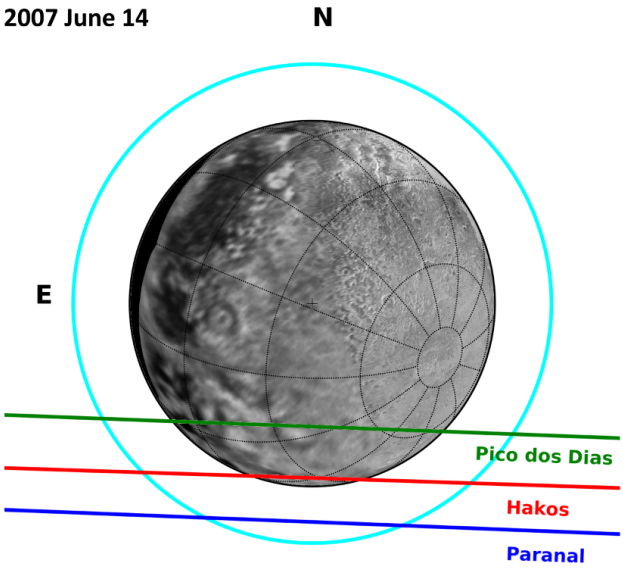

Figure 4.12: The same as Fig. 4.8 for the 2007 June 14 event, except that Pluto's position is now derived entirely from a simultaneous fit to the sites listed in Table 4.2, using the Dias-Oliveira et al. (2015) model. The solid stellar trajectories correspond a each positives observations.

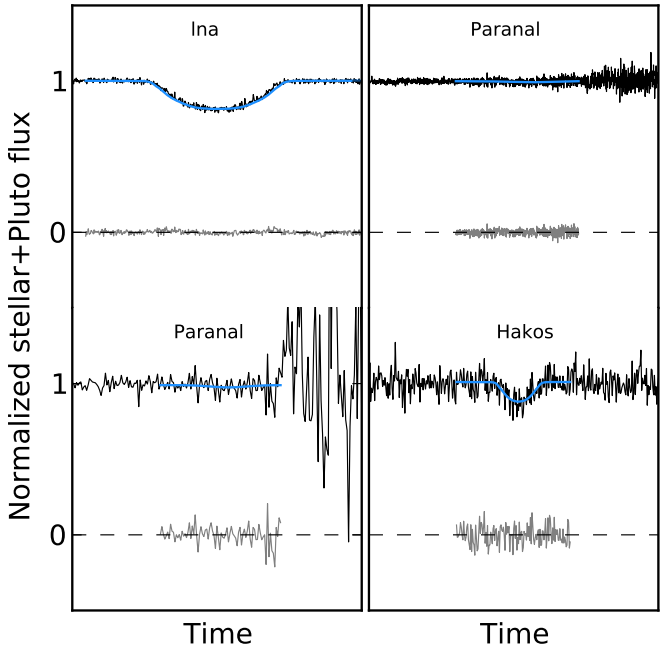

Figure 4.13: Positive Occultation light curves obtained in Brazil, Chili and Namibia on 2007 June 14. Blue curves are a simultaneous fit to the Dias-Oliveira et al. (2015) model, and the residuals are in gray.

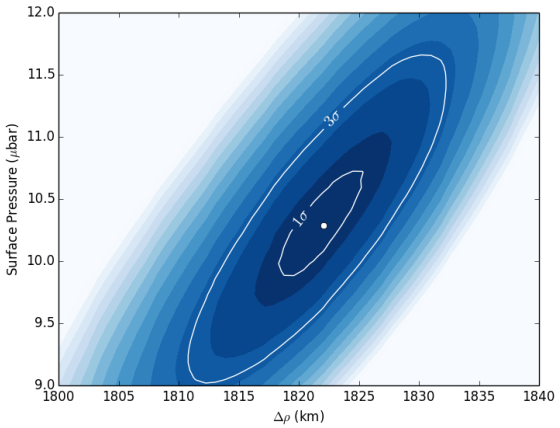

Figure 4.14: The same as Fig. 4.10 for the 2007 June 14 event. The white dot shows the best fit, at $p_{\rm surf} = 10.29 \pm 0.44$ μbar. It corresponds to $\chi^2 = 2504.4$ and uses 1606 data points.

4.5 2008 June 22

This event was observed from Australia. In this campaign, all the light curves were obtained by amateur stations. The circumstances of observations are summarized in Table 4.3 and the occultation light curves are displayed Fig 4.15.

Table 4.3: Circumstances of Observations, 2008 June 22

Site	**Coordinates altitude (m)**	**Telescope Instrument/filter**	**Exp. Time/Cycle (s)**	**Observers**
Bankstown	33 55 56 S	0.275m	1.28/1.28	T. Dobosz
Australia	151 01 45 E	video/clear		
	24.9			
Blue Mountains	33 39 51.9 S	0.25m	1.28/1.28	D. Gault
Australia	150 38 27.9 E	video/clear		
	286			
Reedy Creek	28 06 29.9 S	0.25m	6.30/8.82	J. Broughton
Australia	153 23 52.0 E	CCD/clear		
	65			
Glenlee	23 16 09.6 S	0.30m	0.12/012	S. Kerr
Australia	150 30 00.8 E	video/clear		
	50			
Perth	31 47 21.5 S	0.25m		G. Bolt
Australia	115 45 31.3 E	CCD/clear	2.0	
	45		6.0	

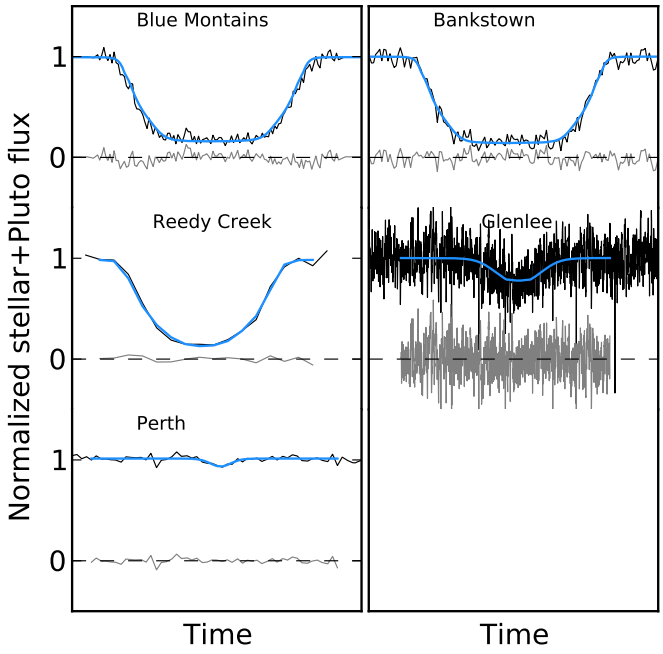

Figure 4.15: The same as Fig. 4.13 for the light curves obtained in Australia on 2008 June 22.

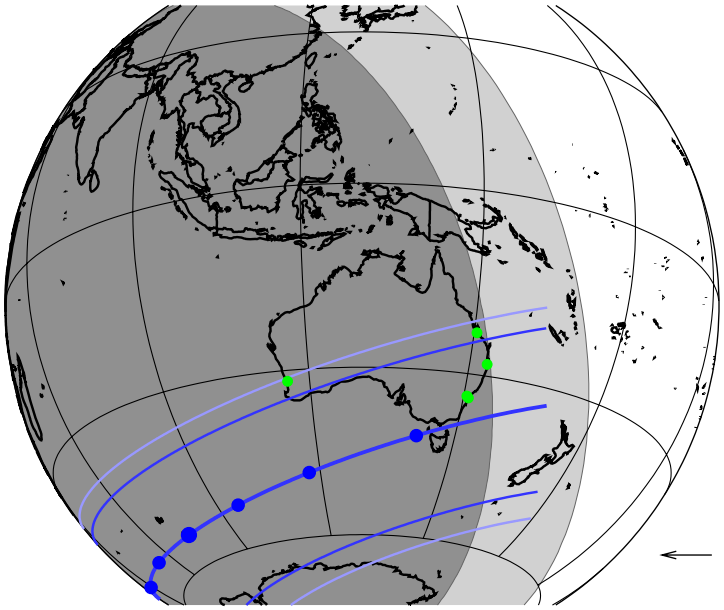

Figure 4.16: Same as Fig. 4.7 for the 2008 June 22 event.

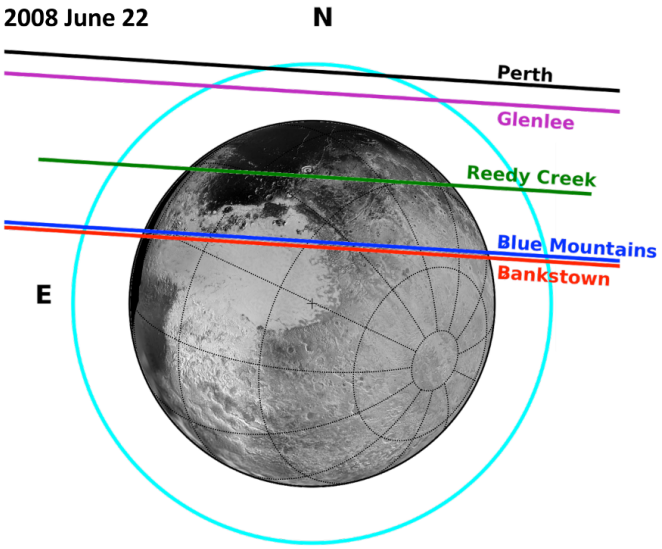

Figure 4.17: The same as Fig. 4.12 for the 2008 June 22 event.

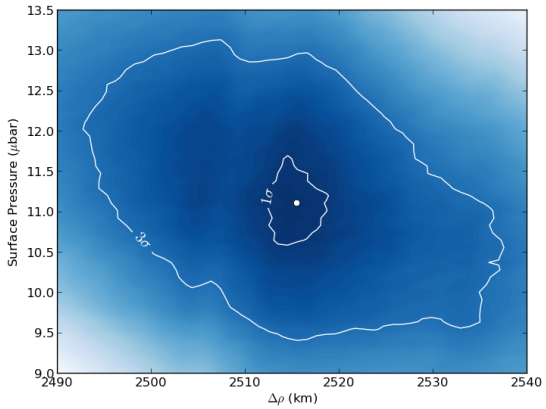

Figure 4.18: The same as Fig. 4.10 for the 2008 June 22 event. The white dot shows the best fit, with $p_{\rm surf} = 11.11 \pm 0.59$ μbar. It corresponds to $\chi^2 = 3589.6$ and uses 3855 data points.

4.6 2008 June 24

This occultation was successful recorded from CFHT in the near IR (K band), see Fig. 4.19. Table 4.4 summarizes the circumstances of observations, Figure 4.20 displays the reconstructed Pluto's shadow path, Figure 4.21 shows the corresponding reconstructed occultation geometry, and Figure 4.22 provides the χ^2 map. Note that because the event was almost central, there was an ambiguity of the shadow path in the pre-Gaia era. As the occulted star position is now in the Gaia DR2 catalog (Gaia Collaboration et al., 2016, 2018), it has been possible to decide which solution is correct one, see Chapter 5.

Table 4.4: Circumstances of Observations, 2008 June 24

Site	**Coordinates altitude (m)**	**Telescope Instrument/filter**	**Exp. Time/Cycle (s)**	**Observers**
CFHT Hawaii	19 49 30.88 N 155 28 07.52 W 4200	3.6m Wircam/K	0.065/0.065	L. Albert

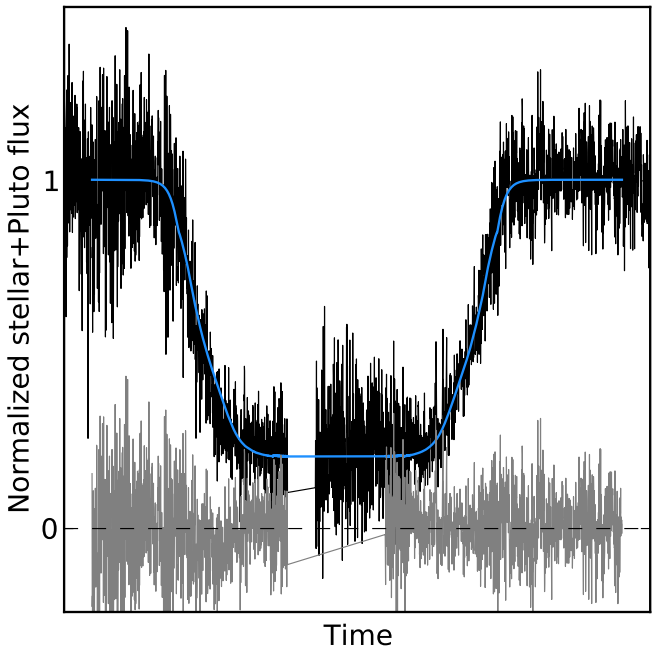

Figure 4.19: The same as Fig. 4.13 for the light curve obtained at CFHT on 2008 June 24.

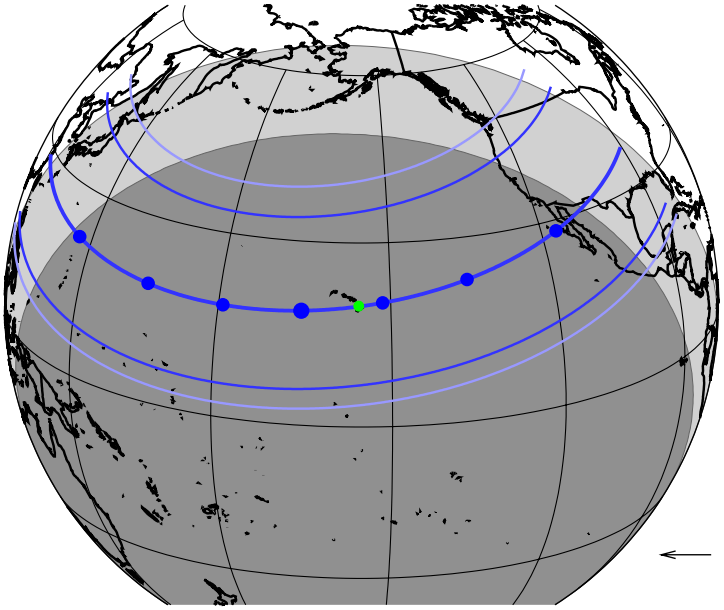

Figure 4.20: Same as Fig. 4.7 for the 2008 June 24 event.

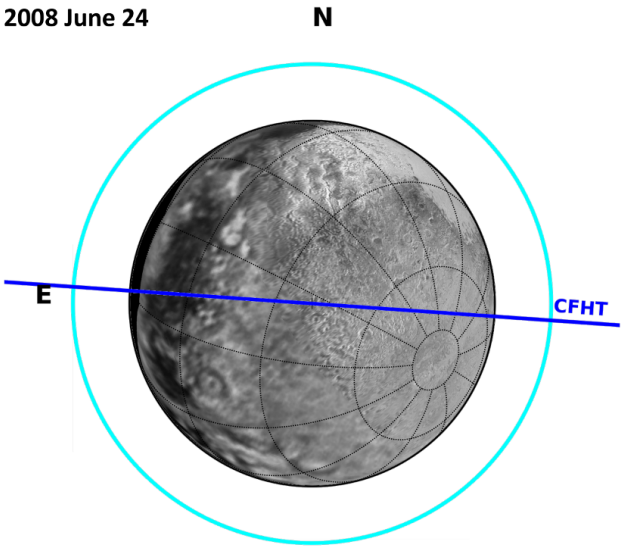

Figure 4.21: The same as Fig. 4.12 for the 2008 June 24 event.

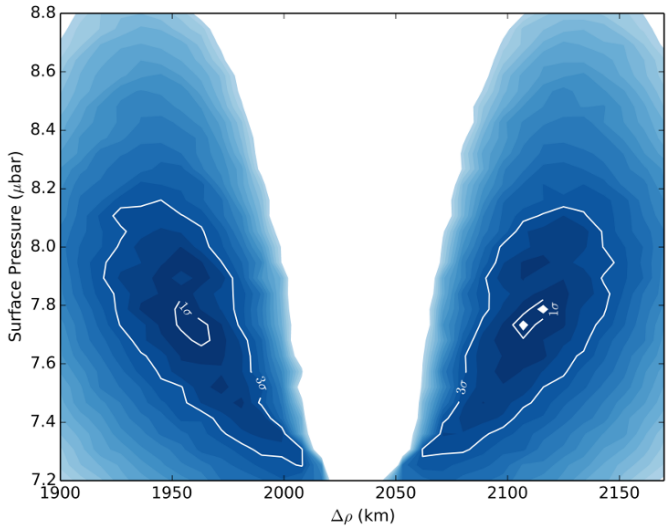

Figure 4.22: The same as Fig. 4.10 for the 2008 June 24 event. The white dot shows the best fit, at $p_{\rm surf} = 10.52 \pm 0.51$ μbar. It corresponds to $\chi^2 = 2701.4$ and uses 2359 data points. Note that there are two possible solutions, due to the almost central configuration of the event (Fig. 4.21). Stellar catalogs and Pluto's ephemeris were not accurate enough at that time to distiguish between the two solutions. The publication of the Gaia DR2 catalog (Gaia Collaboration et al., 2016, 2018) and the fitting of Pluto's orbital elements to our occultation detections allowed us to discriminate between the two solutions and choose the one at right, see Chapter 5.

4.7 2010 February 14

This occultation was recorded in France and Switzerland, see Table 4.5, Fig. 4.23, Figure 4.24 and Fig. 4.25.

I have used three light curves of Fig. 4.23 to fit the Dias-Oliveira et al. (2015) model, see the $\chi 2$ map of Fig. 4.26.

Table 4.5: Circumstances of Observations, 2010 February 14

Site	**Coordinates altitude (m)**	**Telescope Instrument/filter**	**Exp. Time/Cycle (s)**	**Observers**
Pic du Midi	42 56 12.0 N	T1m	0.32/0.32	J. Lecacheux
France	00 08 31.9 E	ccd/clear		
	2862			
Lu	46 37 26.3 N	0.35m	0.35/0.50	C. Olkin,
Switzerland	10 22 00.3 E	video/clear		L. Wasserman
	1933			
Sisteron	44 05 18.20 N	0.3m	0.64/0.64	F. Vachier
France	05 56 16.3 E	Watec 120/clear		
	634			

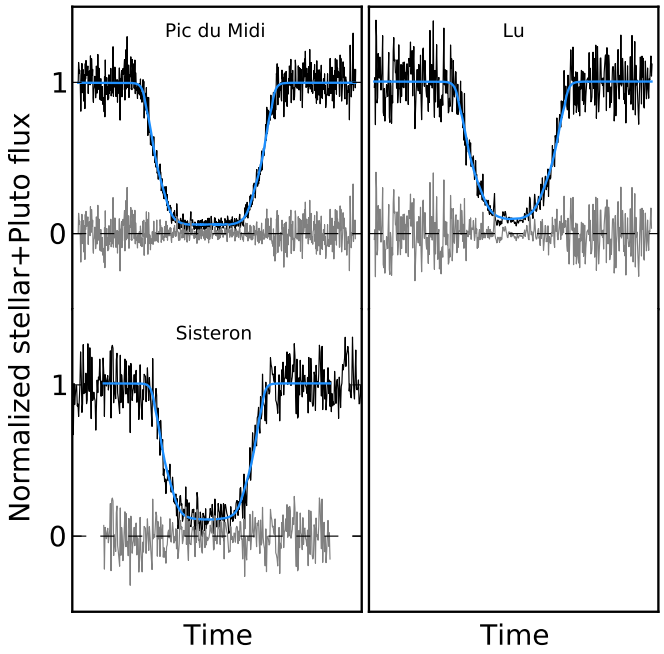

Figure 4.23: The same as Fig. 4.13 for the light curve obtained in Europe on 2010 February 14.

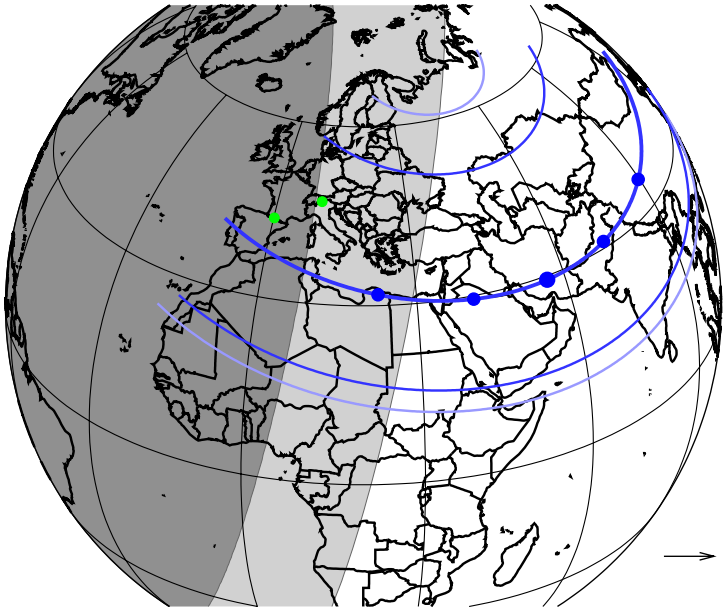

Figure 4.24: Same as Fig. 4.7 for the 2010 February 14 event.

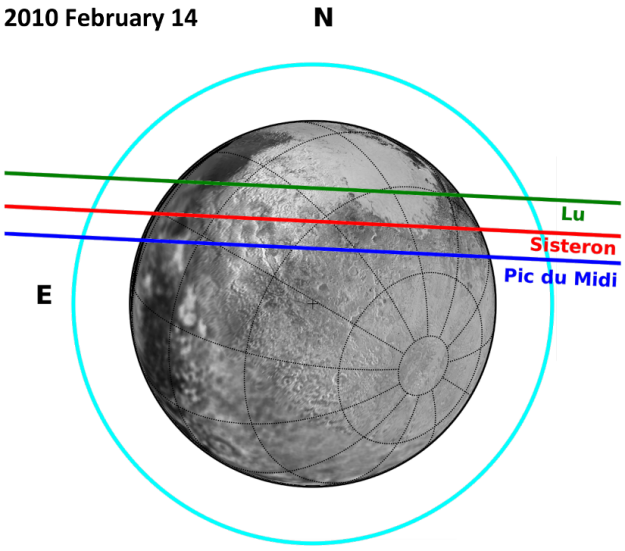

Figure 4.25: The same as Fig. 4.12 for the 2010 February 14 event.

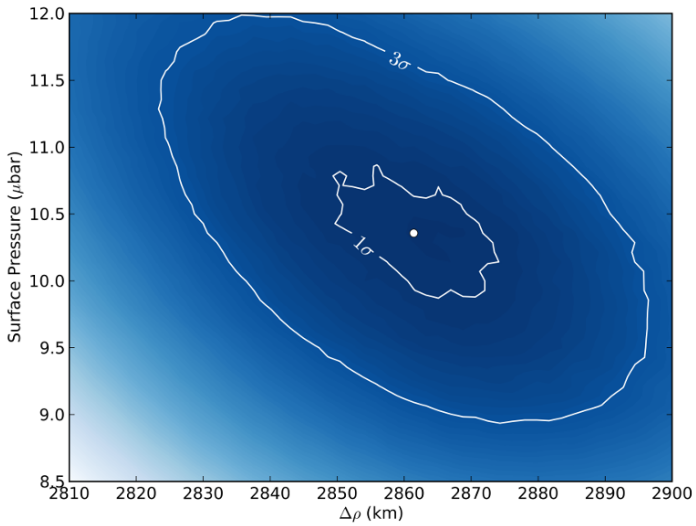

Figure 4.26: The same as Fig. 4.10 for the 2010 February 14 event. The white dot shows the best fit, at $p_{\rm surf} = 10.36 \pm 0.4$ μbar. It corresponds to $\chi^2 = 1559.2$ and uses 1583 data points.

4.8 2010 June 04

This occultation was observed from Australia and New Zealand, see Table 4.6. The results are displayed in Figs. 4.27, 4.28 and Figure 4.29. I have used five light curves of Fig. 4.27 to fit the Dias-Oliveira et al. (2015) model, see Fig. 4.30.

Table 4.6: Circumstances of Observations, 2010 June 04

Site	**Coordinates altitude (m)**	**Telescope Instrument/filter**	**Exp. Time/Cycle (s)**	**Observers**
Mt John	42 50 49.83 S	1m	0.32/0.32	B. Loader,
New Zealand	147 25 55.32 E	ccd/clear		A. Gilmore
	37.5			
Hobart	42 50 49.83 S	1m	1/1	J. Greenhill,
Australia	147 25 55.32 E	Raptor/I		S. Mathers,
	37.5			
Lauder	41 29 36.3 S	0.6m Bootes-3	0.50/1.75	B. Allen
New Zealand	173 50 20.7 E	ccd/r'		
	37.5			
Blenheim	41 29 36.3 S	0.4m	2.5/6	B. Allen
New Zealand	173 50 20.7 E	ccd/clear		
	37.5			
Oxford	43 18 36.78 S	0.3m	0.64/0.64	S. Parker
New Zealand	172 13 07.8 E	Video/clear		
	221			

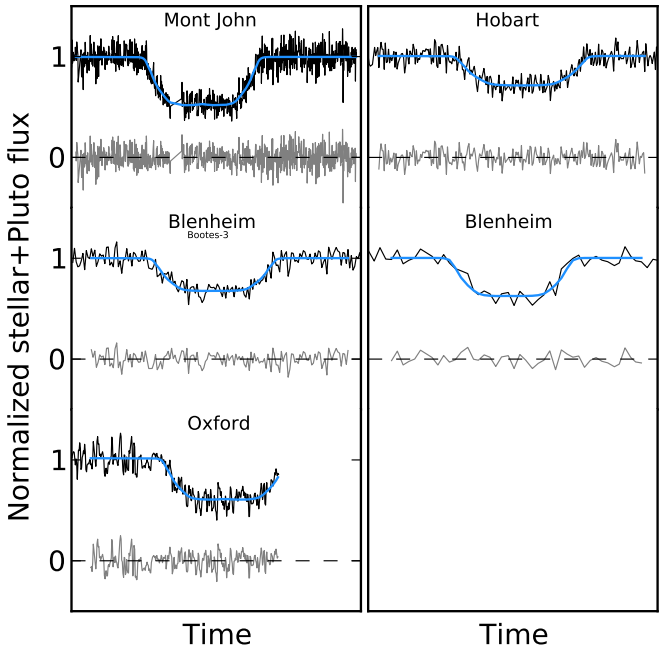

Figure 4.27: The same as Fig. 4.13 for the light curves obtained in Australia and New Zealand on 2010 June 04.

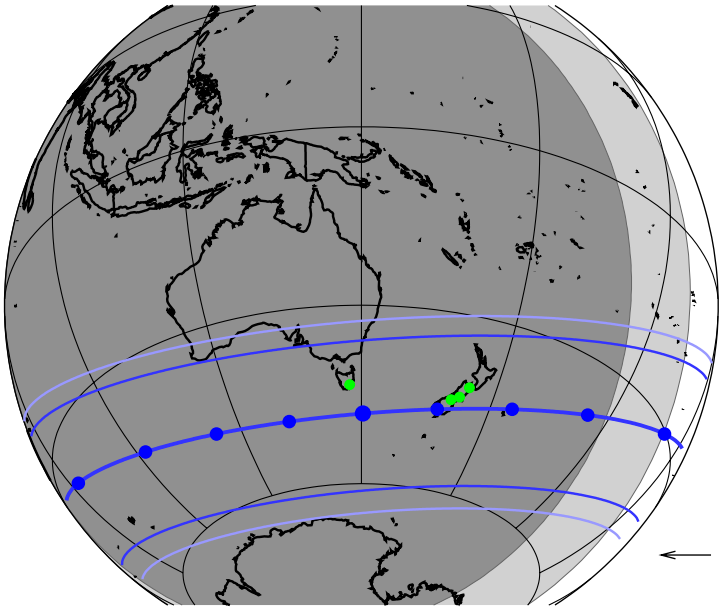

Figure 4.28: The same as Fig. 4.7 for the 2010 June 04 event.

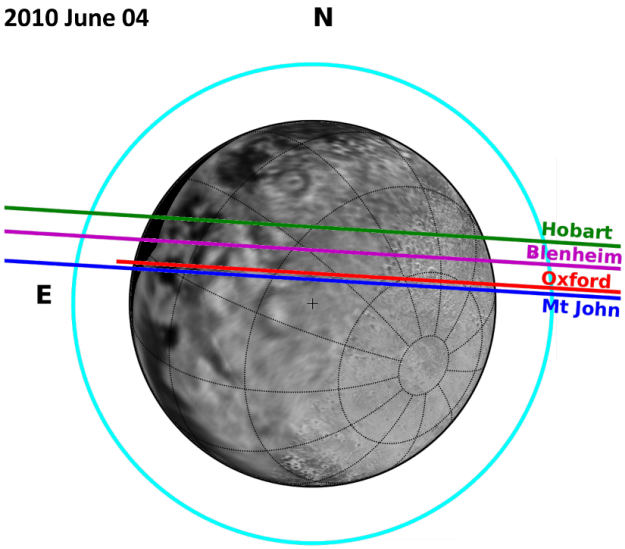

Figure 4.29: The same as Fig. 4.12 for the 2010 June 04 event.

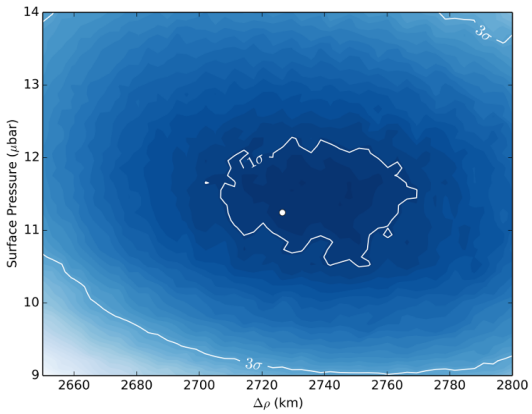

Figure 4.30: The same as Fig. 4.10 for the 2010 June 04 event. The white dot shows the best fit, at $p_{\rm surf} = 11.24 \pm 0.96$ μbar. It corresponds to $\chi^2 = 1724.3$ and uses 1685 data points.

4.9 2011 June 04

This occultation was observed from South America, see Table 4.7. The results are displayed in Figs. 4.31, 4.32 and Figure 4.33. I have used five light curves of Fig. 4.31 to fit the Dias-Oliveira et al. (2015) model, see Fig. 4.34.

Table 4.7: Circumstances of Observations, 2011 June 04

Site	**Coordinates altitude (m)**	**Telescope Instrument/filter**	**Exp. Time/Cycle (s)**	**Observers**
Santa Martina	33 16 09.0 S	0.4m	2/2	R. Leiva
Chile	45 34 57.70 W	EMCCD/clear		
	1450			
La Silla	29 15 16.59 S	TRAPPIST S 0.6m	3/4.4	E. Jehin
Chile	70 44 21.82 W	CCD/clear		
	2315			
San Pedro de	22 57 12.3 S	Caisey 0.5m	2/2.87	A. Maury
Atacama, Chile	68 10 47.6 W	CCD/clear		
	2397			
Pico dos Dias	22 32 7.80 S	1.6m	0.1/0.1	M. Assafin
Brazil	45 34 57.70 W	CCD/clear		
	1864			

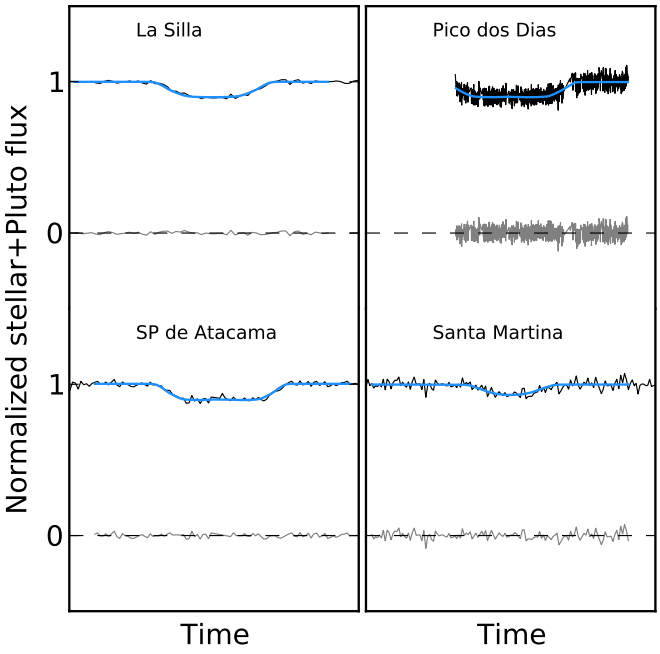

Figure 4.31: The same as Fig. 4.13 for the light curves obtained in South America on 2011 June 04.

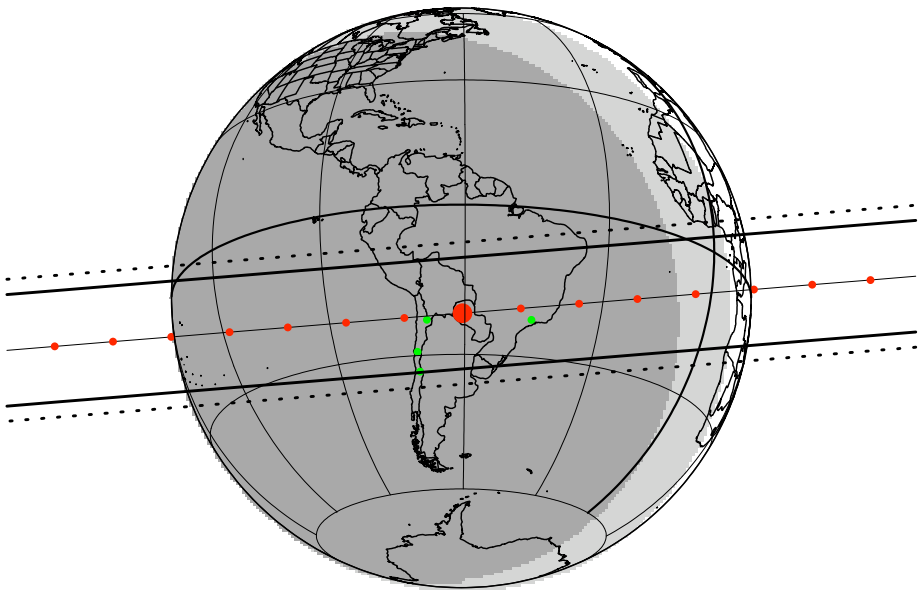

Figure 4.32: The same as Fig. 4.7 for the 2010 June 04 event.

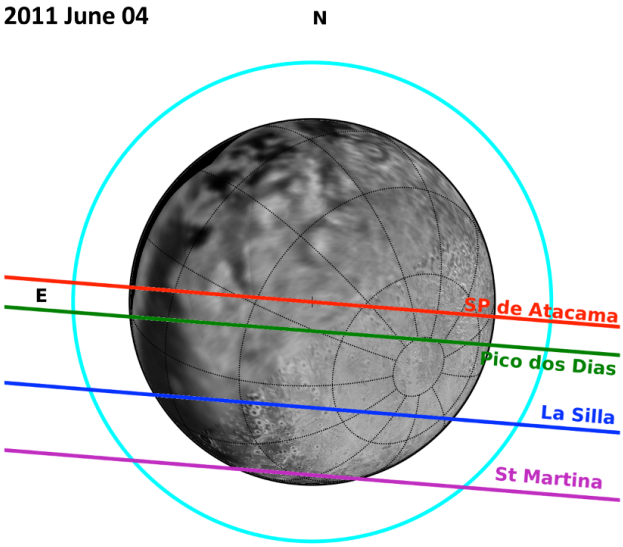

Figure 4.33: The same as Fig. 4.12 for the 2011 June 04 event.

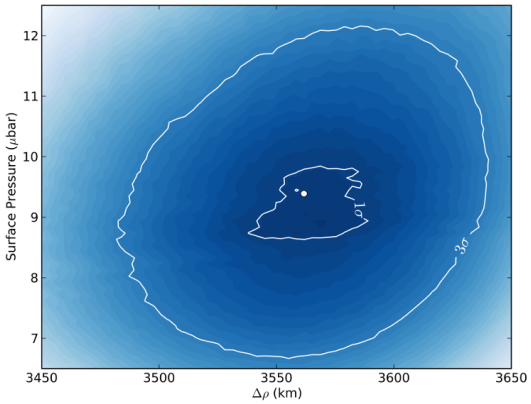

Figure 4.34: The same as Fig. 4.10 for the 2011 June 04 event. The white dot shows the best fit, at $p_{\rm surf} = 9.39 \pm 0.70$ μbar. It corresponds to $\chi^2 = 1721$ and uses 1660 data points.

4.10 2012 July 18

The event was recorded in Chile, Argentina and Peru, seeTable 4.8. It provided the best light curve of all our campaigns thanks to the VLT/NACO observation. Results are displayed in Figs. 4.35, 4.36 and 4.37, while the χ^2 map is shown in 4.38, using the five light curves of Fig. 4.35.

Table 4.8: Circumstances of Observations, 2012 July 18

Site	**Coordinates altitude (m)**	**Telescope Instrument/filter**	**Exp. Time/Cycle (s)**	**Observers**
Santa Martina	33 16 09.0 S	0.4m	1/1	R. Leiva Espinoza
Chile	45 34 57.70 W	CCD/clear		
	1450			
Cerro Burek	31 47 12.4 S	ASH 0.45m	13/15.7	N. Morales
Argentina	69 18 24.5 E	CCD/clear		
	2591			
Paranal	24 37 31.0 S	VLT UT4 8.2m	0.2/0.2	J. Girard
Chili	70 24 08.0 W	NACO/H		
	2635			
San Pedro	22 57 12.3 S	ASH2 0.4m	13/15.44	N. Morales
de Atacama	68 10 47.6 W	CCD/clear		
Chili	2397			
Huancayo	12 02 32.2 S	0.20m	10.24/10.24	E. Meza
Peru	75 19 14.7 W	CCD/clear	5.12/5.12	
	3344			

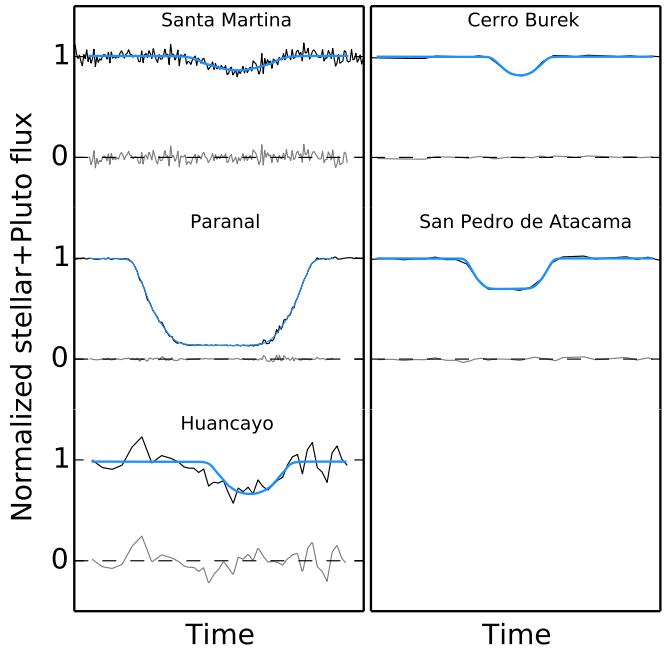

Figure 4.35: The same as Fig. 4.13 for the light curves obtained in South America on 2012 July 18.

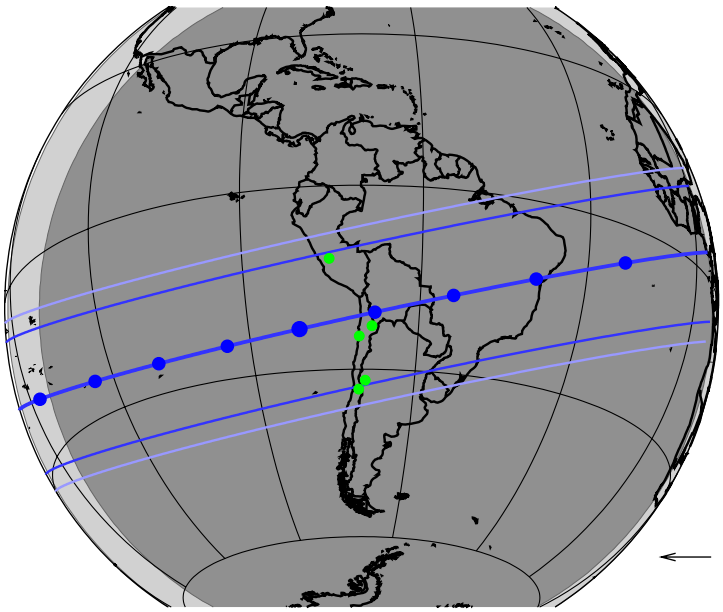

Figure 4.36: Same as Fig. 4.7 for the 2012 July 18 event.

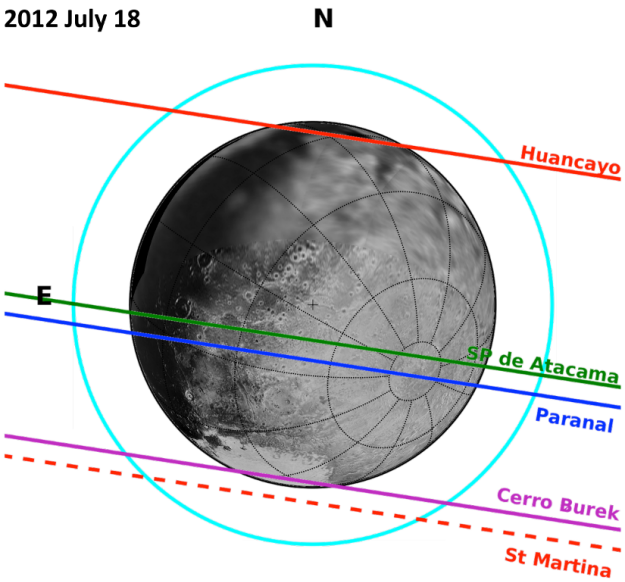

Figure 4.37: The same as Fig. 4.12 for the 2012 July 18 event. Labels for the chords are Hua: Huancayo, Spa: San Pedro de Atacama, Par: Paranal, Bur: Cerro Burek, San: Santa Martina. The light blue circle corresponds to the 1% stellar drop, the detection limit at VLT/Paranal. Pluto's globe as seen at that date has been superimposed to the chords. It is derived from a map obtained during the New Horizons flyby (http://pluto.jhuapl.edu/Mul0media/Science'Photos/pics/pmap_cyl_PS723_HRg.jpg).

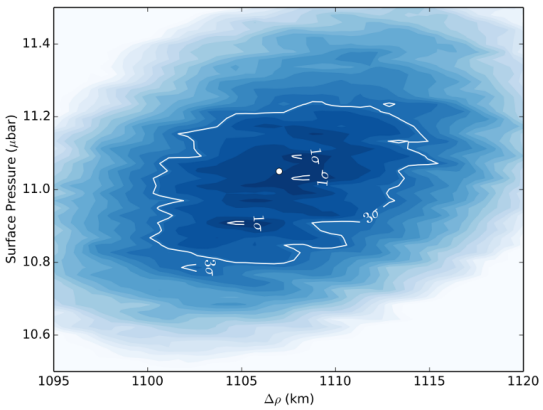

Figure 4.38: The same as Fig. 4.10 for the 2012 July 18 event. The white dot shows the best fit, at $p_{\rm surf} = 11.05 \pm 0.08$ μbar. It corresponds to $\chi^2 = 859.8$ and uses 1402 data points. Note the striations, that are caused by numerical noise, stemming itself from the finite thickness of the layers (30 m) used to generate the synthetic light curves. It is visible here because of the high quality of the Paranal/VLT light curve, see Fig. lc20160719. For the other occultations, the noise is dominated by the photometric quality of the light curves.

4.11 2013 May 04

For this campaign, data were was successfully gathered in Chile, Argentina and Brazil, see Table 4.9 and Fig. 4.39. The reconstructed occultation geometry is displayed in Figs. 4.40 and 4.41.

I have used a total of eight light curves (Fig. 4.39) to retrieve the $\chi 2$ map of Fig. 4.42. Note that a good latitudinal coverage of Pluto was obtained during this campaign.

Table 4.9: Circumstances of Observations, 2013 May 04

Site	**Coordinates altitude (m)**	**Telescope Instrument/filter**	**Exp. Time/Cycle (s)**	**Observers**
Cerro Burek	31 47 14.5 S 69 18 25.9 W 2591	ASH 0.45 m CCD/clear	6/8	J.L. Ortiz
Cerro Tololo	30 10 03.36 S 70 48 19.01 W 2207	PROMPT 0.4m P1, P3, P4, P5 ccd/clear	5/8 P3 offset 2 sec P4 offset 4 sec P5 offset 6 sec	J. Pollock
La Silla	29 15 21.276 S 70 44 20.184 W 2336	Danish 1.54m Lucky Imager/Z (>650nm, CCD/iXon response)	Lucky Imager 0.1/0.1	L. Mancini
La Silla	29 15 16.59 S 70 44 21.82 W 2315	TRAPPIST 0.6m CCD/clear	4.5/6	E. Jehin, A. Decock, M. Gillon, C. Opitom
Pico dos Dias	22 32 07.8 S 45 34 57.7 W 1,811	B&C 0.6m Ccd/I	4.5/6	M. Assafin, A. Ramos Gomes Jr
Cerro Paranal	24 37 31.0 S 70 24 08.0 W 2635.43	UT4 Yepun 8.2m NACO/H	0.2/0.2	G. Hau
San Pedro de Atacama	22 57 12.3 S 68 10 47.6 W 2397	Caisey 0.5m f/8 CCD/V	3/4.58	A. Maury
San Pedro de Atacama	22 57 12.3 S 68 10 47.6 W	Caisey 0.5m f/6.8 CCD/B	4/4.905	L. Nagy

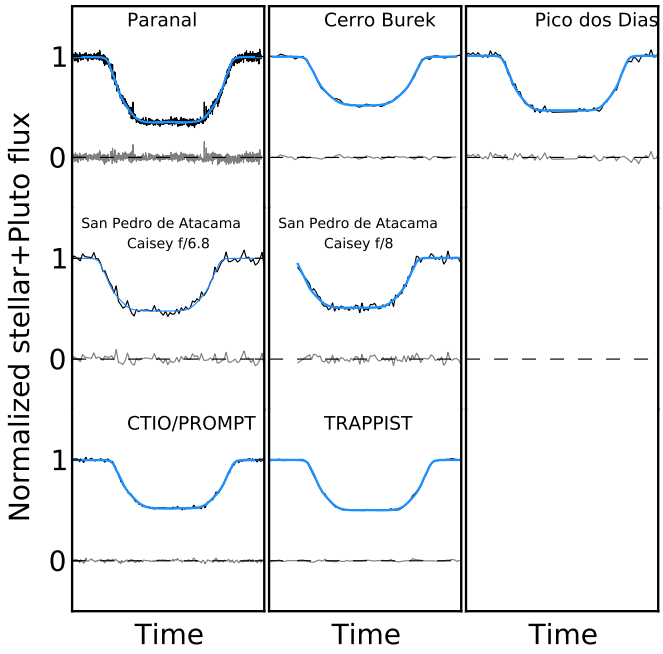

Figure 4.39: The same as Fig. 4.13 for the light curves obtained in South America on 2013 May 04.

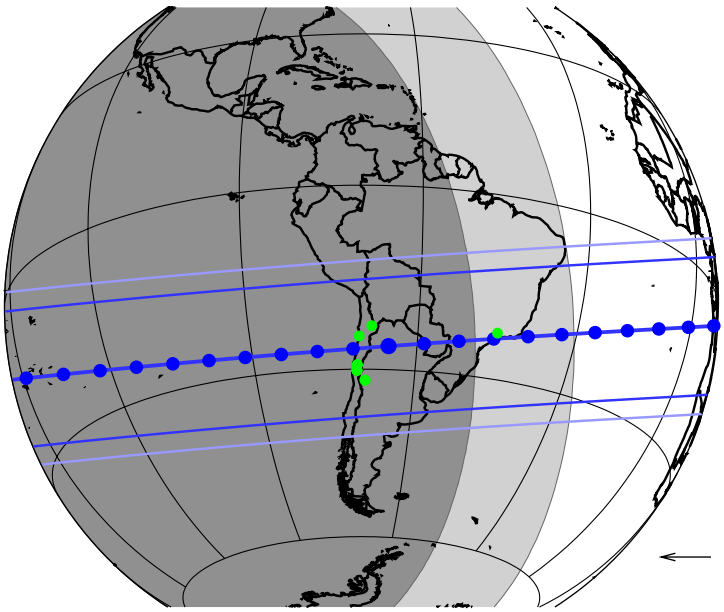

Figure 4.40: Same as Fig. 4.7 for the 2013 May 04 event.

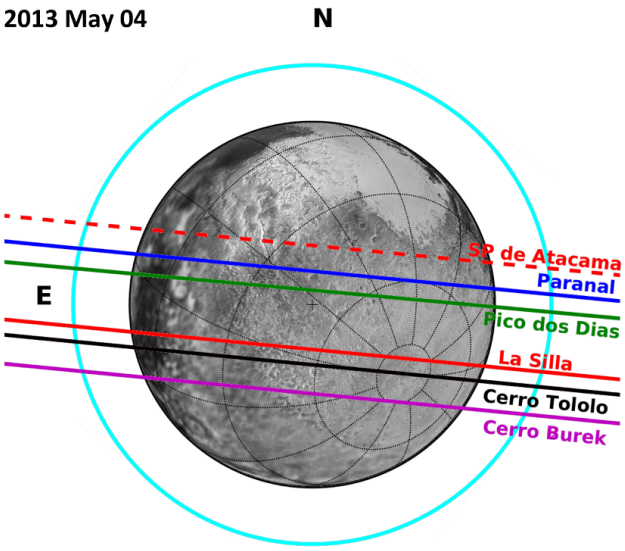

Figure 4.41: The same as Fig. 4.12 for the 2013 May 04 event.

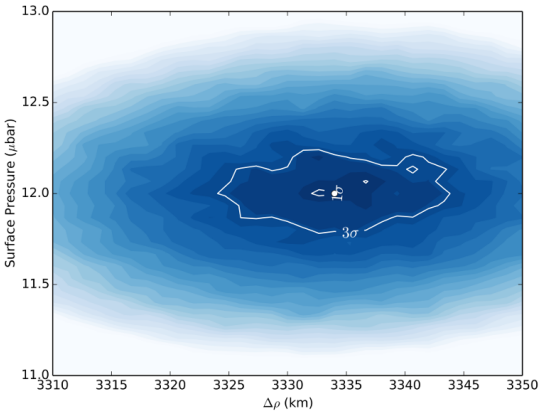

Figure 4.42: The same as Fig. 4.10 for the 2013 May 04 event. The white dot shows the best fit, at $p_{\rm surf} = 12.0 \pm 0.09$ μbar. It corresponds to $\chi^2 = 3300.6$ and uses 2751 data points.

4.12 2015 June 29

The occultation occurred in New Zealand and Australia, see Table 4.10 and Figs. 4.43, 4.44 and 4.45. I have used eight light curves (see Fig. 4.43) to obtain the χ^2 map of Fig. 4.46.

During this campaign, a central flash was observed from two stations in New Zealand (Lauder and Dunedin). It probed deep layers of Pluto's atmosphere, a few kilometers above its surface and was close in time and space to the NASA New Horizons flyby of 14 July 2015. Analysis of this flash and comparison with New Horizons results are presented in Chapter 5.

Table 4.10: Circumstances of Observations, 2015 June 29

Site	**Coordinates altitude (m)**	**Telescope Instrument/filter**	**Exp. Time/Cycle (s)**	**Observers**
Lauder	45 02 17.39 S	Bootes-3 0.60m	0.05633/0.05728	M. Jelinek
New Zealand	169 41 00.88 W	EMCCD / clear		
	382			flash detected
Dunedin	45 54 31 S	0.35m	5.12/5.12	A. Pennell, S. Todd,
New Zealand	170 28 46 E	CCD / clear		M. Harnisch, R. Jansen
	136			flash detected
Spring Hill	42 25 51.80 S	Greenhill H - 1.27m	0.1/0.1	A. A. Cole,
Australia	147 17 15.80 E	EMCCD / B		B. Giles,
	641			K. M. Hill
Darfield	43 28 52.90 S	0.25m	0.32/0.32	B. Loader
New Zealand	172 06 24.40 E	CCD / clear		
	210			
Blenheim 1	41 32 08.60 S	0.28m	0.64/0.64	G. McKay
New Zealand	173 57 25.10 E	CCD / clear		
	18			
Blenheim 2	41 29 36.27 S	04m	0.32/0.32	W. H. Allen
New Zealand	173 50 20.72 E	CCD / clear		
	38			
Martinborough	41 14 17.04 S	0.25m	0.16/0.16	P. Graham
New Zealand	175 29 01.18 E	CCD / B		
	73			
Melbourne	37 50 38.50 S	0.20m	0.32/0.32	J. Milner
Australia	145 14 24.40 E	CCD / clear		
	110			

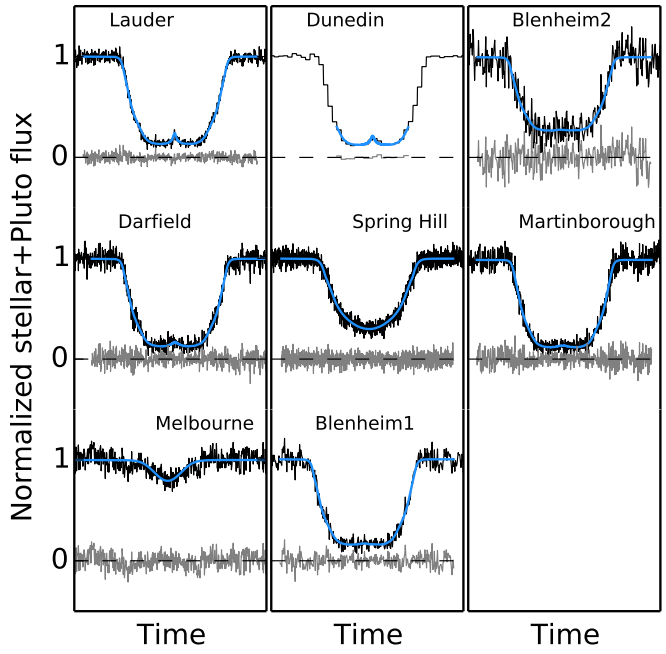

Figure 4.43: The same as Fig. 4.13 for the light curves obtained in Australia and New Zealand on 2015 June 29.

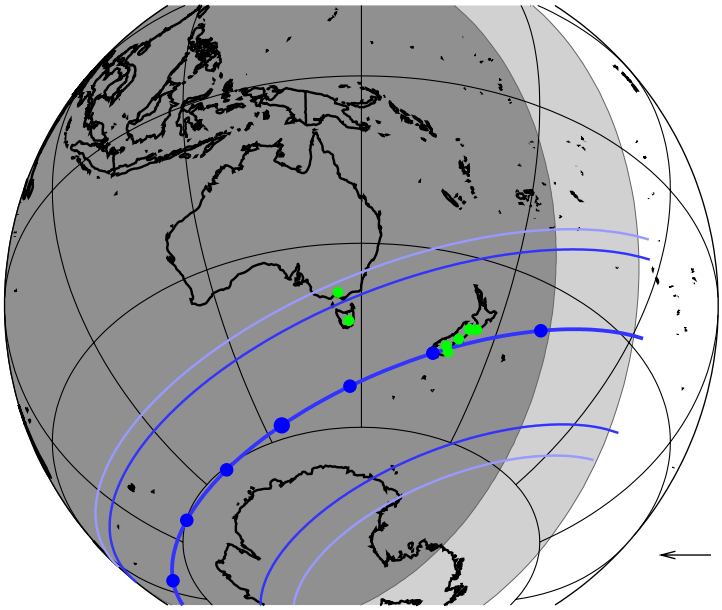

Figure 4.44: Same as Fig. 4.7 for the 2015 June 29 event.

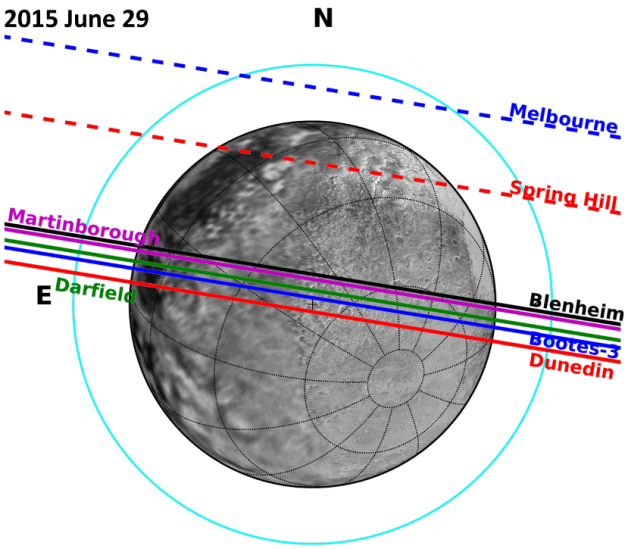

Figure 4.45: The same as Fig. 4.12 for the 2015 June 29 event.

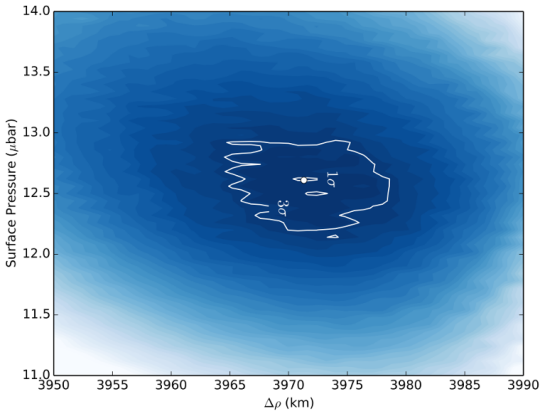

Figure 4.46: The same as Fig. 4.10 for the 2015 June 29 event. The white dot shows the best fit, at $p_{\rm surf} = 12.71 \pm 0.14$ μbar. It corresponds to $\chi^2 = 3933.6$ and uses 4684 data points.

4.13 2016 July 19

This occultation is the second out of two that was recorded in Europe (after the 2010 February 14 event). It was observed from a large number of stations (mostly by amateurs), but we use here a sub-set of data with higher SNR obtained from France, Spain, Italy and Israel, see Table 4.11. The analysis of the other stations is still ongoing, but the final outcome should alter the conclusions reached here (although it will reduce the error bars on the fitted parameters). Figs. 4.48, 4.45 and 4.45 display the geometry of the event.

I have used the six light curves of Fig. 4.47 to obtain the χ^2 map of Fig. 4.50.

Table 4.11: Circumstances of Observations, 2016 July 19

Site	**Coordinates altitude (m)**	**Telescope Instrument/filter**	**Exp. Time/Cycle (s)**	**Observers**
Pic du Midi France	42 56 12.0 N 00 08 31.9 E 2862	1m EMCCD/ clear	0.3/0.3	F. Colas, E. Meza
Val d'Aosta Italy	45 47 22.00 N 7 28 42.00 E 1674	0.81m EMCCD / clear	1/1	B. Sicardy
La Palma Spain	28 45 14.4 N 17 53 20.6 E 2387.2	TNG 3.58m EMCCD / clear	1/5	A. Magazzu
Saint Véran France	44 41 49.88 N 06 54 25.90 E 2936	0.5m EMCCD/ clear	1/1	E. Comunal
Calern France	43 45 13.50 N 06 55 21.80 E 1264	C2PU T1m CCD/ clear	0.3/0.3	D. Vernet, J P. Rivet, P. Bendjoya, M. Devogele
Mitzpe Ramon Israel	30 35 44.40 N 34 45 45.00 E 862	0.28m CCD/ clear	1/2.5	S. Kaspi, D. Polishook, N. Brosh, I. Manulis

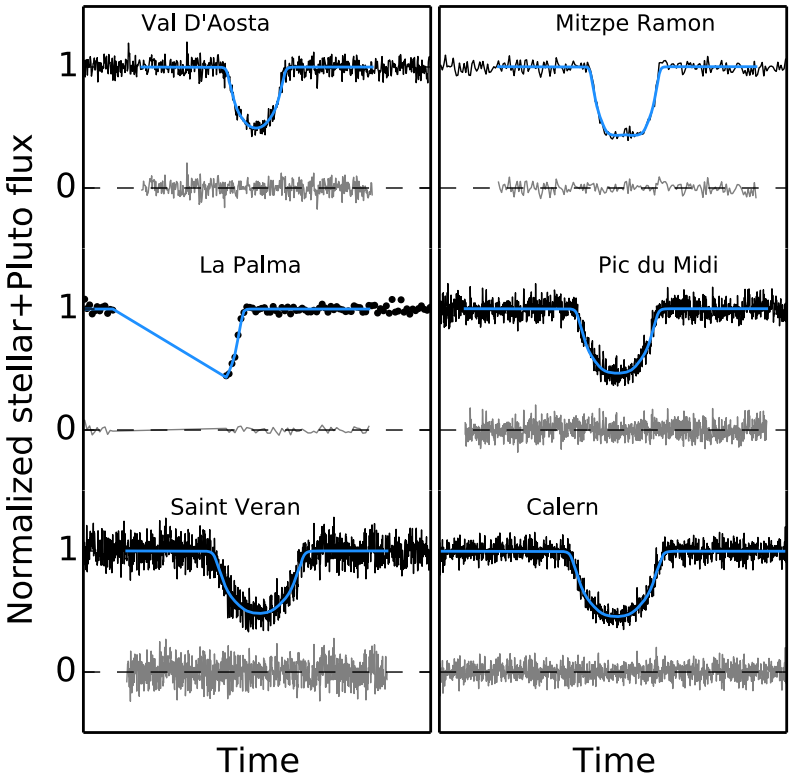

Figure 4.47: The same as Fig. 4.13 for the light curves obtained in Europe on 2016 July 19.

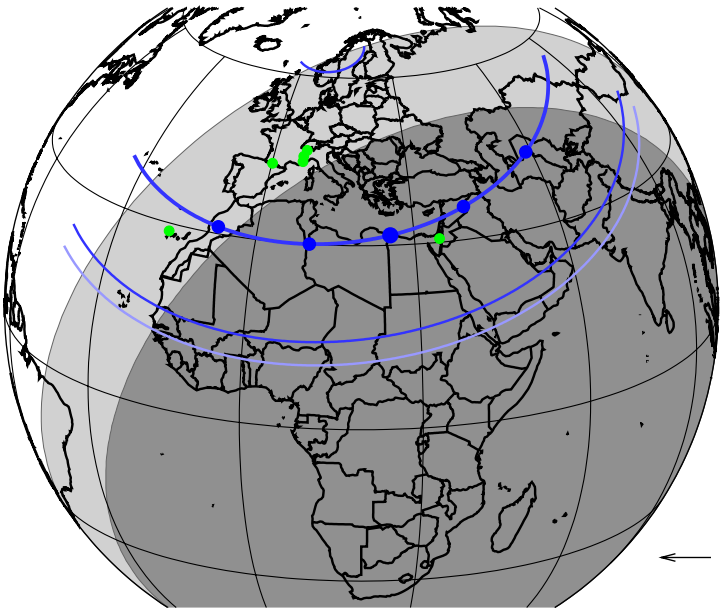

Figure 4.48: Same as Fig. 4.7 for the 2016 July 19 event.

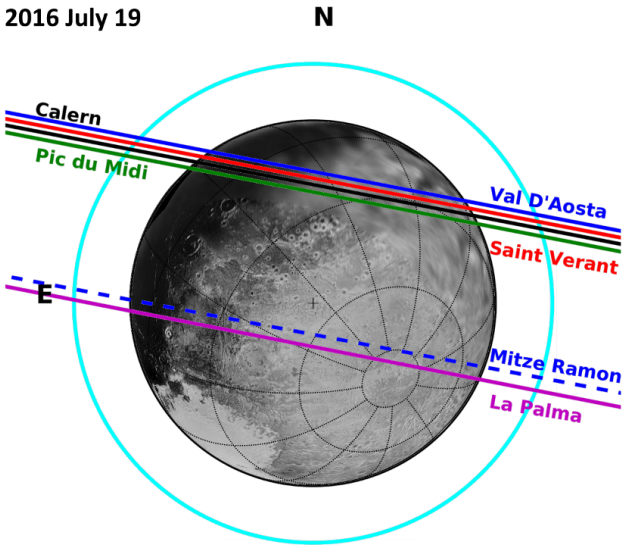

Figure 4.49: The same as Fig. 4.12 for the 2016 July 19 event.

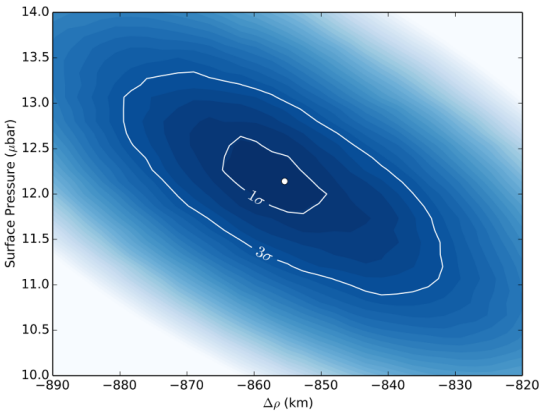

Figure 4.50: The same as Fig. 4.10 for the 2016 July 19 event. The white dot shows the best fit, at $p_{\rm surf} = 12.04 \pm 0.41$ μbar. It corresponds to $\chi^2 = 4716.4$ and uses 4432 data points.

Chapter 5

Pluto's atmospheric structure and ephemeris

Contents

Summary of my work and collaborations

I directly observed two Pluto occultation in 2012 and 2016 (see previous chapter), and participated to the preparation of several other campaigns. Then I analyzed in details 45 light curves of Pluto occultations obtained during a total of 11 campaigns from 2002 to 2016. Those campaigns include a central flash detection on 2015 June 29, two weeks before the New Horizons flyby of 14 July 2015. This detection is particularly important because it probed deeper layers of Pluto's atmosphere.

Beyond this analysis, I collaborated with Tanguy Bertrand and François Forget to interpret the Pluto's atmospheric pressure evolution that I found, based on their LMD (Laboratoire de Météorologie Dyamique) Pluto volatile transport model (Bertrand and Forget, 2016; Forget et al., 2017; Bertrand et al., 2018).

Additionally, I collaborated with Josselin Desmars to use the geometric results of Pluto occultations to derive the offset of the dwarf planet with respect to reference ephemerides. This is turn is used to update the so-called NIMA (Numerical Integration of the motion of an Asteroid, Desmars et al. 2015) ephemerides, which eventually improve predictions of future occultations.

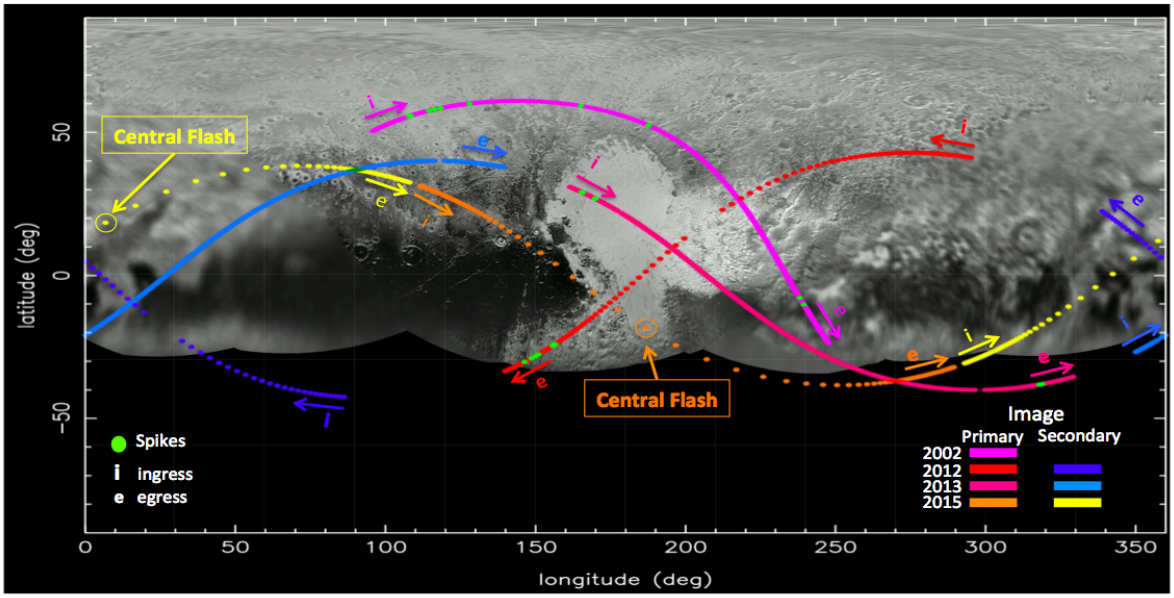

Figure 5.1: Trajectories of the primary and secondary stellar images over Pluto's surface obtained from some of our campaigns between 2002 to 2016, where spikes activity and/or central flash were detected. Note that in the central part the stellar images its faster than the igress and egress. In the background a Pluto map from NH during its flyby (http://pluto.jhuapl.edu/Mul0media/Science'Photos/pics/pmap_cyl_PS723_HRg.jpg).

5.1 Pressure evolution

In 2002, a ground-based stellar occultation revealed that Pluto's atmospheric pressure increased (expansion) by a factor of more than two compared to its estimate in 1988 (Sicardy et al., 2003; Elliot et al., 2003) This may appear as a surprise as one expects a decrease (collapse) after the Pluto perihelion of 1989. However, some years ago models with global volatile transport models (Binzel, 1990; Hansen and Paige, 1996), did predictect this possible trend for the following decades. Those models explored methane and nitrogen cycles. In the recent years they have been improved (Young, 2012; Hansen et al., 2015), and new models were developed (Bertrand and Forget, 2016; Forget et al., 2017; Bertrand et al., 2018). The goal was to simulate possible scenarios for Pluto seasonal changes, both in the past and in the future, accounting for topographic features, as revealed by the New Horizons flyby in July 2015.

However, all models need observables, in our case the Pluto's atmospheric pressure vs. time, in order to constrain different possible solutions. In that context, our team organized and observed several ground-based stellar occultations, which is currently the most powerful technique to achieve this monitoring over long periods of time.

Figure 5.1 show us some selected examples of the paths scanned by the primary and secondary images (see Chapter 2) during some of these campaigns. The occultations of 2012 July 18 and 2013 May 04 were those which provided the best SNR occultation light curves and the best coverage of the planet. This allowed to derive a simple model of Pluto's atmosphere structure, using the Dias-Oliveira et al. (2015) model. I used this model assuming the following:

Composition: a pure nitrogen atmosphere because it is the most abundant element

in the Plutonian atmosphere verified by the flyby of New Horizons in 2015 (see (Gladstone et al., 2016)),

Structure: Pluto's thermal profile is kept constant at all times, meaning a constant temperature both horizontally (parallel to the limb) and with time.

Symmetry: a spherical atmosphere is considered.

clear: no hazes are present (the atmosphere is transparent)

I then applied the ray tracing technique (Chapter 2) to the data set obtained from 2002 to 2016 (Chapter 4) to estimate Pluto's atmospheric surface pressure, as well as at the 1215 km Plutocentric radius (see details in Chapter 4). Table 5.1 summarizes in my results. Note that surface pressure and density have the same accuracy because Pluto's mass is well known, $(8.696 \pm 0.0018) \times 10^{11}$ m^3 s^{-2} (Stern et al., 2015).

Table 5.1: Pluto's atmospheric pressure

Date	Surface pressure, $p_{surface}$ (μbar)	Pressure at 1215 km, p_{1215} (μbar)
2002 August 21	8.08 ± 0.18	4.42 ± 0.093
2007 June 14	10.29 ± 0.44	5.6 ± 0.24
2008 June 22	11.11 ± 0.59	6.05 ± 0.32
2008 June 24	10.52 ± 0.51	5.73 ± 0.21
2010 February 14	10.36 ± 0.4	5.64 ± 0.22
2010 June 04	11.24 ± 0.96	6.12 ± 0.52
2012 July 18	11.05 ± 0.08	6.07 ± 0.044
2013 May 04	12.0 ± 0.09	6.53 ± 0.049
2015 June 29	12.71 ± 0.14	6.92 ± 0.076
2016 July 19	12.04 ± 0.41	6.61 ± 0.22

Figure 5.2 shows that during the time span 2002-2016, Pluto's atmospheric pressure kept on increasing, reaching a factor 2.8 in 2016 compared to its value in 1988. A hint of a possible shrinking after decades of expansion is visible in the figure, but this remains statistically marginal (1σ level) of Pluto's atmospheric.

Note that other works (see e.g. Bosh et al. 2015) compiled various occultation results, but not in a consistent manner, that is using a unique model and approach. The work presented here has in fact more data with generally higher SNR, and is thus better suited to an investigation of atmospheric pressure vs. time.

5.1.1 Interpretation of Pluto's evolution pressure from LMD Pluto volatile transport model

In order to interpret these atmospheric observations, we employed the Laboratoire de Météorologie Dynamique (LMD) Pluto volatile transport model designed to simulate the volatile cycles over seasonal and astronomical timescales on the whole planetary

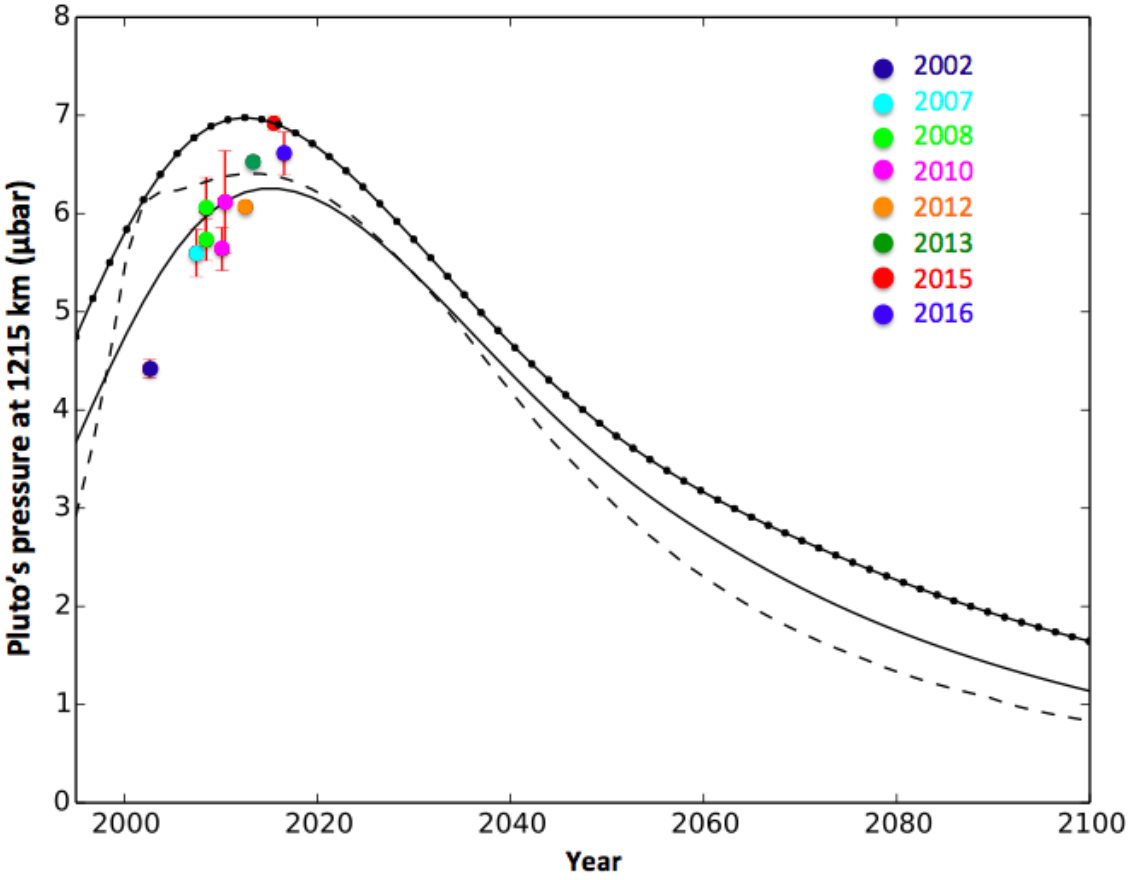

Figure 5.2: Pluto's Pressure at 1215 km from Pluto's center versus year using Dias-Oliveira et al. (2015) model superimposed with models of Pluto's atmosphere evolution by Bertrand and Forget (2016).

sphere (Bertrand and Forget, 2016; Forget et al., 2017; Bertrand et al., 2018). The characteristics of the model are described in detail in Bertrand and Forget (2016). We use the latest, most realistic, version of the model featuring the topography map of Pluto (Schenk et al., 2018) and large ice reservoirs (Bertrand et al., 2018). In particular, we place permanent reservoirs of nitrogen ice in the Sputnik Planitia basin and in the depressions at mid-northern latitudes (30 deg. N 60 deg. N), as detected by New Horizons (Schmitt et al., 2017) and modeled in Bertrand et al. (2018).
Fig. 5.3 shows the annual evolution of surface pressure obtained with the model. This evolution is consistent with the continuous increase of pressure observed since 1988 (a factor of 3 since 1988), and results from the heating of the nitrogen ice in Sputnik Planitia and in the northern mid-latitudes when the areas are exposed to the Sun (just after the northern spring equinox in 1989) and when Pluto is near the Sun, as detailed in Bertrand and Forget (2016).
The model also predicts that atmospheric pressure is expected to reach its peak and drop in the next few years, due to

(1) the orbitally-driven decline of insolation over Sputnik Planitia and the northern mid-latitude deposits, and

(2) the fact that nitrogen condenses more intensely in the colder southern part of

Sputnik Planitia, thus precipitating and hastening the pressure drop.

The number of observation points is a strong constraint for the different parameters of the model, leading to an almost unique solution.

In fact, the models constrain the possible nitrogen ice surface distribution. Indeed, the southern winter hemisphere of Pluto is not expected to be significantly covered by nitrogen ice at the present time, because otherwise the peak of surface pressure would have occurred much earlier than 2015, as suggested by the model simulations. With the model we obtain a peak of pressure after 2015 only when considering little mid-latitudinal nitrogen deposits (or no deposit at all) in the southern hemisphere.

First, in this simulation, nitrogen does not condense efficiently in the polar night (outside Sputnik Planitia), in spite of the length of the southern fall and winter. This is because in Pluto conditions, depending on the deep subsurface thermal inertia, the heat stored in the southern hemisphere during the previous southern hemisphere summer can keep the surface temperature above the nitrogen frost point throughout the cold season or at least drastically limit the nitrogen condensation.

Consequently and secondly, the observation points provide us with a second constraint, which is a relatively high subsurface thermal inertia so that nitrogen does not condense much in the southern polar night. In addition, using a thermal inertia of 800 J $s^{-1/2}$ m^{-2} K^{-1} allows for a surface pressure ratio $p_{s,2015}/p_{s,1988}$ to be around 2.5-3, as observed. Higher thermal inertia tend to lower this ratio, and conversely, see Figure2a of Bertrand and Forget (2016).

Finally, the nitrogen cycle is very sensitive to the nitrogen ice albedo and emissivity, and therefore there is only a small possible range of these parameters that allows the model to match the observations.

Fig. 5.3 illustrates the high sensitivity of the pressure cycle to the nitrogen ice albedo during northern spring-summer. To understand this sensitivity, one can do the thought experiment of imagining Pluto with a flat and isothermal surface at vapor pressure equilibrium. We can roughly estimate the equilibrium temperature for different albedo using the classical equation:

$$\epsilon\sigma T^4 = (1 - A)\,\frac{F}{4}$$

With F the solar constant at Pluto, A the nitrogen ice albedo, ϵ its emissivity and $\sigma = 5.67 \times 10^{-8}$ W m^{-2} K^4 the Stefan-Boltzmann constant. From the temperature T we can then estimate the surface pressure assuming the nitrogen vapor pressure equilibrium (Fray and Schmitt, 2009). Using $\epsilon = 0.8$ and $F = 1.26$ W m^{-2} (solar constant at Pluto in 2015), we find: $P = 1.00$ Pa (10 μbar) and $T = 36.60$ K assuming $A = 0.74$ $P = 1.24$ Pa and $T = 37.01$ K assuming $A = 0.73$. Therefore decreasing the nitrogen ice albedo by 0.01 leads to an increase of surface pressure in 2015 by 0.24 Pa (2.4 μbar), i.e. a 25% increase.

A discussion of the uniqueness of the solutions is provided in the concluding remarks of the last Chapter.

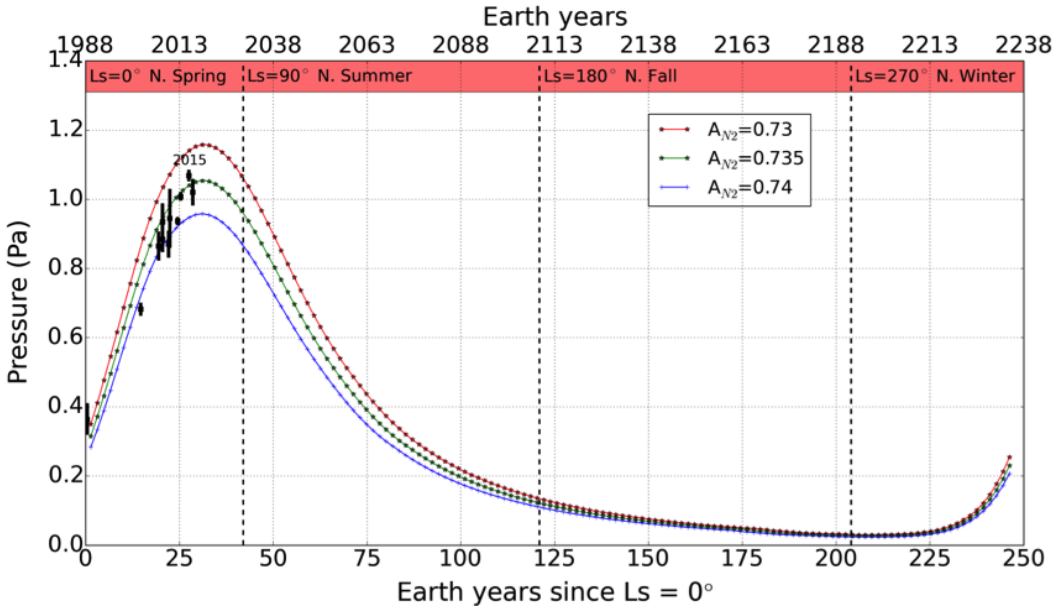

Figure 5.3: Typical modeled annual evolution of surface pressure obtained with LMD Pluto volatile transport model, assuming permanent deposits of N_2 ice inside Sputnik Planitia and in the depression of mid-northern latitudes, a uniform soil seasonal thermal inertia of 800 J $s^{-1/2}$ m^{-2} K^{-1}, an emissivity $\epsilon_{N_2} = 0.8$ and albedos $A_{N_2} = 0.73 - 0.74$ for N_2 ice, chosen to yield a surface pressure near 1-1.1 Pa in July 2015. The black dots with error bars show the surface pressure (P_s) inferred from stellar occultation pressure measurements (this work) at 1215 km from Pluto centre (p_{1215}), assuming the same ratio p_s/p_{1215} as measured in 2015 (from Meza et al 2018).

5.2 The structure of lower Pluto's atmosphere

As an observer gets deeper into Pluto's occultation shadow, the received stellar rays are more and more deviated, which corresponds to deeper and deeper layers probed in the atmosphere.

The deepest possible layers are probed by diametric occultations (see Fig. 5.4). An example is given in Fig. 5.5, where the observed flux is plotted vs. the position z of the observer in the occultation shadow, for a given temperature profile and prescribed surface pressure.

As seen later, Pluto's atmosphere structure is such that for a ground-based stellar occultation, the stellar rays grazing the surface by a few kilometers are deviated near the shadow center, where they create a central flash. The fact that rays grazing the surface cause a flash is not generic, but rather a mere coincidence stemming from the current pressure and temperature on Pluto's surface, the refractivity of molecular nitrogen and the current geocentric distance of the dwarf planet.

Fig. 5.5 calls several comments.

- The ray deviation near the surface is large enough to obtain negative values of z, thus creating two stellar images, as least close enough to the shadow center, see Chapter 2. Note, however, that Pluto is too small angularly (about 0.1 arcsec) for current ground-based imaging systems to detect and separate those two images. Thus only the sum of the fluxes from Pluto and the stellar images is available for

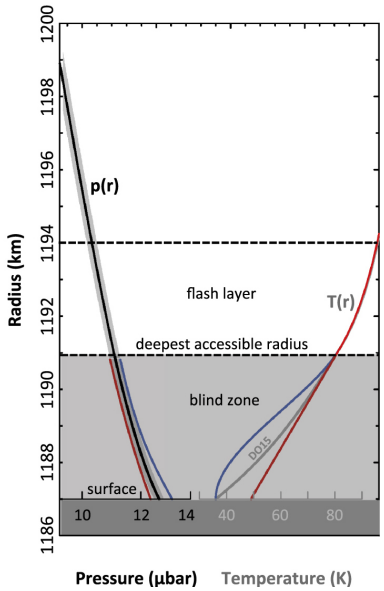

Figure 5.4: Our ray tracing code shows that near the shadow center, the stellar rays come from a "flash layer" about 3 km in thickness just above r=1191 km, thus sitting 4km on top of the assumed surface. The central flash layer roughly lies between the two horizontal dashed lines, above the blind zone below 1191 km (from Sicardy et al. 2016).

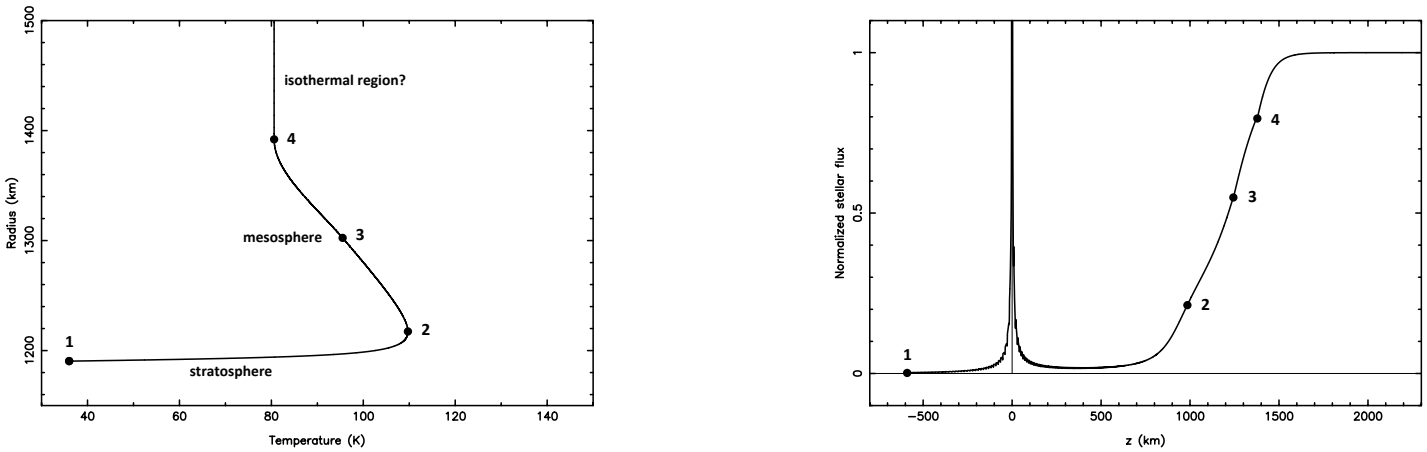

Figure 5.5: Left - The template temperature profile used to generate the density profiles discussed in Dias-Oliveira et al. (2015), starting at the surface (point 1), proceeding into a stratosphere up to a maximum of temperature (point 2), an inflexion point in the mesosphere (point 3) and the connection with an isothermal branch (point 4). Right - The synthetic occultation light curve caused by the nominal temperature profile at left, for Pluto at the geocentric distance of 18 July 2012, and a surface pressure of $p_{\rm surf} = 10.75$ μbar (higher pressures will be considered in this section). The flux is plotted against the distance z of the observer to the shadow center. The points corresponding to the dots at left have been reported in the light curve. Because the light curve extends to negative values of z, a secondary image is observed during the occultation, see text.

the observer.

- The flux deep into the occultation shadow is small, e.g. $\sim 2\%$ of the unocculted stellar flux around $z = 500$ km. Consequently, information is difficult to obtain in this part of the light curve. In effect, it is necessary to first subtract the contribution of the foreground object (Pluto) to the total observed flux. In principle, this can be done when Pluto and the star are angularly far enough to be measured individually, e.g. the night prior or after the event. But Pluto's photometric variation associated with its rotation amounts to several percents per day, thus impairing a reliable calibration. Another solution is to use a reference star in the field of view, and compare the ratio (target star +Pluto)/reference around the occultation to the ratio (target star)/reference during the night prior or after the event, thus providing the searched contribution, Pluto/reference. However, chromatic differential absorption may change the ratio (target star)/reference from one night to the other. Thus, care must be taken to measure the star and the reference at same elevation as during the occultation, but nothing warrants that chromatic effects will be the same as during the occultation.

  In summary, a useful calibration requires a relative photometric accuracy below the 1% level, which is seldom obtained as weather conditions and large telescopes cannot be chosen at will. In fact, among our campaigns, the only event that permitted such calibration is the occultation of 18 July 2012 observed at the Very Large Telescope at Paranal. It showed that the stellar residual flux during that event was around 2 ± 0.8 % (Dias-Oliveira et al., 2015), a measurement which has an important relative error. For the observations presented below, no accurate calibration is available. This point will be discussed later.

- This problem is partly solved if a central flash is observed. The layer that causes the flash amplifies the residual stellar flux by a factor r/z, where r is the closest approach radius of the ray in the atmophere, see Eq. 2.5. This amplification thus allows us to get information on the thermal structure of the layers at few kilometers altitude.

  The flash presents some caveats, though. Its shape and amplitude is very sensitive to small (and unknown) departures from sphericity of the amplifying layer. Moreover, the primary and secondary stellar images come from regions that have different thermal profiles, but their contributions cannot be disentangled. Similarly, each image may be partly absorbed by haze layers (and in different ways) or even be blocked by local topographic features, see below.

5.2.1 The central flash of 29 June 2015

We now turn to the analysis of a specific event, the 29 June 2015 stellar occultation observed from Australia and New Zealand. The circumstances of this event are summarized in Chapter 4 and results already obtained from it are presented in Sicardy et al. (2016).

Among all the campaigns that we conducted, this is the only one that allowed us to detect a central flash. The region where such a flash is observable spans a band of

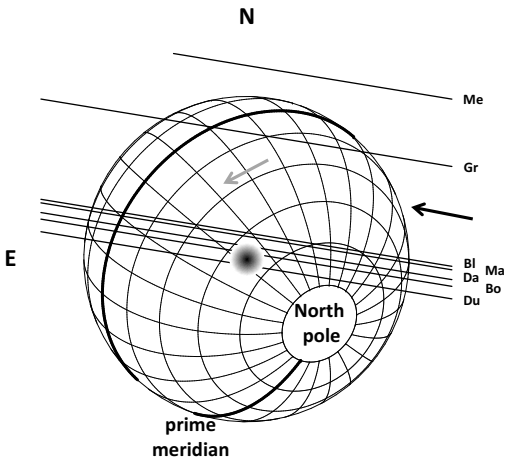

Figure 5.6: The reconstructed geometry of the 29 June 2015 Pluto stellar occultation. The stellar motion relative to Pluto (black arrow) is shown for seven stations, labelled as follows: **Me**: Melbourne, **Gr**: Greenhill, **Bl**: Blenheim, **Ma**: Martinborough, **Da**: Darfield, **Bo**: BOOTES-3, **Du**: Dunedin. The J2000 celestial north and east are indicated by N and E, respectively. Pluto's radius is fixed at 1187 km. The equator and prime meridian (that faces Charon) are drawn as thicker lines, and direction of rotation is along the gray arrow. The meridians are plotted every 15 degrees, thus corresponding to one "hour" of a Pluto's day that would have 24 hours, see Table 5.2. The shaded region at center roughly indicates the zone where a central flash could be detected.

about 100 km encompassing the center line. This corresponds to about 5 milli-arcsec in terms of angular size projected at Pluto (see Fig. 5.6). This is well below the prediction accuracy in the pre-Gaia era, and explains why such observations remained rare.

This flash was thus a unique opportunity to probe Pluto's lower atmosphere, and was even more special as it was observed two weeks before the New Horizons flyby of 14 July 2015, a time difference which is short enough to consider the two observations as simultaneous.

The post-occultation reconstruction geometry of the event is presented in Fig. 5.6. We see that the two southern-most stations Bootes-3 and Dunedin scanned the central flash region. A more detailed view of the occultation geometry is shown in Fig. 5.7, where the motion of the primary and secondary stellar images are plotted for each station. The location of those images have been calculated using the density profiles provided by the REX instrument aboard New Horizons, see Hinson et al. (2017) and more details below. Other models, e.g. the one described in Sicardy et al. (2016), would provide undistinguishable trajectories at the scale of the figure. Note that the primary and secondary images are essentially swapped when passing from Bootes-3 to Dunedin. This is expected as the two stations were basically symmetrical with respect to the shadow center, with a closest approach of 46 km (resp. 45 km) at Bootes-3 (resp. Dunedin), see Sicardy et al. (2016).

The traces of the primary and secondary images at Bootes-3 are shown in Fig. 5.8. The plot also shows the locations of the ingress and egress points probed by the New Horizons radio occultation experiment (REX), see Hinson et al. (2017). Note that

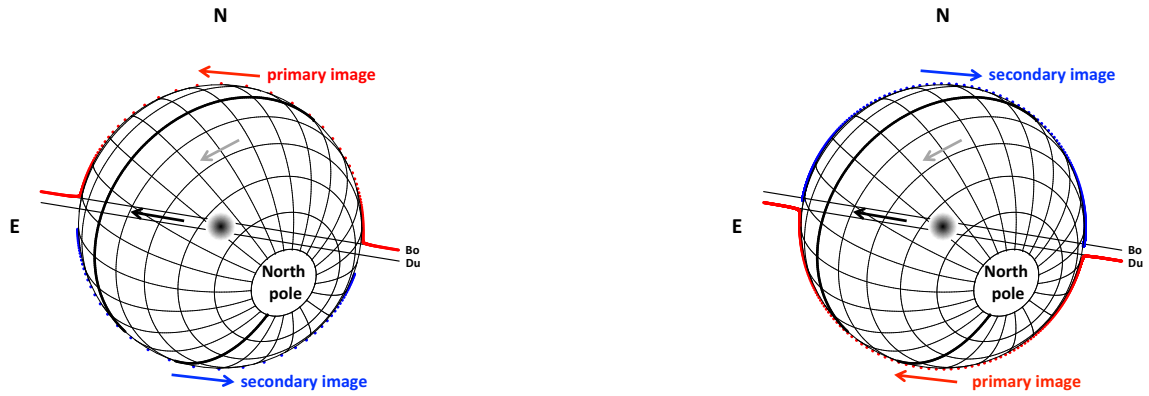

Figure 5.7: The same as Fig. 5.6, but showing the trajectories of the primary (resp. secondary) images in red (resp. blue) as seen from Bootes-3 at left and Dunedin at right. The time sampling of the Bootes-3 station used here is the original 0.344 s, while the Dunedin timing has been re-sampled at 0.1 s intervals (instead of the original 5.12 s) for better viewing, see Sicardy et al. (2016) for details.

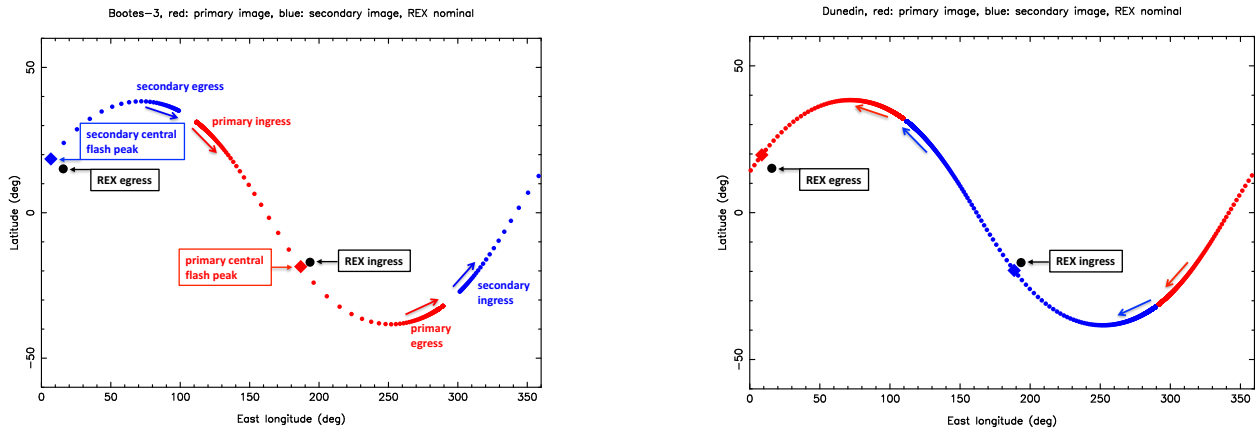

Figure 5.8: Left - Traces of the primary (red) and secondary (blue) stellar images observed at Bootes-3, as deduced from Fig. 5.7. The arrows indicate the direction of motion. The origin of longitude (counted positively toward east) is the prime meridian that faces Charon, see Fig. 5.6. Right - The same for the Dunedin station. Note that the tracks of the primary and secondary images are essentially swapped between the two panels. The diamond-shaped symbols mark the positions of the image at the peak of the respective flashs, corresponding to the closest approach of the stations to the shadow center (Fig. 5.6). However, the flash duration is typically 15 seconds (see Fig. 5.12). Consequently, it corresponds to a total number of about 20 points on each side of the diamond-shaped symbols in the left panel. In other words, the stellar images probed rather large regions. One of the images actually scanned the longitude interval from 310 to 360 degrees and then from 0 to 70 degrees, while the other image scanned the interval from 120 to 270 degrees. The black bullets are the locations of the REX measurements at ingress and egress (Hinson et al., 2017). Note the casual proximity of the REX points and the 29 June 2015 flash peaks.

Table 5.2: Regions probed by the central flash (29 June 2015) and REX experiment (14 July 2015)

	Time (UT)[1]	Location on surface	Local solar time[2]
29 June 2015			
Bootes-3, primary image	16:52:54.8	186.8°E, 18.5°S	7.67 (sunrise)
Bootes-3, secondary image	16:52:54.8	6.8°E, 18.5°N	19.67 (sunset)
Dunedin, primary image	16:52:56.0	8.6°E, 19.7°N	19.79 (sunset)
Dunedin, secondary image	16:52:56.0	188.6°E, 19.7°S	7.79 (sunrise)
New Horizons radio experiment (REX), 14 July 2015			
Ingress	12:45:15.4	193.5°E, 17.0°S	16.52 (sunset)
Egress	12:56:29.0	15.7°E, 15.1°N	4.70 (sunrise)

[1]For the ground-based observations, this is the time of closest approach to shadow center (Sicardy et al., 2016), for the REX experiment, this the beginning and end of occultation by the solid body (Hinson et al., 2017). [2]One "hour" corresponds to a rotation of Pluto of 15°. A local time smaller (resp. larger) than 12.0 h means morning (resp. evening) limb.

those points are very close (by chance) to the location of the stellar images at the peak of the central flashes for both Bootes-3 and Dunedin, i.e. at the moment of closest approach to the shadow center. Because the 29 June 2015 flash probed Pluto's deep atmosphere very close in space and time to the measurements performed by REX, it is an ideal situation to compare our results with those of New Horizons. The local conditions on Pluto during the 29 June 2015 central flash and the REX experiment are summarized in Table 5.2.

5.2.2 Comparison of the ground-based and REX results

Eight instruments were embarked on board of the NASA New Horizons spacecraft (Young et al., 2008). Among them, the Radio EXperiment (REX) instrument has several goals, including the determination of density, pressure and temperature profiles of Pluto's lower atmosphere, as well as radiometry study of its surface (Tyler et al., 2008). The REX instrument has been used in particular to probe Pluto's neutral atmosphere using the stellar radio occultation technique, in which a 4.2 cm-λ signal is transmitted from Earth and received at the spacecraft. During its passage through Pluto's atmosphere, the phase of the signal is shifted, and inversion method provides the an profile $n(r)$, $p(r)$ and $T(r)$ of molecular density, pressure and temperature as a function of the planetocentric radius r (Hinson et al., 2017). Note that, contrary to ground-based occultations, the drop of the radio signal is *not* used to retrieve the profile. In fact, this drop is too small to be detected, due to the proximity of the spacecraft to Pluto (about 50,000 km, vs. more than 30 au for ground-based occultations). Conversely, the phase shift of the stellar signal cannot be determined for ground-based events as the source is not coherent.

The prime result of the REX inversion technique is the density profile $n(r)$, from which the pressure profile is retrieved by integration, and then the temperature profile

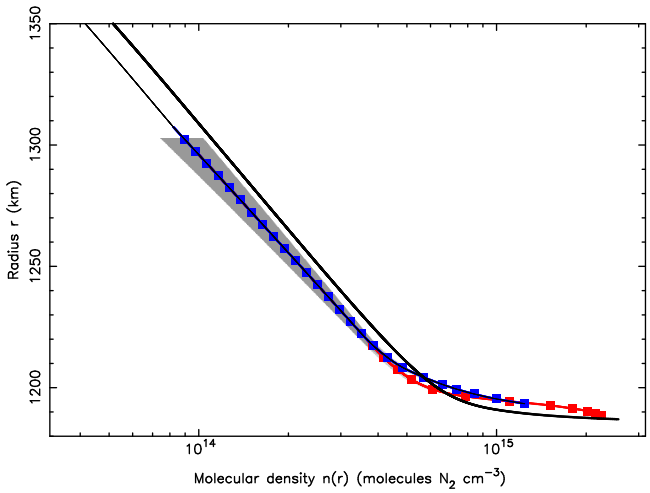

Figure 5.9: Red and blue squares: the density profiles $n(r)$ derived from the REX radio occultation performed during the Pluto flyby of 14 July 2015 at ingress and egress, respectively, assuming pure N_2 (Hinson et al., 2017). The shaded area is the 1σ error bar domain. Below 1220 km, the errors decrease and become unnoticeable in this plot. The ingress (resp. egress) profile is given from $r = 1188.4$ km (resp. 1193.4 km), 1 km above the local surface, up to 1302.4 km, where the error bars become too large for a reliable profile to be retrieved. Note that by construction, the REX ingress and egress profiles are *identical* for $r > 1220$ km. Below that radius, the two profiles diverge significantly, due to different physical conditions of the boundary layer just above the surface at 1187.4 km, see Fig. 5.10 for details. Thicker solid line: the nominal profile obtained from the 29 June 2015 ground-based occultation, with surface pressure of $p_{\rm surf} = 12.7$ μbar (Sicardy et al., 2016). The thickness of the line represents the *formal* 1σ error bar of the profile, without accounting for possible biases, see text. The solid red and blue lines connecting the squares are spline interpolations of the REX density profiles $n(r)$ that are used in our ray tracing code, see text. Those spline representations are extended above 1302.4 km (thinner solid line), using a scaled version of the 29 June 2015 profile that ensures continuity with the REX profile at $r = 1302.4$ km. In this logarithmic plot, this corresponds to a mere horizontal shift of the 29 June 2015 profile to the left in the plot above.

from the ideal gas equation, plus the hydrostatic hypothesis. As for ground-based occultation (Chapter 2), an initial condition T_b at a reference radius r_b has to be chosen. Hinson et al. (2017) have taken $T_b = 95.5$ K at $r_b = 1302.4$ km (top of the REX profile) to be in agreement with the Dias-Oliveira et al. (2015) temperature profile. The REX density profile is displayed in Fig. 5.9, while the temperature and pressure profiles are given in Fig. 5.10. REX provides useful information from the surface, with pressure of about 12 μbar, up to an altitude of about 115 km, where the pressure drops to about 1.2 μbar.

The examination of Figs. 5.9 and 5.10 shows that: (1) the REX and the ground-based-derived density and pressure profiles of Dias-Oliveira et al. (2015) and Sicardy et al. (2016) agree to within $\gtrsim 1\sigma$ above $r = 1220$ km. In that region, the temperature profiles agree to better than 1σ, and show consistent gradients of -0.14 K km^{-1} (REX), vs. -0.17 K km^{-1} for ground-based occultations profiles. (2) Both REX and the ground-

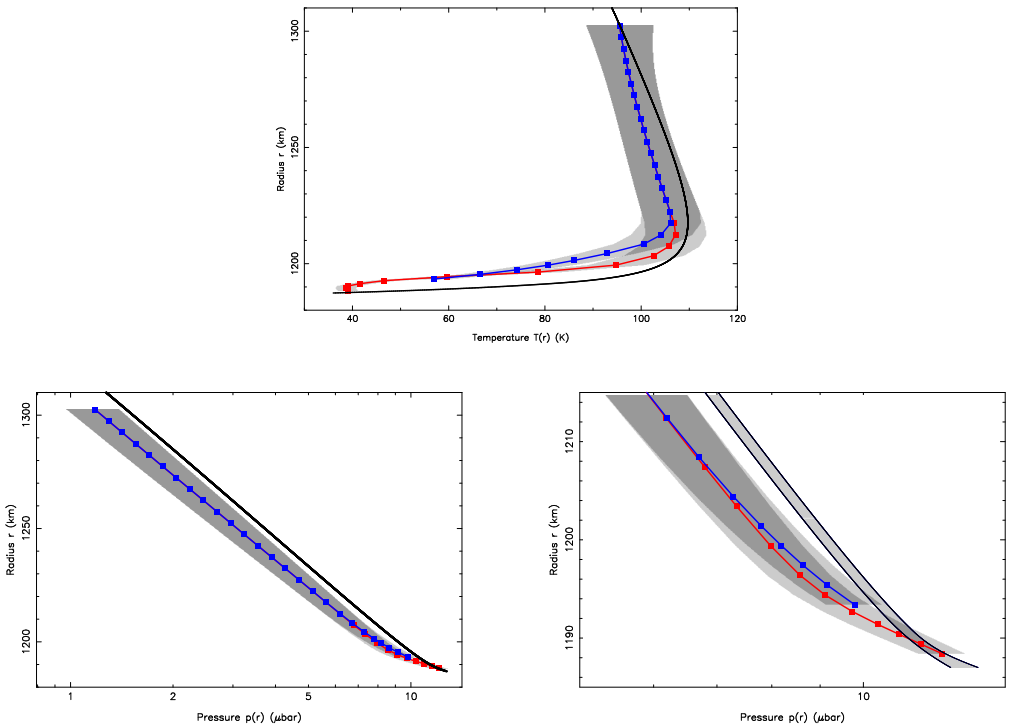

Figure 5.10: Upper panel: the red and blue squares are the temperature profiles $T(r)$ obtained from REX at ingress and egress, respectively. The red and blue curves are just straight lines connecting the REX data points, not spline interpolations. By construction, the REX profile uses $T_b = 95.5$ km at $r_b = 1302.4$ km, taken from the ground-based result of Sicardy et al. 2016, plotted at the solid black line. Thus, the junction of the REX and ground-based profiles $T(r)$ at r_b merely stems from the choice of the boundary condition, and is not the result of a measurement. There is no error bars on the Sicardy et al. 2016's temperature profile, as most of the errors come in this case from biases, see text. Lower left panel: the same as the upper panel, but for the pressure profiles $p(r)$. Again no error bars are indicated. Lower right panel: close-up view of the bottom of the profiles shown at left. The gray region encompassing the Sicardy et al. 2016's profile and delimited by thin solid lines is an uncertainty domain discussed by those authors, using various hypotheses on the temperature profiles near the surface, where the pressure was found to be in the 11.9-13.7 μbar range.

based profiles show a marked temperature maximum near $r = 1215$ km, that defines the limit between the stratosphere and the mesosphere. The temperature maximum is $T_{\rm max} = 107 \pm 6$ K for REX (Hinson et al., 2017), vs. a value $T_{\rm max} = 109.7 \pm 1$ K for Dias-Oliveira et al. (2015). (3) Below $r = 1220$ km, the two REX $T(r)$ profiles and the ground-based derived result all differ. The REX ingress profile has a strong positive gradient in the stratosphere with a peak of $dT/dt = 9.5$ K km^{-1} near 1195 km (pressure 9 μbar). It connects itself to the surface by a small inversion layer of thickness ~ 3.5 km with temperature 38.9 ± 2.1 K and pressure 12.8 ± 0.7 μbar. Conversely, the REX egress profile keeps a milder temperature gradient in the stratosphere with a peak of $dT/dt = 3.9$ K km^{-1} near 9 μbar. It connects itself to the surface at a warmer temperature, 51.6 ± 3.8 K than the ingress profile, and lower pressure 10.2 ± 0.7 μbar. Meanwhile, the 29 June 2015 profile has also a strong gradient, but it occurs quite

closer to the surface than the REX profiles and reaches more than 16 K km^{-1} at the surface.

The position of the spacecraft has an uncertainty of about 3.3 km along its trajectory (Hinson et al., 2017). So, the mismatch between the radii of the radio signal disappearance (1187.4 km vs. 1192.4 km at ingress and egress, respectively) may just the reflect of this uncertainty. For instance, the two Pluto limbs probed by the REX obervations might have the same value, averaged to 1189.9 km. However, the examination of Fig. 5.10 shows that the more probable explanation of this mismatch is that REX probed higher terrains at egress than at ingress, which provides the same pressure at a given planetocentric radius. This is supported by the fact that the ingress probed a terrain near the depressed Sputnik Planitia, while the egress signal probed higher terrains in the Charon-facing hemisphere, with difference of planetocentric radii of some 5 km (Moore et al., 2016; McKinnon et al., 2016). The analysis below will also support this interpretation.

It is important to note that the stellar occultation analysis of Dias-Oliveira et al. (2015) and Sicardy et al. (2016) rely on the template shown in Fig. 5.5, which is itself derived from the best light curve obtained during the 18 July 2012 stellar occultation. This template is used to assess the pressure evolution between 2002 and 2016. It *assumes* that the profile $T(r)$ of Fig. 5.5 is constant in space and time. This is a reasonable assumption at high altitude, considering also the general agreement shown in Fig. 5.10. This approach has then the advantage to compare consistently our various observations since 2002.

This said, the retrieved ground-based stellar occultation profiles below 1215 km should be considered with caution. First because, very little signal from the star is then detected (Fig. 5.5), so that the noise level becomes an important source of uncertainty. Second, the physical conditions in the stratosphere are not constant in space, as shown by REX see Fig. 5.10, and probably not in time during a plutonian day (Hinson et al., 2017). In this context, one cannot use a unique deep atmosphere (stratospheric) template, as the one shown in Fig. 5.5.

As discussed previously, a central flash helps solving the issue of the small residual stellar flux. We have used the REX density profile $n(r)$ of Fig. 5.9 in our ray tracing code to generate synthetic central flashes for the Bootes-3 and Dunedin stations. The REX points have been interpolated by spline functions, using a vertical sampling of 25 meters. This small enough to generate a smooth synthetic light curve, thus avoiding "saw-tooth" jumps that would cause a numeric noise during the fit procedure.

The ray tracing code has been modified compared to that of Dias-Oliveira et al. (2015) in order to account for the fact that the two images that travel along Pluto's limb probe different density profiles (Fig. 5.7).

Fig. 5.11 displays the closest planetocentric distance r_0 of a stellar ray (and thus the deepest layer its probes in the atmosphere) as a function of the observer position z in the shadow. Four scenarios are considered:

(1) We use the nominal model of Sicardy et al. (2016), which provides the graph (z, r_0) shown in upper left panel of Fig. 5.11. This model provides the best fit to the data after adjusting the surface pressure to $p_{\rm surf} = 12.7$ μbar and Pluto's offset with respect to its nominal ephemeris.

(2) We take the REX density profiles at face value, and use the ingress (resp. egress)

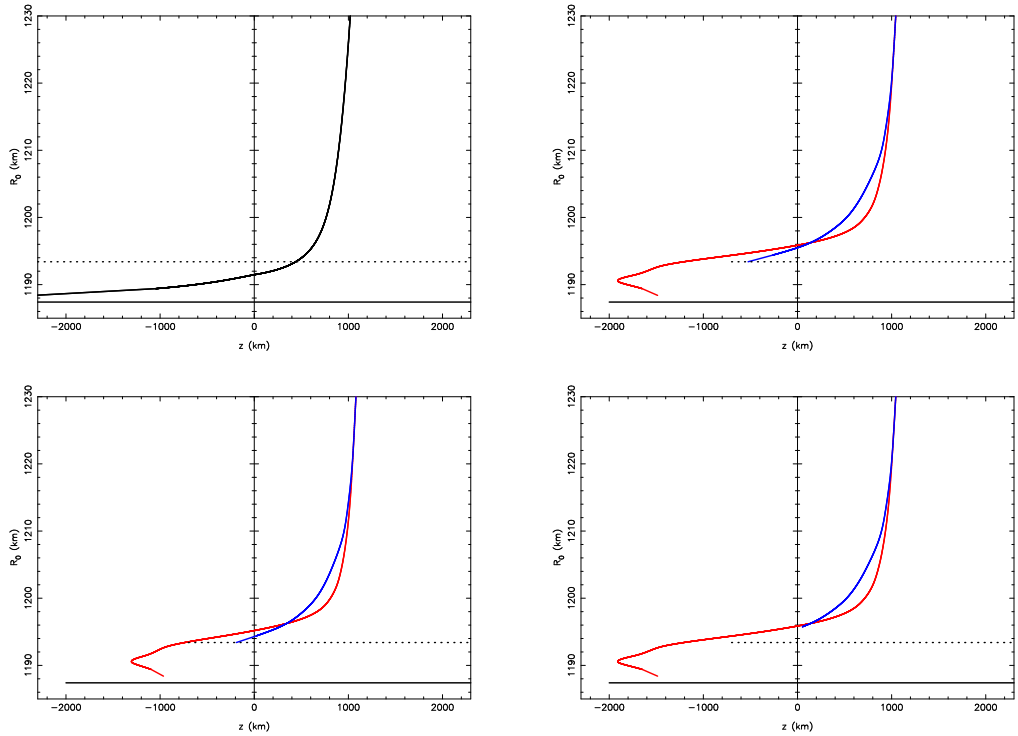

Figure 5.11: In each panel, the radius of closest approach of a ray, r_0, is plotted against the position z of the observed in the shadow, see Fig. 5.5. The parts of the graphs where $z > 0$ (resp. $z < 0$) correspond to primary, or near limb (resp. secondary, or far limb) images. Upper left - the graph (z, r_0) for the model shown in Fig. 5.5, and with surface pressure $p_{\rm surf} = 12.7$ μbar (Sicardy et al., 2016). The horizontal solid (resp. dotted) line is the Pluto radius measured by REX at ingress (resp. egress). Upper right - The graphs (z, r_0) corresponding to the nominal REX profiles of Fig. 5.9 at ingress (red curve) and egress (blue curve). The lowest points have surface pressures of 12.8 and 10.2 μbar, respectively, see Fig. 5.10. Lower left - The same with REX pressures decreased uniformly by a factor 0.805, see text. Lower right - The same, using the nominal surface pressures of upper right panel, but with a topographic feature of height 1.35 km that blocks the contribution of the lowest part of the REX egress profile.

profile to generate the flux from the northern (resp. southern) limb stellar image at Bootes-3 and Dunedin, as justified earlier using Fig. 5.8. The resulting (z, r_0) graph is shown in the upper right panel of Fig. 5.11.

(3) We apply a uniform scaling factor f to the two REX density profiles, keeping the temperature profiles $T(r)$ constant, so that the REX pressure profiles are also scaled by the factor f. We then explore a grid with various values of f and cross-track offset of Pluto's center, which changes the closest approaches of the two stations to the shadow center. The best fitting parameters provide the graph (z, r_0) shown in the lower left panel of Fig. 5.11.

(4) Going back to $f = 1$, we assume that a topographic feature of height h blocks the stellar image generated by the REX egress profile, i.e. that the stellar image that travels along the southern limb (Fig. 5.7) is turned off below the planetocentric radius 1192.4 km $+h$. This provides the lower right panel of Fig. 5.11.

Fig. 5.11 shows that, for a given observer position z, the REX profiles place the stellar images higher than predicted by the 29 June 2015 stellar occultation analysis by Sicardy et al. (2016). The flash being typicallly observed in a region of width $\sim \pm 50$ km around centrality, it corresponds to an altitude of about 4 km for the stellar images if one adopts Sicardy et al. (2016)'s profile, versus an altitude of about 8 km using the REX profiles. Moreover, the inversion 3.5 km-thick inversion layer seen in REX ingress profile creates a double image (mirage), since a given z corresponds to two different r_0. This causes ray crossing and thus caustics that may be interpreted as spikes far away from centrality (Stansberry et al., 1994; Lellouch et al., 2009). This point will not be discussed here.

Note that the REX density and pressure profiles show a deficit of about 23% when compared to the 29 June 2018 occultation profile (Figs. 5.9 and 5.10). The latter is actually derived from a global fits to various light curves (Sicardy et al., 2016) and is mainly sensitive to the half-light level, see Fig. 5.5. This corresponds to a radius close to $r = 1295$ km, i.e. an altitude close to 110 km and a pressure of about 1.6 μbar that corresponds to the top of the REX profiles. As explained before, the ray tracing code uses the REX density profiles that have been extended above $r = 1302.4$ km by scaling the 29 June 2015 profile (see Fig. 5.9). The REX pressure deficit creates a significant global mismatch between the synthetic and observed light curves. To remedy this problem, a new global density profile should be constructed, patching up the ground-based-derived and the REX profiles. Multiple solutions are in fact possible and this remains out of the scope of the present analysis.

Instead, here we restrict ourselves the generation of the synthetic light curves to the bottom parts of the occultation. We also include in the fit two intervals that bracket the event outside the occultation, where we know that the flux must be unity, see Fig. 5.12. Those external parts do not discriminate the various models, but serve to scale properly the general stellar drop. In other words, we test the REX profiles only for the deepest parts of the occultation at Bootes-3 and Dunedin, including the central flash. As mentioned before, two free parameters are adjusted, the pressure at a prescribed level and the cross-track offset of Pluto' shadow center. Since no calibrations of the light curves are available to assess Pluto's contribution ϕ_P to the total observed fluxes, a linear least-square fit of the syntheric flux to the data has been performed before calculating the residuals. This implicitely introduces a supplementary adjustable parameter, ϕ_P, so that the total number of free parameters is $M = 3$, for a given model.

The fits to the Bootes-3 and Dunedin light curves for the four scenarios described above are shown in Fig. 5.12, while Table 5.3 provides the χ^2 values, the number of data points N and the χ^2 per degree of freedom, $\chi^2_{\rm dof} = N - M$, for each fit, recalling that $M = 3$. As in Dias-Oliveira et al. (2015), the χ^2 function is defined by $\chi^2 = \sum_1^N [(\phi_{\rm i,obs} - \phi_{\rm i,syn})/\sigma_i]^2$, where $\phi_{\rm i,obs}$ is the observed flux at the $i^{\rm th}$ data point (restricted to the bottom of the light curve), $\phi_{\rm i,syn}$ is the corresponding synthetic flux and σ_i is the 1σ error bar on that point. In practice σ_i is estimated as the standard deviation at the bottom of the light curve.

The examination of Fig. 5.12 and Table 5.3 shows that:

• The nominal temperature profile $T(r)$ of Sicardy et al. (2016) with surface pressure $p_{\rm surf} = 12.7$ μbar provides a satisfactory fit to the data from Pluto's occultation on 2015. In this case, the Bootes-3 and Dunedin stations passed 46 km north and 45 km

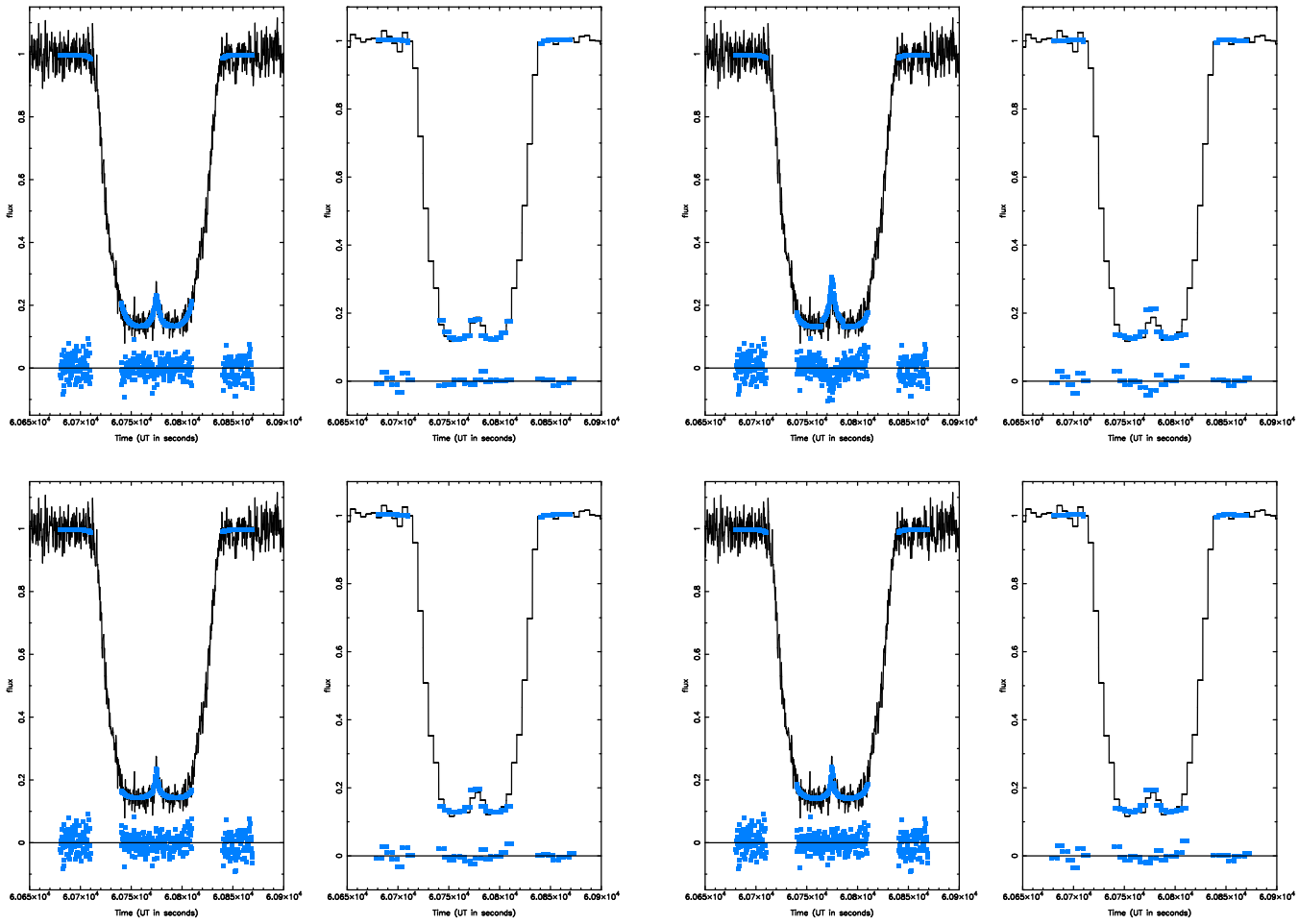

Figure 5.12: Ray-tracing fits to the Bootes-3 and Dunedin stations. The observed light curves (sum of the fluxes from the star and Pluto) are plotted in back and are normalized to unity outside the event. The contribution of Pluto to the total flux is close to 10% for both stations, but no accurate calibration could be obtained from the observations. The synthetic points are plotted in blue, and the residuals (observations minus model) are plotted below each light curve. Each panel contains a pair of light curves, with Bootes-3 at left and Dunedin at right. They each corresponds to one of the four panels shown in Fig. 5.11. Upper left panel - The best fits to the Bootes-3 and Dunedin light curves using the nominal 29 June 2015 result, see Fig. 5.9 (thick line) and Fig. 5.10 (black lines). Upper right panel - The same but using the nominal REX density profile. Note from the residuals that the synthetic flashs are too high at both stations. Lower left panel - The same, after multipying the REX density profiles by a factor $f = 0.805$ and moving Pluto's shadow 17 km north of the solution of Sicardy et al. (2016). Lower right panel - The same using the nominal REX profiles, but with a topographic feature of height $h = 1.35$ km that blocks the stellar image during part of its motion along the southern Pluto limb (Fig. 5.7). Pluto's shadow has now been moved by 19.5 km north of the solution of Sicardy et al. (2016). See text for discussion.

south of the centrality, respectively. However, this result should be taken with care, as the functional form of $T(r)$ between points 1 and 3 in Fig. 5.5 is imposed; here a hyperbolic branch that connects to the surface with a pressure corresponding to the vapor pressure equilibrium with the N_2 surface ice. An infinity of other functional

Table 5.3: Results of fits to the Bootes-3 and Dunedin central flashes.

station	χ^2	N	$\chi^2_{\rm dof} = \chi^2/(N-M)$ (where $M = 3$)
Nominal 29 June 2015 solution $p_{\rm surf} = 12.7$ μbar (Sicardy et al., 2016)			
Bootes	186.4	203	0.932
Dunedin	11.3	14	1.03
Total	197.7	217	0.924
Nominal REX profiles astrometric solution of Sicardy et al. (2016)			
Bootes	280.7	203	1.40
Dunedin	45.4	14	4.13
Total	326.1	217	1.52
REX density profiles $\times 0.805$ Pluto's shadow track moved 17 km north of Sicardy et al. (2016)'s solution			
Bootes	190.8	203	0.954
Dunedin	22.9	14	2.08
Total	213.7	217	0.999
Nominal REX profile Topographic feature $h = 1.35$ km on southern limb Pluto's shadow track moved 19.5 km north of Sicardy et al. (2016)'s solution			
Bootes	174.7	203	0.874
Dunedin	30.5	14	2.77
Total	205.2	217	0.959

forms are obviously possible.

• The nominal REX profiles provide flashes that are too high compared to the observations, see the corresponding large values of the χ^2's. This can be fixed by introducing haze absorption. A typical factor of 0.7 must be applied to the Bootes-3 synthetic flash in order to match the data shown in Figure 5.12, while a typical factor of 0.76 must be applied to the Dunedin synthetic flash. This corresponds to typical optical depths (along the line of sight) in the range $\tau = 0.27 - 0.35$, for rays that went at about 8 km above the 1187.4 km radius. This is comparable to the value 0.24 given by Cheng et al. (2017), see discussion below.

• By reducing the REX pressure profiles by a factor of 0.805 and moving Pluto's shadow center cross-track by 17 km north with respect to the first model, a satisfactory fit to the Bootes-3 flash is obtained, while the Dunedin synthetic flash remains a bit too high. In this case, the Bootes-3 and Dunedin stations passed 29 km north and 62 km south of the centrality, respectively.

• Using again the nominal REX profile, but imposing a topographic feature of

height $h = 1.35$ km on top of the REX egress radius of 1192.4 km, a satisfactory fit to the Bootes-3 flash is obtained, in fact the best of all fits for that station. Meanwhile, the Dunedin synthetic flash remains a bit too high compared to observations. The particular choice of $h = 1.35$ km stems from the fact that lower values would increase even more the Dunedin flash, while higher values would decrease too much the Bootes-3 flash. In this model, Pluto's shadow center has been moved cross-track by 19.5 km north with respect to the first model, so that the Bootes-3 and Dunedin stations passed 26.5 km north and 64.5 km south of the centrality, respectively.

A broader summary of this section is provided in the concluding chapter.

Table 5.4: PLUTO OFFSETS

Date Hour (UT) (yyyy/mm/dd hh:mm:ss) Geocentric distance (km)	Pluto's center (skyplane) f_c km	g_c km	Pluto's ephemeris (J2000) Right Ascension α hh:mm:ss deg.	Declination δ hh:mm:ss deg.	Offset Right Ascension $\Delta\alpha\cos(\delta)$ mas	Declination $\Delta\delta$ mas
			JPL DE405/PLU006			
2002/08/21 06:50:00 4523870353.9460402	-328.4195	-304.7251	16 58 49.4412 254.70600	-12 51 31.7076 -12.85880	-29.7±0.2	-236.3±0.1
			JPL DE413/PLU017			
2007/06/14 01:27:00 4531866115.03948	-2143.1767	1662.8265	17 50 20.7436 267.58643	-16 22 42.286 -16.37841	-97.5±0.1	75.7±0.2
			JPL DE413/PLU017			
2008/06/22 19:07:28 4558337860.00627	-502.4859	2488.8295	17 58 33.0319 269.63763	-17 02 38.6185 -17.04406	-22.7±0.2	112.6±0.2
			JPL DE413/PLU017			
2008/06/24 10:37:00 4558640166.4542999	236.5432	2055.2314	17 58 22.3952 269.59331	-17 02 49.2696 -17.04701	10.7±0.1	93.0±0.7
			JPL DE413/PLU017			
2010/02/14 04:45:00 4847007325.6894636	805.2848	2903.5791	18 19 14.3657 274.80985	-18 16 42.2485 -18.27840	34.3±0.2	123.6±0.5
			JPL DE413/PLU017			
2010/06/04 15:34:00 4622039468.1015949	181.5835	2753.3410	18 18 47.9470 274.69977	-18 12 52.0451 -18.21445	8.1±0.3	122.9±1.3
			JPL DE413/PLU022			
2012/07/18 04:13:00 4682435620.3610048	-461.8221	1050.8267	18 32 14.6762 278.06115	-19 24 19.3534 -19.40537	-20.3±0.1	46.3±0.1
			JPL DE413/PLU031			
2013/05/04 08:22:00 4768821770.1530552	-2745.4414	3083.0224	18 47 52.5416 281.96892	-19 41 24.5364 -19.69014	-118.7±0.1	133.3±0.1
			JPL DE413/PLU100			
2015/06/29 16:02:00 4770690388.8892632	-1931.4599	3708.5210	19 00 49.7182 285.20715	-20 41 40.5588 -20.69459	-83.5±0.1	160.3±0.1
			OD100/PLU100			
2016/07/19 20:53:45 4808573958.4305058	2386.9819	-410.8316	19 07 22.1090 286.84212	-21 10 28.2242 -21.17450	102.4±0.1	-17.6±0.4

5.3 Astrometry of Pluto

Another great product of the model fit is the geometry of the occultation, we can determine its position in the sky relative to the occulted star with internal accuracy of 10 km.

The Chapter 4 shows the reconstructed geometry of each occultation by Pluto where Pluto's position is derived from a fit to the all of the light curves, using the Dias-Oliveira et al. (2015) model and following the procedure described in the Chapter 4 which are summarized in the Table 5.4.

Stellar occultations provide an astrometric position of the body at the time of the occultation. Indeed, at the time of the occultation, for a specific place in the shadow, the positions of the star and the object are almost identical. For multi-chord occultation, it is possible to derive precisely from the geometry the position of the body's center. For single chord occultation, there are usually two solutions (one North and one South).

The precision of the positions mainly depends on the knowledge of the shape and the size of the body, the precision of the timing system, the velocity of the occultation, the exposure time of the camera, and the precision of the stellar position.

Since the publication of the Gaia catalogues (in September 2016 for the first release (Gaia Collaboration et al., 2016) and moreover with the second release in April 2018 (Gaia Collaboration et al., 2018) including proper motions of the stars), the precision of the stellar catalogues can now reach the precision of tenth of a milliarcsec. For comparison, before Gaia catalogue, the precision of stellar catalogues such as UCAC2

or UCAC4, was about 50 to 100 mas including also zonal errors. Consequently, the precision of positions deduced from occultations is expected to be around few mas.

Occultations, thanks to the accuracy of the Gaia catalogue, can provide the most accurate measurement of a body in a outer solar system. In this chapter, we present the astrometric positions we derived from our occultations. We also detail a method to derive astrometric positions knowing the circumstances of occultations in other publications. Finally, we present the refinement of the Pluto's ephemeris, allowing to predict future occultations by Pluto at a mas level accuracy.

5.3.1 Astrometric positions from our occultations

In Chapter 4, we have presented 11 occultations by Pluto from 2002 to 2016. From the geometry of the event, we have determined an offset representing the position of the Pluto's center in comparison to a reference ephemeris.

In more details, the offsets in right ascension and in declination (offset_α, offset_δ), provided in Table 5.4, are given for a reference ephemeris (α_e, δ_e) and a reference stellar position (α_s, δ_s).

From these parameters, an accurate position of Pluto can be derived with the stellar position from Gaia DR2 $(\alpha_{GDR2}, \delta_{GDR2})$ using these relations:

$$\alpha = \alpha_e + \frac{\text{offset}_\alpha}{\cos\delta} + \alpha_{GDR2} - \alpha_s \tag{5.1}$$

$$\delta = \delta_e + \text{offset}_\delta + \delta_{GDR2} - \delta_s \tag{5.2}$$

The star position (α_s, δ_s) used for the offset determination as well as the associated position in Gaia DR2 catalogue $(\alpha_{GDR2}, \delta_{GDR2})$ are provided in Table 5.5.

Date	Gaia source identifier	right ascension	declination	σ_α	σ_δ	Gmag
2002-08-21	4333042833914281856	16 58 49.431538	-12 51 31.85910	1.87	1.12	15.4
2007-06-14	4147858103406546048	17 50 20.744804	-16 22 42.22719	0.83	0.73	15.3
2008-06-22	4144621347334603520	17 58 33.013236	-17 02 38.39643	0.67	0.54	12.3
2008-06-24	4144621244254585728	17 58 22.390423	-17 02 49.36558	0.93	0.78	15.6
2010-02-14	4096385295578625536	18 19 14.378482	-18 16 42.35590	0.50	0.42	10.3
2010-06-04	4096389556186605568	18 18 47.930034	-18 12 51.82967	0.37	0.31	14.8
2011-06-04	4093175335706340480	18 27 53.819996	-18 45 30.78871	0.62	0.50	16.4
2012-07-18	4092849712861519360	18 32 14.673688	-19 24 19.34329	0.19	0.17	14.4
2013-05-04	4086200313156846336	18 47 52.531982	-19 41 24.39714	0.10	0.09	14.2
2015-06-29	4084956039611370112	19 00 49.474124	-20 41 40.81016	0.04	0.04	12.0
2016-07-19	4082062610353732096	19 07 22.117772	-21 10 28.43508	0.05	0.05	13.9

Table 5.5: Gaia DR2 source identifier, right ascension and declination and their standard deviation (in mas) at epoch and magnitude of the stars of the catalogue Gaia DR2 involved in occultations presented in this framework (more occultations in Desmars et al. 2018, , preprint attached in the Appendix)

Finally, Table 5.6 provides the absolute position in right ascension and declination derived from the offsets and from stellar positions of Gaia DR2. The residuals related to

JPL ephemeris[1] DE436 + PLU055 are also indicated as well as the differential positions between Pluto and Pluto's system barycenter used to refine the orbit (see Sect. 5.3.3).

	Pluto's coordinates		O-C (mas)		PLU-BAR (mas)	
date (UT)	right ascension	declination	$\Delta\alpha\cos(\delta)$	$\Delta\delta$	$\Delta\alpha\cos(\delta)$	$\Delta\delta$
2002-08-21 07:00:32.0	16 58 49.4348	-12 51 31.883	20.6	-10.4	-51.2	48.8
2007-06-14 01:27:00.0	17 50 20.7424	-16 22 42.228	14.7	-1.8	-5.2	89.8
2008-06-22 19:07:28.0	17 58 33.0298	-17 02 38.553	14.0	0.0	-59.3	-23.3
2008-06-24 10:37:00.0	17 58 22.3934	-17 02 49.193	17.6	8.1	-35.4	89.6
2010-02-14 04:45:00.0	18 19 14.3615	-18 16 42.168	15.2	3.1	-65.4	55.6
2010-06-04 15:34:00.0	18 18 47.9427	-18 12 51.958	14.9	4.8	47.9	49.2
2012-07-18 04:13:00.0	18 32 14.6765	-19 24 19.355	16.9	7.7	55.2	-76.0
2013-05-04 08:22:00.0	18 47 52.5331	-19 41 24.427	19.3	9.2	-74.6	48.0
2015-06-29 16:02:00.0	19 00 49.7068	-20 41 40.431	22.8	10.7	-41.9	80.3
2016-07-19 20:53:45.0	19 07 22.1091	-21 10 28.232	24.1	11.6	56.5	-71.7

Table 5.6: Right ascension and declination deduced from occultations, Residuals (O-C) in mas related to JPL DE436+PLU055 ephemeris, and differential coordinates between Pluto and Pluto barycenter system position from PLU055 ephemeris.

5.3.2 Astrometric positions from other publications

Several authors have published circumstances of an occultation by Pluto (Elliot et al., 2003; Young et al., 2008; Pasachoff et al., 2016). From these circumstances (coordinates of the observer, mid-time of the occultation and the length of the occultation or sometimes directly the minimum distance to the centrality), it is possible to derive an offset between the observation deduced from these circumstances and a reference ephemeris.

Method

The determination of an occultation's circumstances consists in computing the Besselian elements. The Bessel method makes use of the fundamental plane that passes through the center of the Earth and perpendicular to the line joining the star and the center of the object (to the axis of the shadow). The method is for example described in Urban and Seidelmann (2013). The Besselian elements are usually given for the time of conjunction of the star and the object in right ascension but here the reference time is the time of closest approach between the star and the object.

The Besselian elements are T_0 the UT time of the closest approach, H the Greenwich Hour Angle of the star at T_0, x_0 and y_0 the coordinates of the shadow axis at T_0 in the fundamental plane, x' and y' the rates of changes in x and y at T_0, and α_s, δ_s the

[1]DE436 is a planetary ephemerides from JPL providing the positions of the barycenter of the planets, including the barycenter of Pluto's system. PLU055 is the JPL ephemeris providing the positions of Pluto and its satellites related to the Pluto's system barycenter.

right ascension and the declination of the star. Their computation are fully described in Urban and Seidelmann (2013).

Note that x_0 and y_0 are expressed here in Earth equatorial radius, while x' and y' are expressed in equatorial radii per day. Those quantities depend on the ephemeris of the body and allow to represent the linear motion of the shadow at the time of the occultation.

From T_0, α_s, δ_s and H, the coordinates of the center of the shadow (λ_c, ϕ_c) at T_0 can be derived.

There is no particular reason that the observing site is right on the centrality, so depending on the length of the occultation at the observing site l, we may add a shift (positive or negative, whether the chord is on the North or the South part of the body) to x_0 and y_0:

$$x_0 \to x_0 \pm s\frac{x_0}{\sqrt{x_0^2 + y_0^2}} \tag{5.3}$$

$$y_0 \to y_0 \pm s\frac{y_0}{\sqrt{x_0^2 + y_0^2}} \tag{5.4}$$

where $s = \sqrt{1 - \frac{l^2}{L^2}}$, L is the maximum duration of the occultation (ie. in case of centrality), and assuming the body is spherical.

Given the longitude λ and the latitude ϕ of the observing site, the coordinates in the fundamental plane are given by :

$$u = \cos\phi \sin(\lambda - \lambda_c) \tag{5.5}$$

$$v = \sin\phi \cos\phi_c - \cos\phi \sin\phi_c \cos(\lambda - \lambda_c) \tag{5.6}$$

$$w = \sin\phi \sin\phi_c + \cos\phi \cos\phi_c \cos(\lambda - \lambda_c) \tag{5.7}$$

The time of the closest approach for the observer is given by the relation :

$$t_m = T_0 + \frac{(u - x_0)x' + (v - y_0)y'}{x'^2 + y'^2} \tag{5.8}$$

In fact, t_m is calculated iteratively by replacing λ_c by $\lambda_c - \Omega(t_m - T_0)$, where Ω is the rate of Earth's rotation, to take into account the Earth's rotation during $t_m - T_0$.

If Δt is the difference between the observed time of the occultation for the observer and the nominal time of the occultation T_0, the correction to apply to the Besselian elements x_0, y_0 are :

$$\Delta x = (u - x_0) - x'\Delta t \tag{5.9}$$

$$\Delta y = (v - y_0) - y'\Delta t \tag{5.10}$$

$\Delta x, \Delta y$ are determined iteratively and finally transformed into an offset in right ascension and in declination between the observed occultation and the computed occultation (from the ephemeris).

The position deduced from the occultation is then the ephemeris plus the offset.

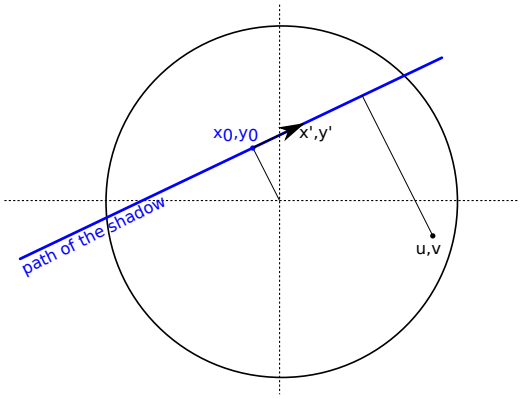

Figure 5.13: Diagram of the fundamental plane and the associated coordinates

Position deduced from publications

Occultation on 20 July 2002

Sicardy et al. (2003) obtained a light curve of the occultation by Pluto in Arica, North of Chile. They derived an astrometric solution of the occultation by giving distance of closest approach to the center of Pluto's shadow for Arica (975 ± 250km).

The Besselian elements for this occultation with Gaia DR2 star and JPL DE436 + PLU055 for Pluto's ephemeris are:

T_0	=	2002-07-20 01:43:39.8
x_0	=	-0.015137748
y_0	=	0.078729716
x'	=	-221.595155776
y'	=	-42.613814665
H	=	45.303191676
α_s	=	255.075123563
δ_s	=	-12.694996935

In Arica, the mid-time of the occultation occurs at 01:44:03 UT, giving $\Delta t = 23.2$s. There are two possible solutions but the occultation was also observed in Mamiña[2] in Chile (Buie, personal communication) so the only possible solution is the South one.

Finally, we derive the offset of $\Delta\alpha \cos\delta = +7.7 \pm 1.9$ mas and $\Delta\delta = -4.4 \pm 11.2$ mas, assuming a precision of 2 s for the mid-time. Each solution provides the following offset related to JPL DE436 + PLU055 ephemeris:

	North	South
$\Delta\alpha \cos\delta$ (mas)	24.8	7.7
$\Delta\delta$ (mas)	-93.4	-4.4

The reconstructed path of the prediction according to the two offsets are presented in Fig. 5.14 (See Desmars et al. 2018 to more details, , preprint attached in the Appendix).

[2]The Mamiña coordinates are 20°04'51.00"S and 69°12'00.00"W.

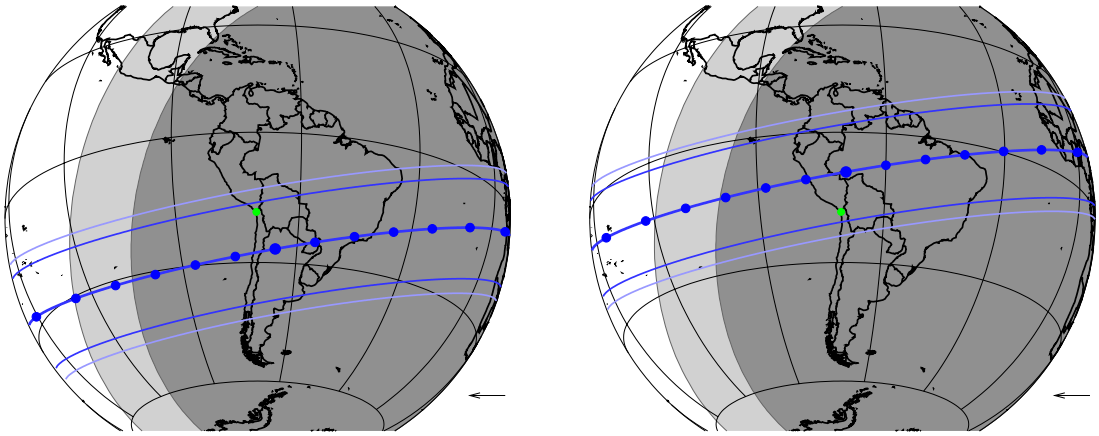

Figure 5.14: Reconstructed path of the occultation on 20 July 2002, considering a North solution (left), and a South solution (right). The legend is similar to Fig.4.7

Occultation on 21 August 2002

Elliot et al. (2003) derived an astrometric solution of the occultation by giving distance of closest approach to the centre of Pluto's shadow for Mauna Kea Observatory (597 ± 32km) and Lick Observatory (600 ± 32km). They observed a positive occultation with three telescopes (two in Hawai and one in Lick Observatory).

The Besselian elements for this occultation with Gaia DR2 star and JPL DE436 + PLU055 for Pluto's ephemeris are:

T_0	=	2002-08-21 07:00:32.0
x_0	=	0.091629552
y_0	=	-0.047418125
x'	=	-41.470159949
y'	=	-80.186411178
H	=	-27.314474978
α_s	=	254.705972362
δ_s	=	-12.858853587

As there are at least two stations observing this occultation, there is a unique solution. According to the mid time of the occultation in the two stations, we derived the following offsets:

observatory	mid-time	ρ (km)	Δt (s)	$\Delta\alpha\cos\delta$ (mas)	$\Delta\delta$ (mas)
CFHT 2.2m	6:50:33.9±0.5	597	-598.1	16.0	-8.0
CFHT 0.6m	6:50:33.9±1.8	597	-598.1	16.0	-8.2
Lick obs.	6:45:48.0±2.8	600	-884.0	14.2	-11.0

Finally, for this occultation, we used an average offset of $\Delta\alpha\cos\delta = +15.4 \pm 1.0$ mas and $\Delta\delta = -9.1 \pm 1.7$ mas. The reconstructed path of the prediction according to this offset is presented in Fig. 5.15.

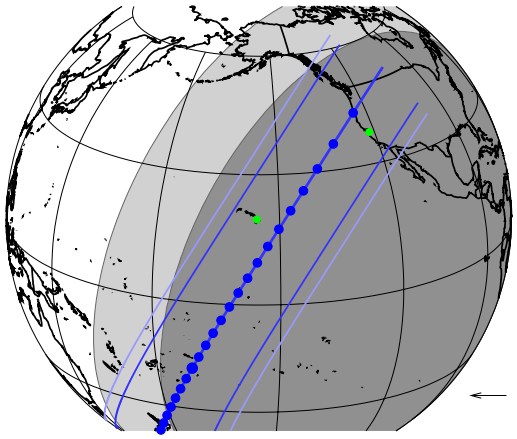

Figure 5.15: Reconstructed path of the occultation on 21 August 2002, considering the offset deduced from Elliot et al. (2003). The legend is similar to Fig.4.7

Occultation on 12 June 2006

The Besselian elements for the occultation on 12 June 2006 with Gaia DR2 star and JPL DE436 + PLU055 for Pluto's ephemeris are:

T_0	=	2006-06-12 16:25:05.8
x_0	=	0.008081468
y_0	=	-0.393907343
x'	=	-320.357408358
y'	=	-6.588025106
H	=	39.386450596
α_s	=	265.300310118
δ_s	=	-15.692941450

Young et al. (2008) published the half light time (ingress and egress) and the impact parameter (closest distance to the center of the shadow) for five stations:

- REE = Reedy Creek Observatory, QLD, AUS (0.5 m aperture).
- AAT = Anglo-Australian Observatory, NSW, AUS (4 m).
- STO = Stockport Observatory, SA, AUS (0.5 m).
- HHT = Hawkesbury Heights, NSW, AUS (0.2 m).
- CAR = Carter Observatory, Wellington, NZ (0.6 m)

These parameters allow us to compute the mid-time of the occultation and to finally derive an offset for each station:

observatory	mid-time	ρ (km)	Δt (s)	$\Delta\alpha\cos\delta$ (mas)	$\Delta\delta$ (mas)
REE	16:23:00.636±2.61	836.6	-125.2	9.4	-0.5
AAT	16:23:19.665±0.05	571.8	-106.1	9.6	-0.5
STO	16:23:59.619±0.80	382.2	-66.2	9.7	-0.5
HHT	16:23:17.705±2.12	302.5	-108.1	9.1	-0.4
CAR	16:22:30.825±1.96	-857.6	-155.0	11.2	-0.4

Finally, for this occultation, we used an average offset of $\Delta\alpha\cos\delta = +9.8 \pm 0.8$ mas and $\Delta\delta = -0.4 \pm 0.1$ mas.

The reconstructed path of the prediction according to this offset is presented in Fig. 5.16.

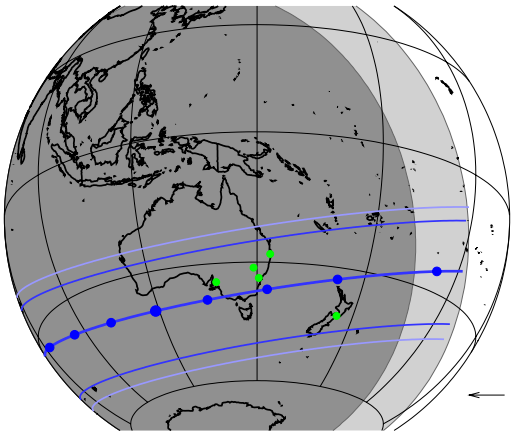

Figure 5.16: Reconstructed path of the occultation on 12 Ju , considering the offset deduced from Young et al. (2008). The legend is similar to Fig.4.7

Occultation on 23 July 2014

Pasachoff et al. (2016) published the observation of two occultations in Mount John (New Zealand) on June 2014. They provided the timing and impact parameter for the two occultations.

The Besselian elements for the occultation on 23 July 2014 with Gaia DR2 star and JPL DE436 + PLU055 for Pluto's ephemeris are:

T_0	=	2014-07-23 14:25:59.1
x_0	=	0.110372760
y_0	=	-0.614706119
x'	=	-300.130385882
y'	=	-53.903828467
H	=	-20.940785660
α_s	=	282.382245191
δ_s	=	-20.373331983

The fitted impact parameter for 23 July is $\rho = 480 \pm 120$km providing two possible solutions and the mid time of the occultation 14:24:31 is derived from the ingress and egress times at 50% and corresponds to $\Delta t = -88.1$s.

Each solution provides the following offset related to JPL DE436 + PLU055 ephemeris:

	North	South
$\Delta\alpha \cos\delta$ (mas)	30.3	22.9
$\Delta\delta$ (mas)	3.7	44.9

The reconstructed path of the prediction according to the two offsets are presented in Fig. 5.17. Finally, for this occultation, we used an average offset of $\Delta\alpha \cos\delta = +9.8 \pm 0.8$ mas and $\Delta\delta = -0.4 \pm 0.1$ mas.

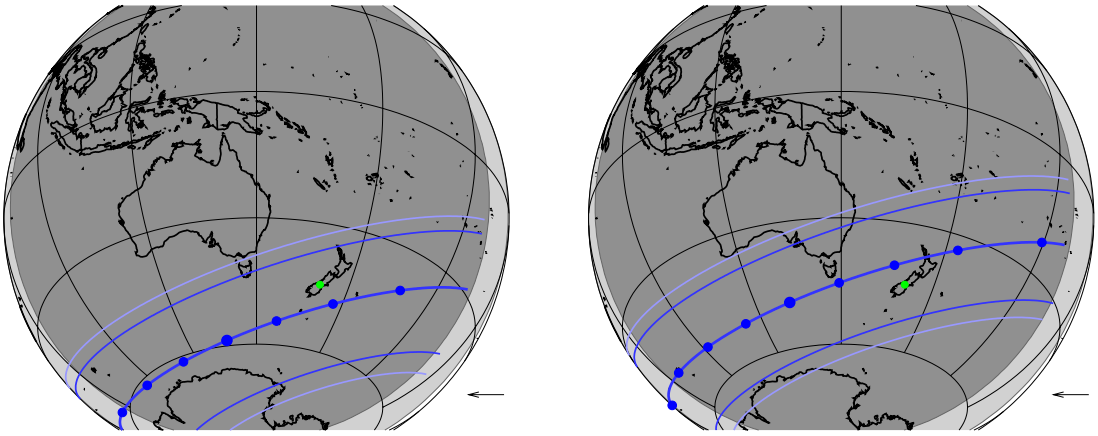

Figure 5.17: Reconstructed path of the occultation on 23 July 2014, considering a North solution (left), and a South solution (right). The legend is similar to Fig.4.7

Occultation on 24 July 2014

Pasachoff et al. (2016) also provides circumstances of the occultation on 24 July 2014 in Mont John Observatory.

The Besselian elements for the occultation on 24 July 2014 with Gaia DR2 star and JPL DE436 + PLU055 for Pluto's ephemeris are:

T_0	=	2014-07-24 11:42:19.9
x_0	=	0.075661748
y_0	=	-0.419500350
x'	=	-297.988040527
y'	=	-53.754831391
H	=	-22.209299195
α_s	=	282.360471376
δ_s	=	-20.376972931

The fitted impact parameter is $\rho = 510 \pm 140$km providing two possible solutions and the mid time of the occultation 11:42:29 is derived from the ingress and egress times at 50% and corresponds to $\Delta t = 9.1$s.

Each solution provides the following offset related to JPL DE436 + PLU055 ephemeris:

	North	South
$\Delta\alpha \cos\delta$ (mas)	3.4	11.3
$\Delta\delta$ (mas)	29.1	-14.6

According to the precisions of the mid-time and of the impact parameter, the estimated precision of the offset is 7.7 mas for $\Delta\alpha \cos\delta$ and 6.1 mas for $\Delta\delta$.

The reconstructed path of the prediction according to the two offsets are presented in Fig. 5.18.

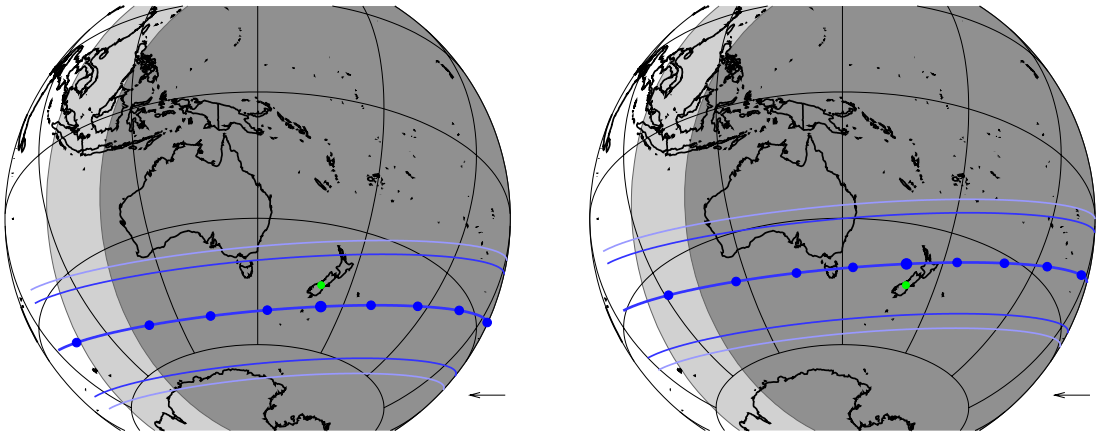

Figure 5.18: Reconstructed path of the occultation on 24 July 2014, considering a North solution (left), and a South solution (right). The legend is similar to Fig.4.7

5.3.3 NIMA ephemeris of Pluto

NIMA (Numerical Integration of the Motion of an Asteroid) has been developed in order to refine the orbits of small bodies, in particular TNOs and Centaurs studied by stellar occultations technique (Desmars et al., 2015). It consists in the numerical integration of the equations of motion perturbated by gravitional accelerations of the planets.

The state vector (which is the heliocentric vector of position and velocity of the body) is refined by fitting to astrometric observations with the least square method. The main advantage of NIMA is to allow to use not only observations published on the Minor Planet Center[3] but also unpublished observations or astrometric positions of occultations.

[3]The Minor Planet Center is in charge of providing astrometric measurements, orbital elements of the solar system small bodies : http://minorplanetcenter.net.

The quality of the observations is taken into account with a specific weighting scheme, in particular, it takes advantages of the high accuracy of previous occultations. Finally, after fitting to the observations, NIMA can provide ephemeris (through a bsp file format readable by the SPICE librairy[4]).

As NIMA is representing the motion of the center of mass of an object, it allows to compute the position of the Pluto's system barycenter. To deal with positions of occultations, we have to use an ephemeris representing the position of Pluto related to the position of the barycenter. For that purpose, we use PLU055 ephemeris[5] which is the most recent one, developed in 2015.

The positions of the occultations are corrected from the offset between Pluto and the Pluto's system barycenter to get position of the barycenter from occultations. Then the ephemeris of the barycenter is fitted to these corrected positions with NIMA.

Fig. 5.19 shows the difference between NIMA[6] and JPLDE436 ephemeris of Pluto's barycenter in right ascension (weighted by $\cos\delta$) and declination. The blue dots and the error bars represent the positions and their estimated precision from our occultations, the red dots represents the positions from other occultations, and the gray area represents the 1σ uncertainty of the NIMAv6 ephemeris.

Table 5.7 provides the residuals (O-C) of the positions from occultations with NIMAv6. The last occultations since 2010 reach less than 1 mas which is much better than any other measurement of Pluto's positions. In that context, other classical observations of Pluto, such as CCD, appear to be useless for short-term ephemeris as the occultations provided the most accurate positions during 2002 to 2016.

The NIMA ephemeris allows very accurate predictions of stellar occultation by Pluto in the next years to the precision of few mas. In particular, we have predicted an occultation by Pluto on August 15, 2018, above North America to the precision of 2.5 mas representing only 60 km on the shadow path.

Concluding remarks of this section are provided in the final chapter.

Figure 5.20 represents the prediction of the occultation by Pluto on August 15, 2018 using two different ephemerides: JPL DE436 + PLU055 and NIMAv6 + PLU055. NIMAv6 allows a better prediction since the precision in time is about 4 sec and 2.5 mas (about 60km at the distance of Pluto) perpendicular to the path, whereas the prediction with JPL ephemeris is shifted by 36.8s and 8 mas Southern in comparison to the prediction with NIMAv6.

[4]The SPICE Toolkit is a librairy developed by NASA dedicated to space navigation and providing in particular a list of routines related to ephemeris: http://naif.jpl.nasa.gov/naif/index.html.

[5]PLU055 is the JPL ephemeris of the Pluto's system developed by R.Jacobson in 2015: https://naif.jpl.nasa.gov/pub/naif/generic_kernels/spk/satellites/plu055.cmt

[6]The version of the NIMA ephemeris is NIMAv6 computed in July 13, 2018 and available on http://lesia.obspm.fr/lucky-star/nima/.

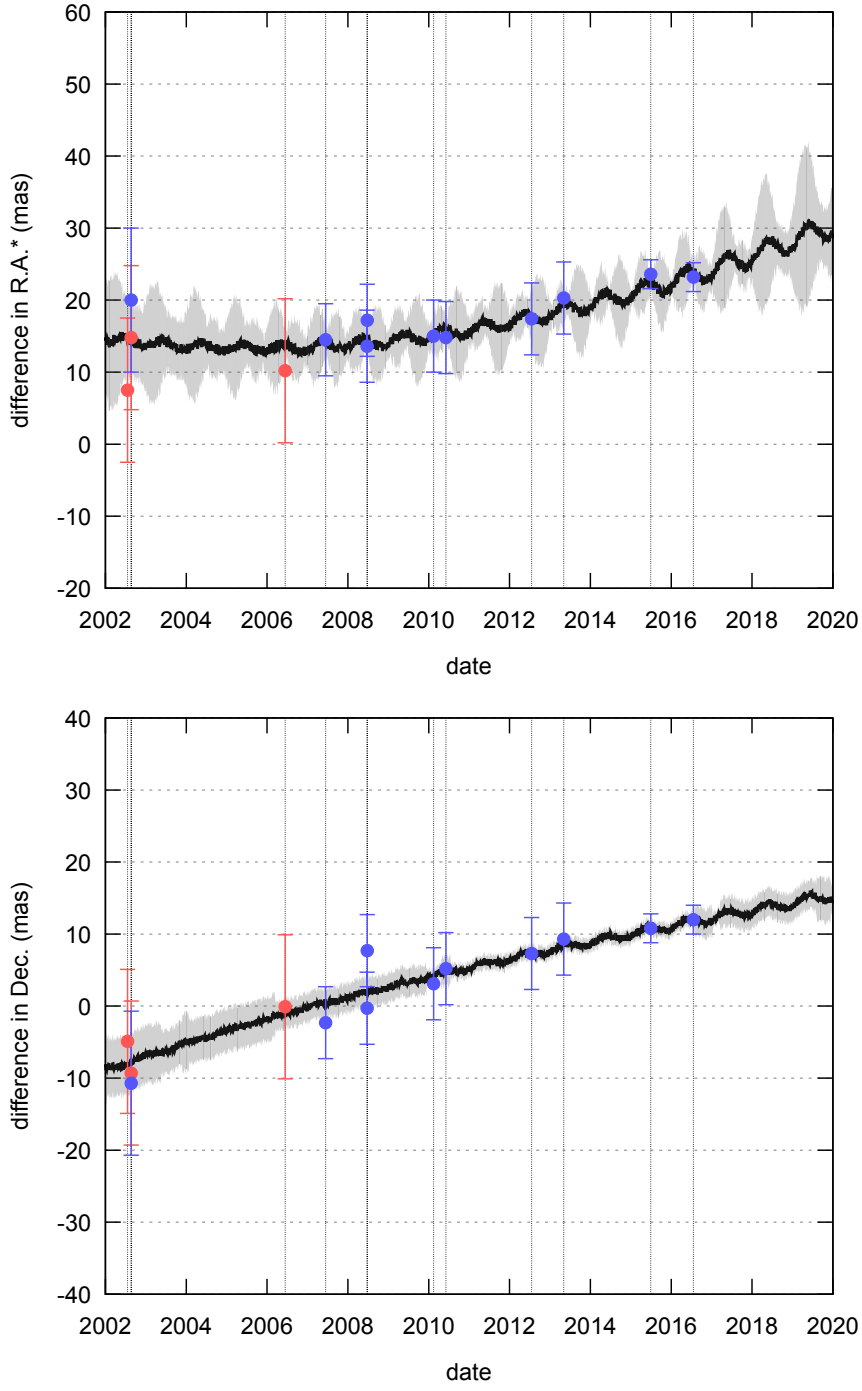

Figure 5.19: Difference between NIMAv6 and JPL DE436 ephemeris of Pluto's system barycenter in right ascension (weighted by $\cos\delta$) and in declination. Blue dots and their estimated precision in error bar represent the positions coming from the occultations studied in this thesis and red dots represent the positions deduced from other publications. The gray area represents the 1σ uncertainty of the NIMA orbit.

date (UT)	$\Delta\alpha\cos(\delta)$ (mas)	$\Delta\delta$ (mas)	σ_α (arcsec)	σ_δ (arcsec)
2002-07-20	-5.0	3.9	0.010	0.015
2002-08-21(from Elliot et al. 2003)	3.0	-1.0	0.010	0.010
2002-08-21	8.2	-2.3	0.010	0.010
2007-06-14	0.5	-2.0	0.005	0.005
2008-06-22	-0.7	-1.8	0.005	0.005
2008-06-24	2.3	2.5	0.005	0.005
2010-02-14	-1.2	-1.0	0.005	0.005
2010-06-04	-1.5	0.5	0.005	0.005
2012-07-18	-0.3	0.5	0.005	0.005
2013-05-04(from Olkin et al. 2015)	-1.1	0.0	0.010	0.010
2013-05-04	-0.5	0.8	0.005	0.005
2015-06-29	0.4	0.1	0.002	0.002
2015-06-29(from Pasachoff et al. 2017)	-0.7	2.0	0.010	0.010
2016-07-19	-0.1	-0.1	0.002	0.002

Table 5.7: Residuals (O-C) related to NIMA ephemeris of Pluto system barycentre. Estimated precision in arcsec in right ascension and declination used for the fit is also indicated (see Desmars et al 2018 in the Appendix for more informations.

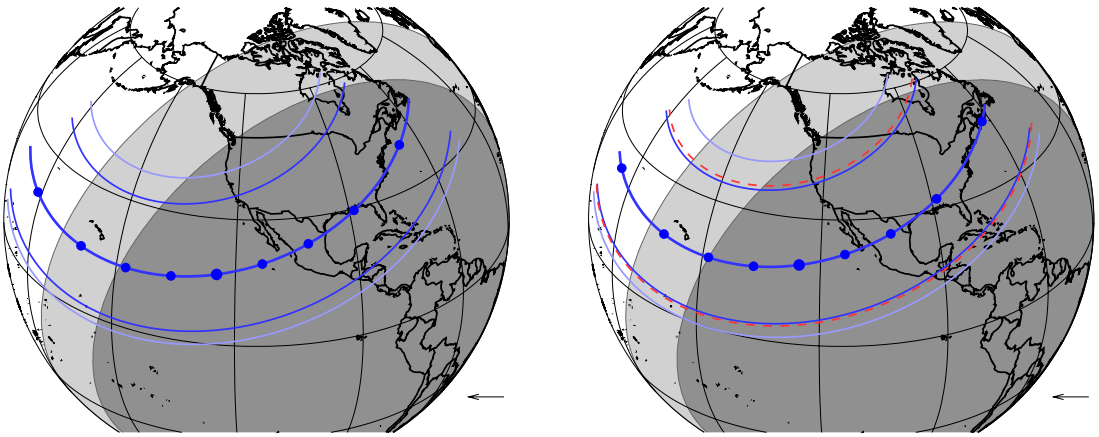

Figure 5.20: Prediction of the occultation by Pluto on 15 August 2018 using JPL DE436 + PLU055 (left) and NIMAv6 + PLU055 (right) ephemerides. The legend is similar to Fig.4.7, in addition, the red dotted lines on right represent the $1-\sigma$ uncertainty on the path.

Chapter 6

Conclusions

Contents

Context

The knowledge of the Pluto's atmosphere is an important problem because that dwarf planet has a thin atmosphere, where its pressure is dominated by the vapor equilibrium pressure at its surface. In addition, there are more objets similar to Pluto, like Triton, and possibly other ones among the Trans Neptunian Objects. This knowledge is progressing thanks to theoretical models. Meanwhile, observational constraints are the best way to validate these models, with spatial and time resolution as large as possible.

To probe Pluto's atmosphere I have used the powerful stellar occultation technique that is able to probe thin atmospheres over decadal periods, 2002 to 2016 in the case of Pluto. In this work, I have:

1) consistently reduced 45 photometric light-curves obtained during ground-based stellar occultations by Pluto between 2002 and 2016.

2) used a template model to fit all of the light-curves for each campaign to estimate the surface pressure and pressure at 1215 km from Pluto's center;

3) used for the first time both the 2015 June 29 central flash detection and the New Horizons temperature profile to probe the deepest layers of the Pluto's atmosphere;

4) used my estimates of Pluto's offset to fine-tune an updated Pluto (NiMA) ephemeris, including and discussing data obtained during the occultations of 1985 and 1988.

My main results are briefly summarized in the following sections.

6.1 Pluto's global atmospheric evolution

Figure 5.3 summarizes my work concerning the evolution of Pluto's atmospheric pressure with time. It shows that the observed trend can be explained by tweaking Pluto's physical parameters in a rather restrictive way.

As noted in Chapter 5, this evolution is consistent with the continuous increase of pressure observed since 1988 (a factor of 3 between 1988 and 2016). It results from the heating of the nitrogen ice in Sputnik Planitia and in the northern mid-latitudes, when the areas are exposed to the Sun (just after the northern spring equinox in 1989) and when Pluto is near the Sun, as detailed in Bertrand and Forget (2016). The model also predicts that atmospheric pressure is expected to reach its peak and drop in the next few years, due to

(1) the orbitally-driven decline of insolation over Sputnik Planitia and the northern mid-latitude deposits, and

(2) the fact that nitrogen condenses more intensely in the colder southern part of Sputnik Planitia, thus precipitating and hastening the pressure drop.

In that context, it is important to continue the monitoring of Pluto's atmosphere using ground-based stellar occultations. As mentioned in Chapter 5, such occultations are becoming unfortunately rarer and rarer. The forthcoming event of 2018 August 15, observable from the USA and Mexico, is thus an important milestone for testing the model presented in this work.

6.2 Pluto's deeper atmosphere

The models presented in the Chapter 5, section 5.2 are not unique and not mutually inconsistent. For instance, one can have at the same time a topographic feature blocking the stellar together with some haze absorption. Also, hazes, if present, will not be uniformly distributed along the limb. Similarly, topographic features will probably not be uniformly distributed along the limb, but rather, have a patchy structure that complicates our analysis. In spite of their limitations, the simple scenarios presented above teach us a few lessons:

(1) Although satisfactory in terms of flash fitting, the nominal temperature profile of Sicardy et al. (2016) can probably be ruled out below the planetocentric radius $\sim$ 1215 km, since it is clearly at variance with the REX profiles (Fig. 5.10), while probing essentially the same zones on Pluto's surface (Fig. 5.8), but with less details.

(2) The REX profiles taken at face value cannot explained the central flashes observed at Bootes-3 and Dunedin, unless hazes are present around the $\sim$ 8 km altitude level, with optical depths along the line of sight in the range $\tau = 0.27 - 0.35$. This is higher but still consistent with the reported value of $\tau = 0.24$ (Cheng et al., 2017).

(3) An alternative solution is to reduce uniformly the REX pressures by a factor 0.805, which would bring the surface values at $p_{\rm surf} = 12.8 \times 0.805 = 10.3$ μbar at ingress and $p_{\rm surf} = 10.2 \times 0.805 = 8.21$ μbar at egress. Those values are at 3.6σ and 2.8σ away from the nominal REX results, using error bars of ± 0.7 μbar for $p_{\rm surf}$ (Hinson et al., 2017). This is not large enough to exclude this possibility at this point.

(4) The topographic feature hypothesis remains a good alternative, as it requires modest elevation (a bit more than 1 km) above the terrain probed by REX at egress. A

more detailed examination of Pluto's elevation maps, confronted with the stellar paths shown in Fig. 5.8, will be most useful to confirm or reject that hypothesis.

As a final comment, we recall that the flashes have been generated by assuming a spherical atmosphere near Pluto's surface. There is no sign of distortion of the Bootes-3 and Dunedin flashes that suggests a departure from sphericity. It would be useful, however to assess such departures, or at least establish an upper limit for them in future works.

6.3 Pluto's orbit

My light curve fitting described in Chapter 5 using stellar occultations between 2002 and 2016 has provided accurate Pluto's ephemeris offset over that period, once the Gaia DR2 catalog has been released (April 2018).

This in turn yields a new, improved Pluto's orbit, as illustrated in Fig. 5.19. The accuracy of this ephemeris for 2018 is of the order of 2-3 milli-arcsec (mas) in declination, a significant improvement when it comes to predict forthcoming occultations.

Note that this result is impossible to reach with classical astrometry. In fact, the presence of the usually unresolved Charon in classical images, causes significant displacements of the photocenter of the system with respect to its barycenter. As a consequence, and even modeling the effect of Charon, accuracies below the 50 mas level are difficult to reach.

The same method has been used for Chariklo, with even better accuracy (of the order of 1 mas), and illustrates the power of stellar occultations not only for better studying those bodies, but also for improving their orbital elements.

6.4 Perspectives

In this thesis my work was developed during an important period concerning ground-based stellar occultations by Pluto. In fact, as Pluto moved in front of the Galactic Center, probability of stellar occultations by Pluto increased during the 2002-2016 period, yielding a few events per year that greatly improve our knowledge of Pluto's atmospheric structure and evolution. That is very important because Pluto is going through a period where important changes are predicted by numerical models and ground-based occultations constrains future scenarios in Pluto's atmosphere evolution. Another important aspect of during my thesis is that ground-based occultations by Pluto set the scene for the NASA New Horizons mission (NH) which flew by the dwarf planet on 2015 July. A fruitful and complementary comparison between the ground-based and NH results ensued another facet of this work.

My fitting of stellar occultations observed between 2002 and 2016 has provided Pluto's position relative to the occulted stars with typical accuracies of 2-3 mas. Meanwhile, the recently released Gaia DR2 catalog provides star positions at epoch with sub-mas accuracy, thanks to the proper motion measurement. This results in a 2-3 mas level accuracy for Pluto's positions for each occultation, and allowed in particular an accurate prediction (at mas-level accuracy) of the August 15, 2018 Pluto occultation.

All above explain, give me a background focused in observations of ground-based stellar occultations and tools that I can readily be applied to new Pluto data sets. In addition, Pluto is a "window" of others TNO's with tenue atmospheres. For instance, this method can also be extended to the analysis of occultations by Triton which has similar atmosphere as Pluto or other targets of LUCKY star Project.

Particularly, in Peru there are new telescopes where I'm able to apply the stellar occultations technique specially to telescopes like OA-UNI T50cm (Meza et al., 2009; Pereyra et al., 2015) of Universidad Nacional de Ingenieria (UNI), T1m on Peruvian southern Andes of Comision Nacional de Investigacion y Desarrollo Aeroespacial (CONIDA) and also in development projects like T60cm (del Mar et al., 2011) of Universidad Nacional San Antonio Abad del Cusco (UNSAAC).

Appendix A

Annexes

Paper Meza at al. 2018 that was submitted to Astronomy and Astrophysics, It summarizes the results of Chapters 4 and 5.

Astronomy & Astrophysics manuscript no. Meza_etal
September 19, 2018

Pluto's lower atmosphere and pressure evolution from ground-based stellar occultations, 1988-2016

E. Meza[1,⋆], B. Sicardy[1], M. Assafin[2], J. L. Ortiz[3], T. Bertrand[4], E. Lellouch[1], J. Desmars[1], F. Forget[5], D. Bérard[1], A. Doressoundiram[1], J. Lecacheux[1], F. Roques[1], T. Widemann[1], F. Colas[6], F. Vachier[6], S. Renner[6,7], R. Leiva[8], F. Braga-Ribas[9,10], G. Benedetti-Rossi[10], J. I. B. Camargo[10], A. Dias-Oliveira[10], B. Morgado[10], A. Ramos-Gomes Jr[10], R. Vieira-Martins[10], R. Behrend[11], A. Castro Tirado[3], R. Duffard[3], N. Morales[3], P. Santos Sanz[3], M. Jelínek[12], R. Cunniffe[13], R. Querel[14], M. Harnisch[15,16], R. Jansen[15,16], A. Pennell[15,16], S. Todd[15,16], V. D. Ivanov[17], M. Gillon[18], E. Jehin[18], J. Manfroid[18], J. Pollock[19], D. E. Reichart[20], A. P. LaCluyze[20], J. B. Haislip[20], K. M. Ivarsen[20],, C. Opitom[17], A. Maury[21], R. Gil-Hutton[22], V. Dhillon[23], S. Littlefair[23], T. Marsh[24], C. Veillet[25], K.-L. Bath[26,27], W. Beisker[26,27], H.-J. Bode[26,27⋆⋆], M. Kretlow[26,27], D. Herald[15,28,29], D. Gault[15,30,31], S. Kerr[15,32], H. Pavlov[28], O. Faragó[27⋆⋆⋆], O. Klös[27], E. Frappa[33], A. A. Cole[34], B. Giles[34], J. Greenhill[34⋆⋆⋆⋆], K. M. Hill[34], M. W. Buie[8], C. S. Olkin[8], E. F. Young[8], L. A. Young[8], L. H. Wasserman[35], R. G. French[36], F. Bianco[37], F. Marchis[1,38], N. Brosch[39], S. Kaspi[39], D. Polishook[40], I. Manulis[40], M. Devogèle[15], M. Ait Moulay Larbi[41], Z. Benkhaldoun[41], A. Daassou[41], Y. El Azhari[41], Y. Moulane[18,41], J. Broughton[15], J. Milner[15], T. Dobosz[42], G. Bolt[43], B. Lade[44], A. Gilmore[45], P. Kilmartin[45], W. H. Allen[15], P. B. Graham[15,46], B. Loader[15,28], G. McKay[15], J. Talbot[15], S. Parker[47], L. Abe[48], Ph. Bendjoya[48], J.-P. Rivet[48], D. Vernet[48], L. Di Fabrizio[49], V. Lorenzi[49,50], A. Magazzú[49], E. Molinari[49,51], K. Gazeas[52], A. Carbognani[53], M. Conti[54], B. Bonnoli[54], G. Leto[55], R. Zanmar Sanchez[55], L. Mancini[56,57,58,59], H. Eichler[27], B. Kattentidt[27], J. Hattenbach[27], M. Dohrmann[27,60], K. Guhl[27,60], W. Rothe[27,60], K. Walzel[60], G. Wortmann[60], A. Eberle[61], D. Hampf[61], J. Ohlert[62,63], G. Krannich[64], G. Murawsky[65], B. Gährken[66], D. Gloistein[67], S. Alonso[68], A. Román[69], J.-E. Communal[70], F. Jabet[71], S. de Visscher[72], J. Sérot[73], T. Janik[74], Z. Moravec[74], P. Machado[75], M. Lavayssière[33], A. Selva[27,76], C. Perelló[27,76], J. Rovina[27,76], A. Marchini[27,77], R. Papini[27,77], F. Salvaggio[27,77], A. Noschese[27,78], V. Tsamis[27], P. Barroy[79], M. Irzyk[79], D. Neel[79], J.P. Godard[79], D. Lanoiselée[79], P. Sogorb[79], D. Vérilhac[80], M. Bretton[81], F. Signoret[82], F. Ciabattari[83], R. Naves[27], M. Boutet[84], J. De Queiroz[27], P. Lindner[27], K. Lindner[27], P. Enskonatus[27], G. Dangl[27], T. Tordal[27], C. Peterson[85], Lawrence A. Molnar[86], and R. Howeell[87]

(Affiliations can be found after the references)

Received mm:dd, yyyy; accepted mm:dd, yyyy, [Version September 19, 2018]

ABSTRACT

Context. Pluto's tenuous nitrogen (N_2) atmosphere undergoes strong seasonal effects due to high obliquity and orbital eccentricity, and has been recently (July 2015) observed by the New Horizons spacecraft.
Aims. Goals are (*i*) monitor Pluto's atmospheric pressure evolution between 2002 and 2016 and (*ii*) constrain the structure of the lower atmosphere using a central flash observed in 2015.
Methods. Eleven stellar occultations by Pluto observed between 2002 and 2016 are used to retrieve atmospheric profiles (density, pressure, temperature) between ~5 km and ~380 km altitude levels (i.e. pressures from ~10 μbar to 10 nbar).
Results. (*i*) Pressure has suffered a monotonic increase from 1988 to 2016, that is compared to a seasonal volatile transport model, from which tight constraints on a combination of albedo and emissivity of N_2 ice are derived. (*ii*) A central flash observed on 2015 June 29 is consistent with New Horizons REX profiles, provided that (a) hazes with tangential optical depth ~0.3 are present and/or (b) the nominal REX pressure values are overestimated by ~20% and/or (c) higher terrains block part of the flash in the Charon facing hemisphere.

Key words. methods: data analysis - methods: observational - planets and satellites: atmospheres - planets and satellites: physical evolution - planets and satellites: terrestrial planets - techniques: photometric

1. Introduction

Pluto's tenuous atmosphere was glimpsed during a ground-based stellar occultation observed on 1985 August 19 (Brosch 1995), and fully confirmed on 1988 June 09 during another occultation (Hubbard et al. 1988; Elliot et al. 1989; Millis et al. 1993) that provided the main features of its structure: temperature, composition, pressure, density, see the review by Yelle & Elliot (1997).

⋆ Partly based on observations made with the Ultracam camera at the Very Large Telescope (VLT Paranal), under program ID 079.C-0345(F), the ESO camera NACO at VLT, under program IDs 079.C-0345(B), 089.C-0314(C) and 291.C- 5016, the ESO camera ISAAC at VLT under program ID 085.C-0225(A) and the ESO camera SOFI at NTT Paranal, under program ID 085.C-0225(B).
⋆⋆ Deceased
⋆⋆⋆ Deceased
⋆⋆⋆⋆ Deceased

Since then, Earth-based stellar occultations have been quite an efficient method to study Pluto's atmosphere. It yields, in the best cases, information from a few kilometers above the surface (pressure ∼10 μbar) up to 380 km altitude (∼10 nbar). As Pluto moved in front of the Galactic Center, the yearly rate of stellar occultations dramatically increased during the 2002-2016 period, yielding a few events per year that greatly improved our knowledge of Pluto's atmospheric structure and evolution.

Ground-based occultations also provided a decadal monitoring of the atmosphere. Pluto has a large obliquity (∼ 120°, the axial inclination to its orbital plane) and high orbital eccentricity (0.25) that takes the dwarf planet from 29.7 to 49.3 AU during half of its 248-year orbital period. Northern spring equinox occurred in January 1988 and perihelion occurred soon after, in September 1989. Consequently, our survey monitored Pluto as it receded from the Sun while exposing more and more of its northern hemisphere to solar rays. More precisely, as of 2016 July 19 (the date of the most recent occultation reported here), Pluto's heliocentric distance has increased by a factor of 1.12 since perihelion, corresponding to a decrease of about 25% in average insolation. Meanwhile, the subsolar latitude has gone from zero degree at equinox to 54° north in July 2016. In this context, dramatic seasonal effects are expected, and observed.

Another important aspect of ground-based occultations is that they set the scene for the NASA New Horizons mission (NH herein) that flew by the dwarf planet in July 2015 (Stern et al. 2015). A fruitful and complementary comparison between the ground-based and NH results ensued – another facet of this work.

Here we report results derived from eleven Pluto stellar occultations observed between 2002 and 2016, five of them yet unpublished, as mentioned below. We analyze them in a unique and consistent way. Including the 1988 June 09 occultation results, and using the recent surface ice inventory provided by NH, we constrain current seasonal models of the dwarf planet. Moreover, a central flash observed during the 2015 June 29 occultation is used to compare Pluto's lower atmosphere structure derived from the flash with profiles obtained by the Radio Science EXperiment instrument on board of NH (REX herein) below an altitude of about 115 km

Observations, data analysis and primary results are presented in Section 2. Implication for current seasonal Pluto's models are discussed in Section 3. The analysis of the 2016 June 29 central flash is detailed in Section 4, together with its consequences for Pluto's lower atmosphere structure. Concluding remarks are provided in Section 5.

2. Observations and data analysis

2.1. Occultation campaigns

Table 4 lists the circumstances of all the Pluto stellar occultation campaigns that our group have organized between 2002 and 2016. The first part of this table lists the eleven events that were used in the present work. In a second part of the table, we list other campaigns that were not used, because the occultation light curves had insufficient signal-to-noise-ratio and/or because the configurations of the occulting chords was ill-configured (grazing chords or single chord) and as such, do not provide relevant measurements of the atmospheric pressure.

Details on the prediction procedures can be found in Assafin et al. 2010, 2012; Benedetti-Rossi et al. 2014. Some of those campaigns are already documented and analyzed in previous publications, namely the 2002 July 20, 2002 August 21, 2007 June 14, 2008 June 22, 2012 July 18, 2013 May 04 and 2015 June 29 events. They were used to constrain Pluto's global atmospheric structure and evolution (Sicardy et al. 2003; Dias-Oliveira et al. 2015; French et al. 2015; Olkin et al. 2015; Sicardy et al. 2016), the structure of the lower atmosphere and CH_4, CO with implications for the HCN abundances (Lellouch et al. 2009, 2015, 2017), the presence of gravity waves (Toigo et al. 2010; French et al. 2015) and Charon's orbit (Sicardy et al. 2011). Finally, one campaign that we organized is absent from Table 4 (2006 April 10). It did not provide any chord on Pluto, but was used to put an upper limit of Pluto's rings (Boissel et al. 2014).

Note that we include here five more (yet unpublished) data sets obtained during the following dates: 2008 June 24, 2010 February 14, 2010 June 04, 2011 June 04 and 2016 July 19.

Table 1. Adopted physical parameter

Pluto's mass[1]	$GM_P = 8.696 \times 10^{11}$ m^3 sec^{-2}
Pluto's radius[1]	$R_P = 1187$ km
N_2 molecular mass	$\mu = 4.652 \times 10^{-26}$ kg
N_2 molecular refractivity[2]	$K = 1.091 \times 10^{-23}$ $+(6.282 \times 10^{-26}/\lambda^2_{\mu m})$ cm^3 molecule^{-1}
Boltzmann constant	$k = 1.380626 \times 10^{-23}$ J K^{-1}
Pluto pole position[3] (J2000)	α_p= 08h 52m 12.94s δ_p= -06d 10' 04.8"

Notes. [1] Stern et al. (2015). [2] Washburn (1930). [3] Tholen et al. (2008).

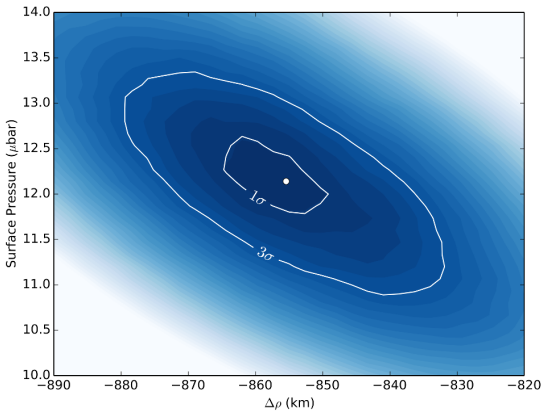

Fig. 1. An example of $\chi^2(\Delta\rho, p_{surf})$ map derived from the simultaneous fit to the light curves obtained during the 2016 July 29 occultation. The quantity $\Delta\rho$ is Pluto's ephemeris offset (expressed in kilometers) perpendicular to the apparent motion of the dwarf planet, as projected in the sky plane. The other parameter (p_{surf}) is the surface pressure of the DO15 atmospheric model. The white dot marks the best fit, where the minimum value χ^2_{min} of χ^2 is reached. The value $\chi^2_{min} = 4716$, using 4432 data points, indicates a satisfactory fit with a χ^2 per degree of freedom of $\chi^2_{dof} \sim 4716/4432 \sim 1.06$. The best fit corresponds to $p_{surf} = 12.04 \pm 0.41$ μbar (1σ level). The error bar is derived from the 1σ curve that delineates the $\chi^2_{min} + 1$ level. The 3σ level curve (corresponding to the $\chi^2_{min} + 9$ level) is also shown.

2.2. Light curve fitting

For all the eleven data sets used here, we used the same procedure as in Dias-Oliveira et al. (2015) (DO15 hereafter) and in Sicardy et al. (2016). It consists of simultaneously fitting the refractive occultation light curves by synthetic profiles generated

by a ray tracing code that uses the Snell-Descartes law. The physical parameters adopted in this code are listed in Table 1.

Note in particular that our adopted Pluto's radius is taken from Stern et al. (2015), who use a global fit to full-disk images provided by the Long-Range Reconnaissance Imager (LORRI) of New Horizons to obtain $R_P = 1187 \pm 4$ km. Nimmo et al. (2017) improve that value to $R_P = 1188.3 \pm 1.6$ km. However, we kept the 1187 km value because it is very close to the deepest level reached by the REX experiment, near the depression Sputnik Planitia, see Section 4. Consequently, it is physically more relevant here when discussing Pluto's lower atmospheric structure.

We assume a pure N_2 atmosphere, which is justified by the fact that the next most important species (CH_4) has an abundance of about 0.5% (Lellouch et al. 2009, 2015; Gladstone et al. 2016), resulting in negligible effects on refractive occultations.

We also assume a transparent atmosphere, which is supported by the NH findings. As discussed in Section 4, the tangential (line-of-sight) optical depth of hazes found by NH for the rays that graze the surface is $\tau_T \sim 0.24$, with a scale height of $\sim$ 50 km (Gladstone et al. 2016; Cheng et al. 2017). As our fits are mainly sensitive to levels around 110 km (see below), this means that haze absorption may be neglected in our ray tracing approach.

Moreover, we take a global spherically symmetric atmosphere, which is again supported by the NH results, at least above the altitude ~35 km, see Hinson et al. (2017) and Fig. 7. This is in line with the global climate models, which predict that wind velocities in the lower atmosphere should not exceed $v \sim$1-10 m s^{-1} (Forget et al. 2017). If uniform, this wind would create an equator to pole radius difference of the corresponding isobar level of at most $\Delta r \sim (R_P v)^2/4GM_P < 0.1$ km, using Eq. 7 of Sicardy et al. (2006) and the values in Table 1. This expected distortion is too small to significantly affect our synthetic profiles.

Finally, the temperature profile $T(r)$ is taken constant. Here, the radius r is counted from Pluto's center, while Pluto's radius found by NH is 1187 km (Table 1). This will be the reference radius from which we calculate altitudes. Fixing the pressure at a prescribed level (e.g. the surface) then entirely defines the density profile $n(r)$ to within a uniform scaling factor for all radii r, using the ideal gas equation, hydrostatic equilibrium assumption, and accounting for the variation of gravity with altitude.

Taking $T(r)$ constant with time is justified by the fact that the pressure is far more sensitive to Pluto's surface temperature – through the vapor pressure equilibrium equation – than is the profile $T(r)$ to seasonal effects and heliocentric distance, at least from a global point of view. For instance, an increase of 1 K of the free N_2 ice at the surface is enough to multiply the equilibrium pressure by a factor of 1.7 (Fray & Schmitt 2009). Note that this is not inconsistent with our assumption that $T(r)$ is time-independent. In fact, the overall atmospheric pressure is controlled by the temperature a few kilometers above the surface, while our fits use a global profile $T(r)$ well above the surface.

Pluto ground-based stellar occultations probe, for the best data sets, altitudes from ~5 km (pressure level ~10 μbar) to ~380 km (~10 nbar level), see DO15. Rays coming from below ~5 km are detectable only near the shadow center (typically less than 50 km) where the central flash can be detected. The analysis is then complicated by the fact that double (or multiple) stellar images contribute to the flux. Moreover, the possible presence of hazes and/or topographic features can reduce the flux, see Section 4.

Conversely, rays coming from above 380 km cause too small stellar drops (<~1%) to be of any use under usual ground-based observing conditions. This said, our ray tracing method is mainly sensitive to the half-light level, where the star flux has been reduced by 50%. This currently corresponds to a radius of about 1295 km (or an altitude ~110 km and pressure ~1.6 μbar).

2.3. Primary results

The ray tracing code returns the best fitting parameters, in particular the pressure at a prescribed radius (e.g. the pressure $p_{\rm surf}$ at the surface, at radius $R_P = 1187$ km) and Pluto's ephemeris offset perpendicular to its apparent motion, $\Delta\rho$. The ephemeris offset along the motion is treated separately, see DO15 for details. Error bars are obtained from the classical function $\chi^2 = \sum_1^N [(\phi_{\rm i,obs} - \phi_{\rm i,syn})/\sigma_i]^2$ that reflects the noise level σ_i of each of the N data points, where $\phi_{\rm i,obs}$ and $\phi_{\rm i,syn}$ are the observed and synthetic fluxes, respectively. An example of $\chi^2(\Delta\rho, p_{\rm surf})$ map is displayed in Fig. 1, using a simultaneous fit to the 2015 June 29 occultation light curves. It shows a satisfactory fit for that event, $\chi^2_{\rm dof}$ ~1.06. Table 2 lists the values of $\chi^2_{\rm dof}$ for the other occultations, also showing satisfactory fits. Note the slightly higher values obtained for the 2002 August 21 and 2007 June 14 events (1.52 and 1.56, respectively). The presence of spikes in the light curve for the 2002 August 21 event (on top of the regular photometric noise) explains this higher value, see Fig. 2. From the same figure, we see that the 2007 June 14 light curves at Paranal were contaminated by clouds, also resulting in a slightly higher value of $\chi^2_{\rm dof}$. All together, those values validate a posteriori the assumptions of pure N_2, transparent, spherical atmosphere with temperature profile constant in time.

In total, we collected and analyzed in a consistent manner 45 occultation light-curves obtained from eleven separate ground-based stellar occultations in the interval 2002-2016 (Table 4). The synthetic fits to the light curves are displayed in Figs 2 and 3. Fig. A.1 shows the occulting chords and Pluto's aspect for each event as see from Earth.

Two main consequences of those results are now discussed in turn: (1) the temporal evolution of Pluto's atmospheric pressure; (2) the structure of Pluto's lower atmosphere using the central flash of June 29, 2015. A third product of these results is the update of Pluto's ephemeris using the occultation geometries between 2002 and 2016. It will be presented in a separate paper (Desmars et al., in preparation).

3. Pluto's atmospheric evolution

3.1. Constraints from occultations

In 2002, a ground-based stellar occultation revealed that Pluto's atmospheric pressure had increased by a factor of almost two compared to its value in 1988 (Elliot et al. 2003; Sicardy et al. 2003), although Pluto had receded from the Sun, thus globally cooling down. In fact, models using global volatile transport did predict this seasonal effect, among different possible scenarios (Binzel 1990; Hansen & Paige 1996).

Those models explored nitrogen cycles, and have been improved subsequently (Young 2012, 2013; Hansen et al. 2015). Meanwhile, new models were developed to simulate possible scenarios for Pluto's changes over seasonal (248 yr) and astronomical (30 Myr) time scales, accounting for topography and ice viscous flow, as revealed by the New Horizons flyby in July 2015 (Bertrand & Forget 2016; Forget et al. 2017; Bertrand et al. 2018).

The measurements obtained here provide new values of pressure vs. time, and are obtained using a unique light curve fitting

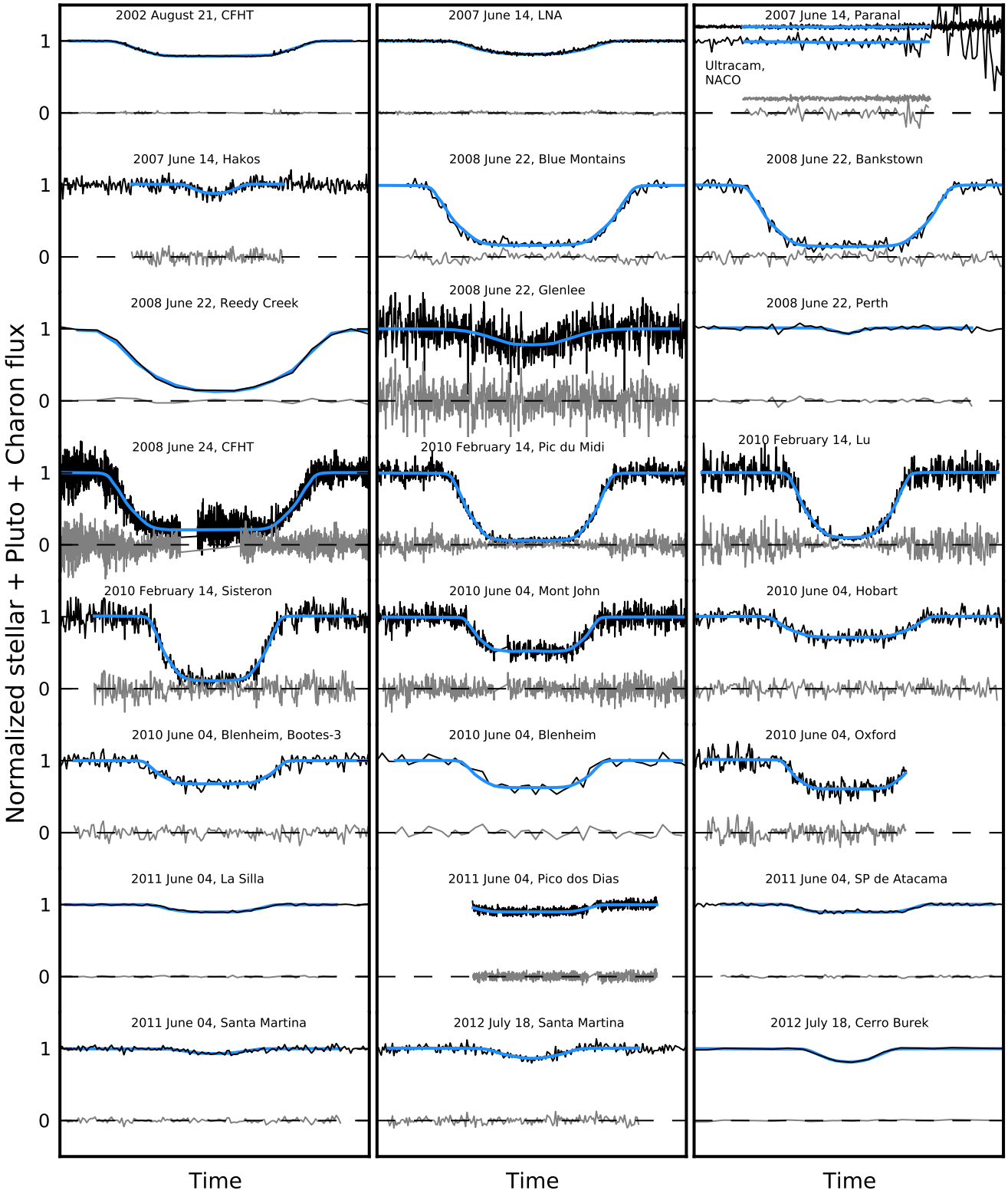

Fig. 2. Pluto occultation light curves obtained between 2002 and 2012. Blue curves are a simultaneous fit using the DO15 temperature-radius $T(r)$ model, see text. The residuals are plotted in gray under each light curve.

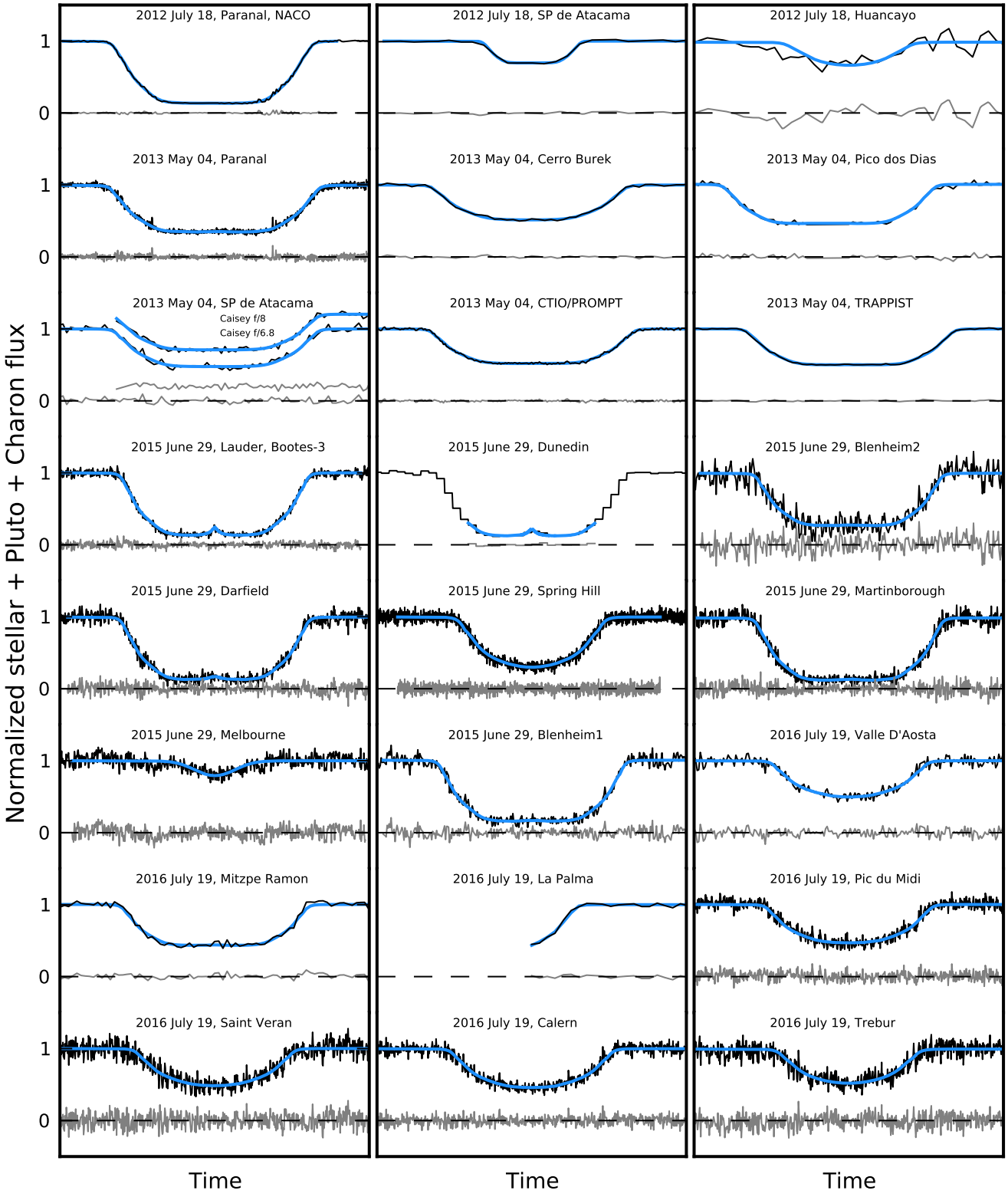

Fig. 3. The same as Fig. 2 for the 2012-2016 period.

Table 2. Pluto's atmospheric pressure

Date	Surface pressure $p_{\rm surf}$ (μbar)	Pressure at 1215 km p_{1215} (μbar)	Fit quality $\chi^2_{\rm dof}$
1988 Jun 09	4.28 ± 0.44	2.33 ± 0.24[1]	NA
2002 Aug 21	8.08 ± 0.18	4.42 ± 0.093	1.52
2007 Jun 14	10.29 ± 0.44	5.6 ± 0.24	1.56
2008 Jun 22	11.11 ± 0.59	6.05 ± 0.32	0.93
2008 Jun 24	10.52 ± 0.51	5.73 ± 0.21	1.15
2010 Feb 14	10.36 ± 0.4	5.64 ± 0.22	0.98
2010 Jun 04	11.24 ± 0.96	6.12 ± 0.52	1.02
2011 Jun 04	9.39 ± 0.70	5.11 ± 0.38	1.04
2012 Jul 18	11.05 ± 0.08	6.07 ± 0.044	0.61
2013 May 04	12.0 ± 0.09	6.53 ± 0.049	1.20
2015 Jun 29	12.71 ± 0.14	6.92 ± 0.076	0.84
2016 Jul 19	12.04 ± 0.41	6.61 ± 0.22	0.86

Notes. [1] The value p_{1215} is taken from Yelle & Elliot (1997). The ratio $p_{\rm surf}/p_{1215}$ = 1.84 of DO15's fitting model was applied to derive $p_{\rm surf}$. The qualities of the fits (values of $\chi^2_{\rm dof}$) are commented in sub-Section 2.3.

model (taken from DO15), except for the 1988 occultation, see Table 2. This model may introduce systematic biases, but it can nevertheless be used to derive the relative evolution of pressure from date to date, and thus discriminates the various models of Pluto's current seasonal cycle. In any case, the DO15 light curve fitting model appears to be close to the results derived from NH, see Hinson et al. (2017) and Section 4 (Fig. 7), so that those biases remain small. Note that other authors also used stellar occultations to constrain the pressure evolution since 1988 (Young et al. 2008; Bosh et al. 2015; Olkin et al. 2015), but with less comprehensive data sets. We do not include their results here, as they were obtained with different models that might introduce systematic biases in the pressure values.

3.2. Pressure evolution vs. a volatile transport model

Table 2 provides the pressure derived at each date, at the reference radius r = 1215 km (altitude 28 km), as well as the pressure previously derived from the 1988 June 09 occultation. Fig. 4 shows that during the time span 2002-2016, Pluto's atmospheric pressure kept on increasing, reaching a factor of almost three in 2016 compared to its value in 1988.

We interpret our occultation results in the frame of the Pluto volatile transport model developed at the Laboratoire de Météorologie Dynamique (LMD). It is designed to simulate the volatile cycles over seasonal and astronomical times scales on the whole planetary sphere (Bertrand & Forget 2016; Forget et al. 2017; Bertrand et al. 2018). We use the latest, most realistic, version of the model featuring the topography map of Pluto (Schenk et al. 2018a) and large ice reservoirs (Bertrand et al. 2018). In particular, we place permanent reservoirs of nitrogen ice in the Sputnik Planitia basin and in the depressions at mid-northern latitudes (30°N, 60°N), as detected by New Horizons (Schmitt et al. 2017) and modeled in Bertrand et al. (2018).

Fig. 4 shows the annual evolution of surface pressure obtained with the model, compared to the data. This evolution is consistent with the continuous increase of pressure observed since equinox in 1988, reaching an overall factor of almost three in 2016. This results from the progressive heating of the nitrogen ice in Sputnik Planitia and in the northern mid-latitudes, when those areas were exposed to the Sun just after the northern spring equinox in 1988, and close in time to the perihelion of 1989, as detailed in Bertrand & Forget (2016).

The model predicts that the pressure will reach its peak value and then drop in the next few years, due to:

(1) the orbitally-driven decline of insolation over Sputnik Planitia and the northern mid-latitude deposits;

(2) the fact that nitrogen condenses more intensely in the colder southern part of Sputnik Planitia, thus precipitating and hastening the pressure drop.

The climate model has several free parameters: the distribution of nitrogen ice, its Bond albedo and emissivity and the thermal inertia of the subsurface (soil). However, the large number of observation points and the recent NH observations provide strong constraints for those parameters, leading to an almost unique solution.

First, our observations restrict the possible N_2 ice surface distribution. Indeed, the southern hemisphere of Pluto is not expected to be significantly covered by nitrogen ice at the present time, because otherwise the peak of surface pressure would have occurred much earlier than 2015, as suggested by the model simulations (Fig. 4). With our model, we obtain a peak of pressure after 2015 only when considering little mid-latitudinal nitrogen deposits (or no deposit at all) in the southern hemisphere.

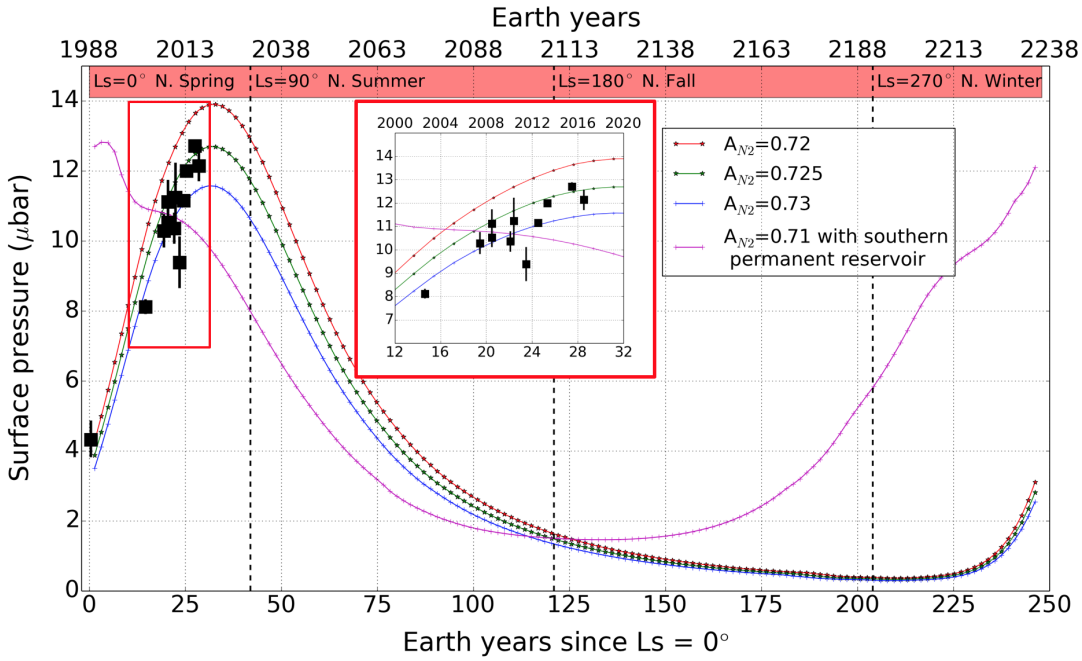

Fig. 4. Typical modeled annual evolution of surface pressure obtained with LMD Pluto volatile transport model, assuming permanent deposits of N_2 ice inside Sputnik Planitia and in the depression of mid-northern latitudes, a uniform soil seasonal thermal inertia of 800 J s$^{-1/2}$ m^{-2} K^{-1}, an emissivity $\epsilon_{N2} = 0.8$ and albedo range $A_{N2} = 0.73 - 0.74$ for N_2 ice, chosen to yield a surface pressure near 10-11 μbar in July 2015. The black dots with error bars show the surface pressure ($p_{\rm surf}$) inferred from stellar occultation pressure measurements (see Table 2). The curve in magenta corresponds to a similar simulation but assuming a permanent N_2 ice reservoir in the south hemisphere between 52.5° and 67.5° S, which leads to a pressure peak in 1990.

In our simulation, nitrogen does not condense much in the polar night (outside Sputnik Planitia), in spite of the length of the southern fall and winter. This is because in Pluto conditions, depending of the subsurface thermal inertia, the heat stored in the southern hemisphere during the previous southern hemisphere summer can keep the surface temperature above the nitrogen frost point throughout the cold season, or at least strongly limit the nitrogen condensation.

Consequently and secondly, the data points provide us with a second constraint, which is a relatively high subsurface thermal inertia so that nitrogen does not condense much in the southern polar night. Using a thermal inertia between 700-900 J s$^{-1/2}$ m^{-2} K^{-1} permits to obtain a surface pressure ratio $p_{\rm surf,2015}/p_{\rm surf,1988}$ to be around 2.5-3, as observed. Higher (resp. lower) thermal inertia tend to lower (resp. increase) this ratio, as shown in Fig. (2a) of Bertrand & Forget (2016).

Finally, the nitrogen cycle is very sensitive to the nitrogen ice Bond albedo A and emissivity ϵ, and only a small range for these parameters allows for a satisfactory match to the observations. Fig. 4 illustrates that point. To understand it, one can do the thought experiment of imagining Pluto with a flat and isothermal surface at vapor pressure equilibrium. A rough estimate of the equilibrium temperature is provided by the classical equation:

$$\epsilon\sigma T^4 = (1 - A)\,\frac{F}{4},$$

where F is the solar constant at Pluto, A is the nitrogen ice Bond albedo, ϵ its emissivity and $\sigma = 5.67 \times 10^{-8}$ W m^{-2} K^4 is the Stefan-Boltzmann constant. The surface pressure $p_{\rm surf}$ is then estimated from the surface temperature $T_{\rm surf}$ assuming N_2 vapor pressure equilibrium (Fray & Schmitt 2009). Consequently, the surface pressure data set inferred from stellar occultations provide us with a constraint on $(1 - A)/\epsilon$. In practice, in the model, we assume large grains for N_2 ice and we fix the emissivity at a relatively high value $\epsilon = 0.8$ (Lellouch et al. 2011). Taking $F = 1.26$ W m^{-2} (in 2015), and assuming $A = 0.74$, we find $p_{\rm surf} = 10$ μbar and $T_{\rm surf} = 36.6$ K. With $A = 0.73$, we obtain $p_{\rm surf} = 12.4$ μbar and $T_{\rm surf} = 37.0$ K. Therefore, decreasing the nitrogen ice albedo by only 0.01 leads to an increase of surface pressure in 2015 by a large amount of 25%.

4. Pluto's lower atmosphere

4.1. The June 29, 2015 occultation

The June 29, 2015 event provided seven chords across Pluto's atmosphere, see Table 4 and Fig. A.1. A first analysis of this event is presented in Sicardy et al. (2016). The two southernmost stations (Bootes-3 and Dunedin) probed the central flash region (Fig. 5). This was a unique opportunity to study Pluto's lower atmosphere a mere fortnight before the New Horizons flyby (July 14, 2015). During this short time lapse, we may assume that the atmosphere did not suffer significant global changes.

For a spherical atmosphere, there are at any moment two stellar images, a primary (near limb) image and a secondary (far limb) image that are aligned with Pluto's center and the star position, as projected in the sky plane, see Fig. 5. Since the ray tracing code provides the refraction angle corresponding to each image, their positions along Pluto's limb can be determined at any time (Fig. 5), and then projected onto Pluto's surface (Fig. 6).

4.2. Comparison with the REX results

The REX instrument recorded an uplinked 4.2 cm radio signal sent from Earth. The phase shift due to the neutral atmosphere was then used to retrieve the $n(r)$, $p(r)$ and $T(r)$ profiles through

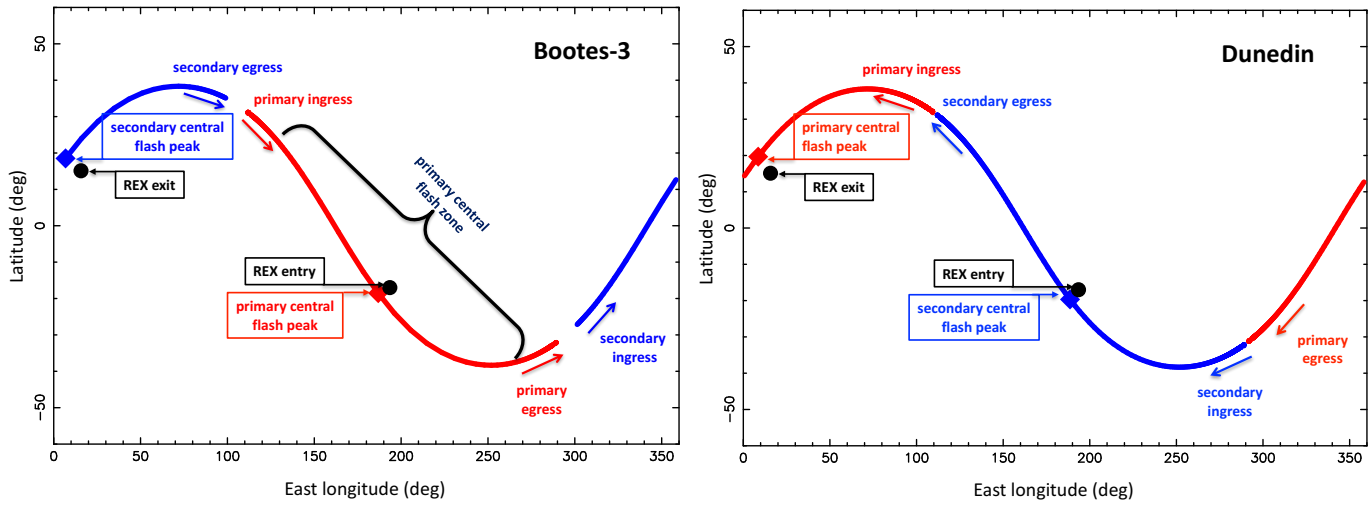

Fig. 6. Left panel - Traces of the primary (red) and secondary (blue) stellar images observed at Bootes-3, as deduced from Fig. 5. The arrows indicate the direction of motion. "Ingress" (resp. "egress") refers to the disappearance (resp. re-appearance) of the images into Pluto's atmosphere. The diamond-shaped symbols mark the positions of the image at the peak of the flash, corresponding to the time of closest approach of the respective station to the shadow center. In total, the primary image scanned longitudes from 120° to 270°, while the secondary image scanned longitudes from 310° to 360° and then from 0 to 70°. The brace indicates the total duration of the primary flash (~15 s, see Fig. 10) at Bootes-3, covering a rather large region of more than 120° in longitude. A similar extension applies to the secondary flash, but the brace has not been drawn for sake of clarity. The black bullets are the locations of the REX measurements at entry and exit (Hinson et al. 2017). Note the casual proximity of the REX points and the June 29, 2015 flash peaks. Right panel - The same for the Dunedin station, where the brace has not been repeated. Note that the tracks and motions of the primary and secondary images are essentially swapped between the two stations.

an inversion method and the usual ideal gas and hydrostatic assumptions (Hinson et al. 2017). The REX radio occultation probed two opposite points of Pluto as the signal disappeared behind the limb (entry) and re-appeared (exit), see Fig. 6. Note that the REX entry point is at the southeast margin of Sputnik Planitia, a depression that is typically 4 km below the surrounding terrains, see Hinson et al. (2017) for details.

Note the (serendipitous) proximity of the regions scanned by the June 29, 2015 central flash and the two zones probed by REX at entry and exit. This permits relevant tests of the REX profiles against the central flash structure. The local circumstances on Pluto for the central flash and the REX occultation are summarized in Table 3. Note that the local time was swapped between the primary image of the flash and the REX occultation, the morning limb of one being the evening limb of the other.

The REX profiles are in good general agreement with those derived by Sicardy et al. (2016) – based itself on the DO15 procedure – between the altitudes of 5 km and 115 km (Figs. 7 and 8), thus validating our approach. However, we see discrepancies between the Sicardy et al. (2016) density and temperature profiles, as well a divergence between the REX entry and exit profiles below the altitude ~25 km (r = 1212 km). Those points are examined below.

Note that the entry REX profile goes deeper than the exit profile. This reflects the fact that the nominal Pluto's radii are at 1187.4 ± 3.6 km at entry and 1192.4 ± 3.6 km at exit (Hinson et al. 2017). This discrepancy is not significant considering the uncertainties on each radius. However, the examination of Fig. 9 shows that the most probable explanation of this mismatch is that REX probed higher terrains at exit than at entry, then providing the same pressure at a given planetocentric radius. This is the hypothesis that we will adopt here, which is furthermore supported by the fact that the REX entry point is actually near the depressed region Sputnik Planitia.

4.3. The June 29, 2015 central flash

The REX profiles extend from the surface (with pressures of 12.8 and 10.2 μbar at entry and exit, respectively) up to about 115 km, where the pressure drops to ~1.2 μbar. Meanwhile, Sicardy et al. (2016) derive a consistent surface pressure of 12.7 μbar, with error domains that are discussed later.

This said, the DO15-type thermal profile for the stratosphere (also called inversion layer) that extends between the surface and the temperature maximum at r = 1215 km is assumed to have a hyperbolic shape. The DO15 profile stops at its bottom at the point where it crosses the vapor pressure equilibrium line, thus defining the surface (assuming no troposphere). While the adopted functional form captures the gross structure of the thermal profile, it remains arbitrary. In fact, as the error bars of the REX profiles decrease with decreasing altitude, it becomes clear that the DO15 profile overestimates the temperature by tens of degrees (compared to REX) in the stratosphere as one approaches the surface. Also, it ends up at the surface with a thermal gradient (16 K km^{-1}, see Fig. 8) that is much stronger than in the REX profiles, where it is always less that 10 K km^{-1} in the stratosphere.

In that context, we have tested the REX profiles after modifying our ray tracing procedure to generate new synthetic central flashes. We now account for the fact that the two stellar images that travel along Pluto's limb probe different density profiles. To simplify as much as possible the problem, we assume that the stellar images that follow the northern and southern limbs probe an atmosphere that, respectively, has the entry and exit REX density profiles, in conformity with the geometry described in Fig. 6. This is an oversimplified approach as the stellar images actually scan rather large portions of the limb, not just the REX entry and exit points (Fig. 6). However, this exercise allows us to assess how different density profiles may affect the shape of the central flash. To ensure smooth synthetic profiles, the discrete REX points have been interpolated by spline functions, us-

Table 3. Regions probed by the central flash (June 29, 2015) and REX experiment (July 14, 2015)

	Time (UT)[1]	Location on surface	Local solar time[2]
June 29, 2015			
Bootes-3, primary image	16:52:54.8	186.8°E, 18.5°S	7.67 (sunrise)
Bootes-3, secondary image	16:52:54.8	6.8°E, 18.5°N	19.67 (sunset)
Dunedin, primary image	16:52:56.0	8.6°E, 19.7°N	19.79 (sunset)
Dunedin, secondary image	16:52:56.0	188.6°E, 19.7°S	7.79 (sunrise)
New Horizons radio experiment (REX), July 14, 2015			
entry	12:45:15.4	193.5°E, 17.0°S	16.52 (sunset)
exit	12:56:29.0	15.7°E, 15.1°N	4.70 (sunrise)

Notes. [(1)] For the ground-based observations, this is the time of closest approach to shadow center (Sicardy et al. 2016), for the REX experiment, this the beginning and end of occultation by the solid body (Hinson et al. 2017). [(2)] One "hour" corresponds to a rotation of Pluto of 15°. A local time smaller (resp. larger) than 12.0 h means morning (resp. evening) limb.

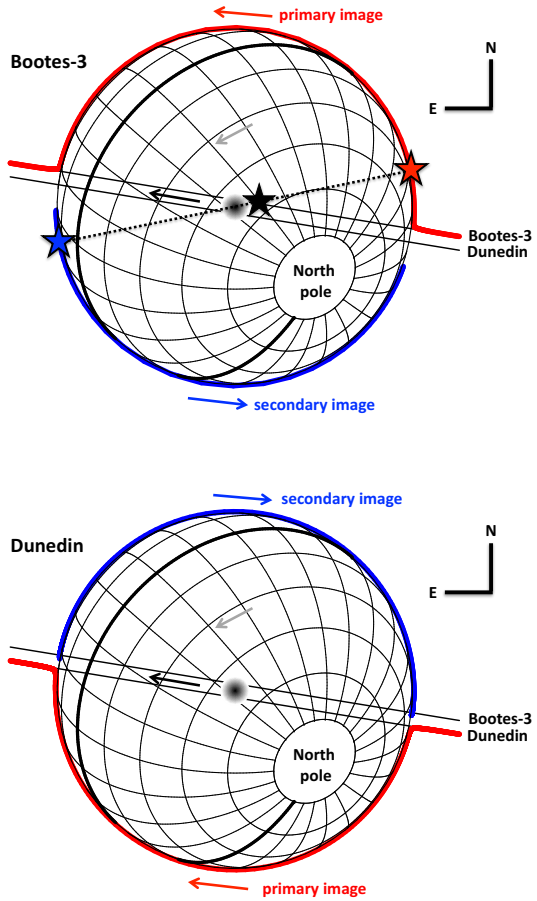

Fig. 5. The reconstructed geometry of the June 29, 2015 Pluto stellar occultation. Celestial north is at top and celestial east at left, see labels N and E. The equator and prime meridian (facing Charon) are drawn as thicker lines. The direction of Pluto's rotation is along the gray arrow. In the two panels, the stellar motion relative to Pluto is shown as black solid lines as seen from the Bootes-3 and Dunedin stations, with direction of motion marked by the black arrow. The shaded region at center roughly indicates the zone where a central flash could be detected. The red and blue lines are the trajectories of, respectively, the primary and secondary stellar images as seen from Bootes (upper panel) and Dunedin (lower panel). For a spherical atmosphere, the position of the star in the sky plane, the center of Pluto and the two images are aligned, as shown in the upper panel (see the dotted line connecting the star symbols).

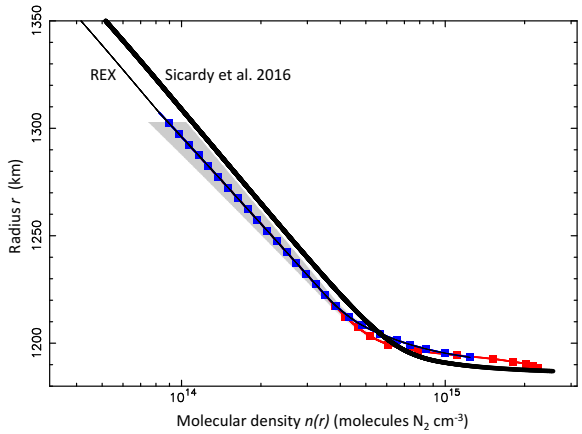

Fig. 7. Red and blue squares: the REX radio occultation N_2 density profiles, with the shaded area indicating the 1σ error bar domain (Hinson et al. 2017). Below 1220 km, the errors decrease and become unnoticeable in this plot. The entry (resp. exit) profile is given from $r = 1188.4$ km (resp. 1193.4 km), up to 1302.4 km, where the error bars become too large for a reliable profile to be retrieved. Note that by construction, the REX entry and exit profiles are *identical* for $r > 1220$ km. Below that radius, the two profiles diverge significantly, due to different physical conditions of the boundary layer just above the surface (Fig. 8). The solid red and blue lines connecting the squares are spline interpolations of the REX profiles that are used in our ray tracing code, see text. The REX profile is extended above $r = 1302.4$ km as a thin solid line, by adopting a scaled version of the June 29, 2015 profile (i.e. a mere translation of the thick solid line in this $(\log_{10}(n), r)$ plot), while ensuring continuity with the REX profile. Thick solid line: the profile derived by Sicardy et al. (2016) using the DO15 light curve fitting model. The formal 1σ error bar of this profile is smaller than the thickness of the line, but does not account for possible biases, see text.

ing a vertical sampling of 25 meters. Finally, above the radius $r = 1302.4$ km, the REX profiles have been extrapolated using a scaled version of the DO15 profile (see details in Fig. 7).

Because we want to test the shape of the central flash only, we restrict the generation of the synthetic light curves to the bottom parts of the occultation. We also include in the fit two intervals that bracket the event outside the occultation, where we know that the flux must be unity (Fig. 10). Those external parts do not discriminate the various models, but serve to scale properly the general stellar drop. Thus, the steep descents and ascents of the occultation light curves are avoided, as they would provide

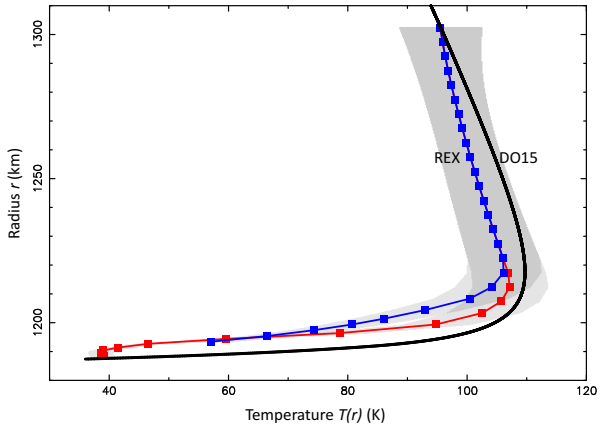

Fig. 8. The same as in Fig. 7 for the temperature profiles $T(r)$. By construction, the REX profile uses a boundary condition $T_b = 95.5$ km at the reference radius $r_b = 1302.4$ km, in order to connect it to the DO15 profile (solid black line). Thus, the intersection of the REX and DO15 profiles at r_b is a mere result of the choice of T_b, not a measurement. There is no formal error bars on the Sicardy et al. 2016's temperature profile, as most of the errors come in this case from biases, see text.

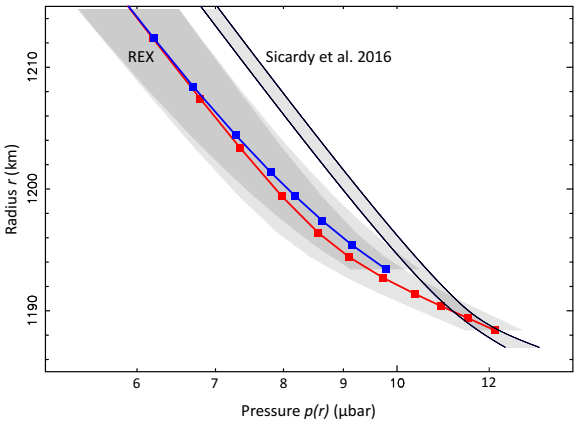

Fig. 9. The same as in Fig. 7, but for the pressure profiles $p(r)$. The gray region encompassing the Sicardy et al. 2016's profile and delimited by thin solid lines is the uncertainty domain discussed by those authors.

too much weight to the fits. Finally, since no calibrations of the light curves are available to assess Pluto's contribution ϕ_P to the observed flux, a linear least-square fit of the synthetic flux to the data has been performed before calculating the residuals. This introduces a supplementary adjustable parameter, ϕ_P to the fits.

Four simple scenarios are considered. (1) We first use the original model of Sicardy et al. (2016) to generate the light curves. (2) We take the REX density profiles at face value and use the modified ray tracing model described above, fixing Pluto's ephemeris offset as determined in case (1). (3) We apply an adjustable, uniform scaling factor f to the two REX density profiles, and we adjust Pluto's ephemeris offset accordingly. (4) Turning back to the REX density profiles of case (2), we assume that a topographic feature of height h (on top of the REX exit radius, 1192.4 km) blocks the stellar image generated by the REX exit profile, i.e. that the stellar image that travels along the southern limb (Fig. 5) is turned off below a planetocentric radius $1192.4 + h$ km.

The fits are displayed in Fig. 10. Their qualities are estimated through the χ^2 value. Depending on the fits, there are 1 to 3 free parameters (the pressure at a prescribed level, off-track displacement of Pluto with respect to its ephemeris and Pluto's contribution ϕ_P to the flux). In all the fits, there are $N = 217$ data points adjusted. Note that the value of h in case (4) has been fixed to 1.35 km, i.e. is not an adjustable parameter. This is discussed further in the points below:

1. The nominal temperature profile $T(r)$ of Sicardy et al. (2016) with surface pressure $p_{\rm surf} = 12.7$ μbar provides a satisfactory fit with $\chi^2 = 198$ ($\chi^2_{\rm dof} = 0.924$ per degree of freedom). In this case, the Bootes-3 and Dunedin stations passed 46 km north and 45 km south of the shadow center, respectively.
2. The nominal REX profiles result in flashes that are too high compared to the observations, as noted by a visual inspection of the figure (and from $\chi^2 = 326$, $\chi^2_{\rm dof} = 1.52$). This can be fixed by introducing haze absorption. A typical factor of 0.7 must be applied to the Bootes-3 synthetic flash in order to match the data, while a typical factor of 0.76 must be applied to the Dunedin synthetic flash. This corresponds to typical tangential optical depths (along the line of sight) in the range $\tau_T = 0.27 - 0.35$, for rays that went at about 8 km above the REX 1187.4 km radius. Changing Pluto's off-track offset does not help in this case, as one synthetic flash increases while the other decreases. This could be accommodated by adjusting accordingly the optical depths τ_T, but this introduces too many adjustable parameters to be relevant.
3. A satisfactory best fit is obtained ($\chi^2 = 214$, $\chi^2_{\rm dof} = 0.999$) by reducing uniformly the REX pressure profiles by a factor of 0.805 and by moving Pluto's shadow center cross-track by 17 km north with respect to Case (1), the Bootes-3 and Dunedin stations passing 29 km north and 62 km south of the shadow center, respectively. Note that a satisfactory fit to the Bootes-3 flash is obtained, while the Dunedin synthetic flash remains a bit too high.
4. Using again the nominal REX profiles of case (2), but imposing a topographic feature of height $h = 1.35$ km on top of the REX exit radius of 1192.4 km, a satisfactory fit to the Bootes-3 flash is obtained ($\chi^2 = 205$, $\chi^2_{\rm dof} = 0.959$), in fact the best of all fits for that station. Meanwhile, the Dunedin synthetic flash remains a bit too high compared to observations. In this model, Pluto's shadow center has been moved cross-track by 19.5 km north with respect to the first model, so that the Bootes-3 and Dunedin stations passed 26.5 km north and 64.5 km south of the shadow center, respectively. The particular choice of $h = 1.35$ km stems from the fact that lower values would increase even more the Dunedin flash, while higher values would decrease too much the Bootes-3 flash. We have not explored further other values of h by tweaking the density profiles. So, this is again an exercise to show that reasonably high topographic features may explain the observed flash.

5. Concluding remarks

5.1. Pluto's global atmospheric evolution

Fig. 4 summarizes our results concerning the evolution of Pluto's atmospheric pressure with time. It shows that the observed trend

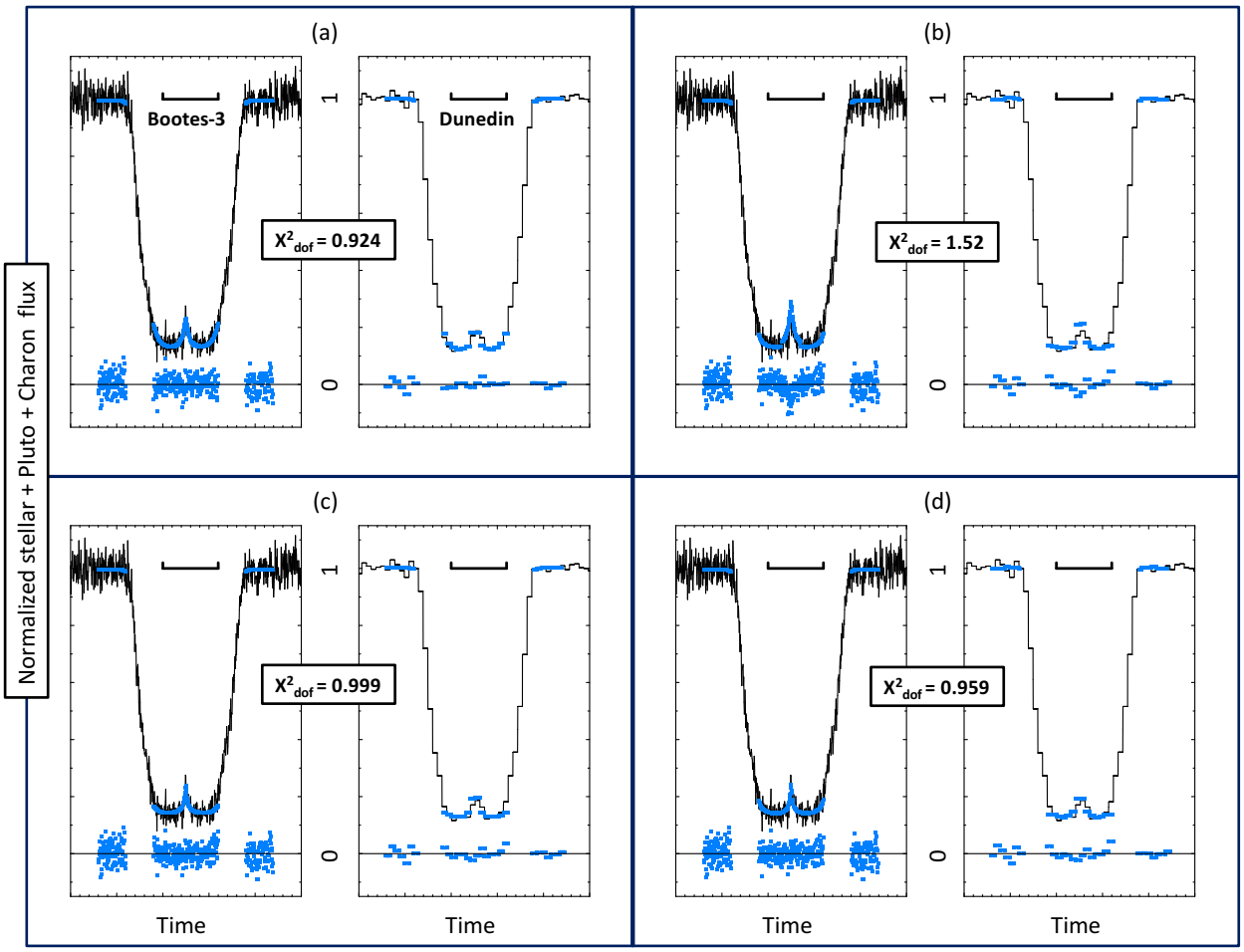

Fig. 10. In each panel, the synthetic fits to the Bootes-3 (left) and Dunedin (right) observations of June 29, 2015 are shown as blue points, together with the residuals (observations minus model) under each light curve. The tick marks on the time axis are plotted every 10 s, and the horizontal bars above each curve show the one-minute interval from 16h 52m 30 to 16h 53m 30s UT. (a) The best fits to the Bootes-3 and Dunedin light curves using the DO15 light curve fitting model (Sicardy et al. 2016), see also Figs. 7-8. (b) The same but using the nominal REX density profile. Note that the synthetic flashes are too high at both stations. (c) The same, after multiplying the REX density profiles by a factor $f = 0.805$ and moving Pluto's shadow 17 km north of the solution of Sicardy et al. (2016). (d) The same using the nominal REX profiles, but with a topographic feature of height $h = 1.35$ km that blocks the stellar image during part of its motion along the southern Pluto limb (Fig. 5). Pluto's shadow has now been moved by 19.5 km north of the solution of Sicardy et al. (2016). In each panel, the value of the χ^2 function per degree of freedom ($\chi^2_{\rm dof}$) provides an estimation of the quality of the fit, see text for discussion.

can be explained by adjusting Pluto's physical parameters in a rather restrictive way.

As noted in Section 3, this evolution is consistent with the continuous increase of pressure observed since 1988 (a factor of almost three between 1988 and 2016). It results from the heating of the nitrogen ice in Sputnik Planitia and in the northern mid-latitudes, when the areas are exposed to the Sun (just after the northern spring equinox in 1989) and when Pluto is near the Sun (Bertrand & Forget 2016). The model also predicts that atmospheric pressure is expected to reach its peak and drop in the next few years, due to

(1) the orbitally-driven decline of insolation over Sputnik Planitia and the northern mid-latitude deposits, and

(2) the fact that nitrogen condenses more intensely in the colder southern part of Sputnik Planitia, thus precipitating and hastening the pressure drop.

In that context, it is important to continue the monitoring of Pluto's atmosphere using ground-based stellar occultations. Unfortunately, as Pluto moves away from the Galactic plane, such occultations will become rarer and rarer.

5.2. Pluto's lower atmosphere

The models presented in the Section 4 and illustrated in Fig. 10 are not unique and not mutually exclusive. For instance, one can have at the same time a topographic feature blocking the stellar rays, together with some haze absorption. Also, hazes, if present, will not be uniformly distributed along the limb. Similarly, topographic features will probably not be uniformly distributed along the limb, but rather, have a patchy structure that complicates our analysis. In spite of their limitations, the simple scenarios presented above teach us a few lessons:

(1) Although satisfactory in terms of flash fitting, the nominal temperature profile of Sicardy et al. (2016) can probably be ruled out below the planetocentric radius $\sim$ 1215 km, since it is clearly at variance with the REX profiles (Fig. 8), while probing essentially the same zones on Pluto's surface (Fig. 6).

(2) The REX profiles taken at face value cannot explain the central flashes observed at Bootes-3 and Dunedin, unless hazes are present around the $\sim$ 8 km altitude level, with optical depths along the line of sight in the range $\tau = 0.27$-0.35. This is higher but consistent with the reported value of $\tau \sim 0.24$ derived from NH image analysis (Gladstone et al. 2016; Cheng et al. 2017). In fact, the two values are obtained by using quite different meth-

ods. Cheng et al. (2017) assume tholin-like optical constant, which is not guaranteed. Moreover, their 0.24 value is the scattering optical depth, while we measure the aerosol extinction (absorption plus scattering). Chromatic effects might also be considered to explain those discrepancies, as the Bootes-3, Dunedin and the NH instruments have different spectral responses. Our data are too fragmentary, though, to permit such a discussion.

(3) An alternative solution is to reduce uniformly the REX pressures by a factor 0.805, which would bring the surface values at $p_{\rm surf} = 12.8 \times 0.805 = 10.3$ μbar at entry and $p_{\rm surf} = 10.2 \times 0.805 = 8.21$ μbar at exit. This is at 3.6σ and 2.8σ away from the nominal REX results, respectively, considering the error bars of ± 0.7 μbar quoted by Hinson et al. (2017), and thus statistically possible. It poses a problem, though, as the underdense versions of the REX profiles disagree formally (i.e. beyond the internal error bars of the DO15 light curve fitting model) when extrapolated to the overlying half-light level around $r = 1300$ km. A remedy would be to patch up ground-based-derived profiles with the underdense REX profiles, and re-run global fits. This remains out of the scope of the present analysis.

(4) The topographic feature hypothesis remains an attractive alternative, as it requires modest elevation (a bit more than 1 km) above the REX exit region, that is known to be higher than the entry region, Spunik Planitia. A more detailed examination of Pluto's elevation maps, confronted with the stellar paths shown in Fig. 6, should be undertaken to confirm or reject that hypothesis. This said, such ± 1 km topographic variations are actually observed all over Pluto's surface (Schenk et al. 2018b).

As a final comment, we recall that the flashes have been generated by assuming a spherical atmosphere near Pluto's surface. There is no sign of distortion of the Bootes-3 and Dunedin flashes that suggests a departure from sphericity. It would be useful, however to assess such departures, or at least establish an upper limit for them in future works.

Acknowledgements. This article is dedicated to the memory of H.-J. Bode, J. Greenhill and O. Faragó for their long-standing support and participation to occultation campaigns. The work leading to this results has received funding from the European Research Council under the European Community's H2020 2014-2020 ERC Grant Agreement n° 669416 "Lucky Star". EM thanks support from Concytec-Fondecyt-PE and GA, FC-UNI for providing support during the 2012 July 18 occultation. BS thanks Ph. Beaulieu for helping us accessing to the Hobart Observatory facilities and B. Warner, B. L. Gary, C. Erickson, H. Reitsema, L. Albert, P. J. Merritt, T. Hall, W. J. Romanishin, Y. J. Choi for providing data during the 2007 March 18 occultation. MA thanks support from the CNPq (Grants 473002/2013-2 and 308721/2011-0) and FAPERJ (Grant E-26/111.488/2013). FBR acknowledges CNPq support process 309578/2017-5. TRAPPIST-North is a project funded by the University of Liège, in collaboration with Cadi Ayyad University of Marrakech (Morocco). TRAPPIST-South is a project funded by the Belgian Fonds (National) de la Recherche Scientifique (F.R.S.-FNRS) under grant FRFC 2.5.594.09.F, with the participation of the Swiss National Science Foundation (FNS/SNSF). KG acknowledges help from the team of Archenhold-Observatory, Berlin, and AR thanks G. Román (Granada) for help during the observation of the 2016 July 19 occultation. AJCT acknowledges support from the Spanish Ministry Project AYA2015-71718-R (including EU funds). We thank Caisey Harlingten for the repeated use of his 50 cm telescopes in San Pedro de Atacama, Chile. Based on observations made with the Italian Telescopio Nazionale Galileo (TNG) operated on the island of La Palma by the Fundación Galileo Galilei of the INAF (Istituto Nazionale di Astrofisica) at the Spanish Observatorio del Roque de los Muchachos of the Instituto de Astrofisica de Canarias. L.M. acknowledges support from the Italian Minister of Instruction, University and Research (MIUR) through FFABR 2017 fund. L.M. acknowledges support from the University of Rome Tor Vergata through "Mission: Sustainability 2016" fund. The Astronomical Observatory of the Autonomous Region of the Aosta Valley (OAVdA) is managed by the Fondazione Clément Fillietroz-ONLUS, which is supported by the Regional Government of the Aosta Valley, the Town Municipality of Nus and the "Unité des Communes valdôtaines Mont-Émilius". The research was partially funded by a 2016 "Research and Education" grant from Fondazione CRT.

References

Assafin, M., Camargo, J. I. B., Vieira Martins, R., et al. 2010, A&A, 515, A32
Assafin, M., Camargo, J. I. B., Vieira Martins, R., et al. 2012, A&A, 541, A142
Benedetti-Rossi, G., Vieira Martins, R., Camargo, J. I. B., Assafin, M., & Braga-Ribas, F. 2014, A&A, 570, A86
Bertrand, T. & Forget, F. 2016, Nature, 540, 86
Bertrand, T., Forget, F., Umurhan, O. M., et al. 2018, Icarus, 309, 277
Binzel, R. 1990, in baas, Vol. 22, Bulletin of the American Astronomical Society, 1128
Boissel, Y., Sicardy, B., Roques, F., et al. 2014, A&A, 561, A144
Bosh, A. S., Person, M. J., Levine, S. E., et al. 2015, Icarus, 246, 237
Brosch, N. 1995, MNRAS, 276, 571
Cheng, A. F., Summers, M. E., Gladstone, G. R., et al. 2017, Icarus, 290, 112
Dias-Oliveira, A., Sicardy, B., Lellouch, E., et al. 2015, ApJ, 811, 53
Elliot, J. L., Ates, A., Babcock, B. A., et al. 2003, Nature, 424, 165
Elliot, J. L., Dunham, E. W., Bosh, A. S., et al. 1989, Icarus, 77, 148
Forget, F., Bertrand, T., Vangvichith, M., et al. 2017, Icarus, 287, 54 , special Issue: The Pluto System
Fray, N. & Schmitt, B. 2009, Planet. Space Sci., 57, 2053
French, R. G., Toigo, A. D., Gierasch, P. J., et al. 2015, Icarus, 246, 247
Gladstone, G. R., Stern, S. A., Ennico, K., et al. 2016, Science, 351, aad8866
Hansen, C., Paige, D., & Young, L. 2015, Icarus, 246, 183 , special Issue: The Pluto System
Hansen, C. J. & Paige, D. A. 1996, Icarus, 120, 247
Hinson, D. P., Linscott, I. R., Young, L. A., et al. 2017, Icarus, 290, 96
Hubbard, W. B., Hunten, D. M., Dieters, S. W., Hill, K. M., & Watson, R. D. 1988, Nature, 336, 452
Lellouch, E., de Bergh, C., Sicardy, B., et al. 2015, Icarus, 246, 268
Lellouch, E., Gurwell, M., Butler, B., et al. 2017, Icarus, 286, 289
Lellouch, E., Sicardy, B., de Bergh, C., et al. 2009, A&A, 495, L17
Lellouch, E., Stansberry, J., Emery, J., Grundy, W., & Cruikshank, D. P. 2011, Icarus, 214, 701
Millis, R. L., Wasserman, L. H., Franz, O. G., et al. 1993, Icarus, 105, 282
Nimmo, F., Umurhan, O., Lisse, C. M., et al. 2017, Icarus, 287, 12
Olkin, C. B., Young, L. A., Borncamp, D., et al. 2015, Icarus, 246, 220
Schenk, P., Beyer, R., Moore, J., et al. 2018a, in Lunar and Planetary Science Conference, Vol. 49, Lunar and Planetary Science Conference, 2300
Schenk, P. M., Beyer, R. A., McKinnon, W. B., et al. 2018b, Icarus, 314, 400
Schmitt, B., Philippe, S., Grundy, W., et al. 2017, Icarus, 287, 229 , special Issue: The Pluto System
Sicardy, B., Bolt, G., Broughton, J., et al. 2011, AJ, 141, 67
Sicardy, B., Colas, F., Widemann, T., et al. 2006, Journal of Geophysical Research (Planets), 111, E11S91
Sicardy, B., Talbot, J., Meza, E., et al. 2016, ApJ, 819, L38
Sicardy, B., Widemann, T., Lellouch, E., et al. 2003, Nature, 424, 168
Stern, S. A., Bagenal, F., Ennico, K., et al. 2015, Science, 350, aad1815
Tholen, D. J., Buie, M. W., Grundy, W. M., & Elliott, G. T. 2008, AJ, 135, 777
Toigo, A. D., Gierasch, P. J., Sicardy, B., & Lellouch, E. 2010, Icarus, 208, 402
Washburn, E. W. 1930, International Critical Tables of Numerical Data: Physics, Chemistry and Technology. (Vol. 7, McGraw-Hill, New York, 1930)
Yelle, R. V. & Elliot, J. L. 1997, Atmospheric Structure and Composition: Pluto and Charon, ed. S. A. Stern & D. J. Tholen, 347
Young, E. F., French, R. G., Young, L. A., et al. 2008, AJ, 136, 1757
Young, L. A. 2012, Icarus, 221, 80
Young, L. A. 2013, ApJ, 766, L22

[1] LESIA, Observatoire de Paris, PSL Research University, CNRS, Sorbonne Université, UPMC Univ. Paris 6, Univ. Paris Diderot, Sorbonne Paris Cité
e-mail: Erick.Meza@obspm.fr
[2] Observatório do Valongo/UFRJ, Ladeira Pedro Antonio 43, Rio de Janeiro, RJ 20080-090, Brazil
[3] Instituto de Astrofísica de Andalucía (IAA-CSIC). Glorieta de la Astronomía s/n. 18008-Granada, Spain
[4] National Aeronautics and Space Administration (NASA), Ames Research Center, Space Science Division, Moffett Field, CA 94035, United States
[5] Laboratoire de Météorologie Dynamique, IPSL, Sorbonne Université, UPMC Univ. Paris 06, CNRS, 4 place Jussieu, 75005 Paris, France
[6] IMCCE/Observatoire de Paris, CNRS UMR 8028, 77 Avenue Denfert Rochereau, 75014 Paris, France
[7] Université de Lille, Observatoire de Lille, 1, impasse de l'Observatoire, F-59000 Lille, France.

[8] Southwest Research Institute, Dept. of Space Studies, 1050 Walnut Street, Suite 300, Boulder, CO 80302, United States
[9] Federal University of Technology - Paraná (UTFPR/DAFIS), Rua Sete de Setembro 3165, CEP 80230-901 Curitiba, Brazil
[10] Observatório Nacional/MCTIC, Laboratório Interinstitucional de e-Astronomia-LIneA and INCT do e-Universo, Rua General José Cristino 77, Rio de Janeiro CEP 20921-400, Brazil
[11] Geneva Observatory, 1290 Sauverny, Switzerland
[12] Astronomical Institute (ASÚ AVČR), Fričova 298, Ondřejov, Czech Republic
[13] Institute of Physics (FZÚ AVČR), Na Slovance 2, Prague, Czech Republic
[14] National Institute of Water and Atmospheric Research (NIWA), Lauder, New Zealand
[15] Occultation Section of the Royal Astronomical Society of New Zealand (RASNZ), Wellington, New Zealand
[16] Dunedin Astronomical Society, Dunedin, New Zealand
[17] ESO (European Southern Observatory) - Alonso de Cordova 3107, Vitacura, Santiago, Chile
[18] Space sciences, Technologies & Astrophysics Research (STAR) Institute, University of Liège, Liège, Belgium
[19] Physics and Astronomy Department, Appalachian State University, Boone, North Carolina 28608, United States
[20] Department of Physics and Astronomy, University of North Carolina - Chapel Hill, North Carolina 27599, United States
[21] San Pedro de Atacama Celestial Explorations, San Pedro de Atacama, Chile
[22] Grupo de Ciencias Planetarias, Departamento de Geofísica y Astronomía, Facultad de Ciencias Exactas, Físicas y Naturales, Universidad Nacional de San Juan, Argentina
[23] Department of Physics and Astronomy, University of Sheffield, Sheffield S3 7RH, United Kingdom
[24] Department of Physics, University of Warwick, Coventry CV4 7AL, United Kingdom
[25] Large Binocular Telescope Observatory, 933 N Cherry Av, Tucson, AZ 85719, United States
[26] Internationale Amateursternwarte (IAS) e. V., Bichler Straße 46, D-81479 München, Germany
[27] International Occultation Timing Association – European Section (IOTA-ES), Am Brombeerhag 13, D-30459 Hannover, Germany
[28] International Occultation Timing Association (IOTA), PO Box 7152, Kent, WA 98042, USA
[29] Canberra Astronomical Society, Canberra, ACT, Australia
[30] Western Sydney Amateur Astronomy Group (WSAAG), Sydney, NSW, Australia
[31] Kuriwa Observatory, Sydney, NSW, Australia
[32] Astronomical Association of Queensland, QLD, Australia
[33] Euraster, 1 rue du Tonnelier 46100 Faycelles, France
[34] School of Physical Sciences, University of Tasmania, Private Bag 37, Hobart, TAS 7001, Australia
[35] Lowell Observatory, 1400 W Mars Hill Rd, Flagstaff, AZ 86001, United States
[36] Department of Astronomy, Wellesley College, Wellesley, MA 02481, United States
[37] NYU-Center for Urban Science & Progress, NYU-Center for Cosmology & Particle Physics, 370 Jay Street, Brooklyn, NY 11201, United States
[38] SETI Institute, Carl Sagan Center, 189 Bernardo Av., Mountain View, CA 94043, United States
[39] School of Physics & Astronomy and Wise Observatory, Tel Aviv University, Tel Aviv 6997801, Israel
[40] Department of Earth and Planetary Sciences, Weizmann Institute of Science, Rehovot 0076100, Israel
[41] Oukaimeden Observatory, LPHEA, FSSM, Cadi Ayyad University, Marrakech Morocco
[42] Bankstown, 115 Oxford Avenue, Sydney 2200, New South Wales, Australia
[43] Craigie, 295 Camberwarra Drive, West Australia 6025, Australia
[44] Stockport Observatory, Astronomical Society of South Australia, Stockport, SA, Australia
[45] University of Canterbury, Mt. John Observatory, P.O. Box 56, Lake Tekapo 7945, New Zealand
[46] Wellington Astronomical Society (WAS), Wellington, New Zealand
[47] BOSS - Backyard Observatory Supernova Search, Southland Astronomical Society, New Zealand
[48] Université Côte d'Azur, Observatoire de la Côte d'Azur, CNRS, Laboratoire Lagrange, Bd de l'Observatoire CS 34229 - 06304 NICE Cedex 4, France
[49] INAF-Telescopio Nazionale Galileo, Rambla J.A. Fernández Pérez, 7, 38712 Breña Baja, Spain
[50] Instituto de Astrofísica de Canarias, C/ Vía Láctea, s/n, 38205 La Laguna, Spain
[51] INAF Osservatorio Astronomico di Cagliari, Via della Scienza 5 - 09047 Selargius CA, Italy
[52] Section of Astrophysics, Astronomy and Mechanics, Department of Physics, National and Kapodistrian University of Athens, GR-15784 Zografos, Athens, Greece
[53] Astronomical Observatory of the Autonomous Region of the Aosta Valley, Aosta - Italy
[54] Astronomical Observatory, Dipartimento di Scienze Fisiche, della Terra e dell'Ambiente, University of Siena, Italy
[55] INAF - Catania Astrophysical Observatory, Italy
[56] Department of Physics, University of Rome Tor Vergata, Via della Ricerca Scientifica 1, I-00133 – Roma, Italy
[57] Max Planck Institute for Astronomy, Königstuhl 17, D-69117 – Heidelberg, Germany
[58] INAF – Astrophysical Observatory of Turin, Via Osservatorio 20, I-10025 – Pino Torinese, Italy
[59] International Institute for Advanced Scientific Studies (IIASS), Via G. Pellegrino 19, I-84019 – Vietri sul Mare (SA), Italy
[60] Archenhold Sternwarte, Alt-Treptow 1, 12435 Berlin, Germany
[61] Schwäbische Sternwarte e.V., Zur Uhlandshöhe 41, 70188 Stuttgart, Germany
[62] Astronomie Stiftung Trebur, Fichtenstr. 7, 65468 Trebur, Germany
[63] University of Applied Sciences, Technische Hochschule Mittelhessen, Wilhelm-Leuschner-Straße 13, D-61169 Friedberg, Germany
[64] Roof Observatory Kaufering, Lessingstr. 16, D-86916 Kaufering, Germany
[65] Medical University of Bialystok, Faculty of Medicine, 15-089 Bialystok, Poland
[66] Hieronymusstr. 15b, 81241, München, Germany
[67] Stallhofen Observatory, Graz, Austria
[68] Software Engineering Department, University of Granada, Fuente Nueva s/n 18071 Granada, Spain
[69] Sociedad Astronómica Granadina (SAG), Apartado de Correos 195, 18080 Granada, Spain
[70] Raptor Photonics Llt, Willowbank Business Park, Larne Co. Antrim BT40 2SF Northern Ireland
[71] AiryLab SARL, 34 rue Jean Baptiste Malon, 04800 Gréoux Les Bains
[72] Gamaya S.A. Batiment C, EPFL innovation park, CH-1015, Lausanne, Switzerland
[73] Université Clermont-Auvergne, 49 bd François Mitterrand, CS 60032, 63001 Clermont-Ferrand, France
[74] Teplice Observatory, Písečný vrch 2517, 415 01 Teplice, Czech Republic
[75] Institute of Astrophysics and Space Sciences, Observatório Astronómico de Lisboa, Ed. Leste, Tapada da Ajuda, 1349-018 Lisbon, Portugal
[76] Agrupación Astronómica de Sabadell, Carrer Prat de la Riba, s/n, 08206 Sabadell, Catalonia, Spain
[77] Osservatorio Astronomico Universitá di Siena, Via Roma 56, 53100 Siena, Italy
[78] Osservatorio Elianto, via Vittorio Emanuele III, 84098 Pontecagnano, Italy
[79] Télescope Jean-Marc Salomon, Planète Sciences, Buthiers, 77060, France
[80] Club Astro de Mars, Maison communale 07320 Mars, France
[81] Observatoire des Baronnies Provenaçles, 05150 Moydans, France

[82] GAPRA, 2 rue Marcel Paul, 06160 Antibes, France
[83] Osservatorio Astronomico di Monte Agliale, Cune, 55023 Borgo a Mozzano, Lucca, Italy
[84] Balcon des Étoiles du pays toulousain, observatoire des Pléiades, 31310 Latrape, France
[85] Cloudbait Observatory, Colorado, United States
[86] Calvin College, United States
[87] Dept. of Geology and Geophysics, University of Wyoming, Laramie, WY 82071, United States

6. Circumstances of Observations

Putting the long table in the appendix environment does not work well! I force Latex to proceed forward and get some ~acceptable results.

Appendix A: Reconstructed geometries of the occultations

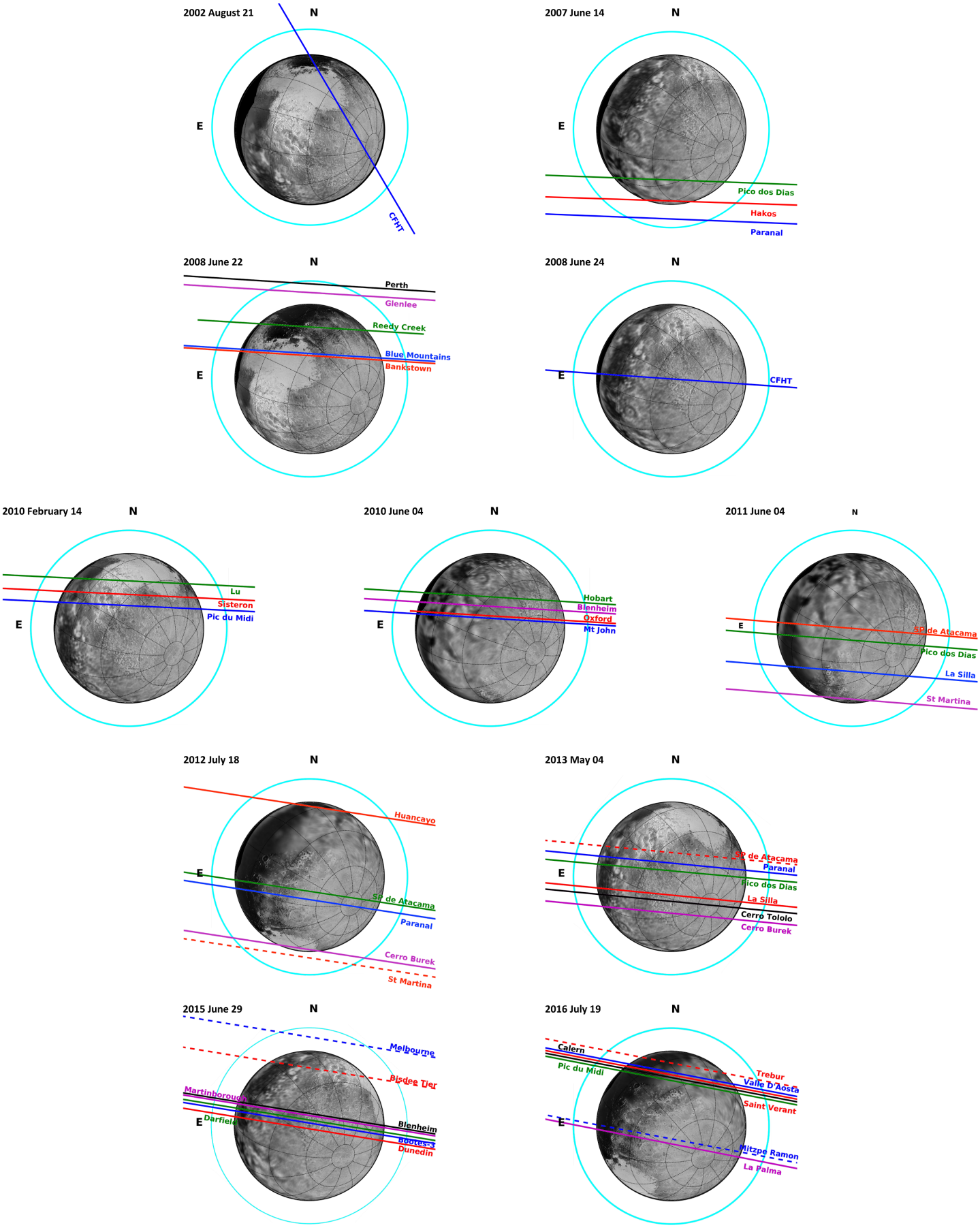

Fig. A.1. The occultation geometries reconstructed from the fits shown in Figs. 2 and 3. Labels N and E show the J2000 celestial north and east directions, respectively. The cyan circle corresponds to the 1% stellar drop, the practical detection limit for the best data sets. The purpose of the dashed lines is to distinguish between lines with the same color, and have no other meaning. In the background, a Pluto map taken by NH during its flyby.

Table 4. Circumstances of Observations

Site	Coordinates altitude (m)	Telescope Instrument/filter	Exp. Time/Cycle (s)	Observers
		DATE		
		2002 August 21		
CFHT	19 49 30.88 N	3.6m	1/1.583	C. Veillet
Hawaii	155 28 07.52 W	I (0.83 ± 0.1 μm)		
	4200			
		2007 June 14		
Pico dos Dias	22 32 7.80 S	1.6m	0.4/0.4	F. Braga-Ribas
Brazil	45 34 57.70 W	CCD/clear		D. Silva Neto
	1864			
Hakos	23 14 50.4 S	IAS 0.5m	1.373/1.373	M. Kretlow
Namibia	16 21 41.5 E	TC245 IOC/clear		
	1825.			
Paranal	24 37 39.44 S	UT1 8.2m	0.1/0.1	V. Dhillon
Chile	70 24 18.27 W	Ultracam/i'		S. Littlefair
	2635			A. Doressoundiram
Paranal	29 15 16.59 S	VLT Yepun 8.2m	1/1	B. Sicardy
Chile	70 44 21.82 W	NACO/Ks		
	2315.			
		2008 June 22		
Bankstown	33 55 56 S	0.275m	1.28/1.28	T. Dobosz
Australia	151 01 45 E	video/clear		
	24.9			
Blue Mountains	33 39 51.9 S	0.25m	1.28/1.28	D. Gault
Australia	150 38 27.9 E	video/clear		
	286			
Reedy Creek	28 06 29.9 S	0.25m	6.30/8.82	J. Broughton
Australia	153 23 52.0 E	CCD/clear		
	65			
Glenlee	23 16 09.6 S	0.30m	0.12/012	S. Kerr
Australia	150 30 00.8 E	video/clear		
	50			
Perth	31 47 21.5 S	0.25m		G. Bolt
Australia	115 45 31.3 E	CCD/clear	2.0	
	45		6.0	
		2008 June 24		
CFHT	19 49 30.88 N	3.6m	0.065/0.065	L. Albert
Hawaii	155 28 07.52 W	Wircam/K		
	4200			
		2010 February 14		
Pic du Midi	42 56 12.0 N	T1m	0.32/0.32	J. Lecacheux
France	00 08 31.9 E	CCD/clear		
	2862			
Lu	46 37 26.3 N	0.35m	0.35/0.50	C. Olkin,
Switzerland	10 22 00.3 E	video/clear		L. Wasserman
	1933			
Sisteron	44 05 18.20 N	0.3m	0.64/0.64	F. Vachier
France	05 56 16.3 E	Watec 120/clear		
	634			
		2010 June 04		
Mt John	43 59 13.6 S	1m	0.32/0.32	B. Loader,
New Zealand	170 27 50.2 E	CCD/clear		A. Gilmore, P. Kilmartin
	1020			
Hobart	42 50 49.83 S	1m	1/1	J. Greenhill,
Australia	147 25 55.32 E	Raptor/I		S. Mathers,
	38			
Blenheim	41 29 36.3 S	Bootes-3 0.6m	0.50/1.75	W. H. Allen
New Zealand	173 50 20.7 E	CCD/r'		
	37.5			
Blenheim	41 29 36.3 S	0.4m	2.5/6	W. H. Allen

Continued on next page

Table 4 – *Continued from previous page*

Site	Coordinates altitude (m)	Telescope Instrument/filter	Exp. Time/Cycle (s)	Observers
		DATE		
New Zealand	173 50 20.7 E 37.5	CCD/clear		
Oxford New Zealand	43 18 36.78 S 172 13 07.8 E 221	0.3m Video/clear	0.64/0.64	S. Parker
		2011 June 04		
Santa Martina Chile	33 16 09.0 S 45 34 57.70 W 1450	0.4m EMCCD/clear	2/2	R. Leiva
La Silla Chile	29 15 16.59 S 70 44 21.82 W 2315	TRAPPIST S 0.6m CCD/clear	3/4.4	E. Jehin
San Pedro de Atacama, Chile	22 57 12.3 S 68 10 47.6 W 2397	Caisey 0.5m CCD/clear	2/2.87	A. Maury
Pico dos Dias Brazil	22 32 7.80 S 45 34 57.70 W 1864	1.6m CCD/clear	0.1/0.1	M. Assafin
		2012 July 18		
Santa Martina Chile	33 16 09.0 S 45 34 57.70 W 1450	0.4m CCD/clear	1/1	R. Leiva
Cerro Burek Argentina	31 47 12.4 S 69 18 24.5 E 2591	ASH 0.45m CCD/clear	13/15.7	N. Morales
Paranal Chile	24 37 31.0 S 70 24 08.0 W 2635	VLT Yepun 8.2m NACO/H	0.2/0.2	J. Girard
San Pedro de Atacama, Chile	22 57 12.3 S 68 10 47.6 W 2397	ASH2 0.4m CCD/clear	13/15.44	N. Morales
Huancayo Peru	12 02 32.2 S 75 19 14.7 W 3344	0.20m CCD/clear	10.24/10.24 5.12/5.12	E. Meza
		2013 May 04		
Pico dos Dias Brazil	22 32 07.8 S 45 34 57.7 W 1,811	B&C 0.6m CCD/I	4.5/6	M. Assafin, A. Ramos Gomes Jr
Cerro Burek Argentina	31 47 14.5 S 69 18 25.9 W 2591	ASH 0.45 m CCD/clear	6/8	J.L. Ortiz
Cerro Tololo Chile	30 10 03.36 S 70 48 19.01 W 2207	PROMPT 0.4m P1, P3, P4, P5 CCD/clear	5/8 P3 offset 2 sec P4 offset 4 sec P5 offset 6 sec	J. Pollock
La Silla Chile	29 15 21.276 S 70 44 20.184 W 2336	Danish 1.54m Lucky Imager/Z (>650nm CCD/iXon response)	Lucky Imager 0.1/0.1	L. Mancini
La Silla Chile	29 15 16.59 S 70 44 21.82 W 2315	TRAPPIST S 0.6m CCD/clear	4.5/6	E. Jehin, A. Decock, M. Gillon, C. Opitom
Cerro Paranal Chile	24 37 31.0 S 70 24 08.0 W 2635.43	VLT Yepun 8.2m NACO/H	0.2/0.2	G. Hau
San Pedro de Atacama, Chile	22 57 12.3 S 68 10 47.6 W 2397	Caisey 0.5m f/8 CCD/V	3/4.58	A. Maury
San Pedro de Atacama, Chile	22 57 12.3 S 68 10 47.6 W	Caisey 0.5m f/6.8 CCD/B	4/4.905	L. Nagy

Continued on next page

Table 4 – *Continued from previous page*

Site	Coordinates altitude (m)	Telescope Instrument/filter	Exp. Time/Cycle (s)	Observers
		DATE		
		2015 June 29		
Lauder	45 02 17.39 S	Bootes-3/YA 0.60m	0.05633/0.05728	M. Jelínek
New Zealand	169 41 00.88 W	EMCCD/clear		*central flash detected*
	382			
Dunedin	45 54 31 S	0.35m	5.12/5.12	A. Pennell, S. Todd,
New Zealand	170 28 46 E	CCD/clear		M. Harnisch, R. Jansen
	136			*central flash detected*
Darfield	43 28 52.90 S	0.25m	0.32/0.32	B. Loader
New Zealand	172 06 24.40 E	CCD/clear		*central flash detected*
	210			
Blenheim 1	41 32 08.60 S	0.28m	0.64/0.64	G. McKay
New Zealand	173 57 25.10 E	CCD/clear		
	18			
Blenheim 2	41 29 36.27 S	04m	0.32/0.32	W. H. Allen
New Zealand	173 50 20.72 E	CCD/clear		
	38			
Martinborough	41 14 17.04 S	0.25m	0.16/0.16	P. B. Graham
New Zealand	175 29 01.18 E	CCD/ B		
	73			
Bisdee Tier	42 25 51.80 S	Greenhill H - 1.27m	0.1/0.1	A. A. Cole,
Australia	147 17 15.80 E	EMCCD/ B		B. Giles,
	641			K. M. Hill
Melbourne	37 50 38.50 S	0.20m	0.32/0.32	J. Milner
Australia	145 14 24.40 E	CCD/clear		
	110			
		2016 July 19		
Pic du Midi	42 56 12.0 N	1m	0.3/0.3	F. Colas,
France	00 08 31.9 E	EMCCD/clear		E. Meza
	2862			
Valle d'Aosta	45 47 22.00 N	0.81m	1/1	B. Sicardy
Italy	7 28 42.00 E	EMCCD/clear		A. Carbognani
	1674			
La Palma	28 45 14.4 N	TNG 3.58m	1/5	L. di Fabrizio, A. Magazzú
Spain	17 53 20.6 E	EMCCD/clear		V. Lorenzi, E. Molinari
	2387.2			
Saint Véran	44 41 49.88 N	0.5m	0.3/0.3	J.-E. Communal,
France	06 54 25.90 E	EMCCD/clear		S. de Visscher, F. Jabet,
	2936	0.62m	0.2/0.2	J. Sérot
		near IR camera/		
		RG 850 long pass		
Calern	43 45 13.50 N	C2PU T1m	0.3/0.3	D. Vernet, J.-P. Rivet,
France	06 55 21.80 E	CCD/clear		Ph. Bendjoya, M. Devogèle
	1264			
Mitzpe Ramon	30 35 44.40 N	0.28m	1/2.5	S. Kaspi, D. Polishook,
Israel	34 45 45.00 E	CCD/clear		N. Brosh, I. Manulis
	862			
Trebur	49 55 31.6 N	1m	0.3/0.3	J. Ohlert
Germany	08 24 41.1 E	CMOS/clear		
	90			
		Data sets not included in this work		
		2002 July 20		
Arica	18 26 53.8 S	0.3m	2/2	F. Colas
Chile	69 45 51.5 W	CCD/clear		
	2500			
		2006 June 12		
Stockport	34 19 55.31 S	0.50m	1.5/2	B. Lade
Australia	138 43 45.38 E	CCD/clear		

Continued on next page

Table 4 – *Continued from previous page*

Site	Coordinates altitude (m)	Telescope Instrument/filter	Exp. Time/Cycle (s)	Observers
	DATE			
	24			
Blue Montains Australia	33 39 51.9 S 150 38 27.9 E 286	0.25m CCD/clear	1/2	D. Gault
Hobart Australia	42 50 49.83 S 147 25 55.32 E 38	0.4m	1.6/1.6	W. Beisker A. Doressoudiram
		2007 March 18		
Catalina Mts. USA	32 25 00 N 110 43 57 W 2790	Kuiper 1.53m CCD/clear	0.68/0.68	T. Widemann
Palmer Divide USA	39 05 05 N 104 45 04 W 2302	0.35m CCD/clear	16.9/16.9	B. Warner
Calvin Rehoboth USA	35 31 32 N 108 39 23 W 2024	0.4m CCD/I	8.5/8.5	Lawrence A. Molnar
Cloudbait USA	38 47 10 N 105 29 01 W 2767	0.305m CCD/clear	29/29	C. Peterson
Hereford USA	31 27 08 N 110 14 16 W 1420	0.36m CCD/clear	3/5.1	B. Gary
Oklahoma USA	35 12 09 N 97 26 39 W 382	0.4m CCD/R+I	4/6.2	W. Romanishin
Mt Lemmon USA	32 26 32 N 110 47 19 W 2776	Kasi 1m CCD/I	17.6/17.6	Y.-J. Choi
		2007 June 09		
Cerro Pachón Chile	30 14 16.80 S 70 44 1.35 W 2715	SOAR 4.1m CCD/dual B & R	0.66/0.66	W. Beisker
		2008 August 25		
Lick USA	37 20 24.6 121 38 43.8 1281	Shane 3.0m IR mosaic/K	0.8/0.8	F. Marchis
Grands Rapids USA	42 55 50 N 85 35 18 W 253	0.4m CCD/I	10/13.3	Lawrence A. Molnar
		2010 May 19		
Paranal Chile	24 37 36.64 S 70 24 16.32 W 2635	VLT Melipal 8.2m ISAAC/Ks	0.5/0.5	B. Sicardy
La Silla Chile	29 15 32.1 S 70 44 0.15 W 2375	NTT 3.58m SOFI/Ks	0.5/0.5	V. D. Ivanov
Cerro Pachón Chile	30 14 16.80 S 70 44 1.35 W 2715	SOAR 4.1m CCD/clear	2.5/3.5	M. Assafin
		2011 June 23		
San Pedro Mártir Mexico	31 02 39 N 115 27 49 W 2800 m	2.1m IR mosaic/K	1/1.52	R. Howell
San Pedro Mártir Mexico	31 02 43.1 N 115 27 57.7 W 2811 m	0.84m CCD/clear	0.35/0.35	R. French
Hale A'a BB	19 09 29.6 N 155 45 19.1 W	0.6m CCD/clear	1/1	E. Young

Continued on next page

Table 4 – *Continued from previous page*

Site	Coordinates altitude (m)	Telescope Instrument/filter	Exp. Time/Cycle (s)	Observers
	DATE			
	1509 m			
Hale A'a CE	19 09 29.6 N	0.4m	1/1	C. Erickson
	155 45 19.1 W	CCD/clear		
	1509 m			
Haleakala	20 42 27.0 N	FTN 2m	0.093/0.09974	F. Bianco
	156 15 21.0 W	CCD/I		
	3055 m			
Kekaha	21 58 15.15 N	0.4m	0.3/0.3	T. Widemann
	159 43 21.558 W	CCD/clear		M. Buie, T. Hall
	20 m			
KEASA	21 59 05.7 N	0.35m	0.333/0.333	J. Merrit
	159 45 09.8 W	CCD/clear		
	10 m			
Maui	20 54 43.2 N	0.35m	1/1	H.-J. Bode
	156 41 28.9 W	CCD/clear		
	47 m	(partly cloudy)		
Majuro	07 04 06.6 N	0.4m	0.8/0.8	C. Olkin,
	171 17 39.8 W	CCD/I		H. Reitsema
	8 m			
		2012 June 14		
Marrakech	31 35 16.2 N	0.6m	0.5/0.5	S. Renner, Z. Benkhaldoun
Morocco	08 00 46.9 W	EMCCD/clear		M. Ait Moulay Larbi,
	494 m			A. Daassou, Y. El Azhari
Pico Veleta	37 03 51 N	1.52m	1.5/2	J. L. Ortiz
Spain	03 23 49 W	CCD/clear		
	2925			
		2016 July 14		
Oukameïden	31 12 23.2 N	TRAPPIST N 0.6m	2/3	S. Jehin, Z. Benkhaldoun
Morocco	07 51 59.3 W	CCD/clear		A. Daassou, Y. Moulane
	2720 m			
Pico Veleta	37 03 51 N	0.9m	2/3.5	J. L. Ortiz
Spain	03 23 49 W	CCD/clear		
	2925			
Granada	36 59 33.2 N	Dobson 0.6m	3.5/3.5	S. Alonso, D. Bérard
Spain	03 43 19.9 W	CCD/clear		A. Román
	1130			

A.1 Contributed papers

The contributed papers listed below correspond to my participation and analysis of Pluto stellar occultations. The articles corresponding to Chariklo and Haumea stem from my participation to the corresponding occultation campaigns, and to the derivation of some of the occultation light curves.

Astronomy & Astrophysics manuscript no. aa
December 10, 2018

Pluto's ephemeris from ground-based stellar occultations (1988-2016)

J. Desmars[1], E. Meza[1], B. Sicardy[1], M. Assafin[2], J. I. B. Camargo[3], F. Braga-Ribas[4,3], G. Benedetti-Rossi[3], A. Dias-Oliveira[3], B. Morgado[3], A. Ramos-Gomes Jr[3], R. Vieira-Martins[3], R. Behrend[5], J. L. Ortiz[6], A. Castro Tirado[6], R. Duffard[6], N. Morales[6], and P. Santos Sanz[6]

[1] LESIA, Observatoire de Paris, PSL Research University, CNRS, Sorbonne Université, UPMC Univ. Paris 6, Univ. Paris Diderot, Sorbonne Paris Cité
e-mail: josselin.desmars@obspm.fr
[2] Observatório do Valongo/UFRJ, Ladeira Pedro Antonio 43, Rio de Janeiro, RJ 20080-090, Brazil
[3] Observatório Nacional/MCTIC, Laboratório Interinstitucional de e-Astronomia-LIneA and INCT do e-Universo, Rua General José Cristino 77, Rio de Janeiro CEP 20921-400, Brazil
[4] Federal University of Technology - Paraná (UTFPR/DAFIS), Rua Sete de Setembro 3165, CEP 80230-901 Curitiba, Brazil
[5] Geneva Observatory, 1290 Sauverny, Switzerland
[6] Instituto de Astrofísica de Andalucía (IAA-CSIC). Glorieta de la Astronomía s/n. 18008-Granada, Spain

Received September XX, XXXX; accepted March XX, XXX

ABSTRACT

Context. From 1988 to 2016, several stellar occultations have been observed to study Pluto's atmosphere and its evolution (Meza et al. 2018). From these stellar occultations, an accurate astrometric position of Pluto at each occultation epoch is derived. These positions mainly depend on the position of the occulted star and the precision of the timing.
Aims. We present Pluto's astrometric positions derived from 18 occultations from 1988 to 2016. Using Gaia DR2 for the positions of the occulted stars, the precision of these positions is estimated to 2-10 milliarcsec depending on the observation circumstances. From these astrometric positions, we derive an ephemeris of Pluto's system barycentre using the NIMA code (Desmars et al. 2015).
Methods. The astrometric positions are mainly derived by fitting the occultations light curves. The fits provide an offset between the observed position of the body's centre and the ephemeris. Other publications usually provide circumstances of the occultation such as the coordinates of the stations, the timing, and the impact parameter (i.e. the closest distance between the station and the centre of the shadow). From these parameters, we use a procedure based on the Bessel method to derive an astrometric position.
Results. We derive accurate Pluto's astrometric positions from 1988 to 2016. These positions are used to refine the orbit of Pluto'system barycentre providing an ephemeris, accurate to the milliarcsec level, over the period 2000-2020, allowing better predictions for future stellar occultations.

Key words. Astrometry – Celestial mechanics – Ephemerides – Occultations

1. Introduction

Stellar occultation is a unique technique to obtain the physical parameters of distant objects or to probe their atmosphere. Meza et al. (2018) have used 10 stellar occultations by Pluto from 2002 to 2016 to study the evolution of Pluto's atmosphere. Occultations also provide the relative position of the body's centre compared to the position of the occulted star, leading to an accurate astrometric position of Pluto at the time of occultation.

The precision of the positions mainly depends on the knowledge of the shape and the size of the body, the modelling of the atmosphere, the precision of the timing system, the velocity of the occultation, the exposure time of the camera, and the precision of the stellar position. Since the publication of the Gaia catalogues in September 2016 for the first release (Gaia Collaboration et al. 2016) and moreover with the second release in April 2018 (Gaia Collaboration et al. 2018) including proper motions of the stars, the precision of the stellar catalogues can now reach a tenth of a milliarcsec (mas). For comparison, before Gaia catalogue, the precision of stellar catalogues such as UCAC2 (Zacharias et al. 2004) or UCAC4 (Zacharias et al. 2013), was about 50 to 100 mas per star with also zonal errors. Consequently, the precision of positions deduced from occultations is expected to be around few mas. Thanks to the accuracy of the Gaia catalogue, occultations can provide the most accurate astrometric measurement of a body in a outer solar system. In this paper, we present the astrometric positions we derived from occultations presented in Meza et al. (2018). We also detail a method to derive astrometric positions from other publications, knowing the circumstances of occultations (timing and impact parameter). Finally, we present a refined Pluto's ephemeris, allowing to better predict future occultations by Pluto at a mas level accuracy.

2. Astrometric positions from occultations

In this section, we present the astrometric positions we derived from occultations published in Meza et al. (2018). We also present astrometric positions of Pluto derived from occultations presented in other publications. The method used to derive these positions is presented in Appendix A.

2.1. Astrometric positions from occultations in Meza et al. (2018)

Meza et al. (2018) include 10 occultations by Pluto from 2002 to 2016. Beyond the parameters related to Pluto's atmosphere, another product of the occultations is the astrometric position of the body. From the geometry of the events, we determine an offset representing the position of the Pluto's centre compared to a reference ephemeris.

More precisely, the offsets in right ascension and in declination (offset_α, offset_δ), provided in Table 1, are given for a reference ephemeris (α_e, δ_e) at a reference date and a reference stellar position (α_s, δ_s). They are used as reference to derive an astrometric position. Another star position or ephemeris would lead to different offsets but the final position would remain the same.

Finally, from these parameters, an accurate position of Pluto can be derived with the stellar position from Gaia DR2 $(\alpha_{GDR2}, \delta_{GDR2})$ using the relations:

$$\alpha = \alpha_e + \frac{\mathrm{offset}_\alpha}{\cos\delta} + \alpha_{GDR2} - \alpha_s \quad (1)$$

$$\delta = \delta_e + \mathrm{offset}_\delta + \delta_{GDR2} - \delta_s \quad (2)$$

Pluto's ephemeris (α_e, δ_e), the offset derived from the geometry of the event and its precision, the star position (α_s, δ_s) used for the offset determination are provided in Table 1. The associated position of the occulted stars in Gaia DR2 catalogue $(\alpha_{GDR2}, \delta_{GDR2})$ are listed in Table 2. The positions are taking into account the proper motions and the parallax from Gaia DR2 and the table also presents the Gaia source identifier and the estimated precision in right ascension and declination taking into account precision of the stellar position and the proper motions, for all the occultations studied in this paper.

Finally, Table 3 provides the absolute position in right ascension and declination of Pluto's centre derived from the offsets and from stellar positions of Gaia DR2. The residuals related to JPL ephemeris[1] DE436 + PLU055 are also indicated as well as the differential positions between Pluto and Pluto's system barycentre used to refine the orbit (see Sect. 3). A flag indicates if the position is used in the ephemeris determination. Finally, the reconstructed paths of the occultations are presented in Fig. 5.

2.2. Astrometric positions from other publications

Several authors have published circumstances of an occultation by Pluto (Millis et al. 1993; Sicardy et al. 2003; Elliot et al. 2003; Young et al. 2008; Person et al. 2008; Gulbis et al. 2015; Olkin et al. 2015; Pasachoff et al. 2016; Pasachoff et al. 2017). From these circumstances (coordinates of the observer, mid-time of the occultation and impact parameter), it is possible to derive an offset between the observation deduced from these circumstances and a reference ephemeris. The procedure, based on the Bessel method used to predict stellar occultations, is described in Appendix A and the details of computation for each occultation are presented in Appendix B. The Pluto's positions deduced from occultations published in other articles besides those of Meza et al. (2018) are presented in Table 3.

The positions derived from Pasachoff et al. (2016) involving faint occulted stars, are not accurate enough to discriminate North and South solutions and to be used in the orbit determination.

3. NIMA ephemeris of Pluto

NIMA (Numerical Integration of the Motion of an Asteroid) has been developed in order to refine the orbits of small bodies, in particular TNOs and Centaurs studied by stellar occultations technique (Desmars et al. 2015). It consists in the numerical integration of the equations of motion perturbed by gravitational accelerations of the planets.

The state vector (the heliocentric vector of position and velocity of the body at a specific epoch) is refined by fitting to astrometric observations with the least square method. The main advantage of NIMA is to allow to use not only observations published on the Minor Planet Center[2] but also unpublished observations or astrometric positions of occultations. The quality of the observations is taken into account with a specific weighting scheme, in particular, it takes advantages of the high accuracy of occultations. Finally, after fitting to the observations, NIMA can provide an ephemeris through a bsp file format readable by the SPICE library[3].

As NIMA is representing the motion of the centre of mass of an object, it allows to compute the position of the Pluto's system barycentre. To deal with positions derived from occultations, we have to use an ephemeris representing the position of Pluto relative to the barycentre. For that purpose, we use the most recent ephemeris PLU055 developed in 2015.

The occultation-derived positions are then corrected from the offset between Pluto and the Pluto's system barycentre (see Table 3) to get the barycentric positions from the occultations, then used in the NIMA fitting procedure.

The precisions of the offset in right ascension and in declination derived from the occultations are provided in Table 1 for occultations presented in Meza et al. (2018) and in Appendix B for other publications. This precision is deduced from a specific model and reduction (for occultations in Meza et al. 2018) and from the precisions of timing and impact parameters (for other publications), without any estimation of systematic errors. For a realistic estimation of the orbit precision, the weighting scheme in the orbit fit needs to take into account the systematic errors (see Desmars et al. 2015 for details). The global precision for the positions used in the fitting depends on the precision of the stellar positions (from 0.1 to 2 mas), the precision of the offset (from 0.1 mas to 11 mas), and the precision of the Pluto body-Pluto system barycenter ephemeris (estimated to 1-5 mas). The reconstructed geometry of the occultations may also have some systematic errors due to the modelling of the atmosphere and timing issues during the observations, especially for single-chord occultation. These systematic errors are hard to estimate but a comparison between the positions derived from different reductions of the same occultation (see for example in Table 4, occultations on 21 August 2002, 4 May 2013 and 29 June 2015) indicates differences of few mas, which is much higher than the respective

[1] DE436 is a planetary ephemerides from JPL providing the positions of the barycentre of the planets, including the barycentre of Pluto's system. PLU055 is the JPL ephemeris providing the positions of Pluto and its satellites related to the Pluto's system barycentre, developed by R.Jacobson in 2015 and based on an updated ephemeris of Brozović et al. (2015): `https://naif.jpl.nasa.gov/pub/naif/generic_kernels/spk/satellites/plu055.cmt`

[2] The Minor Planet Center is in charge of providing astrometric measurements, orbital elements of the solar system small bodies : `http://minorplanetcenter.net`.

[3] The SPICE Toolkit is a library developed by NASA dedicated to space navigation and providing in particular a list of routines related to ephemeris: `http://naif.jpl.nasa.gov/naif/index.html`.

Table 1: Date, timing and coordinates used for the reference ephemeris, offset in right ascension and declination and their precision (in mas), and the coordinates of the occulted star in the reference catalogue.

Reference date	reference Pluto's ephemeris		position of reference star		offset (mas)	
	right ascension	declination	right ascension	declination	$\Delta\alpha\cos\delta$	$\Delta\delta$
2002-08-21 07:00:32	16 58 49.4413	-12 51 31.708	16 58 49.4360	-12 51 31.920	-29.7±0.2	-236.3±0.1
2007-06-14 01:27:00	17 50 20.7436	-16 22 42.286	17 50 20.7392	-16 22 42.210	-97.5±0.1	75.7±0.2
2008-06-22 19:07:28	17 58 33.0319	-17 02 38.617	17 58 33.0138	-17 02 38.349	-22.7±0.2	112.6±0.2
2008-06-24 10:37:00	17 58 22.3952	-17 02 49.270	17 58 22.3930	-17 02 49.349	10.7±0.1	93.0±0.7
2010-02-14 04:45:00	18 19 14.3657	-18 16 42.249	18 19 14.3851	-18 16 42.313	34.3±0.2	123.6±0.5
2010-06-04 15:34:00	18 18 47.9470	-18 12 52.045	18 18 47.9349	-18 12 51.794	8.1±0.3	122.9±1.3
2011-06-04 05:42:00	18 27 53.8241	-18 45 30.902	18 27 53.8249	-18 45 30.725	-8.6±0.3	161.1±0.3
2012-07-18 04:13:00	18 32 14.6762	-19 24 19.353	18 32 14.6720	-19 24 19.295	-20.3±0.1	46.3±0.1
2013-05-04 08:22:00	18 47 52.5417	-19 41 24.536	18 47 52.5322	-19 41 24.374	-118.7±0.1	133.3±0.1
2015-06-29 16:02:00	19 00 49.7182	-20 41 40.559	19 00 49.4796	-20 41 40.778	-83.5±0.1	160.3±0.1
2016-07-19 20:53:45	19 07 22.1091	-21 10 28.224	19 07 22.1242	-21 10 28.445	102.4±0.1	-17.6±0.4

Notes. In this paper, right ascension are presented in hour, minutes and seconds of arc and declination are presented in degrees, minutes and seconds of degrees.

Table 2: Gaia DR2 source identifier, right ascension and declination and their standard deviation (in mas) at epoch and magnitude of the stars of the catalogue Gaia DR2 involved in occultations presented in this paper.

Date	Gaia source identifier	right ascension	declination	σ_α	σ_δ	Gmag
1988-06-09	3652000074629749376	14 52 09.962000	+00 45 03.30297	2.14	2.06	12.1
2002-07-20	4333071455580364160	17 00 18.029957	-12 41 42.01220	1.12	0.73	12.6
2002-08-21	4333042833914281856	16 58 49.431538	-12 51 31.85910	1.87	1.12	15.4
2006-06-12	4124931567980280832	17 41 12.074271	-15 41 34.47421	0.63	0.49	14.7
2007-03-18	4144912550502784384	17 55 05.699098	-16 28 34.36682	0.74	0.60	14.8
2007-06-14	4147858103406546048	17 50 20.744804	-16 22 42.22719	0.83	0.73	15.3
2008-06-22	4144621347334603520	17 58 33.013236	-17 02 38.39643	0.67	0.54	12.3
2008-06-24	4144621244254585728	17 58 22.390423	-17 02 49.36558	0.93	0.78	15.6
2010-02-14	4096385295578625536	18 19 14.378482	-18 16 42.35590	0.50	0.42	10.3
2010-06-04	4096389556186605568	18 18 47.930034	-18 12 51.82967	0.37	0.31	14.8
2011-06-04	4093175335706340480	18 27 53.819996	-18 45 30.78871	0.62	0.50	16.4
2011-06-23	4093163211131448704	18 25 55.479351	-18 48 07.09094	0.35	0.31	14.0
2012-07-18	4092849712861519360	18 32 14.673688	-19 24 19.34329	0.19	0.17	14.4
2013-05-04	4086200313156846336	18 47 52.531982	-19 41 24.39714	0.10	0.09	14.2
2014-07-23	4085914882468876672	18 49 31.736687	-20 22 23.82473	0.21	0.19	17.2
2014-07-24	4085914745029913216	18 49 26.511650	-20 22 36.98627	0.39	0.35	18.1
2015-06-29	4084956039611370112	19 00 49.474124	-20 41 40.81016	0.04	0.04	12.0
2016-07-19	4082062610353732096	19 07 22.117772	-21 10 28.43508	0.05	0.05	13.9

Notes. The coordinates and their precision are provided for the epoch of the occultation taking into account the proper motions and the parallax, and their precision.

internal precisions (order of 0.1 mas). Finally, we adopt the estimated precision presented in Table 4, for the weighting scheme in the orbit fit.

Figure 1 shows the difference between NIMA[4] and JPLDE436 ephemeris of Pluto's barycentre in right ascension (weighted by $\cos\delta$) and declination. The blue dots and the error bars represent the positions and their estimated precision from our occultations, the red dots represent the positions from occultations not listed in Meza et al. (2018): Millis et al. (1993); Sicardy et al. (2003); Elliot et al. (2003); Young et al. (2008); Person et al. (2008); Gulbis et al. (2015); Olkin et al. (2015); Pasachoff et al. (2017), and the gray area represents the 1σ uncertainty of the NIMAv8 ephemeris.

[4] The NIMAv8 ephemeris is available on `http://lesia.obspm.fr/lucky-star/nima/`.

Table 4 and Fig. 2 provide the residuals (O-C) of the positions derived from the occultations, compared with the NIMAv8 ephemeris, and the estimated precision of the positions used in the weighting scheme. After 2010, residuals are below the mas level, which is much better than any other measurement of Pluto's positions. In that context, other classical observations of Pluto, such as CCD, appear to be useless for short-term ephemeris, since the occultations provide the most accurate positions during the 1988-2016 period.

4. Discussion

The NIMA ephemeris allows very accurate predictions of stellar occultation by Pluto in the forthcoming years a few mas level. In particular, we have predicted an occultation by Pluto on Au-

Table 3: Right ascension and declination of Pluto deduced from occultations, Residuals (O-C) in mas related to JPL DE436+PLU055 ephemeris, and differential coordinates between Pluto and Pluto barycenter system position from PLU055 ephemeris.

	Pluto's coordinates		O-C (mas)		PLU-BAR (mas)			
date (UT)	right ascension	declination	$\Delta\alpha\cos(\delta)$	$\Delta\delta$	$\Delta\alpha\cos(\delta)$	$\Delta\delta$	flag	reference
1988-06-09 10:39:17.0	14 52 09.96347	+00 45 03.1506	19.9	-33.5	-8.8	79.6	*	Millis et al. (1993)
2002-07-20 01:43:39.8	17 00 18.03018	-12 41 41.9934	7.7	-4.4	-52.9	24.7	*	Sicardy et al. (2003)
2002-08-21 07:00:32.0	16 58 49.43477	-12 51 31.8833	20.6	-10.4	-51.2	48.8	*	This paper
2002-08-21 07:00:32.0	16 58 49.43442	-12 51 31.8820	15.4	-9.1	-51.2	48.8	*	Elliot et al. (2003)
2006-06-12 16:25:05.7	17 41 12.07511	-15 41 34.5896	9.8	-0.4	-47.0	-40.8	*	Young et al. (2008)
2007-03-18 10:59:33.1	17 55 05.69430	-16 28 34.0886	10.7	0.8	67.1	-39.4	*	Person et al. (2008)
2007-06-14 01:27:00.0	17 50 20.74243	-16 22 42.2275	14.7	-1.8	-5.2	89.8	*	This paper
2008-06-22 19:07:28.0	17 58 33.02976	-17 02 38.5534	14.0	0.0	-59.3	-23.3	*	This paper
2008-06-24 10:37:00.0	17 58 22.39339	-17 02 49.1932	17.6	8.1	-35.4	89.6	*	This paper
2010-02-14 04:45:00.0	18 19 14.36152	-18 16 42.1678	15.2	3.1	-65.4	55.6	*	This paper
2010-06-04 15:34:00.0	18 18 47.94272	-18 12 51.9579	14.9	4.8	47.9	49.2	*	This paper
2011-06-04 05:42:00.0	18 27 53.81859	-18 45 30.8046	15.6	9.3	71.7	7.1	*	This paper
2011-06-23 11:23:48.2	18 25 55.47963	-18 48 06.9712	16.1	5.5	73.2	0.2	*	Gulbis et al. (2015)
2012-07-18 04:13:00.0	18 32 14.67647	-19 24 19.3554	16.9	7.7	55.2	-76.0	*	This paper
2013-05-04 08:21:41.8	18 47 52.53356	-19 41 24.4265	18.7	8.4	-74.6	47.9	*	Olkin et al. (2015)
2013-05-04 08:22:00.0	18 47 52.53305	-19 41 24.4265	19.3	9.2	-74.6	48.0	*	This paper
2014-07-23 14:25:59.1	18 49 31.74100	-20 22 23.9915	30.4	3.7	-7.5	-79.7		Pasachoff et al. (2016)
2014-07-23 14:25:59.1	18 49 31.74048	-20 22 23.9502	23.0	44.9	-7.5	-79.7		Pasachoff et al. (2016)
2014-07-24 11:42:20.0	18 49 26.51393	-20 22 37.1172	11.3	-14.6	-65.8	-28.7		Pasachoff et al. (2016)
2014-07-24 11:42:20.0	18 49 26.51337	-20 22 37.0734	3.4	29.1	-65.8	-28.7		Pasachoff et al. (2016)
2015-06-29 16:02:00.0	19 00 49.70680	-20 41 40.4308	22.8	10.7	-41.9	80.3	*	This paper
2015-06-29 16:54:41.4	19 00 49.47778	-20 41 40.9707	22.1	12.7	-39.4	81.2	*	Pasachoff et al. (2017)
2016-07-19 20:53:45.0	19 07 22.10999	-21 10 28.2320	24.1	11.6	56.5	-71.7	*	This paper

Notes. A flag is indicated if the position was used in the NIMA fit (see Sec. 3).

Table 4: Residuals (O-C) related to NIMAv8 ephemeris of Pluto system barycentre. Estimated precision in arcsec in right ascension and declination used for the fit is also indicated.

date (UT)	$\Delta\alpha\cos(\delta)$ (mas)	$\Delta\delta$ (mas)	σ_α (arcsec)	σ_δ (arcsec)
1988-06-09	-0.7	1.3	10.0	10.0
2002-07-20	-5.3	3.8	10.0	15.0
2002-08-21[1]	2.9	-1.1	10.0	10.0
2002-08-21	8.1	-2.4	10.0	10.0
2006-06-12	-4.0	1.2	10.0	10.0
2007-03-18	-4.1	0.6	10.0	10.0
2007-06-14	0.6	-2.2	5.0	5.0
2008-06-22	-0.4	-2.1	5.0	5.0
2008-06-24	2.6	2.2	5.0	5.0
2010-02-14	-1.1	-1.2	5.0	5.0
2010-06-04	-1.3	0.2	5.0	5.0
2011-06-04	-1.7	3.2	5.0	5.0
2011-06-23	-0.2	-0.5	10.0	10.0
2012-07-18	0.2	0.3	5.0	5.0
2013-05-04[2]	-1.1	-0.2	10.0	10.0
2013-05-04	-0.5	0.6	5.0	5.0
2015-06-29	0.5	-0.1	2.0	2.0
2015-06-29[3]	-0.7	1.8	10.0	10.0
2016-07-19	-0.1	-0.2	2.0	2.0

Notes. [1] Taken from Elliot et al. (2003). [2] Taken from Olkin et al. (2015). [3] Taken from Pasachoff et al. (2017).

gust 15, 2018, above North America to the precision of 2.5 mas, representing only 60 km on the shadow path and a precision of 4 s in time. As shown in Meza et al. (2018), the observation of a central flash allows to probe the deepest layers of Pluto's atmosphere. The central flash can be observed in an small band about 50 km around the centrality path. By reaching a precision of tens of km, we were able to gather observing stations along the centrality and to highly increase the probability of observing a central flash. Preliminary results of this campaign show that the prediction was accurate to about 3 s in time and less than 20 km in distance.

Figure 3 represents the prediction of the occultation by Pluto on August 15, 2018 using two different ephemerides: JPL DE436 + PLU055 and NIMAv8 + PLU055. The prediction using JPL ephemerides is shifted by 36.8 s and 8 mas south (representing about 190 km) compared to the prediction with NIMAv8 ephemeris. Thus, NIMAv8 and Gaia DR2 rise the probability to observe a central flash to more than 50% for this occultation, whereas the observation of this event using the prediction with JPL ephemeris would have been possible only by chance. The precision remains at few mas up to 2025 (in particular in declination) and it is even more important since the apparent position of Pluto as seen from Earth is moving away from the Galactic centre, making occultations by Pluto more and more rare.

Another point of interest is to look at previous occultations. In particular, for the occultation of August 19, 1985, Brosch & Mendelson (1985) reported a single chord occultation of a magnitude 11.1 star[5] by Pluto, showing a gradual shape possibly due to Pluto's atmosphere. The observation was done at Wise obser-

[5] The star position in Gaia DR2 at the epoch of the occultation is 14 23 43.4575 in right ascension and +03 06 46.874 in declination.

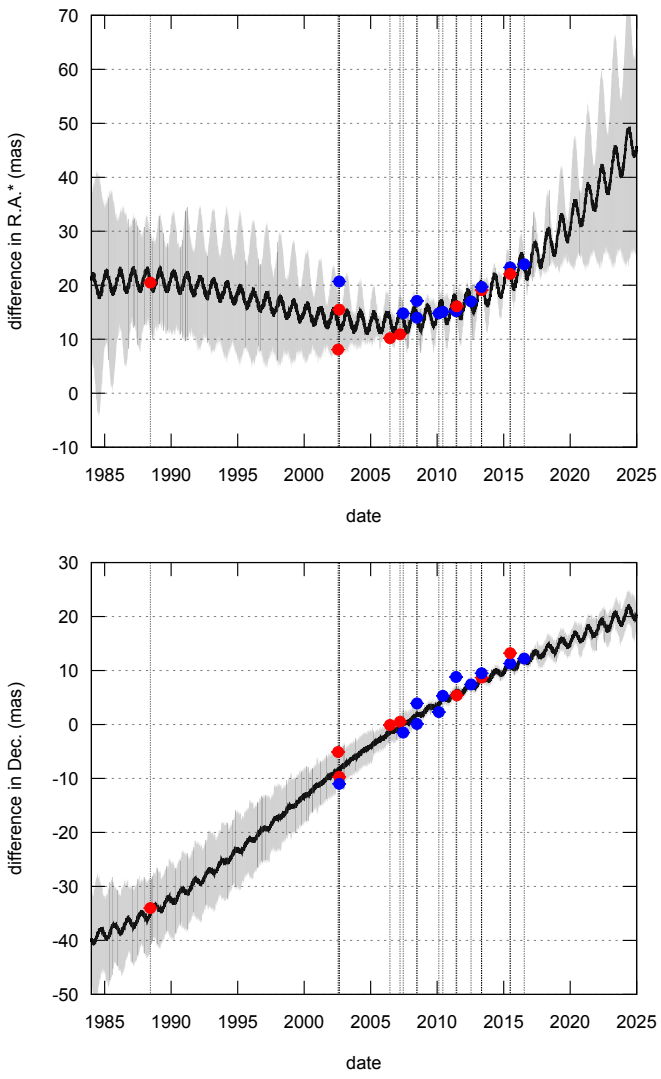

Fig. 1: Difference between NIMAv8 and JPL DE436 ephemeris of Pluto's system barycentre in right ascension (weighted by $\cos\delta$) and in declination. Blue dots and their estimated precision in error bar represent the positions coming from the occultations studied in this work and red dots represent the positions deduced from other publications. The gray area represents the 1σ uncertainty of the NIMA orbit.

vatory in Israel in poor conditions (low elevation, close to twilight). Thanks to Gaia DR2, providing the proper motion of the star and to NIMAv8, we make a postdiction of the occultation on August 19, 1985 (Fig. 4). The nominal time for the occultation (the time of the closest approach between the geocentre and the centre of the shadow) is 17:58:55.8 leading to a predicted mid-time of 17:59:48.5 at Wise observatory. Brosch (1995) gave an approximate observed mid-time of the occultation for Wise observatory at 17:59:54 (about 6 s later than the prediction). The predicted shadow of Pluto at the same time is presented on the figure as well as the observatory's place as a green dot. The uncertainty in time for this occultation is about 20 s whereas the uncertainty on the path is about 10 mas (representing 220 km). This is fully consistent with the fact that the occultation was indeed observed at Wise observatory.

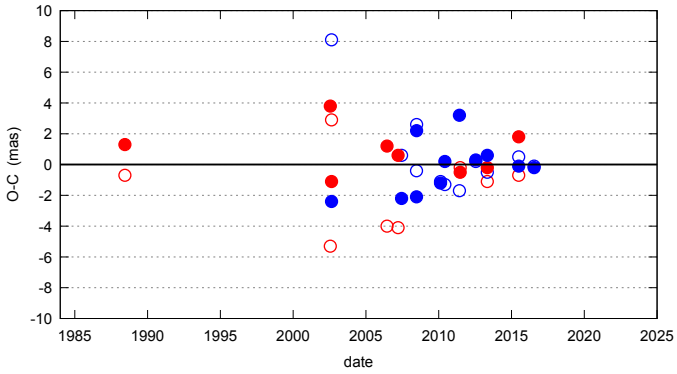

Fig. 2: Residuals of Pluto's system barycentre positions compared to NIMAv8. Circles are for right ascension weighted by $\cos\delta$ and dots are for declination. Blue color is used for the positions coming from the occultations studied in this work and red color is for the positions deduced from other publications

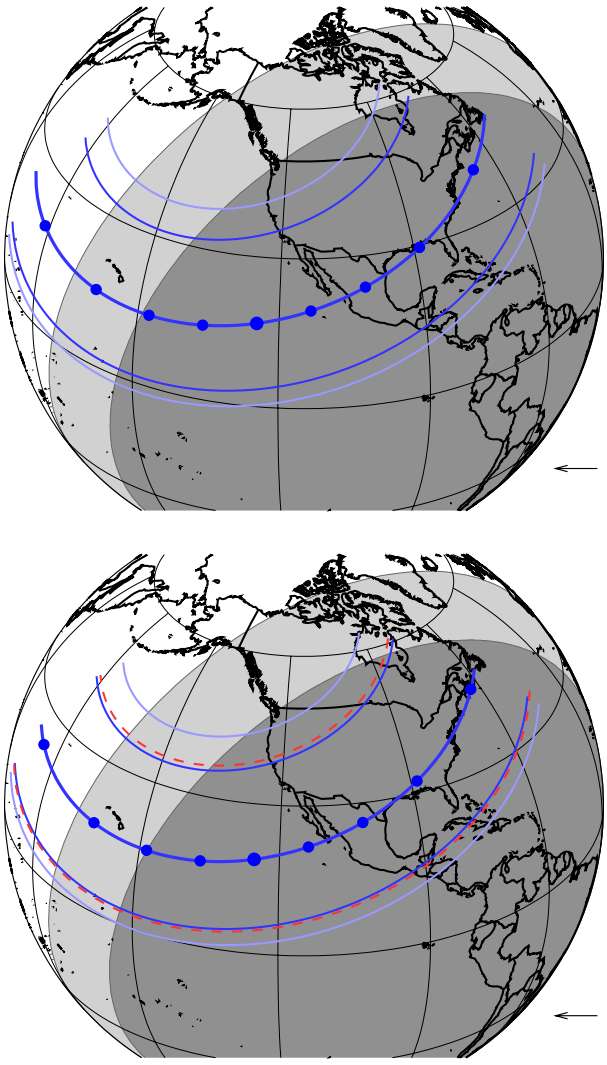

Fig. 3: Prediction of the occultation by Pluto on 15 August 2018, using JPL DE436 + PLU055 (top) and NIMAv8 + PLU055 (bottom) ephemerides. The red dotted lines represent the 1σ uncertainty on the path.

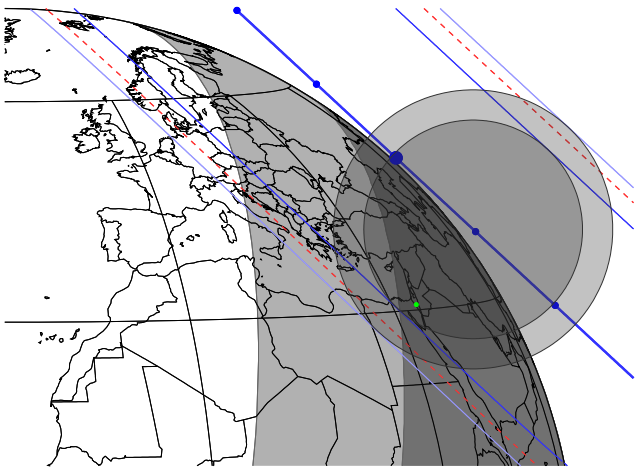

Fig. 4: Prediction of the occultation by Pluto on 19 August 1985, using NIMAv8 + PLU055 ephemerides. The shadow of Pluto at 17:59:54 (the mid-time of the occultation provided in Brosch (1995)) is represented. The green dot represents the WISE observatory. The red dotted lines on right represent the 1σ uncertainty on the path.

5. Conclusions

Stellar occultations by Pluto provide accurate astrometric positions thanks to Gaia DR2. These positions are deduced for the global fitting of the atmosphere providing also the position of Pluto's centre as in Meza et al. (2018) or by using a specific method (as described in Appendix A). We finally determine 18 astrometric positions of Pluto from 1988 to 2016 with an estimated precision of 2 to 10 mas.

These positions are used to compute an ephemeris of Pluto system's barycentre thanks to NIMA procedure with an unprecedented precision on the 1985-2015 period. This ephemeris NIMAv8 was used to study the possible occultation of Pluto observed in 1985 as well to predict the recent occultation by Pluto on August 15th, 2018 or the forthcoming occultations[6] with a precision of 2 mas, a result impossible to reach with classical astrometry. In fact, the presence of the usually unresolved Charon in classical images, causes significant displacements of the photocentre of the system with respect to its barycentre. As a consequence, and even modeling the effect of Charon, accuracies below the 50 mas level are difficult to reach.

This method can be extended, for instance for Chariklo, with an even better accuracy of the order of 1 mas (Desmars et al. 2017) and illustrates the power of stellar occultations not only for better studying those bodies, but also for improving their orbital elements.

Acknowledgements. Part of the research leading to these results has received funding from the European Research Council under the European Community's H2020 (2014–2020/ERC Grant Agreement No. 669416 "LUCKY STAR"). This work has made use of data from the European Space Agency (ESA) mission *Gaia* (`https://www.cosmos.esa.int/gaia`), processed by the *Gaia* Data Processing and Analysis Consortium (DPAC, `https://www.cosmos.esa.int/web/gaia/dpac/consortium`). Funding for the DPAC has been provided by national institutions, in particular the institutions participating in the *Gaia* Multilateral Agreement.

[6] See the predictions on the Lucky Star webpage `http://lesia.obspm.fr/lucky-star/predictions/`.

References

Brosch, N. 1995, MNRAS, 276, 571
Brosch, N. & Mendelson, H. 1985, IAU Circ., 4097
Brozović, M., Showalter, M. R., Jacobson, R. A., & Buie, M. W. 2015, Icarus, 246, 317
Desmars, J., Camargo, J., Bérard, D., et al. 2017, in AAS/Division for Planetary Sciences Meeting Abstracts, Vol. 49, AAS/Division for Planetary Sciences Meeting Abstracts #49, 216.03
Desmars, J., Camargo, J. I. B., Braga-Ribas, F., et al. 2015, A&A, 584, A96
Elliot, J. L., Ates, A., Babcock, B. A., et al. 2003, Nature, 424, 165
Gaia Collaboration, Brown, A. G. A., Vallenari, A., et al. 2018, A&A, 616, A1
Gaia Collaboration, Brown, A. G. A., Vallenari, A., et al. 2016, A&A, 595, A2
Gulbis, A. A. S., Emery, J. P., Person, M. J., et al. 2015, Icarus, 246, 226
Meza, E., Sicardy, B., Ortiz, J. L., et al. 2018, A&A, in press
Millis, R. L., Wasserman, L. H., Franz, O. G., et al. 1993, Icarus, 105, 282
Olkin, C. B., Young, L. A., Borncamp, D., et al. 2015, Icarus, 246, 220
Pasachoff, J. M., Babcock, B. A., Durst, R. F., et al. 2017, Icarus, 296, 305
Pasachoff, J. M., Person, M. J., Bosh, A. S., et al. 2016, The Astronomical Journal, 151, 97
Person, M. J., Elliot, J. L., Gulbis, A. A. S., et al. 2008, AJ, 136, 1510
Sicardy, B., Widemann, T., Lellouch, E., et al. 2003, Nature, 424, 168
Urban, S. E. & Seidelmann, P. K. 2013, Explanatory supplement to the astronomical almanac (University Science Books)
Young, E. F., French, R. G., Young, L. A., et al. 2008, AJ, 136, 1757
Zacharias, N., Finch, C. T., Girard, T. M., et al. 2013, AJ, 145, 44
Zacharias, N., Urban, S. E., Zacharias, M. I., et al. 2004, AJ, 127, 3043

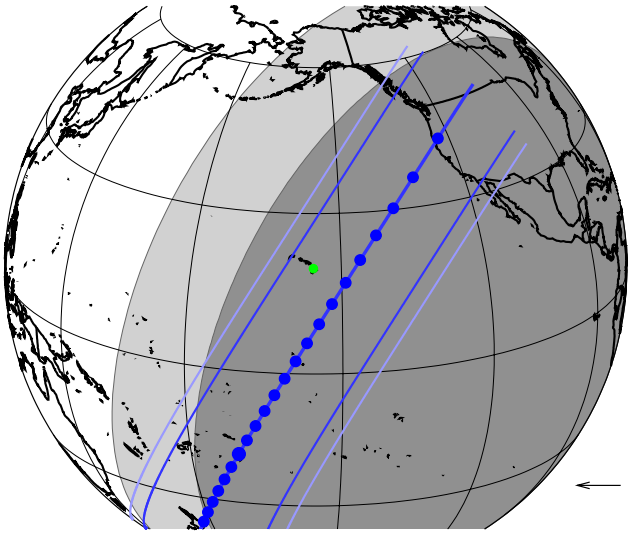

(a) 2002-08-21

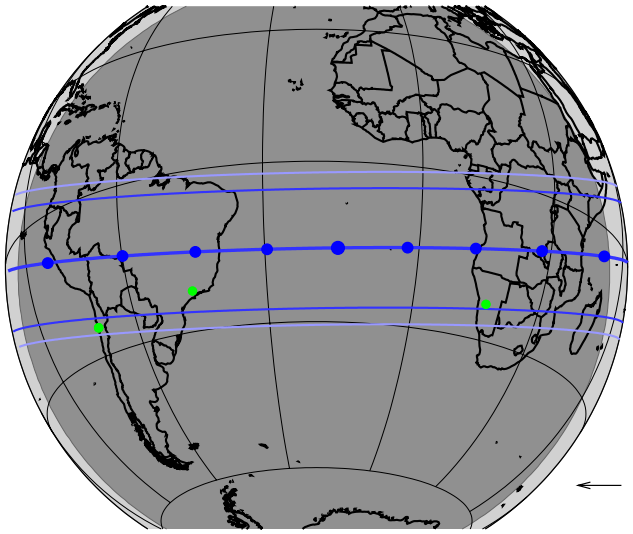

(b) 2007-06-14

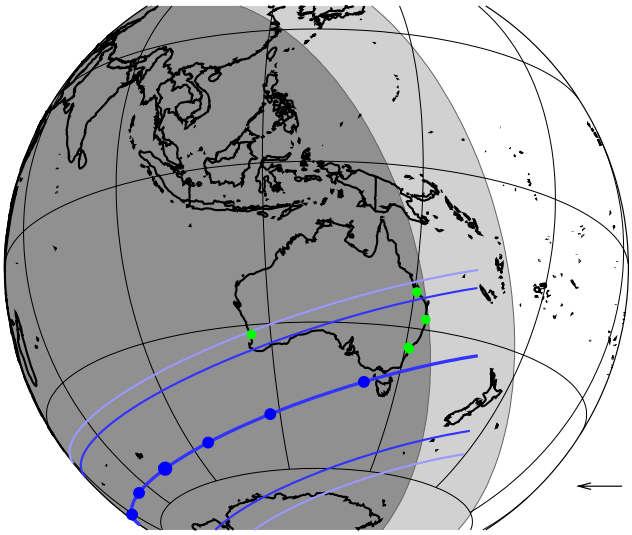

(c) 2008-06-22

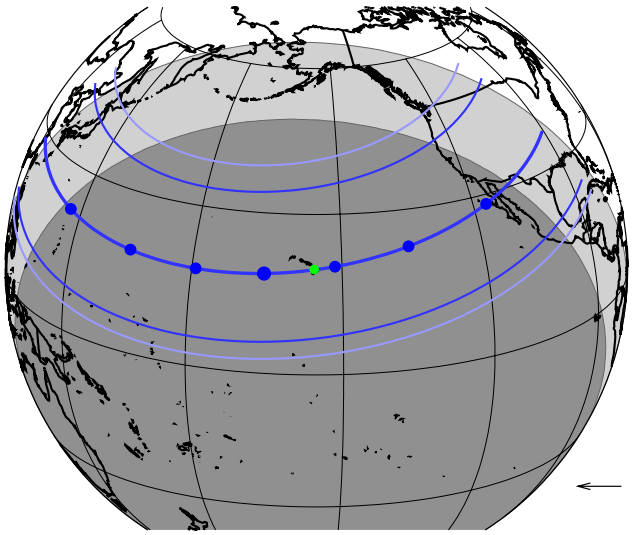

(d) 2008-06-24

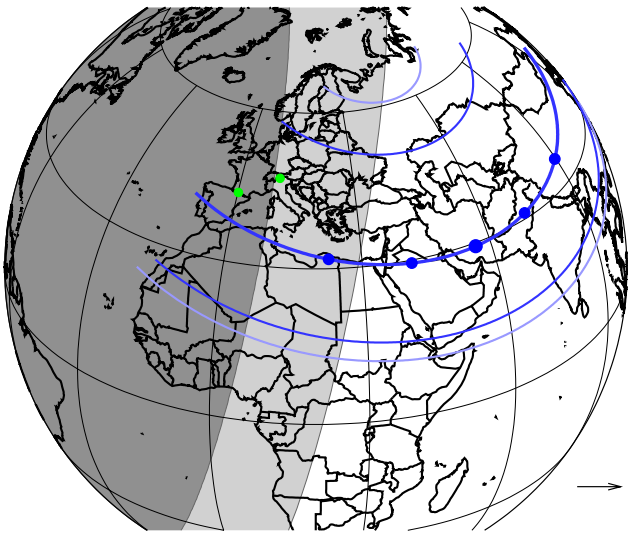

(e) 2010-02-14

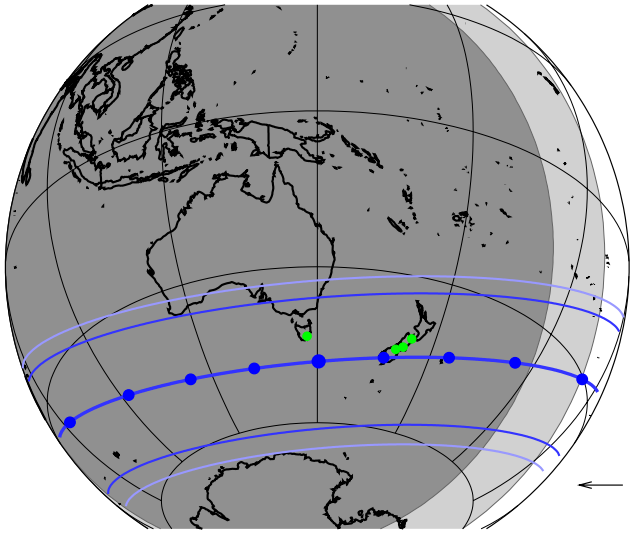

(f) 2010-06-04

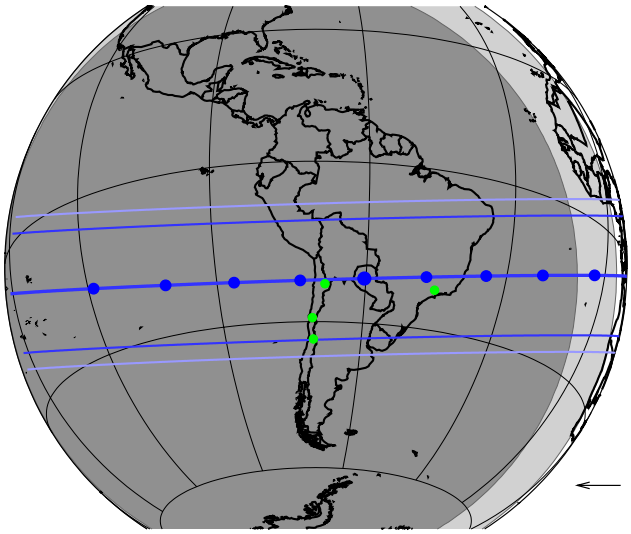

(g) 2011-06-04

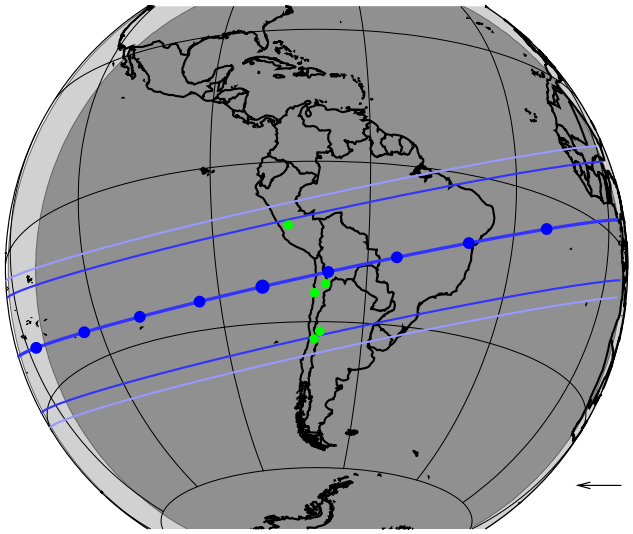

(h) 2012-07-18

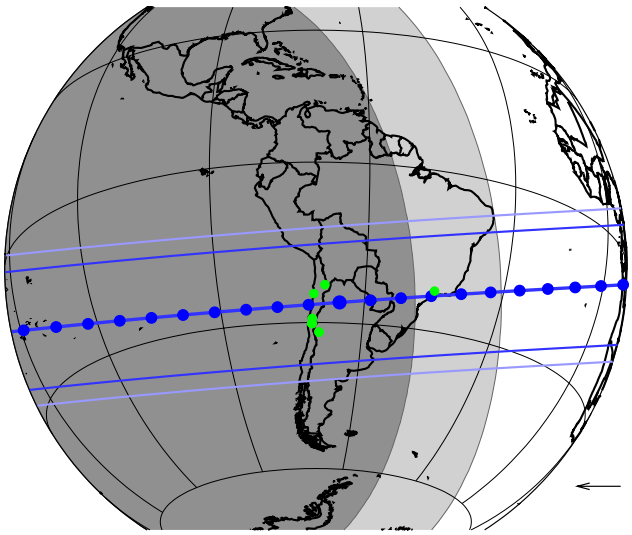

(i) 2013-05-04

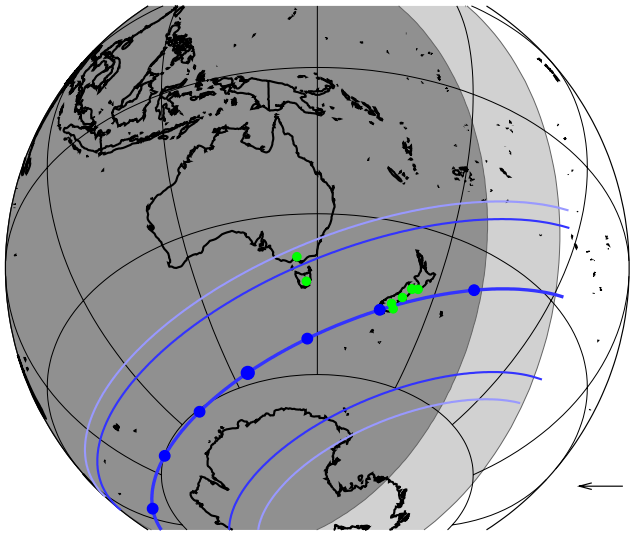

(j) 2015-06-29

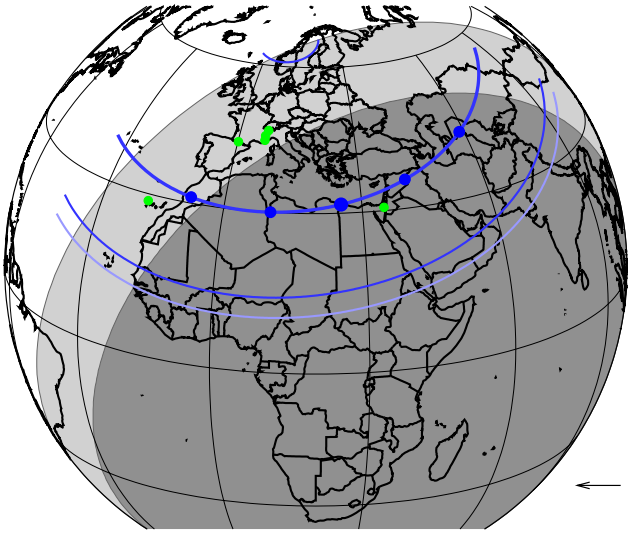

(k) 2016-07-19

Fig. 5: Reconstruction of Pluto's shadow trajectories on Earth for occultations observed from 2002 to 2016; see details in Meza et al. (2018). The dots on the shadow central line are plotted every minute, and the black arrow represents the shadow motion direction (see arrow al lower right corner). The dark and light blue thinner lines are the shadow limits corresponding the stellar half-light level and 1 % stellar drop level (the practical detection limit), respectively. The green dots correspond to the site with positive occultation used in the fit. Areas in dark gray corresponds to full night (Sun elevation below -18°) and areas in light grey corresponds to twilight (Sun elevation between -18° to 0°), while day time is in white.

Appendix A: Method to derive astrometric positions from occultation's circumstances

We present in this section a method to derive an astrometric position from an occultation's observation, knowing the occultation's circumstances. The determination of an occultation's circumstances consists in computing the Besselian elements. The Bessel method makes use of the fundamental plane that passes through the centre of the Earth and perpendicular to the line joining the star and the centre of the object (to the axis of the shadow). The method is for example described in Urban & Seidelmann (2013). The Besselian elements are usually given for the time of conjunction of the star and the object in right ascension but in this paper the reference time is the time of closest approach between the star and the object.

The Besselian elements are T_0 the UT time of the closest approach, H the Greenwich Hour Angle of the star at T_0, x_0 and y_0 the coordinates of the shadow axis at T_0 in the fundamental plane, x' and y' the rates of changes in x and y at T_0, and α_s, δ_s the right ascension and the declination of the star. Their computation are fully described in Urban & Seidelmann (2013).

The quantities x_0, y_0, x' and y' depend on the ephemeris of the body and allow to represent the linear motion of the shadow at the time of the occultation. In this paper, x_0, y_0 are expressed in Earth radius unit and x', y' are in Earth radius per day.

From T_0, α_s, δ_s and H, the coordinates[1] of the shadow centre (λ_c, ϕ_c) at T_0 can be derived.

For an observing site, the method requires the local circumstances which are the mid-time of the occultation and the impact parameter ρ, the distance of closest approach between the site and the centre of the shadow in the fundamental plane. Usually, the impact parameter is given in kilometres and when the occultation has only one chord, two solutions (North and South) can be associated.

The first step is to add a shift to x_0 and y_0 to take into account the impact parameter, i.e. the fact that the observing site is not right on the centrality of the occultation.

$$x_0 \rightarrow x_0 \pm s\frac{x_0}{\sqrt{x_0^2+y_0^2}} \tag{A.1}$$

$$y_0 \rightarrow y_0 \pm s\frac{y_0}{\sqrt{x_0^2+y_0^2}} \tag{A.2}$$

where s is the ratio between ρ and Earth radius.

Given the longitude λ and the latitude[1] ϕ of the observing site, the coordinates in the fundamental plane are given by :

$$u = \cos\phi \sin(\lambda - \lambda_c) \tag{A.3}$$

$$v = \sin\phi\cos\phi_c - \cos\phi\sin\phi_c\cos(\lambda - \lambda_c) \tag{A.4}$$

$$w = \sin\phi\sin\phi_c + \cos\phi\cos\phi_c\cos(\lambda - \lambda_c) \tag{A.5}$$

The time of the closest approach for the observer is given by the relation :

$$t_m = T_0 + \frac{(u-x_0)x' + (v-y_0)y'}{x'^2 + y'^2} \tag{A.6}$$

[1] Latitude refers to geocentric latitude. Usually coordinates provide geodetic latitude that need to be converted to geocentric latitude.

In fact, t_m, u, v, w are calculated iteratively by replacing λ_c by $\lambda_c - \Omega(t_m - T_0)$, where Ω is the rate of Earth's rotation, to take into account the Earth's rotation during $t_m - T_0$.

If Δt is the difference between the observed time of the occultation for the observer and the nominal time of the occultation T_0, the correction to apply to the Besselian elements x_0, y_0 are :

$$\Delta x = (u - x_0) - x'\Delta t \tag{A.7}$$

$$\Delta y = (v - y_0) - y'\Delta t \tag{A.8}$$

$\Delta x, \Delta y$ are determined iteratively and finally transformed into an offset in right ascension and in declination between the observed occultation and the predicted occultation (from the ephemeris).

For single chord occultation, they are two solutions (North and South) whereas for multi-chord occultation there is a unique solution. In that case, the astrometric position deduced from the occultation is the reference ephemeris plus the average offset deduced from all the observing sites.

This method is powerful to derive astrometric positions from occultation. It only requires local circumstances of the occultation for the observing sites such as the mid-time of the occultation and the impact parameter. If the impact parameter is not provided, one can derive from the timing of immersion and emmersion knowing the size of the object and assuming it is spherical. So the method can be used for any object.

Appendix B: Astrometric positions from other occultations

In this section, we derive astrometric positions from occultations published in various articles using the method previously presented. The Besselian elements corresponding to the occultations are presented in Table B.1 and the reconstructed shadow trajectories of occultation are presented in Fig. B.1.

Appendix B.1: Occultation of 9 June 1988

Millis et al. (1993) presented an occultation by Pluto on June 9, 1988. They derived an astrometric solution by giving the impact parameter for the eight stations that recorded the event.

According to the mid-time of the occultation derived from the paper, we determine the following offsets:

observatory	mid-time	ρ (km)	Δt (s)	$\Delta\alpha\cos\delta$ (mas)	$\Delta\delta$ (mas)
Charters Towers	10:41:27.1±1.23	985	130.0	20.6	-33.5
Toowoomba	10:40:50.5±0.55	188	93.4	18.4	-33.6
Mt Tamborine	10:40:17.4±0.95	168	60.3	-4.3	-33.9
Auckland	10:39:03.3	-687	-13.8	26.6	-33.9
Hobart	10:41:00.6±1.95	-1153	103.5	19.5	-33.8
KAO	10:37:26.9±0.15	868	-110.2	19.5	-33.0
Mt John	10:39:19.6±0.78	-1281	2.5	19.9	-33.6

For Black Birch, there is only the immersion timing so the mid-time of the occultation can not be derived. The average offset of this occultation was determined using the same set of the prefereed astrometric solution of Millis et al. (1993), i.e. data from Charters Towers, Hobart, Kuiper Airbone Observatory (KAO) and Mount John.

Finally, we derive the average offset of $\Delta\alpha\cos\delta = +19.9 \pm 0.5$ mas and $\Delta\delta = -33.5 \pm 0.3$ mas.

Appendix B.2: Occultation of 20 July 2002

Sicardy et al. (2003) obtained a light curve of the occultation by Pluto in Arica, North of Chile. They derived an astrometric solution of the occultation by giving distance of closest approach to the centre of Pluto's shadow for Arica (975 ± 250km).

In Arica, the mid-time of the occultation occurs at 01:44:03 UT, giving Δt = 23.2s. There are two possible solutions but the occultation was also observed in Mamiña[7] in Chile (Buie, personal communication) so the only possible solution is the South one.

Finally, we derive the offset of $\Delta\alpha\cos\delta = +7.7 \pm 1.9$ mas and $\Delta\delta = -4.4 \pm 11.2$ mas, assuming a precision of 2 s for the mid-time.

Appendix B.3: Occultation of 21 August 2002

Elliot et al. (2003) derived an astrometric solution of the occultation by giving distance of closest approach to the centre of Pluto's shadow for Mauna Kea Observatory (597 ± 32km) and Lick Observatory (600 ± 32km). They observed a positive occultation with three telescopes (two in Hawai and one in Lick Observatory).

As there are at least two stations observing this occultation, there is a unique solution. According to the mid-time of the occultation in the two stations, we derived the following offsets:

observatory	mid-time	ρ (km)	Δt (s)	$\Delta\alpha\cos\delta$ (mas)	$\Delta\delta$ (mas)
CFHT 2.2m	6:50:33.9±0.5	597	-598.1	16.0	-8.0
CFHT 0.6m	6:50:33.9±1.8	597	-598.1	16.0	-8.2
Lick obs.	6:45:48.0±2.8	600	-884.0	14.2	-11.0

Finally, for this occultation, we used an average offset of $\Delta\alpha\cos\delta = +15.4 \pm 1.0$ mas and $\Delta\delta = -9.1 \pm 1.7$ mas.

Appendix B.4: Occultation of 12 June 2006

Young et al. (2008) presented the analysis of an occultation by Pluto on 12 June 2006. They published the half light time (ingress and egress) and the impact parameter (closest distance to the centre of the shadow) for five stations:

- REE = Reedy Creek Observatory, QLD, AUS (0.5 m aperture).
- AAT = Anglo-Australian Observatory, NSW, AUS (4 m).
- STO = Stockport Observatory, SA, AUS (0.5 m).
- HHT = Hawkesbury Heights, NSW, AUS (0.2 m).
- CAR = Carter Observatory, Wellington, NZ (0.6 m)

These parameters allow us to compute the mid-time of the occultation and to finally derive an offset for each station:

observatory	mid-time	ρ (km)	Δt (s)	$\Delta\alpha\cos\delta$ (mas)	$\Delta\delta$ (mas)
REE	16:23:00.636±2.61	836.6	-125.2	9.4	-0.5
AAT	16:23:19.665±0.05	571.8	-106.1	9.6	-0.5
STO	16:23:59.619±0.80	382.2	-66.2	9.7	-0.5
HHT	16:23:17.705±2.12	302.5	-108.1	9.1	-0.4
CAR	16:22:30.825±1.96	-857.6	-155.0	11.2	-0.4

Finally, for this occultation, we used an average offset of $\Delta\alpha\cos\delta = +9.8 \pm 0.8$ mas and $\Delta\delta = -0.4 \pm 0.1$ mas.

[7] The Mamiña coordinates are 20°04'51.00"S and 69°12'00.00"W.

Appendix B.5: Occultation of 18 March 2007

Person et al. (2008) presented an analysis of an occultation by Pluto observed in several places in USA on 18 March 2007.

From five stations, they derived the geometry of the event by providing the mid-time of the event at 10:53:49±00:01 (giving $\Delta t = -344.1$s) and an impact parameter of 1319 ± 4 km for the Multiple Mirror Telescope Observatory (MMTO).

According to the geometry of the event, the South solution ($\rho = -1319$ km) has to be adopted, giving the offset related to JPL DE436 + PLU055 ephemeris of $\Delta\alpha\cos\delta = 10.7 \pm 0.3$ mas and $\Delta\delta = 0.8 \pm 0.2$mas.

Appendix B.6: Occultation of 23 June 2011

Gulbis et al. (2015) presented a grazing occultation by Pluto observed in IRTF (Mauna Kea Observatory) on 23 June 2011. They derived an impact parameter of 1138 ± 3 km and a mid-time of the event at 11:23:03.07 UT (±0.10 s).

The single chord leads to two possible solutions providing the following offset related to JPL DE436 + PLU055 ephemeris:

	North	South
$\Delta\alpha\cos\delta$ (mas)	16.1	5.3
$\Delta\delta$ (mas)	5.5	106.1

According to Gulbis et al. (2015), the North solution has to be adopted. Finally, the offset is $\Delta\alpha\cos\delta = 16.1 \pm 0.1$ mas and $\Delta\delta = 5.5 \pm 0.1$mas, assuming the estimated precision of the timing and the impact parameter.

Appendix B.7: Occultation of 04 May 2013

Olkin et al. (2015) presented the occultation by Pluto on 4 May 2013 observed in South America.

They derived the mid-time of the event at 08:23:21.60±0.05s (giving Δt = 99.8s) and an impact parameter of 370 ± 5 km for the LCOGT in Cerro Tololo.

From these circumstances, we derived an offset related to JPL DE436 + PLU055 ephemeris of $\Delta\alpha\cos\delta = 18.7 \pm 0.1$ mas and $\Delta\delta = 8.4 \pm 0.2$mas

Appendix B.8: Occultation of 23 July 2014

Pasachoff et al. (2016) published the observation of two occultations in Mont John (New Zealand) on June 2014. They provided the timing and impact parameter for the two occultations.

The fitted impact parameter for 23 July is $\rho = 480 \pm 120$km providing two possible solutions and the mid-time of the occultation 14:24:31±4s is derived from the ingress and egress times at 50% and corresponds to $\Delta t = -88.1$s.

Each solution provides the following offset related to JPL DE436 + PLU055 ephemeris:

	North	South
$\Delta\alpha\cos\delta$ (mas)	30.3	22.9
$\Delta\delta$ (mas)	3.7	44.9

According to the precisions of the mid-time and of the impact parameter, the estimated precision of the offset is 4.0 mas for $\Delta\alpha\cos\delta$ and 5.2 mas for $\Delta\delta$.

Appendix B.9: Occultation of 24 July 2014

Pasachoff et al. (2016) also provided circumstances of the occultation on 24 July 2014 in Mont John Observatory.

The fitted impact parameter is $\rho = 510 \pm 140$km providing two possible solutions and the mid-time of the occultation 11:42:29±8s is derived from the ingress and egress times at 50% and corresponds to $\Delta t = 9.1$s.

Each solution provides the following offset related to JPL DE436 + PLU055 ephemeris:

	North	South
$\Delta\alpha \cos\delta$ (mas)	3.4	11.3
$\Delta\delta$ (mas)	29.1	-14.6

According to the precisions of the mid-time and of the impact parameter, the estimated precision of the offset is 7.7 mas for $\Delta\alpha \cos\delta$ and 6.1 mas for $\Delta\delta$.

Appendix B.10: Occultation of 29 June 2015

Pasachoff et al. (2017) presented the occultation by Pluto on 29 June 2015.

They derived the mid-time of the event at 16:52:50 (giving $\Delta t = -111.4$s) and an impact parameter of −53.1 km for the Mont John Observatory in New Zealand.

From these circumstances, we derived an offset of $\Delta\alpha \cos\delta = 22.1$mas and $\Delta\delta = 12.7$mas related to JPL DE436 + PLU055 ephemeris. The precision of the offset cannot be determined since the precision in mid-time and in the impact parameter are not indicated.

Table B.1: Besselian elements for occultations listed in the appendix derived with Gaia DR2 for the star's position and JPL DE436 + PLU055 for Pluto's ephemeris.

T_0	x_0	y_0	x'	y'	H	α_s	δ_s
1988-06-09 10:39:17.1	0.006535856	-0.390599080	-242.990271254	-4.176391160	-47.003163462	223.041508925	0.750884462
2002-07-20 01:43:39.8	-0.015137748	0.078729716	-221.595155776	-42.613814665	45.303191676	255.075123563	-12.694996935
2002-08-21 07:00:32.0	0.091629552	-0.047418125	-41.470159949	-80.186411178	-27.314474978	254.705972362	-12.858853587
2006-06-12 16:25:05.8	0.008081468	-0.393907343	-320.357408358	-6.588025106	39.386450596	265.300310118	-15.692941450
2007-03-18 10:59:33.1	-0.283497691	0.985999061	92.267892934	26.509008184	-58.153737570	268.773723165	-16.476135950
2011-06-23 11:23:48.2	-0.043316318	0.403059932	-320.782100593	-34.487845936	50.562763031	276.481160400	-18.801937982
2013-05-04 08:21:41.8	0.013860759	-0.136954904	-137.646799082	-13.969616086	16.003277103	281.968884350	-19.690120815
2014-07-23 14:25:59.1	0.110372760	-0.614706119	-300.130385882	-53.903828467	-20.940785660	282.382245191	-20.373331983
2014-07-24 11:42:19.9	0.075661748	-0.419500350	-297.988040527	-53.754831391	-22.209299195	282.360471376	-20.376972931
2015-06-29 16:54:41.4	0.106938572	-0.628240925	-318.341422110	-54.232339089	-2.294494383	285.206150857	-20.694717628

Notes. T_0 is the UT time of the closest approach, x_0, y_0 are the coordinates of the shadow axis in the fundamental plane at T_0 (in Earth's radius unit), x', y' are the rate of change in x and y at T_0 (in Earth's radius per day), H is the Greenwich Hour Angle of the star at T_0 (in degrees), and α_s, δ_s are the right ascension and declination of the star (in degrees).

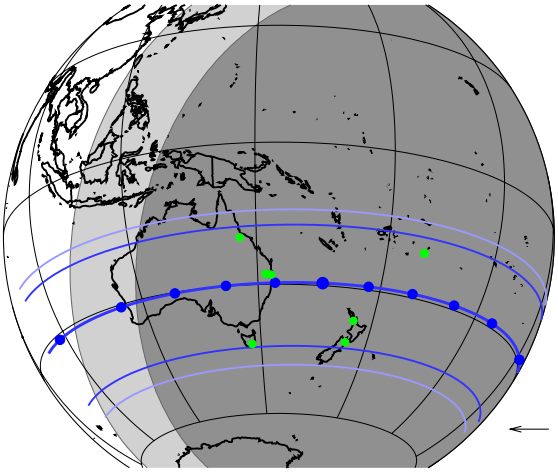

(a) 1988-06-09

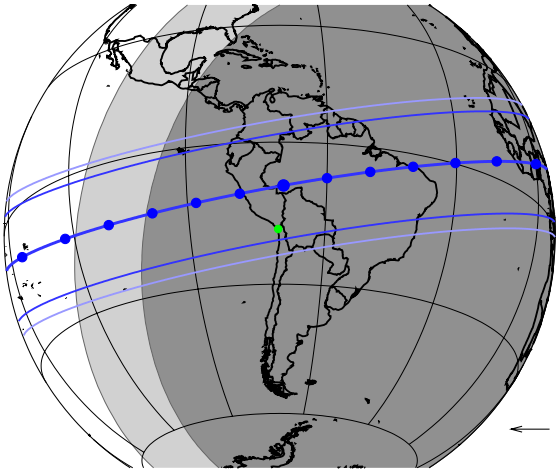

(b) 2002-07-20

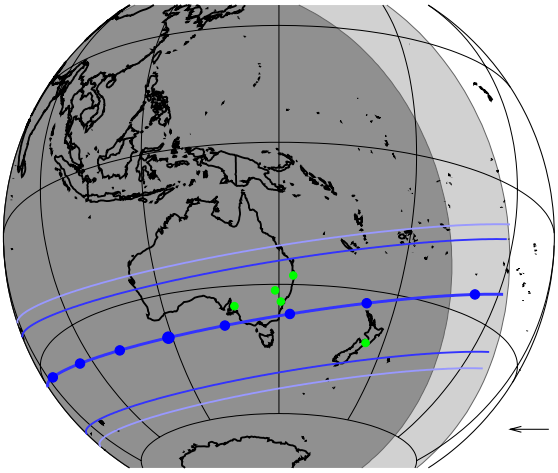

(c) 2006-06-12

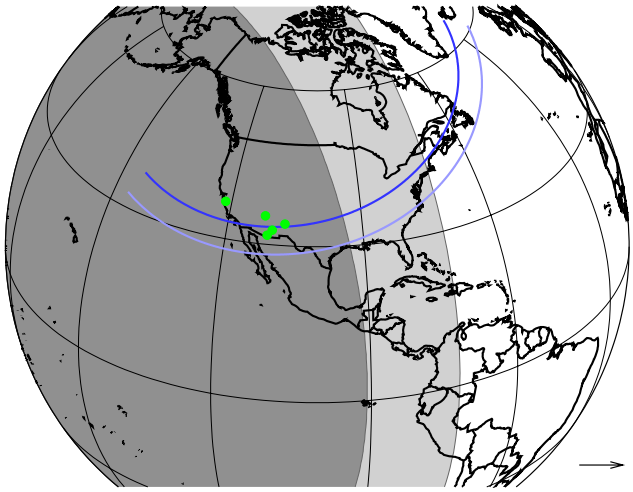

(d) 2007-03-18

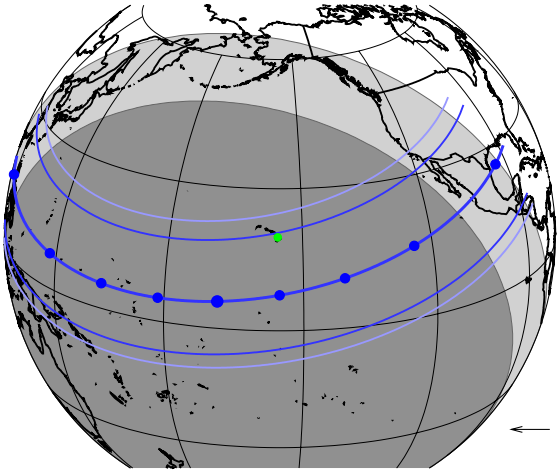

(e) 2011-06-23

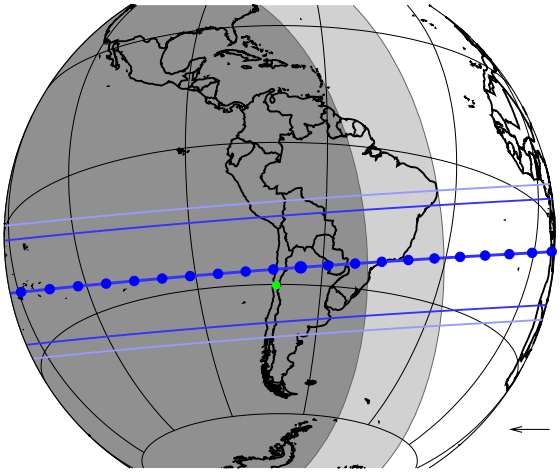

(f) 2013-05-04

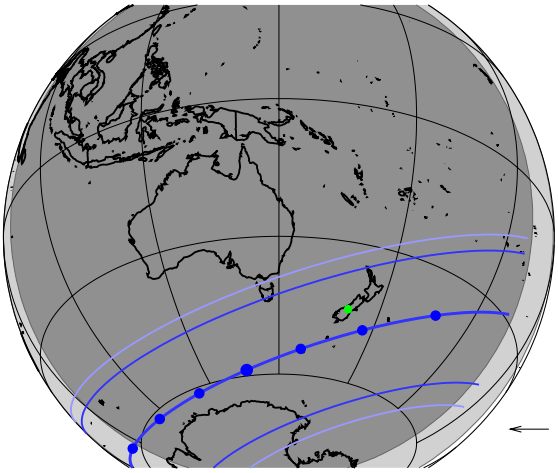

(g) 2014-07-23 (North solution)

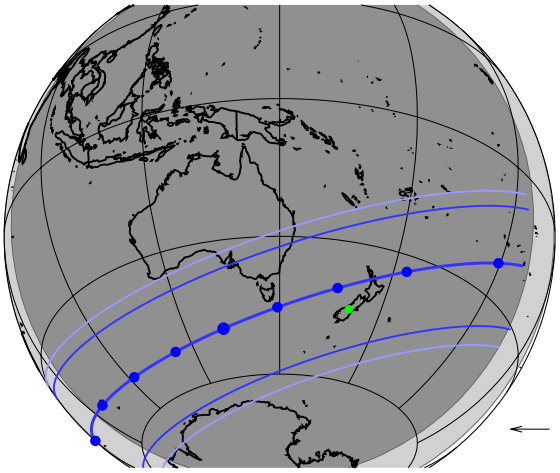

(h) 2014-07-23 (South solution)

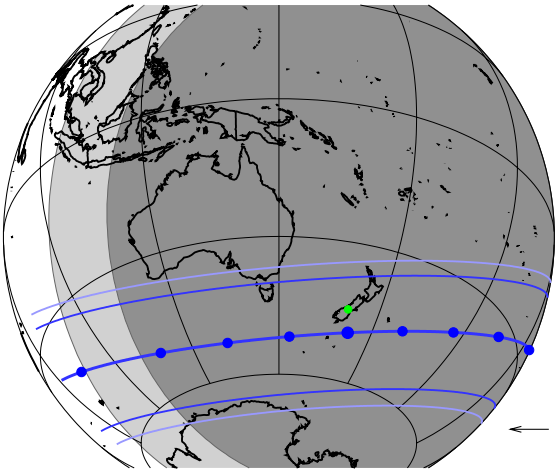

(i) 2014-07-24 (North solution)

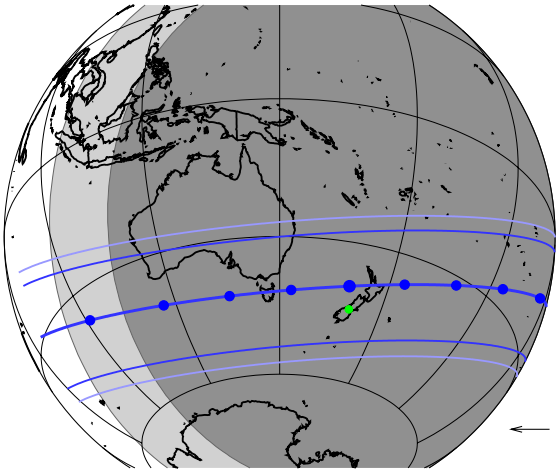

(j) 2014-07-24 (South solution)

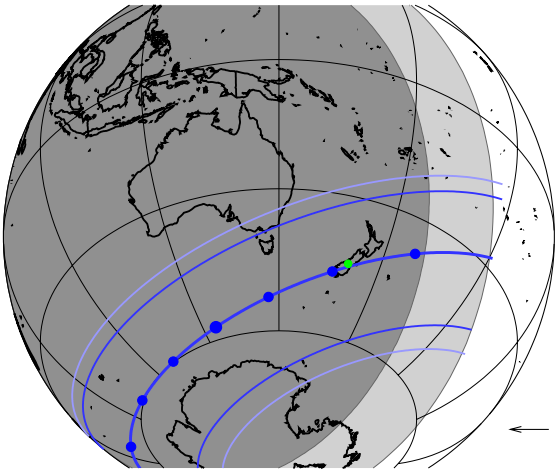

(k) 2015-06-29

Fig. B.1: Reconstruction of Pluto's shadow trajectories on Earth for occultations presented in other publications from 1988 to 2015. The legend is similar to Fig.5.

The Astrophysical Journal Letters, 819:L38 (8pp), 2016 March 10 doi:10.3847/2041-8205/819/2/L38

PLUTO'S ATMOSPHERE FROM THE 2015 JUNE 29 GROUND-BASED STELLAR OCCULTATION AT THE TIME OF THE NEW HORIZONS FLYBY*

B. Sicardy[1], J. Talbot[2], E. Meza[1], J. I. B. Camargo[3,4], J. Desmars[5], D. Gault[6,7], D. Herald[2,7,8], S. Kerr[2,9], H. Pavlov[7], F. Braga-Ribas[3,4,10], M. Assafin[11], G. Benedetti-Rossi[3], A. Dias-Oliveira[3], A. R. Gomes-Júnior[11], R. Vieira-Martins[3], D. Bérard[1], P. Kervella[1,12], J. Lecacheux[1], E. Lellouch[1], W. Beisker[13], D. Dunham[7], M. Jelínek[14,15], R. Duffard[15], J. L. Ortiz[15], A. J. Castro-Tirado[15,16], R. Cunniffe[15], R. Querel[17], P. C. Yock[18], A. A. Cole[19], A. B. Giles[19], K. M. Hill[19], J. P. Beaulieu[20], M. Harnisch[2,21], R. Jansen[2,21], A. Pennell[2,21], S. Todd[2,21], W. H. Allen[2], P. B. Graham[2,22], B. Loader[2,7], G. McKay[2], J. Milner[2], S. Parker[23], M. A. Barry[2,24], J. Bradshaw[7,25], J. Broughton[2], L. Davis[6], H. Devillepoix[26], J. Drummond[27], L. Field[2], M. Forbes[2,22], D. Giles[6,28], R. Glassey[29], R. Groom[30], D. Hooper[2], R. Horvat[6], G. Hudson[2], R. Idaczyk[2], D. Jenke[31], B. Lade[31], J. Newman[8], P. Nosworthy[6], P. Purcell[8], P. F. Skilton[2,32], M. Streamer[8], M. Unwin[2], H. Watanabe[33], G. L. White[6], and D. Watson[2]

[1] LESIA/Observatoire de Paris, PSL, CNRS UMR 8109, University Pierre et Marie Curie, University Paris-Diderot, 5 place Jules Janssen, F-92195 Meudon Cédex, France; bruno.sicardy@obspm.fr
[2] Occultation Section of the Royal Astronomical Society of New Zealand (RASNZ), Wellington, New Zealand
[3] Observatório Nacional/MCTI, R. General José Cristino 77, Rio de Janeiro—RJ, 20.921-400, Brazil
[4] Laboratório Interinstitucional de e-Astronomia—LIneA, Rua Gal. José Cristino 77, Rio de Janeiro, RJ 20921-400, Brazil
[5] IMCCE/Observatoire de Paris, 77 Avenue Denfert Rochereau, Paris, F-75014, France
[6] Western Sydney Amateur Astronomy Group (WSAAG), Sydney, NSW, Australia
[7] International Occultation Timing Association (IOTA), PO Box 7152, Kent, WA 98042, USA
[8] Canberra Astronomical Society, Canberra, ACT, Australia
[9] Astronomical Association of Queensland, QLD, Australia
[10] Federal University of Technology—Paraná (UTFPR/DAFIS), Rua Sete de Setembro, 3165, CEP 80230-901, Curitiba, PR, Brazil
[11] Universidade Federal do Rio de Janeiro, Observatório do Valongo, Ladeira do Pedro Antônio 43, CEP 20080-090, Rio de Janeiro, Brazil
[12] Unidad Mixta Internacional Franco-Chilena de Astronomía (CNRS UMI 3386), Departamento de Astronomía, Universidad de Chile, Camino El Observatorio 1515, Las Condes, Santiago, Chile
[13] IOTA/ES, Bartold-Knaust-Strasse 8, D-30459 Hannover, Germany
[14] Astronomical Institute of the Czech Academy of Sciences, Fričova 298, CZ-25165 Ondřejov, Czech Republic
[15] Instituto de Astrofísica de Andalucía-CSIC, Aptd 3004, E-18080, Granada, Spain
[16] Departamento de Ingeniería de Sistemas y Automática, E.T.S. de Ingenieros Industriales, Universidad de Málaga, Unidad Asociada al CSIC, Málaga, Spain
[17] National Institute of Water and Atmospheric Research (NIWA), Lauder, New Zealand
[18] Department of Physics, University of Auckland, Private Bag 92019, Auckland, New Zealand
[19] School of Physical Sciences, University of Tasmania, Private Bag 37, Hobart, TAS 7001, Australia
[20] Sorbonne Universités, Université Pierre et Marie Curie et CNRS, UMR 7095, Institut d'Astrophysique de Paris, 98 bis bd Arago, F-75014 Paris, France
[21] Dunedin Astronomical Society, Dunedin, New Zealand
[22] Wellington Astronomical Society (WAS), Wellington, New Zealand
[23] Backyard Observatory Supernova Search (BOSS), Oxford, Canterbury, New Zealand
[24] Electrical and Information Engineering Department, University of Sydney, Camperdown, NSW 2006, Australia
[25] Samford Valley Observatory, QLD, Australia
[26] International Centre for Radio Astronomy Research (ICRAR), and the Department of Applied Geology, Curtin University, Bentley, WA 6102, Australia
[27] Possum Observatory, Patutahi, New Zealand
[28] Penrith Observatory, Western Sydney University, Sydney, NSW, Australia
[29] Canterbury Astronomical Society, Christchurch, New Zealand
[30] Astronomical Society of Western Australia, P.O. Box 421, Subiaco, Perth, WA 6904, Australia
[31] Stockport Observatory, Astronomical Society of South Australia, Stockport, SA, Australia
[32] Mornington Peninsula Astronomical Society, Mount Martha, VIC, Australia
[33] Japan Occultation Information Network (JOIN), Japan
Received 2016 January 20; accepted 2016 February 25; published 2016 March 10

ABSTRACT

We present results from a multi-chord Pluto stellar occultation observed on 2015 June 29 from New Zealand and Australia. This occurred only two weeks before the NASA New Horizons flyby of the Pluto system and serves as a useful comparison between ground-based and space results. We find that Pluto's atmosphere is still expanding, with a significant pressure increase of 5 ± 2% since 2013 and a factor of almost three since 1988. This trend rules out, as of today, an atmospheric collapse associated with Pluto's recession from the Sun. A central flash, a rare occurrence, was observed from several sites in New Zealand. The flash shape and amplitude are compatible with a spherical and transparent atmospheric layer of roughly 3 km in thickness whose base lies at about 4 km above Pluto's surface, and where an average thermal gradient of about 5 K km^{-1} prevails. We discuss the possibility that small departures between the observed and modeled flash are caused by local topographic features (mountains) along Pluto's limb that block the stellar light. Finally, using two possible temperature profiles, and extrapolating

* Partly based on observations made with the ESO WFI camera at the 2.2 m Telescope (La Silla), under program ID 079.A-9202(A) within the agreement between the ON/MCTI and the Max Planck Society, with the ESO camera NACO at the Very Large Telescope (Paranal), under program ID 089.C-0314 (C), and at the Pico dos Dias Observatory/LNA, Brazil.

our pressure profile from our deepest accessible level down to the surface, we obtain a possible range of 11.9–13.7 μbar for the surface pressure.

Key words: Kuiper belt objects: individual (Pluto) – occultations – planets and satellites: atmospheres – techniques: photometric

1. INTRODUCTION

Ground-based stellar occultations probe Pluto's atmosphere at radii ranging from $r \sim 1190$ km from the planet center (pressure $p \sim 10$ μbar) up to $r \sim 1450$ km ($p \sim 0.1$ μbar). In a previous work (Dias-Oliveira et al. 2015, DO15 hereafter), we analyzed high signal-to-noise ratio occultations observed in 2012 and 2013, and derived stringent constraints on Pluto's atmospheric profiles (density, pressure and temperature profiles), and on Pluto's radius ($R_P = 1190 \pm 5$ km, assuming no troposphere). We also found a pressure increase of $6 \pm 1\%$ between 2012 and 2013.

Here we analyze a stellar occultation, observed on 2015 June 29 from Australia and New Zealand, which occurred two weeks before the NASA New Horizons (NH hereafter) flyby of the Pluto system. Our goals are: (1) assess further pressure changes between 2013 and 2015 (eventually providing useful constraints on Pluto's seasonal models); (2) analyze the central flash that was detected for the first time ever from multiple stations. It constrains the thermal structure of a layer immediately above Pluto's surface, its possible departure from sphericity and/or presence of hazes; and (3) constrain the pressure at Pluto's surface. Besides serving as a useful comparison with the NH results, our work is one more benchmark in the long-term survey of Pluto's atmosphere over the forthcoming years.

2. THE 2015 JUNE 29 OCCULTATION

The prediction procedures are described in DO15, Assafin et al. (2010), and Benedetti-Rossi et al. (2014). The event was monitored from Australia and New Zealand (Table 1), from which we obtained eight occultation detections. The reconstructed occultation geometry is displayed in Figure 1, see also Table 2. The light curves were obtained from classical aperture photometry, after correction of low frequency variations (caused by changing sky conditions) by means of nearby reference stars, when available. The resulting light curves $\phi(t)$ give the total flux from the star and Pluto's system, normalized to unity outside the occultation, as a function of time t (Figure 2). The observed flux ϕ can be written:

$$\phi = (1 - \phi_P) \cdot F_\star + \phi_P, \quad (1)$$

where $F_\star$ is the (useful) stellar flux alone, normalized between zero and unity. Thus, ϕ_P and $1 - \phi_P$ are the contributions of Pluto's system and the unocculted stellar flux to ϕ, respectively.

The quantity ϕ_P is in principle measured independently when Pluto and the occulted star are angularly resolved, providing $F_\star$. It is difficult in practice and requires high photometric accuracy on the star, Pluto and nearby reference stars hours or days away from the event. During that time, sky and instrument conditions may vary. Moreover, for data taken without a filter (broadband), chromatic dependence of the extinction adds further systematic biases, especially if calibrations are not made at the same airmass.

One station that went deep into Pluto's shadow (BOOTES-3, broadband, Castro-Tirado et al. 2012) obtained calibration images hours before the event, as the star and Pluto were marginally resolved. However, the overlap of the star and Pluto images prevents the useful determination of the Pluto/star ratio at the required accuracy (1% or better). Moreover the airmass variation (1.1 during calibration versus 1.6 during the occultation) introduces unmodeled chromatic effects due to color differences between the star and Pluto. More images taken the following night at very high airmass (3.6) do not provide further constraints on ϕ_P.

One light curve (Dunedin) was affected by nonlinearity caused by a so-called "γ factor" (Poynton 1997) that modified the pixel values to increase the image dynamical range. The (supposedly) reverse transformation provides an event that is globally not deep enough considering its duration, indicating residual nonlinearities. Thus, for this station, we only used the bottom part of the light curve (Figure 2), assuming that in this range, the retrieved flux ϕ is an affine function of the stellar flux, $\phi = a \cdot F_\star + b$.

In spite of the lack of accurate measurements for ϕ_P, the amplifying effect of the central flash still constrains the thermal structure of Pluto's deepest atmospheric layers (see Section 4).

3. PRESSURE EVOLUTION

The DO15 model uses the simplest possible hypotheses, i.e., Pluto's atmosphere (1) is pure nitrogen (N_2), (2) is spherically symmetric, (3) has a time-independent thermal structure, derived itself from the light curves, and (4) is transparent (haze-free). The validity of hypotheses (1)–(3) is discussed in DO15. Hypothesis (4) is discussed later in view of the NH results. Adjusting the pressure p_0 at a reference radius r_0 (for a given event) uniquely defines the molecular density profile $n(r)$, from which synthetic light curves are generated and compared to the data. Note that p_0 monitors the evolution of Pluto's atmospheric pressure as a whole. In practice, most of the contribution to the fits comes from the half-light level ($F_\star \sim 0.5$, $r \sim 1295$ km, $p \sim 1.7$ μbar), with a tapering off above $r \sim 1450$ km ($F_\star \sim 0.9$, $p \sim 0.1$ μbar) and below $r \sim 1205$ km ($F_\star \sim 0.1$, $p \sim 8$ μbar).

The parameters of our model are listed in Table 2 and our simultaneous fits are displayed in Figure 2. They have χ^2 per degree of freedom close to unity, indicating satisfactory fits. Two minor modifications were introduced, relative to the DO15 model. First, we updated for consistency Pluto's mass factor to $GM = 8.696 \times 10^{11}$ m^3 s^{-2} (Stern et al. 2015), instead of 8.703×10^{11} m^3 s^{-2}, causing negligible changes at our accuracy level. Second, we use the NH-derived Pluto radius ($R_P = 1187$ km) as a boundary condition for the DO15 model. This new value modifies (at a few percent level) the retrieved pressure at a given radius compared to DO15. Moreover, changing R_P translates vertically all the profiles near the surface by an equivalent amount. In other words, all the quantities of interest (pressure, density, temperature) are well defined in terms of altitude above the surface, if not in absolute radius.

Table 1
Circumstances of Observations

Site	Lat. (d:m:s) Lon. (d:m:s) Altitude (m)	Telescope Instrument Filter	Exp. Time/ Cycle (s)	Observers Remarks
Melbourne Australia	37 50 38.50 S 145 14 24.40 E 110	0.20 m CCD/clear	0.32 0.32	J. Milner occultation detected
Spring Hill Greenhill Obs. Australia	42 25 51.55 S 147 17 15.49 E 650	Harlingten/1.27 m EMCCD/B	0.1 0.1	A. A. Cole, A. B. Giles K. M. Hill occultation detected
Blenheim1 New Zealand	41 32 08.59 S 173 57 25.09 E 18	0.28 m CCD/clear	0.64 0.64	G. McKay occultation detected
Blenheim2 New Zealand	41 29 36.27 S 173 50 20.72 E 38	0.40 m CCD/clear	0.32 0.32	W. H. Allen occultation detected
Martinborough New Zealand	41 14 17.04 S 175 29 01.18 E 73	0.25 m CCD/B	0.16 0.16	P. B. Graham occultation detected
Oxford New Zealand	43 18 36 S 172 13 08 E 66	0.35 m CCD/clear	1.28 1.28	S. Parker occultation detected, partially cloudy, not yet analyzed
Darfield New Zealand	43 28 52.90 S 172 06 24.04 E 210	0.25 m CCD/clear	0.32 0.32	B. Loader occultation detected, flash
Christchurch New Zealand	43 31 41 S 172 34 54 E 16	0.15 m CCD/clear	0.25 0.25	R. Glassey occultation detected not yet analyzed
BOOTES-3 station Lauder New Zealand	45 02 17.39 S 169 41 00.88 E 370	Yock-Allen/0.6 m EMCCD/clear	0.34368 0.34463	M. Jelínek occultation detected, flash
Dunedin New Zealand	45 54 31. S 170 28 46. E 118	0.35 m CCD/clear	5.12 5.12	A. Pennell, S. Todd M. Harnisch, R. Jansen occultation detected, flash
Glenlee Australia	23:16:09.6 S 150:30:00.8 E 50	0.30 m CCD/clear	0.32 0.32	S. Kerr no occultation detected
Reedy Creek Australia	28 06 29.9 S 153 23 52.0 E 65	0.25 m CCD/clear	0.64 0.64	J. Broughton no occultation detected
Linden Australia	33 42 30.0 S 150 29 43.5 E 583	0.76 m, 0.2 m CCD/clear	0.133, 1.28 0.133, 1.28	D. Gault, R. Horvat L. Davis no occultation detected
Leura Australia	33 43 09.0 S 150 20 53.9 E 903 m	0.20 m visual	n.a. n.a.	P. Nosworthy no occultation detected
Penrith Australia	33 45 43.31 S 150 44 30.30 E 96	0.62 m CCD/Clear	0.533 0.533	D. Giles M. A. Barry no occultation detected
St Clair, Australia	33 48 37 S 150 46 37 E 41	0.35 m CCD/Clear	0.04 0.04	H. Pavlov no occultation detected

Table 1
(Continued)

Site	Lat. (d:m:s) Lon. (d:m:s) Altitude (m)	Telescope Instrument Filter	Exp. Time/ Cycle (s)	Observers Remarks
Murrumbateman Australia	34 57 31.50 S 148 59 54.80 E 594	0.40 m and 0.35 m CCD/clear	0.16 and 2 0.16 and 2	D. Herald, M. Streamer no occultation detected
Nagambie Australia	36 47 05.71 S 145 07 59.14 E 129	0.20 m CCD/clear	0.64 0.64	D. Hooper no occultation detected

The pressures p_0 at $r_0 = 1215$ and 1275 km are given in Table 2. They are useful benchmarks, respectively corresponding to the stratopause (maximum temperature of 110 K), and the half-light level layer. Figure 3 displays the pressure evolution over 2012–2015. The formal error bars assume an invariant temperature profile, but this assumption should not affect the *relative* pressure changes in 2012–2015. Relaxing that constraint, we can retrieve p_0 by inverting individual light curves and testing the effects of the inversion parameters. This yields possible biases estimated to ± 0.2, $\pm$ 0.8 and ± 0.5 μbar in 2012, 2013 and 2015, respectively. We have added for comparison occultation results from 1988 (Yelle & Elliot 1997) and 2002 (Sicardy et al. 2003). They stem from different analyses and may also be affected by biases. However, Figure 3 should capture the main trend of Pluto's atmosphere, i.e., a monotonic increase of pressure since 1988.

4. CENTRAL FLASH

Nearly diametric occultation light curves (but still avoiding the central flash) have flat bottoms (Figure 2). Our ray tracing code shows that near the shadow center, the stellar rays come from a "flash layer" about 3 km in thickness just above $r = 1191$ km, thus sitting 4 km on top of the assumed surface ($R_P = 1187$ km, Figure 3).

Let us denote by F a model for the stellar flux (distinguishing it from the observed flux $F_\star$). Deep inside Pluto's shadow, F is roughly proportional to the local density scale-height, $H_n = -n/(dn/dr) = T/[\mu g/k + (dT/dr)]$, where μ is the molecular weight, g is the acceleration of gravity and k is Boltzmann's constant (DO15). For a spherical atmosphere, we have also $F \propto 1/z$, where z is the distance to the shadow center. Writing $z = \sqrt{\rho^2 + l^2}$, where ρ is the closest approach distance to the shadow center and l is the distance traveled from that point, we obtain:

$$F \propto \frac{H_n}{z} = \frac{T}{\mu g/k + dT/dr} \cdot \left(\frac{1}{\sqrt{\rho^2 + l^2}} \right). \qquad (2)$$

For an approximately pure N_2 atmosphere (corresponding to $\mu = 4.652 \times 10^{-26}$ kg), we obtain $\mu g/k \sim 2$ K km^{-1}. As the thermal gradient dT/dr is several degrees per kilometer at the flash layer (see below), the flash amplitude is significantly controlled by dT/dr.

Our best model minimizes the χ^2 function defined by $\chi^2 = \sum_i \{\phi_i - [(1 - \phi_P)F_i + \phi_P]\}^2/\sigma_i^2$, where σ_i^2 is the variance of ϕ_i associated with the noise for the ith data point.

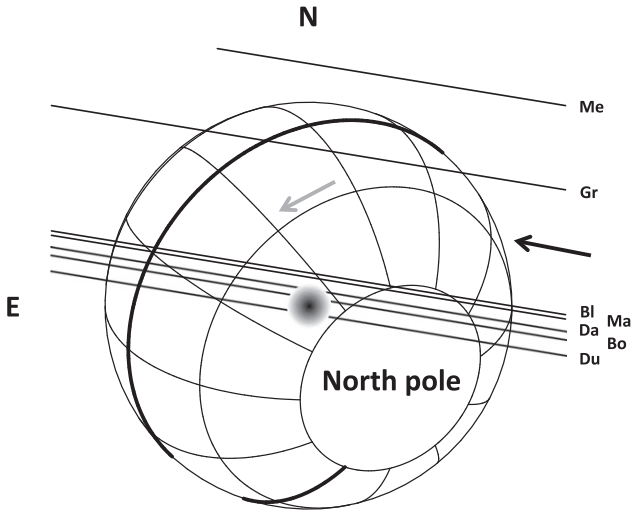

Figure 1. Geometry of the 2015 June 29 Pluto stellar occultation. The stellar motion relative to Pluto (black arrow) is shown for seven stations, Me: Melbourne, Gr: Greenhill, Bl: Blenheim, Ma: Martinborough, Da: Darfield, Bo: BOOTES-3, Du: Dunedin. The J2000 celestial north and east are indicated by N and E, respectively. Pluto's radius is fixed at 1187 km. The equator and prime meridian are drawn as thicker lines, and direction of rotation is along the gray arrow. The shaded region at center indicates the central flash zone.

As we do not measure ϕ_P, we considered it as a free, adjustable parameter. Among the data sets analyzed by DO15, only one had sufficient quality—from the 2012 July 18 ESO Very Large Telescope—to permit a measurement of ϕ_P and thus constrain dT/dr in the deepest accessible layer. It showed that the residual stellar flux, $F_{\rm res}$, at the bottom part of the light curve lay in the range 0.010–0.031, thus imposing a thermal gradient near the surface (and imposing ϕ_P for the other light curves). Since $F_{\rm res}$ was determined to within a factor of three, a large error bar on dT/dr deep in Pluto's atmosphere was obtained, causing difficulties when extrapolating the pressure down to the surface. In doing so, we obtained a possible range $p_{\rm surf} = 10$–12 μbar for the surface pressure in 2012, estimated at $r = 1190 \pm 5$ km.

As F is roughly constant at the bottom of occultation light curves (far from the flash), there is a degeneracy between F and ϕ_P: higher values of ϕ_P can be accommodated by smaller values of F, i.e., smaller H_n. This is not true anymore within the flash, as F suffers significant variations. The χ^2-minimization provides both ϕ_P and H_n through $\partial\chi^2/\partial\phi_P = 0$ and $\partial\chi^2/\partial H_n = 0$. Although our ray tracing code generates exact values of F for a

Table 2
Input Parameters and Results

Input Parameters			
Star			
Coordinates at epoch (J2000)[a]	$\alpha = 19^{\rm h}\ 00^{\rm m}\ 49\overset{\rm s}{.}4801 \pm 11$ mas, $\delta = -20^{\rm d}\ 41'\ 40\overset{''}{.}801 \pm 17$ mas		
B, V, R, K magnitudes[b]	12.8, 12.2, 12.8, 10.6		
Pluto Parameters			
Pluto's geocentric distance, shadow velocity[c]	4.77070×10^9 km, 24.1 km s^{-1} (at 16:53 UT)		
Pluto's mass and radius[d] (Stern et al. 2015)	$GM = 8.696 \times 10^{11}$ m^3 s^{-2}, $R_P = 1187$ km		
Sub-observer and sub-solar latitudes[d]	$B = +51\overset{\circ}{.}66$, $B' = +51\overset{\circ}{.}46$		
Pluto's north pole position angle[d]	$P = +228\overset{\circ}{.}48$		
Results			
Thermal Profile (Input Values for the DO15 Model)			
r_1, T_1, $dT/dr\,(r_1)$, r_2, T_2	1191.1 km, 81.7 K, 8.5 K km^{-1}, 1217.3 km, 109.7 K		
r_3, T_3, r_4, T_4	1302.4 km, 95.5 K, 1392.0 km, 80.6 K		
$c1$, $c2$, $c3$	$1.42143317 \times 10^{-3}$, $2.52794288 \times 10^{-3}$, $-2.12108557 \times 10^{-6}$		
$c4$, $c5$, $c6$	$-4.88273258 \times 10^{-7}$, $-7.04714651 \times 10^{-8}$, -3.3716945×10^{4}		
$c7$, $c8$, $c9$	7.7271133×10^{1}, $-5.86944930 \times 10^{-2}$, $1.48175559 \times 10^{-5}$		
Longitudes and Latitudes of Half-light Sub-occultation Points[e]			
Ingress			
Greenhill (154°E, 06°N, MT), Blenheim (120°E, 28°N, MT), Martinborough (119°E, 28°N, MT)			
Darfield (115°E, 30°N, MT), Bootes-3 (113°E, 31°N, MT), Dunedin (108°E, 32°N, MT)			
Egress			
Greenhill (232°E, 37°S, MT), Blenheim (280°E, 35°S, ET), Martinborough (282°E, 34°S, ET)			
Darfield (286°E, 33°S, ET), Bootes-3 (288°E, 33°S, ET), Dunedin (293°E, 31°S, ET)			
Pressure (Quoted Errors at 1σ Level[f])			
	2012 July 18	2013 May 04	2015 June 29
Pressure at 1215 km, p_{1215}	6.07 ± 0.04 μbar	6.61 ± 0.03 μbar	6.94 ± 0.08 μbar
Pressure at 1275 km, p_{1275}	2.09 ± 0.015 μbar	2.27 ± 0.01 μbar	2.39 ± 0.03 μbar
Surface pressure (Figure 3)			$11.9 - 13.7$ μbar
Astrometry			
Time of closest approach to shadow center (UT)		Closest approach to shadow center	
BOOTES-3: $16^{\rm h}\ 52^{\rm m}\ 54.8 \pm 0\overset{\rm s}{.}1$		45.9 ± 2 km N of shadow center	
Dunedin: $16^{\rm h}\ 52^{\rm m}\ 56.0 \pm 0\overset{\rm s}{.}1$		44.6 ∓ 2 km S of shadow center	
Geocenter: $16^{\rm h}\ 55^{\rm m}\ 04.9 \pm 0\overset{\rm s}{.}1$		3911.5 ± 2 km N of shadow center	

Notes.
[a] See title's footnote for information.
[b] Zacharias et al. (2013), Cutri et al. (2003), Cutri (2012).
[c] PLU043/DE433 ephemeris.
[d] Using Pluto's north pole J2000 position: $\alpha_{\rm p} = 08^{\rm h}\ 52^{\rm m}\ 12\overset{\rm s}{.}94$, $\delta_{\rm p} = -06^{\rm d}\ 10'\ 04\overset{''}{.}8$ (Tholen et al. 2008).
[e] MT—morning terminator, ET—evening terminator.
[f] Formal errors (except for the surface pressure). Possible systematic biases are ±0.2, ±0.8, and ±0.5 μbar in 2012, 2013, and 2015, respectively (Section 3).

given model, it is convenient here (for sake of illustration) to note that F is essentially proportional to H_n (Equation (2)), so that $\partial F/\partial H_n \sim F/H_n$. Detailed calculations show that at minimum χ^2, we have $\partial^2\chi^2/\partial H_n^2 = (2\,N/H_n^2)(\sigma_F^2/\sigma^2)$ for $F \ll 1$, where $\sigma_F^2 = \overline{F^2} - \overline{F}^2$ is the variance of F (the bars denoting average values) and N is the number of data points. Thus, the relative error on the scale-height is $\delta H_n/H_n \sim (\sigma/\sigma_F)/\sqrt{N}$, which is small if the flash (and then σ_F) is large.

Since F increases as H_n increases or ρ decreases, H_n and ρ are correlated. However, the full width at half maximum (FWHM) of the flash is proportional to ρ, while H_n controls homogeneously the flash amplitude, keeping its FWHM constant. This disentangles the effects of H_n and ρ. More importantly, the BOOTES-3 and Dunedin stations exhibit flashes with similar amplitudes (Figure 2). This robustly forces the two stations to be symmetrically placed with respect to the

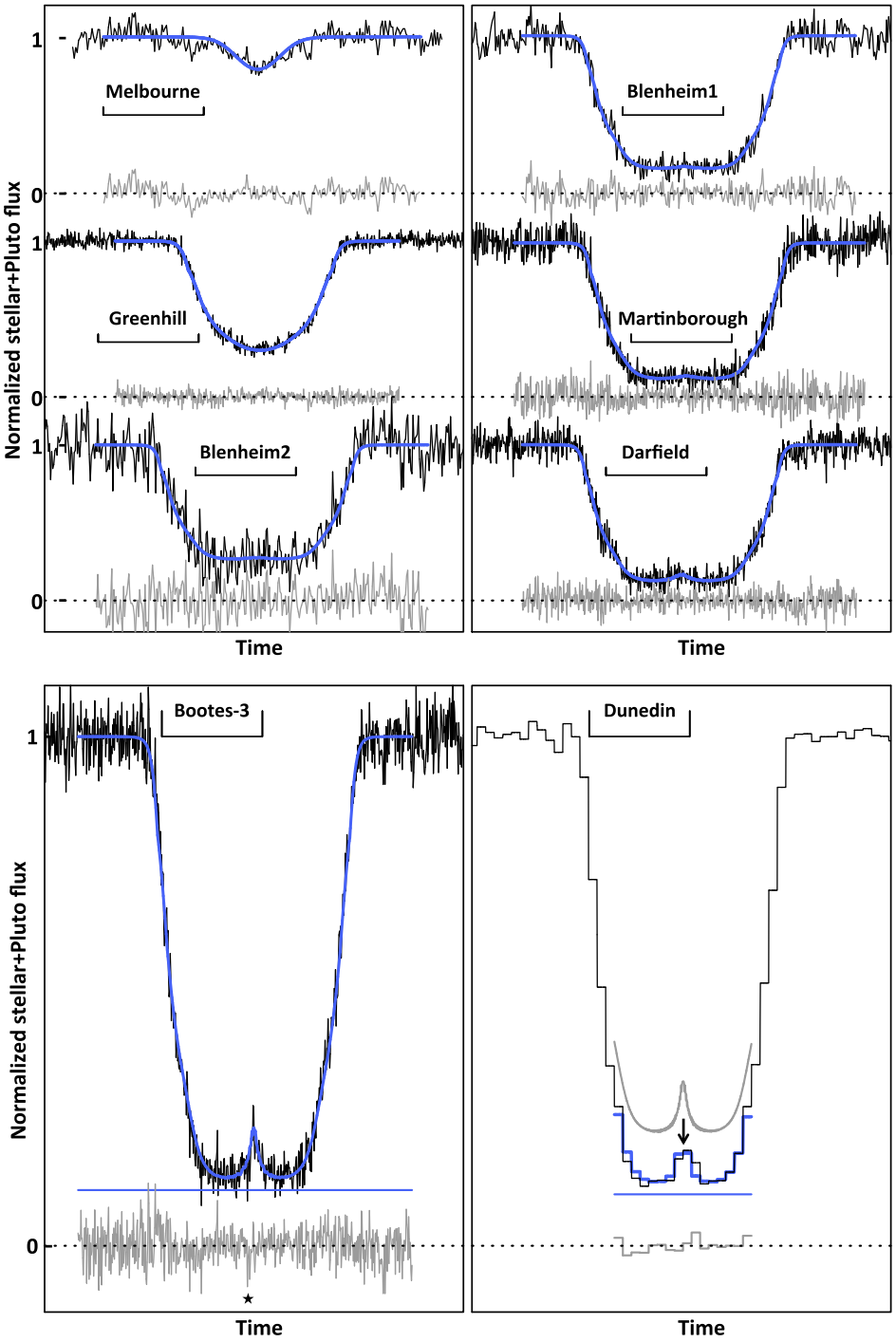

Figure 2. Simultaneous fits to our 2015 June 29 occultation light curves. The intervals under each name correspond to the time-span $16^{h}\ 52^{m}$–$16^{h}\ 53^{m}$ UT. The model is overplotted in blue, and the residuals are in gray. In the lower panels, the blue horizontal lines are the fitted values of Pluto's contribution to the flux (ϕ_P, Equation (1)). The star symbol under the BOOTES-3 curve indicates a small flux deficit relative to the model. In the Dunedin panel, the smooth curve is the central flash at high resolution, before convolution by the exposure time (5.12 s), and vertically shifted for better viewing.

shadow center (Figure 1), thus imposing $\rho \approx 45 \pm 2$ km for both stations, independently of H_n (Table 2).

The χ^2-value is minimized for $dT/dr = 8.5 \pm 0.25$ K km^{-1} at 1191 km in our model. This particular value must be considered with caution, as it is not representative of the entire flash layer. Due to the functional dependence of $T(r)$ (a branch of hyperbola, DO15), the gradient dT/dr varies rapidly around 1191 km. The average thermal gradient in the flash layer is in fact ~5 K km^{-1}, consistent with a previous flash analysis (Olkin et al. 2014). Besides, it is typical of what is expected from the heating by methane (D. Strobel 2015, private communication). Other functional forms of $T(r)$ could be tested, but this remains outside the scope of this paper. We note in passing that our best 2015 fit implies a residual stellar flux $F_{\rm res} = 0.028$ (Figure 2) that is compatible with the possible range (0.010–0.031) mentioned earlier for 2012.

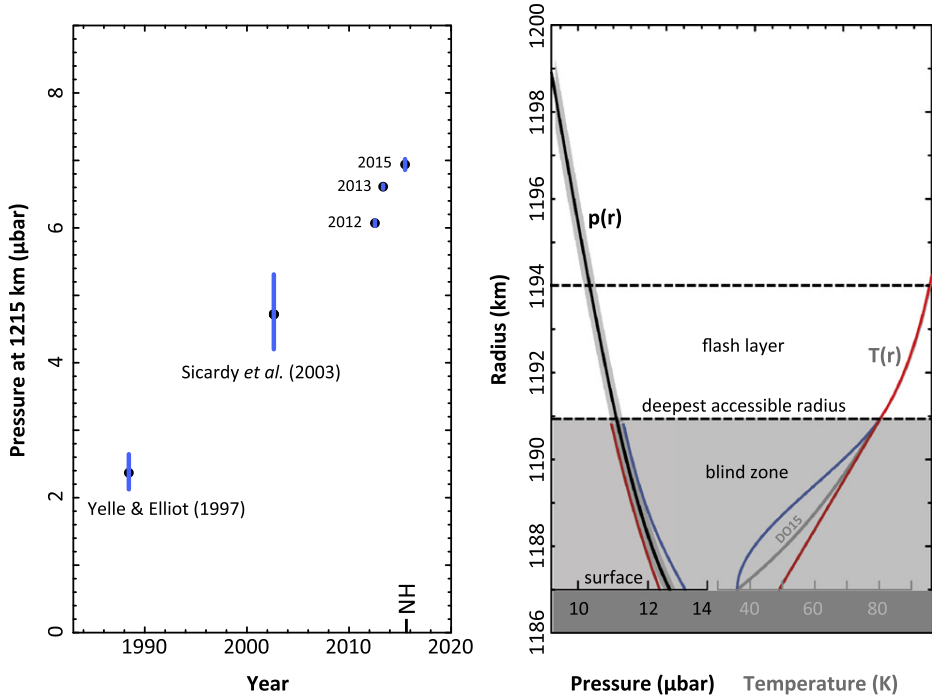

Figure 3. Left: Pluto's atmospheric pressure at $r = 1215$ km vs. time in 2012, 2013, and 2015 (our work), and from previous works (Yelle & Elliot 1997; Sicardy et al. 2003), with 1σ error bars. The New Horizons Pluto flyby date (NH) is essentially coincident with our most recent dot. Right: our best pressure profile $p(r)$ for 2015 June 29, with formal 1σ-error domain. The central flash layer roughly lies between the two horizontal dashed lines, above the blind zone below 1191 km. Two possible extrapolations (beside the DO15 model) of temperature profiles $T(r)$ into the blind zone are shown: one with a thermal gradient that reaches zero at the surface (shallow troposphere, blue), and one with a constant gradient 8.5 K km^{-1} (red).

Our spherical, transparent atmospheric model essentially captures the correct shape and height of the central flash (Figure 2). A closer examination of that figure reveals a small flux deficit (relative to the model) at the left side of the BOOTES-3 flash. It remains marginal, however, considering the general noise level. That said, it could be caused by an unmodeled departure of the flash layer from sphericity, but this is not anticipated. An atmosphere of radius r rotating at angular velocity ω has an expected oblateness $\epsilon \sim r^3\omega^2/2GM \sim 10^{-4}$ for a rotation period of 6.4 days, $r \sim 1190$ km and Pluto's GM. Such oblateness causes a diamond-shaped caustic (Elliot et al. 1977) with a span of $4\epsilon r < \sim 1$ km in the shadow plane. This is negligible considering the closest approach distances involved here (~45 km). Moreover, expected zonal winds of less than a few meters per second near 1191 km (Vangvichith 2013; Zalucha & Michaels 2013) would have even smaller effects. More complex distortions may arise, as varying thermal conditions along Pluto's limb may slightly tilt the local iso-density layer, but its modeling remains outside the scope of this paper.

A possible explanation of the small discrepancy is that the primary and/or secondary stellar images hit topographic features while moving around Pluto's limb. Curvature effects strongly stretch the images parallel to the limb during the central flash, by a ratio equal to the flash layer radius (1191 km) divided by the closest approach distance, about 45 km. From the star magnitudes (Table 2 and Kervella et al. 2004), we estimate its diameter as 33 μas, or 0.76 km projected at Pluto. The length of the stellar image is then $0.76 \times (1191/45) \sim 20$ km. It moves at about 4 km above the surface, which is comparable to the local topographic features reported from NH (Stern et al. 2015). It is thus possible that part of the stellar flux was partially blocked by mountains, causing the small observed drop. This can be tested by studying the topography derived from NH, noting that the primary and secondary stellar images at BOOTES-3 probed regions near longitude 190°E and latitude 20°S, and 10°E and 20°N, respectively, during the flash.

Finally, NH images reveal tenuous hazes with normal optical depth $\tau_N \sim 0.004$ and scale-height $H = 50$ km (Stern et al. 2015). This implies an optical depth along the line of sight of $\tau \sim \sqrt{2\pi r/H} \cdot \tau_N \sim 0.05$, which is indistinguishable from the noise level (Figure 2), supporting our transparent-atmosphere hypothesis.

5. SURFACE PRESSURE

Figure 3 displays our best pressure profile, with $p_{1191} = 11.0 \pm 0.2$ μbar at the deepest accessible level. To estimate the surface pressure, we need to extrapolate $p(r)$ into the blind zone. Two possible temperature profiles are considered, beside the DO15 model (Figure 3). One has a temperature gradient in the blind zone that tends to zero at the surface, where $p_{\rm surf} = 13.0$ μbar and $T_{\rm surf} = 36$ K. This describes a shallow troposphere that is in vapor pressure equilibrium with the surface, an example of a locally sublimating N_2 frost layer. The other profile has a constant gradient of 8.5 K km^{-1}, with $p_{\rm surf} = 12.6$ μbar and $T_{\rm surf} = 49$ K. Such warmer regions are indeed observed on Pluto (Lellouch et al. 2000), and they do not sublimate due to the absence of free N_2 frost. Considering the formal error bar ± 0.2 μbar on p_{1191}, we obtain a range of 12.4–13.2 μbar for the surface pressure under hypotheses (1)–(4) of Section 3, and

11.9–13.7 μbar accounting for the already discussed possible bias of $\sim\pm0.5$ μbar. Other thermal profiles could be considered at this point, but they would not change significantly our result due to the proximity ($\sim$4 km) of our deepest accessible level to the surface, leaving little freedom for $p_{\rm surf}$.

6. CONCLUSIONS

The 2015 June 29 stellar occultation provided a snapshot of Pluto's atmosphere, after years of similar observations. Moreover, this was the first event with multi-chord cuts into the central flash. Assuming a spherical and transparent atmosphere as in DO15, we satisfactorily fit all the light curves, including the central flash part (Figure 2).

We find that Pluto's atmospheric pressure has been increasing monotonically since 1988, with an augmentation of $5 \pm 2\%$ between 2013 and 2015, and an overall factor of almost three between 1988 and 2015 (Figure 3). This trend between 1988 and 2013 was confirmed by independent works by Elliot et al. (2003), Pasachoff et al. (2005), Person et al. (2013), Young (2013), Bosh et al. (2015). It is now extended to 2015 and rules out an ongoing atmospheric collapse associated with Pluto's recession from the Sun. This is consistent with high thermal inertia models with a permanent N_2 ice cap over Pluto's north pole, that preclude such collapse (Olkin et al. 2015). Other possible models where N_2 condenses on an unlit cap might announce a pressure decrease in the forthcoming years (Hansen et al. 2015). Further monitoring with occultations and a detailed analysis of the NH data will allow discrimination between those scenarios.

The central flash comes from a $\sim$3 km thick layer whose base is 4 km on top of Pluto's surface. The amplitude of the flash is consistent with an average thermal gradient of $\sim$5 K km^{-1} in that layer. Small departures from the model might be caused by topographic features along Pluto's limb that block the stellar images.

Extrapolating possible temperature profiles down to the surface, we find a possible range of 11.9–13.7 μbar for the surface pressure. This is larger than, but compatible with the entry value 11 ± 1 μbar derived from the NH radio occultation experiment (Hinson et al. 2015; Gladstone et al. 2016). At this stage, more detailed investigations of both techniques should be undertaken to see if this difference is significant, or the result of unaccounted effects. In any case, the two techniques validate each other, an excellent prospect for future monitoring of Pluto's atmosphere from ground-based occultations.

We acknowledge support from the French grant "Beyond Neptune II" ANR-11-IS56-0002, and Labex ESEP. The research leading to these results has received funding from the European Research Council under the European Community's H2020 (2014-2020/ERC Grant Agreement 669416 "LUCKY STAR"). E.M. acknowledges support from the contrato de subvención 205-2014-Fondecyt, Peru. J.I.B.C. acknowledges the CNPq/PQ2 fellowship 308489/2013-6. M.A. acknowledges the FAPERJ grant 111.488/2013, CNPq/PQ2 fellowship 312394/2014-4, and grants 482080/2009-4 and 473002/2013-2. J.L.O. acknowledges funding from Proyecto de Excelencia de la Junta de Andalucía J. A.2012-FQM1776, Spanish grant AYA-2014-56637-C2-1-P, and FEDER funds. A.J.C.T. acknowledges support from the Junta de Andalucía (Project P07-TIC-03094) and Univ. of Auckland and NIWA for installing of the Spanish BOOTES-3 station in New Zealand, and support from the Spanish Ministry Projects AYA2012-39727-C03-01 and 2015-71718R Development of the Greenhill Observatory was supported under the Australian Research Council's LIEF funding scheme (project LE110100055). We thank C. Harlingten for the use of the H127 Telescope, and D. and M. Warren for long term support. We thank L. Beauvalet for running the ODIN Pluto's system model, M. W. Buie, S. Gwyn, and L. A. Young for providing pre-event Pluto's ephemeris and astrometry, D. P. Hinson and D. F. Strobel for most useful discussions, and the reviewer for useful comments.

REFERENCES

Assafin, M., Camargo, J. I. B., Vieira Martins, R., et al. 2010, A&A, 515, A32
Benedetti-Rossi, G., Vieira Martins, R., Camargo, J. I. B., Assafin, M., & Braga-Ribas, F. 2014, A&A, 570, A86
Bosh, A. S., Person, M. J., Levine, S. E., et al. 2015, Icar, 246, 237
Castro-Tirado, A. J., Jelínek, M., Gorosabel, J., et al. 2012, ASInC, 7, 313
Cutri, R. M. 2012, yCat, 2, 311
Cutri, R. M., Skrutskie, M. F., van Dyk, S., et al. 2003, yCat, 2, 246
Dias-Oliveira, A., Sicardy, B., Lellouch, E., et al. 2015, ApJ, 811, 53
Elliot, J. L., Ates, A., Babcock, B. A., et al. 2003, Natur, 424, 165
Elliot, J. L., French, R. G., Dunham, E., et al. 1977, ApJ, 217, 661
Gladstone, G. R., Stern, S. A., Ennico, K., et al. 2016, Sci, in press
Hansen, C. J., Paige, D. A., & Young, L. A. 2015, Icar, 246, 183
Hinson, D. P., Linscott, I., Tyler, L., et al. 2015, BAAS, 47, 105.01
Kervella, P., Thévenin, F., Di Folco, E., & Ségransan, D. 2004, A&A, 426, 297
Lellouch, E., Laureijs, R., Schmitt, B., et al. 2000, Icar, 147, 220
Olkin, C. B., Young, L. A., Borncamp, D., et al. 2015, Icar, 246, 220
Olkin, C. B., Young, L. A., French, R. G., et al. 2014, Icar, 239, 15
Pasachoff, J. M., Souza, S. P., Babcock, B. A., et al. 2005, AJ, 129, 1718
Person, M. J., Dunham, E. W., Bosh, A. S., et al. 2013, AJ, 146, 83
Poynton, C. 1997, Chapter 6: Gamma (New York: Wiley)
Sicardy, B., Widemann, T., Lellouch, E., et al. 2003, Natur, 424, 168
Stern, S. A., Bagenal, F., Ennico, K., et al. 2015, Sci, 350, aad1815
Tholen, D. J., Buie, M. W., Grundy, W. M., & Elliott, G. T. 2008, AJ, 135, 777
Vangvichith, M. 2013, Thèse de Doctorat, Ecole Polytechnique, France
Yelle, R. V., & Elliot, J. L. 1997, in Pluto and Charon, ed. S. A. Stern, & D. J. Tholen (Tucson, AZ: Univ. Arizona Press), 347
Young, L. A. 2013, ApJL, 766, L22
Zacharias, N., Finch, C. T., Girard, T. M., et al. 2013, AJ, 145, 44
Zalucha, A. M., & Michaels, T. I. 2013, Icar, 223, 819

The Astrophysical Journal, 811:53 (20pp), 2015 September 20 doi:10.1088/0004-637X/811/1/53

PLUTO's ATMOSPHERE FROM STELLAR OCCULTATIONS IN 2012 AND 2013*

A. Dias-Oliveira[1,2], B. Sicardy[2], E. Lellouch[2], R. Vieira-Martins[1,3,4], M. Assafin[5], J. I. B. Camargo[1,4], F. Braga-Ribas[1,6], A. R. Gomes-Júnior[5], G. Benedetti-Rossi[1], F. Colas[3], A. Decock[2,7], A. Doressoundiram[2], C. Dumas[7], M. Emilio[8], J. Fabrega Polleri[9], R. Gil-Hutton[10,11], M. Gillon[12], J. H. Girard[7], G. K. T. Hau[7], V. D. Ivanov[13,14], E. Jehin[12], J. Lecacheux[2], R. Leiva[15], C. Lopez-Sisterna[10], L. Mancini[16,17], J. Manfroid[12], A. Maury[18], E. Meza[2,19], N. Morales[20], L. Nagy[18], C. Opitom[12], J. L. Ortiz[20], J. Pollock[21], F. Roques[2], C. Snodgrass[22], J. F. Soulier[23], A. Thirouin[24], L. Vanzi[15], T. Widemann[2], D. E. Reichart[25], A. P. LaCluyze[25], J. B. Haislip[25], K. M. Ivarsen[2], M. Dominik[26], U. Jørgensen[27], and J. Skottfelt[27,28]

[1] Observatório Nacional/MCTI, Rua General José Cristino 77, Rio de Janeiro—RJ, 20.921-400, Brazil; alexoliveira@on.br
[2] LESIA/Observatoire de Paris, CNRS UMR 8109, Université Pierre et Marie Curie, Université Paris-Diderot, 5 place Jules Janssen, F-92195 Meudon Cédex, France
[3] IMCCE/Observatorie de Paris, 77 Avenue Denfert Rochereau, Paris, F-75014, France
[4] Laboratório Interinstitucional de e-Astronomia—LIneA, Rua General José Cristino, 77, Rio de Janeiro, RJ 20921-400, Brazil
[5] Observatório do Valongo/UFRJ, Ladeira Pedro Antonio 43, Rio de Janeiro—RJ, 20080-090, Brazil
[6] Federal University of Technology—Paraná (UTFPR/DAFIS), R. Sete de Setembro 3165, Curitiba—PR, 80230-901, Brazil
[7] ESO, Alonso de Cordova 3107, Vitacura, 7630355 Santiago, Chile
[8] Observatório Astronômico Departamento de Geociências, Universidade Estadual de Ponta Grossa, Paraná, Brazil
[9] Observatorio Panameño en San Pedro de Atacama (OPSPA), Chile
[10] Complejo Astronómico El Leoncito (CASLEO-CONICET), Av. España 1512 sur, J5402DSP San Juan, Argentina
[11] Universidad Nacional de San Juan, Complejo Universitario "Islas Malvinas," Av. Ignacio de la Roza 590 oeste, J5402DCS—San Juan, Argentina
[12] Institut d'Astrophysique, de Géophysique et Océanographie, Université de Liège, Allée du 6 août 17, B-4000 Liége, Belgium
[13] ESO, Karl-Schwarzschild-Str. 2, D-85748 Garching bei, München, Germany
[14] ESO, Alonso de Cordova 3107, Casilla 19001, Santiago 19, Chile
[15] Instituto de Astrofísica, Facultad de Física, Pontificia Universidad Católica de Chile, Av. Vicuña Mackenna 4860, Santiago 7820436, Chile
[16] Max Planck Institute for Astronomy, Königstuhl 17, D-69117, Heidelberg, Germany
[17] INAF—Osservatorio Astrofisico di Torino, via Osservatorio 20, I-10025—Pino Torinese, Italy
[18] San Pedro de Atacama Celestial Explorations (S.P.A.C.E.), San Pedro de Atacama, Chile
[19] Grupo Astronomía, Facultad de Ciencias, Universidad Nacional de Ingienería, Lima, Peru
[20] Instituto de Astrofísica de Andalucía-CSIC, Apt 3004, E-18080, Granada, Spain
[21] Department of Physics and Astronomy, Appalachian State University, Boone, NC 28608, USA
[22] Planetary and Space Sciences, Department of Physical Sciences, The Open University, Milton Keynes, MK7 6AA, UK
[23] Association Des Étoiles pour Tous, 19 Rue Saint Laurent, Maisoncelles, F-77320 Saint Martin du Boschet, France
[24] Lowell Observatory, 1400 W Mars Hill Rd, Flagstaff, Arizona, USA
[25] Department of Physics and Astronomy, University of North Carolina—Chapel Hill, North Carolina 27599, USA
[26] SUPA, University of St Andrews, School of Physics & Astronomy, North Haugh, St Andrews, KY16 9SS, UK
[27] Niels Bohr Institute, University of Copenhagen, Juliane Maries vej 30, DK-2100 Copenhagen Ø, Denmark
[28] Centre for Electronic Imaging, Department of Physical Sciences, The Open University, Milton Keynes, MK7 6AA, UK
Received 2015 June 22; accepted 2015 August 10; published 2015 September 18

ABSTRACT

We analyze two multi-chord stellar occultations by Pluto that were observed on 2012 July 18th and 2013 May 4th, and respectively monitored from five and six sites. They provide a total of fifteen light curves, 12 of which were used for a simultaneous fit that uses a unique temperature profile, assuming a clear (no haze) and pure N_2 atmosphere, but allowing for a possible pressure variation between the two dates. We find a solution that satisfactorily fits (i.e., within the noise level) all of the 12 light curves, providing atmospheric constraints between ~1190 km (pressure ~11 μbar) and ~1450 km (pressure ~0.1 μbar) from Pluto's center. Our main results are: (1) the best-fitting temperature profile shows a stratosphere with a strong positive gradient between 1190 km (at 36 K, 11 μbar) and $r = 1215$ km (6.0 μbar), where a temperature maximum of 110 K is reached; above it is a mesosphere with a negative thermal gradient of -0.2 K km^{-1} up to ~1390 km (0.25 μbar), where the mesosphere connects itself to a more isothermal upper branch around 81 K; (2) the pressure shows a small (6%) but significant increase (6σ level) between the two dates; (3) without a troposphere, Pluto's radius is found to be $R_P = 1190 \pm 5$ km. Allowing for a troposphere, R_P is constrained to lie between 1168 and 1195 km; and (4) the currently measured CO abundance is too small to explain the mesospheric negative thermal gradient. Cooling by HCN is possible, but only if this species is largely saturated. Alternative explanations like zonal winds or vertical compositional variations of the atmosphere are unable to explain the observed mesospheric negative thermal gradient.

Key words: methods: data analysis – methods: observational – planets and satellites: atmospheres – planets and satellites: physical evolution – planets and satellites: terrestrial planets – techniques: photometric

1. INTRODUCTION

Stellar occultations are a very powerful tool for discovering and studying, among other things, tenuous atmospheres around remote bodies. Pluto's atmosphere was discovered using this technique (Hubbard et al. 1988; Elliot et al. 1989;

* Partly based on observations made with the ESO camera NACO at the Very Large Telescope (Paranal), under program IDs 089.C-0314(C) and 291.C-5016. The prediction uses observations made with the WFI camera at the 2.2 m Telescope, under program ID 079.A-9202(A).

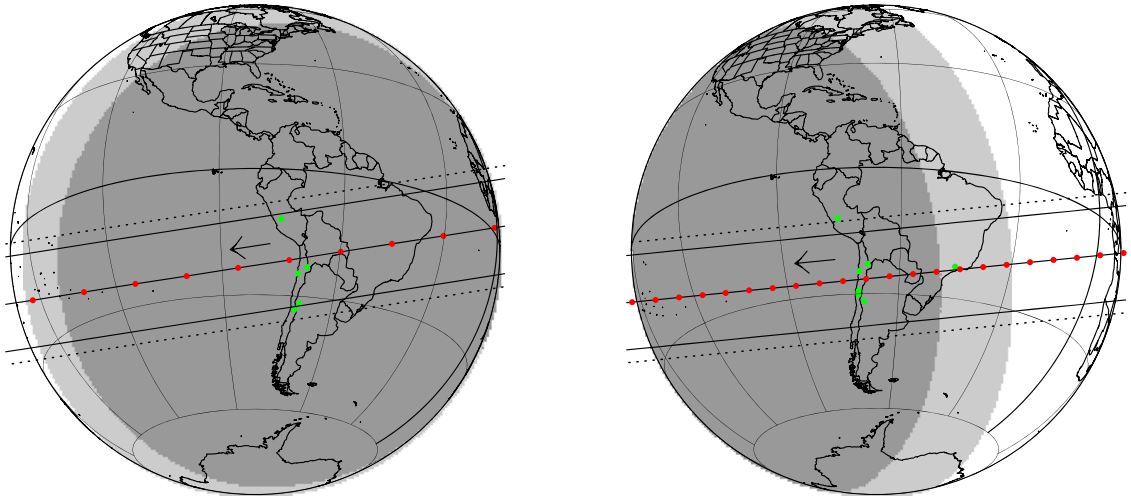

Figure 1. Post-occultation, reconstructed paths of Pluto's shadow for the two events studied here. The red dots indicate the shadow center every minute and the arrows show the direction of motion. The green dots mark the sites where data were obtained. The black solid lines correspond to the half-light stellar level, while the dotted lines correspond to the 1% stellar drop, thus marking the practical region of detectability of the occultations. Left: the 2012 July 18 event. The first red dot at right is at 04^h09^m UT, the last one at left corresponds to 04^h18^m UT. Right: the 2013 May 4 event. The first red dot at right is at 08^h12^m UT, and the last one at left corresponds to 08^h33^m UT.

Brosch 1995), and its spectacular twofold expansion between 1988 and 2003 was also revealed using stellar occultations (Elliot et al. 2003; Sicardy et al. 2003). Other trans-Neptunian objects were explored with this technique and so far none of them have exhibited atmospheres at the 10 nbar pressure level (that is, three orders of magnitude smaller than for Pluto). This includes Charon (Sicardy et al. 2006), Eris (Sicardy et al. 2011), Makemake (Ortiz et al. 2012), and Quaoar (Braga-Ribas et al. 2013).

All of those bodies have sizes and surface gravities that are comparable to those of Pluto, within a factor of two. As such, the derived upper limits constrain the physical conditions necessary for the appearance and maintenance of atmospheres around a body with a given ice composition and heliocentric distance.

Here we analyze results derived from two Pluto stellar occultations (2012 July 18 and 2013 May 04) that provide signal-to-noise ratios (S/Ns) that are among the best ever obtained during such events. They are furthermore combined with well-sampled multi-chord coverages, providing a good absolute radial scale for the atmosphere extension.

We use the simplest possible model, assuming a spherically symmetric, clear (no haze), pure N_2 atmosphere with a constant temperature both horizontally and with time. Our model satisfactorily fits 12 of the selected light curves and provides accurate density, pressure, and temperature profiles for radii between 1190 km (11 μbar pressure level) and 1450 km ($\sim$0.1 μbar) from Pluto's center, while also providing constraints on Pluto's radius.

As Pluto's atmospheric pressure is dominated by the vapor equilibrium pressure at its surface, it is very sensitive to tiny changes of temperature and the available amount of exposed ice. This induces strong seasonal effects over the Plutonian year (Hansen & Paige 1996) that can be monitored and analyzed through stellar occultations (Young 2013). In that context, our data reveal a small but significant increase of pressure between 2012 and 2013, which can be used for constraining current Pluto seasonal models (see Olkin et al. 2015 for a detailed analysis).

Our results are obtained in the context of the forthcoming flyby of the dwarf planet by the NASA *New Horizons* spacecraft in 2015 July. Consequently, they can be used as a basis of comparison with the *New Horizons* findings.

2. THE 2012 AND 2013 PLUTO STELLAR OCCULTATIONS

2.1. Predictions

From astrometric observations along Pluto's path onto the sky plane between 2008 and 2015, performed at the European Southern Observatory (ESO)'s 2.2 m telescope, Assafin et al. (2010) made accurate predictions for stellar occultations involving the dwarf planet and its satellites.

In this context, the two occultations analyzed here, one on 2012 July 18 and the other on 2013 May 04, stood out as promising events, owing to the magnitudes of the candidate stars and to the presence of several potential observing sites along the shadow path.

Follow-up astrometric observations of the stars were carried out in order to improve the predictions. These observations were made with the 1.6 m (Perkin-Elmer) and 0.6 m (Boller & Chivens) telescopes, at Pico dos dias Observatory (OPD, IAU code 874), and they are done wherever possible within our access time.

Moreover, 16 positive detections of other occultations by Pluto, which occured between 2005 and 2013, were used to improve Pluto's ephemeris offset (see Benedetti-Rossi et al. 2014 for details).

Days before the event, we carried out observations with Pluto and the occulted star present in the same field of view of our charge-coupled devices (CCDs) in order to minimize systematic biases like catalog errors.

2.2. Observations

The 2012 July 18 Pluto occultation was observed near its zenith from five sites in South America (Figure 1). The circumstances and technical details of the observations are

Table 1
Circumstances of the 2012 July 18 Pluto Occultation

Site	Lat. (d:m:s) Lon. (d:m:s) alt (m)	Telescope Instrument/Filter	Exp. Time/Cycle (s)[a]	Observers
Observatory UC (Santa Martina)	33:16:09.0 S 70:32:04.0 W 1450	0.4 m CCD/clear	1.0/1.0	R. Leiva Espinoza
Cerro Burek	31:47:12.4 S 69:18:24.5 W 2591	ASH[b] 0.45 m SBIG-STL11000/clear	13.0/15.7	N. Morales
Paranal	24:37:31.0 S 70:24:08.0 W 2635	VLT Yepun 8.2 m NACO/H	0.2/0.2	J. Girard
San Pedro de Atacama	22:57:12.3 S 68:10:47.6 W 2397	ASH2 0.4 m SBIG-STL11000/clear	13.0/15.44	N. Morales
Huancayo	12:02:32.2 S 75:19:14.7 W 3344	0.2 m CCD/clear	10.24/10.24[c] 5.12/5.12[c]	E. Meza

Notes.
[a] Cycle is defined as the exposure time plus the readout time, which is also known as dead time. Observations with the same exposure time and cycle have no dead time.
[b] ASH—Astrograph for the Southern Hemisphere.
[c] Exposure time was changed at 04:11:46 UT.

provided in Table 1. The 2013 May 04 event was recorded from six sites, under similar conditions (Figure 1), providing ten light curves (Table 2). Various astrometric, photometric, and physical parameters associated with each event are summarized in Table 3.

Figure 2 displays the reconstructed geometries of each event, showing the Plutocentric latitudes and altitudes probed by the primary stellar image at each site; see the Appendix for details. For Paranal (2012 July 18), for the sake of illustration we plot the trajectories of both primary and secondary stellar images. As we shall mention later, the contribution of the secondary image is small but not negligible compared to that of the primary image near the shadow center. Note that in the ingress, the primary image probes the hemisphere that is in summer conditions, and at the egress the image probes the hemisphere that is in winter conditions.

2.3. Photometry and Calibration

Classical bias, dark, flat-field, and sky subtraction provide the occultation light curves displayed in Figures 3–5. In all cases, a reference star brighter that is than the target was used to correct for low-frequency sky-transparency variations.

As expected, the best S/N light curve was obtained at Paranal on 2012 July 18, using the NAOS-CONICA[28] (NACO; Lenzen et al. 2003; Rousset et al. 2003) camera attached to the 8.2 m "Yepun" Very Large Telescope (VLT) of the ESO, in open-loop (without adaptive optics), at a continuous rate of 5 frames per second (achieved windowing the detector in "cube mode" as in Girard et al. 2010) in the *H*-band. Moreover, this is the only data set for which we have an accurate photometric calibration, which allows us to subtract the contribution of Pluto and Charon from the occultation light curve (see below). As such, the 2012 July 18 data provide the best constraints on Pluto's atmospheric structure. However, on average the 2013 May 04 light curves have better S/Ns than those of 2012 July 18, as well as a better spatial sampling, thus providing better constraints on the absolute vertical scale of the atmosphere.

Calibration images were taken with NACO some 20 minutes before the 2012 event. They show resolved images of Pluto, Charon, and the star under excellent seeing conditions (Figure 6). Digital coronagraphy (Assafin et al. 2008, 2009) was used to remove the star contamination from Pluto and Charon images. Classical aperture photometry finally provided the Pluto + Charon flux relative to the occulted star. This allows us to estimate the residual stellar flux in the deepest part of the 2012 July 18 occultation at Paranal, with a value that varied from 2.3 ± 0.8% to 1.8 ± 0.8% of its unocculted value in the central part of the occultation (Figure 7).

3. MODELING OF PLUTO'S ATMOSPHERE

The general idea for modeling Pluto's atmosphere is to use an iterative procedure, combining both direct ray-tracing and inversion approaches. We first invert our best S/N light curve to retrieve Pluto's atmospheric density, pressure, and temperature profiles (see the Appendix and Vapillon et al. 1973). The retrieved temperature profile is then used as a guide to generate, through direct ray-tracing, synthetic occultation light curves that are simultaneously fitted to all of the observed light curves obtained at a given date. This pins down the location of Pluto's shadow center relative to the occultation chords for both the 2012 and 2013 events (Figure 2). Finally, the inversion of the best light curve is performed again and the procedure is resumed. This iterative process eventually provides the accurate geometry of each event, as well as consistent density, pressure, and temperature profiles that best fit all of the occultation light curves.

Simplifying assumptions are made in our procedure (possible caveats are discussed later): (i) Pluto and its atmosphere are spherically symmetric, and all quantities

[28] NAOS-CONICA is Nasmyth Adaptive Optics System (NAOS) and Near-Infrared Imager and Spectrograph (CONICA).

Table 2
Circumstances of the 2013 May 04 Pluto Occultation

Site	Lat. (d:m:s) Lon. (d:m:s) alt meters	Telescope Instrument/Filter	Exp. Time/Cycle (s)	Observers
Cerro Burek	31:47:12.4 S 69:18:24.5 W 2591 m	ASH 0.45 m SBIG-STL11000/clear	6/8	J.L. Ortiz N. Morales
CASLEO (Leoncito)	31:47:55.6 S 69:17:44.9 W 2,492 m	Jorge Sahade 2.15 m CCD/R	5/6.8	R. Gil-Hutton C. Lopez-Sisterna
Cerro Tololo	30:10:03.4 S 70:48:19.0 W 2,207	PROMPT[a] 0.4 m P1, P3, P4, P5 CCD/clear	5/8 P3 offset 2 s P4 offset 4 s P5 offset 6 s	J. Pollock
La Silla	29 15 21.276 S 70 44 20.184 W 2,336	Danish 1.54 m Lucky Imager/Z (λ> 650 nm CCD/iXon response)	0.1/0.1 Several interruptions due to image cube writing	L. Mancini
La Silla	29 15 16.59 S 70 44 21.82 W 2,315	TRAPPIST[b] 0.6 m CCD/clear	4.5/6	E. Jehin, A. Decock, M. Gillon C. Opitom
Pico dos Dias	22 32 07.8 S 45 34 57.7 W 1,811	B&C[c] 0.6 m CCD/I	5/5.40	M. Assafin, A. Ramos-Gomes Jr
Ponta Grossa	25 05 24.00 S 50 09 36.00 W 909	Meade 16 0.4 m CCD/clear	5 Technical Problems	M. Emilio
Cerro Paranal	24:37:31.0 S 70:24:08.0 W 2635	UT4 Yepun 8.2 m NACO/H	0.2/0.2	G. Hau
San Pedro de Atacama	22:57:12.3 S 68:10:47.6 W 2397	Caisey 0.5 m f/8 CCD/V	3/4.58	A. Maury
	...	Caisey 0.5 m f/6.8 CCD/B	4/4.905	L. Nagy
	...	CAO[d] 0.4 m CCD/R	4/6.35	J.F. Soulier
	...	ASH2 0.4 m	STL11000 Technical problem	N. Morales
	...	OPSPA[e] 0.3 m CCD/clear	5/11.1	J. Fabrega Polleri
Huancayo	12:02:32.2 S 75:19:14.7 W 3344	Meade 8 0.2 m CCD/clear	10.24/10.24 Negative chord (no occultation)	E. Meza

Notes.
[a] PROMPT: Panchromatic Robotic Optical Monitoring and Polarimetry Telescopes.
[b] Jehin et al. (2011).
[c] B&C: Boller & Chivens.
[d] CAO: Campo Catino Observatory.
[e] OPSPA: Observatorio Panameño en San Pedro de Atacama.

Table 3
Parameters of the Two Occultations

	2012 July 18	2013 May 04
Star coordinates[a]	$\alpha = 18^{h}32^{m}14\overset{s}{.}6720$ $\delta = -19^{d}24'19\overset{''}{.}295$	$\alpha = 18^{h}47^{m}52\overset{s}{.}5322$ $\delta = -19^{d}41'24\overset{''}{.}3738$
Ephemeris	DE413/PLU022	DE413/PLU031
Pluto geocentric distance	4.68244×10^{9} km (at 04:13 UT)	4.76882×10^{9} km (at 08:23 UT)
Sub-observer and sub-solar latitudes[b]	$B = +47.10$ days, $B' = +47.54$ days	$B = +49.95$ days, $B' = +48.64$ days
Pluto's north pole position angle[b]	$P = -56.88$ days	$P = -52.91$ days
Shadow velocity	≈ 23.0 km s^{-1}	≈ 10.6 km s^{-1}
Magnitudes[c]	$V = 14.7$, $R = 13.7$, $K = 10.9$	$V = 14.1$, $R = 14.0$, $K = 12.4$

Notes.
[a] J2000, UCAC2 system.
[b] Assuming Pluto's north pole position (J2000) of Tholen et al. (2008): $\alpha_{p} = 08^{h}52^{m}12\overset{s}{.}94$, $\delta_{p} = -06^{d}10'04\overset{''}{.}8$.
[c] From the NOMAD catalog (Zacharias et al. 2004).

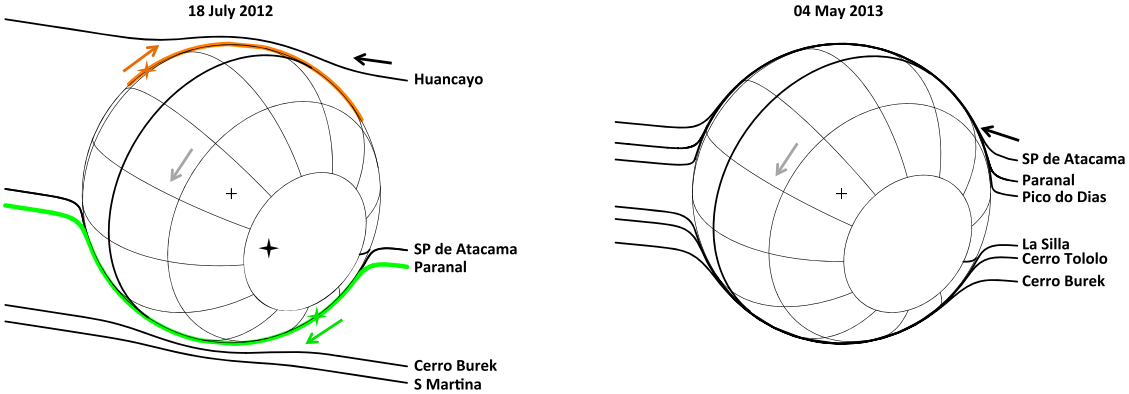

Figure 2. Left: the trajectories of the primary stellar images relative to Pluto, as seen from the five stations used on 2012 July 18; see Table 1. The black arrow shows the general direction of stellar motion. Here, Pluto's stellar motion has an assumed radius of $R_{P} = 1190$ km (see the text), and its center is indicated by the cross symbol. The gray arrow inside the disk indicates the direction of rotation. In the case of Paranal, we have plotted the path of the primary image in green, *and* the associated path of the secondary image in orange (see also Figure 7). The green and orange arrows show the corresponding local stellar motion along Pluto's limb. Note that the two images move in opposite directions. The black star symbol shows the star position as seen from Paranal at a given, arbitrary moment, while the green and orange star symbols indicate the associated primary and secondary images at that time, respectively. Note that the three star symbols and the cross are aligned. Right: the same as the left panel for the 2013 May 04 occultation, with only the paths of the primary stellar images plotted. In both panels, the summer, with Pluto's hemisphere permanently lit, is at right, and the low-insolation winter limb is at left.

depend only on the radius r (defined as the distance to Pluto's body center). (ii) The atmosphere is transparent (no haze present). (iii) It is an ideal gas in hydrostatic equilibrium; in our case, it is a pure molecular nitrogen N_2 atmosphere, neglecting other minor species like methane. (iv) Moreover, we assume that $T(r)$ is time-independent, i.e., the temperature profiles are the same in 2012 and 2013. Once $T(r)$ is derived, as detailed later, the density and pressure profiles $n(r)$ and $p(r)$ are derived from the hydrostatic and ideal gas equations (Equation (5)) once a boundary condition is provided, i.e., the pressure at a given radius. (v) Although $T(r)$ is taken as time-independent, the pressure is not. This is justified by the fact that the pressure is very sensitive to Pluto's surface temperature through the vapor pressure equilibrium equation. For instance, a 1 K temperature increase at the surface results in a twofold increase of pressure or so (Figure 8). Thus, the pressure is a free parameter in our fits. More precisely, Equation (5) requires a boundary condition once $T(r)$ is fixed. So we use the pressure p_r at an arbitrary radius r as a free parameter. We choose $r = 1275$ km for an easier comparison with other works that provide the pressure at that level (see, e.g., Olkin et al. 2015). This level corresponds to a normalized stellar flux of ≈0.45 in the shadow plane. Once p_{1275} is given, the density and pressure profiles $n(r)$ and $p(r)$ are uniquely defined.

We choose the 2012 July 18 occultation light curve obtained at VLT/NACO to perform the first inversion. We use this particular light curve because it has the highest S/N of all (Figure 3), and also because this is the only one for which we have a reliable measurement of the background contribution from Pluto and Charon (Figure 7), which is necessary to correctly invert any occultation light curve. The successive steps of our procedure are as follows:

(1) The inversion reveals a strong increase of temperature just above the surface (stratosphere), followed by a turning point where the temperature reaches a maximum (stratopause), then a region with a mild negative gradient (mesosphere), and finally an isothermal upper branch (see the Appendix and Figure 13). Using the prescriptions described by Equations (4), we adjust the coefficients $c_1,\ldots c_9$, controlling the profile $T(r)$ in order to best-fit the inverted temperature profiles (see Table 4).

(2) Keeping the profile $T(r)$ fixed in shape, we simultaneously fit seven of the light curves obtained on 2013 May 04. The free parameters of that fit are the two coordinates defining the shadow center, the pressure p_{1275} at radius 1275 km, and the value of r_1, the deepest point that we consider in our profile.

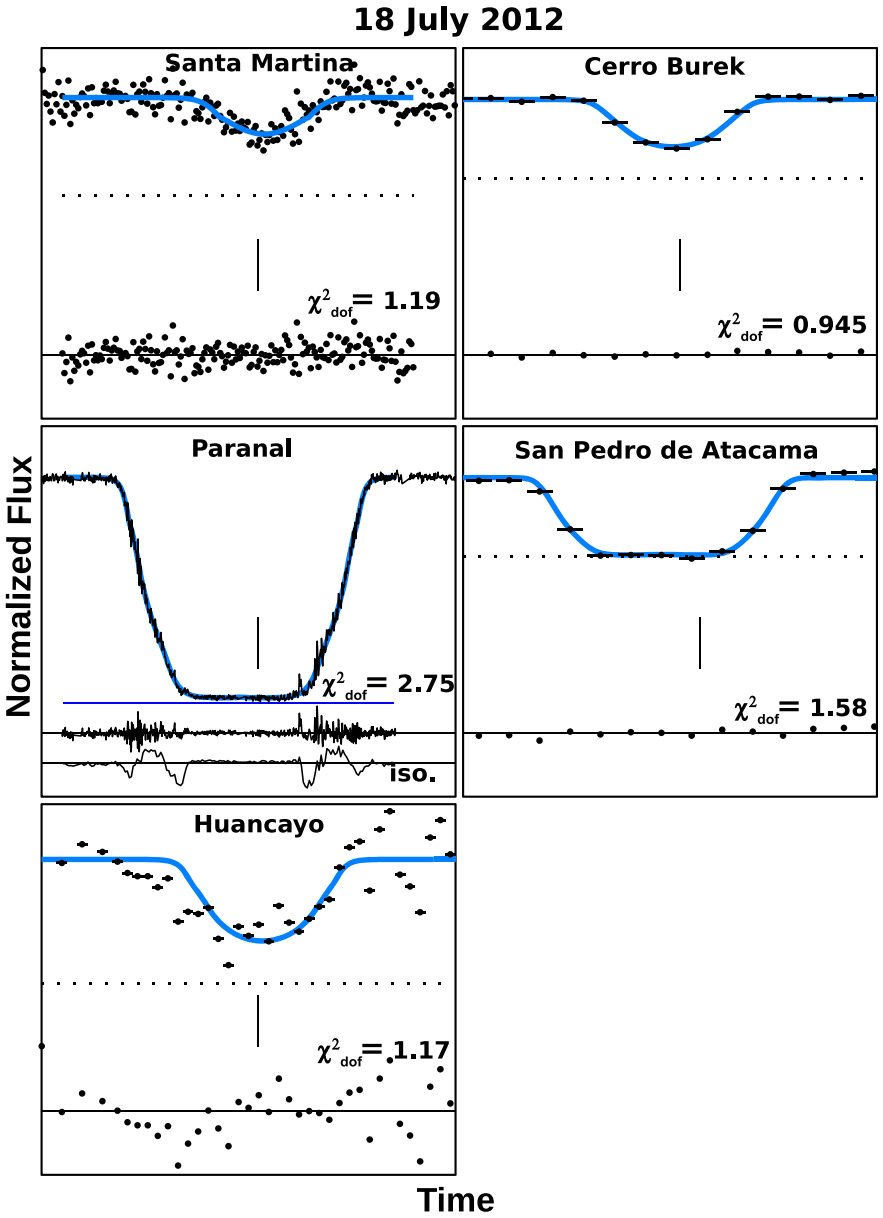

Figure 3. Blue curves are a simultaneous fit to the 2012 July 18 light curves, using the best atmospheric model described in Table 4 and Figure 13. The number at the lower right of each panel is the value of χ^2_{dof} (Equation (11)), i.e., the χ^2 per degree of freedom for each corresponding fit. Each panel spans 3 minutes of data, with the vertical tick marks located at 04:13 UT. All of the light curves show the total flux (star+Pluto+Charon) plotted at the same vertical scale. The horizontal bars on the Cerro Burek, San Pedro de Atacama, and Huancayo data points represent the respective integration times. The zero flux is indicated by the solid horizontal line at the bottom of each panel, together with the residuals (data minus model). The dotted horizontal lines mark the fitted zero stellar fluxes (or equivalently, the Pluto+Charon contribution to the total flux), obtained using our best Pluto atmospheric model. The blue horizontal line in the Paranal panel marks the measured zero stellar flux at that station, the only one at which a photometric calibration was possible (see the text and Figures 6 and 7). In the Paranal panel, we have also added the residuals (labeled "iso.") obtained by forcing an isothermal mesosphere at $T_{iso} = 95.5$ K. The residuals have been averaged over 5 s time intervals and shifted vertically by −0.12 to better show the clear discrepancy between the isothermal mesospheric model and the data. Other values chosen for T_{iso} would result in the same qualitative behavior. In essence, isothermal mesospheres do not provide satisfactory fits to the NACO light curve.

At this stage, when r_1 is varied, all of the other radii, r_2, r_3, and r_4, defining $T(r)$ (see Equation (4)), are changed by the same amount. In other words, the entire profile $T(r)$ is vertically displaced by this amount. Thus, r_1 eventually fixes the absolute vertical scale of the atmospheric profile. Note that r_1 is *not*, a priori, the radius of the stratobase, nor Pluto's surface radius. In practice, the choice of r_1 is made so that the stellar rays from the faint secondary image passing at r_1 have a contribution to the total flux that is negligible compared to the light curve noise level. Thus, taking larger values of r_1 would create artificial discontinuities in the synthetic light curve, while smaller values would require useless computation time. To find Pluto's shadow center, we separate the fit along the direction of the star motion relative to Pluto from the fit perpendicular to that direction. This is because the fit along the star motion is essentially independent of the atmospheric model and is generally more accurate than the fit perpendicular to that direction.

Note that the 2013 light curves generally have a better S/N than those of 2012 (excluding the VLT data set) because of a

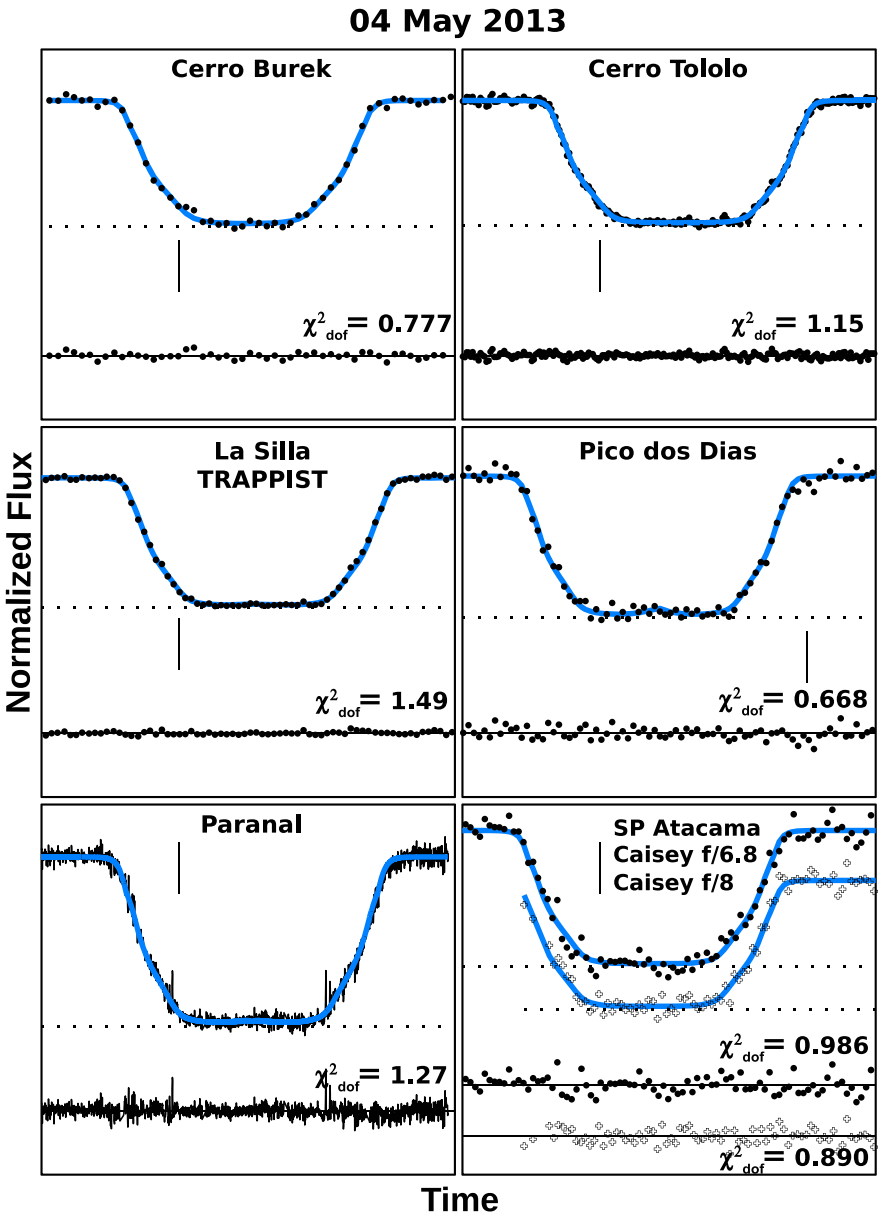

Figure 4. Same as Figure 3 for the 2013 May 04 event. Each panel now represents 6 minutes of data, with the vertical tick mark located at 08:22 UT. Note that the two light curves from San Pedro ("SP") de Atacama have been displaced vertically by ±0.1 for better viewing.

better distribution of the chords (Figure 2). Consequently, the 2013 occultation light curves provide a better constraint for r_1, or equivalently, for the absolute vertical scale of the atmospheric model, than those of 2012.

(3) Fixing r_1 to its value found in step (2), we turn back to the 2012 July 18 data set and simultaneously fit the five corresponding light curves, varying Pluto's shadow center and p_{1275}.

The procedure is then resumed at point (1). It is a converging process that provides consistent solutions for the shape of the profile $T(r)$, the absolute vertical scale for $T(r)$, the centers of Pluto's shadow for both events, and the two boundary conditions p_{1275} for the 2012 July 18 and 2013 May 04 events. This fitting procedure has a total of 12 free parameters: the nine coefficients $c_1,\ldots c_9$, the two coordinates that define Pluto's shadow center, and the pressure p_{1275}.

As commented before, the 2012 July 18 NACO light curve is the only one for which the Pluto + Charon contribution is measured (Figure 7). Thus, the stellar flux was normalized between that value and the full unocculted flux before starting the fit procedure.

For the other light curves, the inverse approach was used: the background Pluto + Charon flux was imposed by linearly adjusting the normalized, synthetic stellar flux to the actual occultation light curve, through a least-squares fit. As the residual stellar flux well inside the shadow is mainly controlled by the density scale height of the deep stratosphere (Equation (15)), this means that the structure of that region is in fact dominated by the NACO, 2012 July 18 data. The other light curves thus mainly serve to constrain the atmospheric structure above that level (mesosphere).

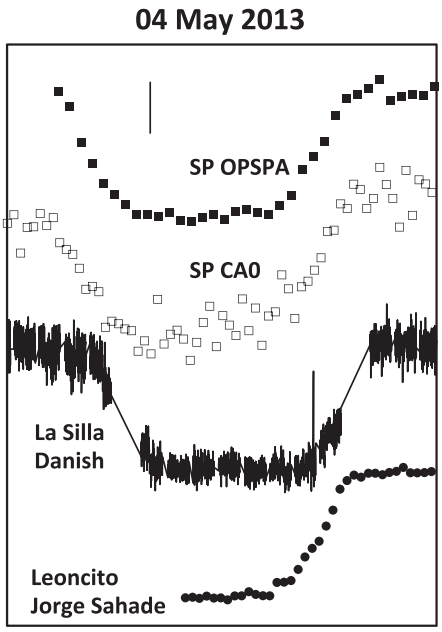

Figure 5. Same as Figure 4, but for the light curves that were not included in the fit, either due to lower S/N, or interruptions during the acquisition. See Table 2 for instrumental details ("SP" refers to San Pedro de Atacama and acronyms refer to telescope used in that station.). Note that the Leoncito, Danish, and SP light curves duplicate the observations of the Cerro Burek, La Silla TRAPPIST, and Caisey telescopes, respectively.

4. GENERAL ATMOSPHERIC STRUCTURE

The best fits of our synthetic light curves to the data are shown in Figures 3 and 4. For each light curve, the residuals are displayed at the bottom of the corresponding panel. They show that a unique global model satisfactorily explains all of the observations, with χ^2 values per degree of freedom ($\chi^2_{\rm dof}$; see Equation (11)) close to unity, except for the 2012 July 18 NACO data (Figures 3 and 4). In fact, due to the quality of this particular data set, the residuals are dominated by spikes associated with wave activity, as illustrated in Figure 7. The wave activity, including the one observed in the NACO data, is discussed in detail elsewhere (see French et al. 2015).

The parameters of the best atmospheric model are listed in Table 4. Note that the only parameter that differs between 2012 July 18 and 2013 May 04 is the boundary condition, i.e., the pressure p_{1275} at $r = 1275$ km. Table 4 reveals a small (6%) but significant (6σ level) increase of pressure, from $p_{1275} = 2.16 \pm 0.02$ μbar in 2012 July to $p_{1275} = 2.30 \pm 0.01$ μbar in 2013 May, corresponding to an average pressure increase rate of 7.5% per year.

Based on various occultation data collected, Young (2013) and Olkin et al. (2015) report a general pressure increase of some 3.5%–7.5% per year between 2006 and 2013, consistent with our result above. Note that our value of $p_{1275} = 2.30 \pm 0.01$ μbar for 2013 May differs from Olkin et al.'s (2015) result (2.70 ± 0.2 μbar) by a barely significant 0.4 ± 0.2 μbar. Part of this difference could be due to the different methods used to derive those numbers, as Olkin et al. (2015) use an isothermal fit to the upper part of the light curves, while we use a combination of the mesosphere with a negative thermal gradient and an upper isothermal branch (Figure 13).

Figure 8 displays the density versus radius, the temperature versus pressure, the temperature versus radius, and the temperature gradient of our best model. Also shown superimposed in that figure are the ingress and egress profiles retrieved from the inversions of the 2012 July 18 NACO light curve, respectively corresponding to the summer and winter hemispheres, as far as the primary stellar image is concerned. Figure 9 is a more detailed view of the bottom of the temperature and temperature gradient profiles, close to Pluto's surface.

The shaded areas in Figures 8 and 9 indicate the 1σ error envelopes caused by (i) the photometric noise in the NACO light curve, which mainly affects the upper parts of the profiles, and (ii) the uncertainty on the Pluto + Charon contribution to the total observed flux, which mainly affects the lower parts of the profiles. The methods for calculating these uncertainty domains are described in the Appendix. The temperature profiles are furthermore affected by another source of uncertainty, namely (iii) the a priori unknown temperature boundary condition, inherent to the nature of Equation (5) (a first order differential equation). As examples, we show in Figure 8 (gray lines in panels (b)–(d)) the profiles obtained by changing by ± 5 K the nominal boundary condition ($T = 80.5$ K at $r = 1390$ km) of the egress, inverted NACO temperature profile.

Both the photometric noise and the ignorance of the temperature boundary condition cause an exponential divergence of the uncertainty domain for T and dT/dr as r increases, with an e-folding distance equal to the density scale height H (Equation (14) and Figure 8). Nevertheless, we note that *if* we have independent information on Pluto's atmosphere, e.g., from theoretical models or forthcoming observations from the *New Horizons* mission, then we can constrain our temperature at rather high altitudes. For instance, at radius $r = 1450$ km (pressure ~ 0.1 μbar), the 1σ uncertainty on T caused by photometric noise is about ± 2.5 K. Conversely, the two alternative solutions $T(r)$ given as examples in Figure 8 (the gray lines in panel (c)), using different boundary conditions, differ from each other by 30 K at that same radius. Consequently, they can be distinguished well above the noise level if we dispose of independent constraints on the thermal properties of the atmosphere at that radius.

For instance, the warmer gray profile with strong positive temperature gradient in Figure 8 can be discarded if we adopt current models that predict that UV heating is efficient only at much higher levels (Zhu et al. 2014). The same is true for the cooler gray temperature profile in panel (c) of Figure 8: it shows a negative gradient in the 1400–1450 km range that is too strong, considering that atmospheric escape may cause temperatures as low as ~ 60 K, but only much higher in the atmosphere (Zhu et al. 2014).

Figure 8 reveals three regions in our thermal profile, from bottom to top: a stratosphere with a strong positive gradient that starts around 1190 km, with a temperature near 36 K and a pressure 11 μbar, and reaches a maximum temperature of 110 K at the stratopause (near $r = 1215$ km, 6.0 μbar). It then follows a mesosphere with a mild negative thermal gradient of -0.2 K km^{-1} up to the mesopause ($r \sim 1390$ km, 0.25 μbar), where it connects itself to a more isothermal upper part around 81 K. These regions are now described in detail.

5. STRATOSPHERE

As explained in the Appendix, the residual stellar flux in the mid-part of the occultation is proportional to the local density

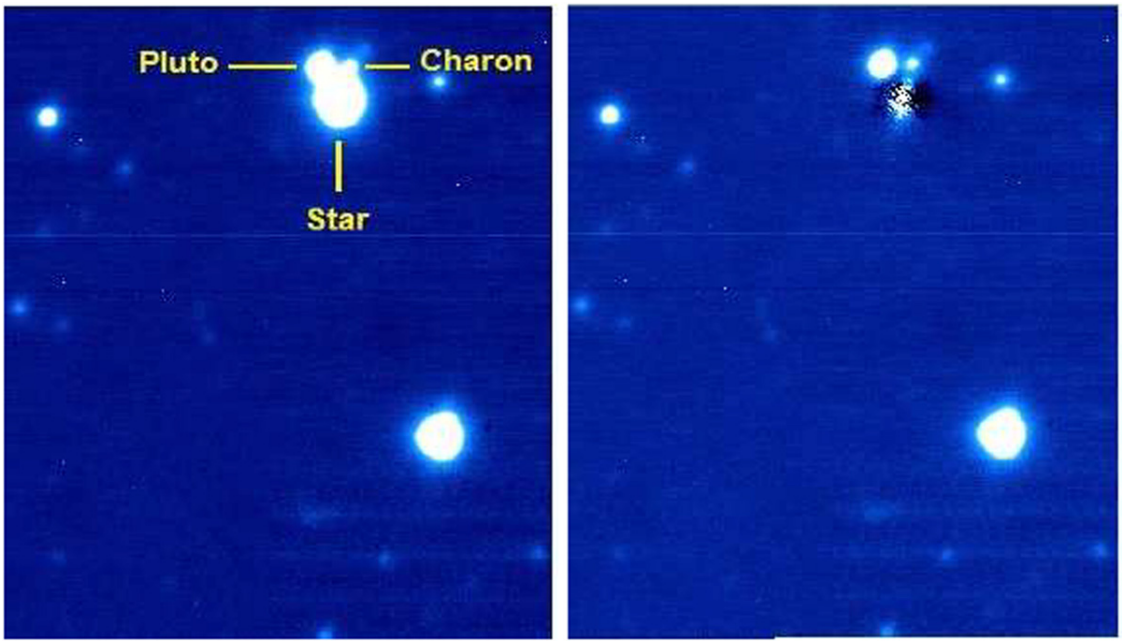

Figure 6. Photometric calibration of the 2012 July 18 event (Paranal/VLT, NACO H-band). Left: image taken some 20 minutes before the event, showing the small separation between Pluto, Charon, and the star (∼1"). Right: the same image after a digital coronagraphy treatment that removed the stellar image. See the text for details.

scale height H, which is itself related to the strong stratospheric temperature gradient (Equation (15)).

It is important to note that at its closest approach to Pluto's shadow center on 2012 July 18, our model predicts that the secondary image observed at Paranal contributes by 20% to the total, primary + secondary stellar residual flux (Figure 7). This is not negligible and explains why we have to extend our ray-tracing model *below* the deepest radius obtained for the inverted temperature profiles (red and blue lines in Figure 9). In fact, the inversion procedure assumes that there is only one (primary) stellar image contributing to the flux at any moment, while the direct ray-tracing procedure does account for the presence of the two images. When the secondary image appears and disappears (at the extremities of the orange trajectory shown in Figure 2), it reaches the radius r_1=1190.4 km (Table 4). Its appearance and disappearance cause small discontinuities in the synthetic flux, but they are too small to be distinguished from the noise (Figure 7).

Due to the uncertainty on the Pluto + Charon flux contribution, the deepest point of our model is determined to be at 1190 ± 5 km (Figure 9). At that point, nitrogen reaches its saturation vapor pressure (Figure 8), and thus condenses in principle into ice, i.e., it reaches Pluto's surface. In that context, we obtain a solution with a clear nitrogen atmosphere and a Pluto radius of 1190 ± 5 km, which consistently explains all of our observations, accounting for the presence of both the primary and secondary images.

Other models are possible though. Based on a more incomplete and lower quality data set than used here, Lellouch et al. (2009) conclude that the nitrogen condensation level occurs somewhere in the range 1187–1197 km, consistent with the present work. However, a shallow adiabatic troposphere with dry or wet nitrogen (or methane) may exist below 1190 km. Nevertheless, there is little freedom for such tropospheric models because (i) they tend to create caustics in the light curves that are not observed and (ii) they provide a cold methane column density that would be detected by other means. More precisely, using spectral data, Lellouch et al. (2009) find possible tropospheric solutions in a narrow region of the parameter space, with depths that cannot exceed 17 km. Similarly, again combining constraints from spectra with a preliminary analysis of the occultation data presented in this work, Lellouch et al. (2015a) concluded that Pluto's radius should be between 1180–1188 km, some 2–8 km below the condensation radius of 1190 km derived above.

That said, we assume here that the atmosphere is haze-free, a subject of debate since the discovery of Pluto's atmosphere. Analyzing a high S/N occultation observed in 2006, Young et al. (2008) conclude that a haze-only explanation for the light curve is extremely unlikely. In fact, the clear-atmosphere model implies a temperature profile that naturally connects the maximum temperature of ∼110 K near 1215 km to the surface at average temperature of ∼50 K (Lellouch et al. 2000, 2013; see Figure 8).

Other constraints come from a central flash observation during a stellar occultation in 2007 July. From that event, Olkin et al. (2014) conclude that the flash is consistent with a transparent atmosphere with a temperature gradient of 5 K km^{-1} at 1196 km, fully consistent with our results (Figure 9). Olkin et al. (2014) exclude in particular a haze-only model to explain the central flash, although combinations of a thermal gradient and a haze mechanism are possible. In the same vein, Gulbis et al. (2015) use a wavelength-resolved occultation from 2011 to constrain the presence of hazes in Pluto's atmosphere. Although haze models do improve the fit residuals, a clear atmosphere with a steep thermal gradient at the bottom is also consistent with the observations.

Finally, we note that the residual stellar flux exhibits a significant decrease in the bottom of the light curve, from 2.3% to 1.8% of its unocculted value, in the central part of the occultation as observed from Paranal on 2012 July 18

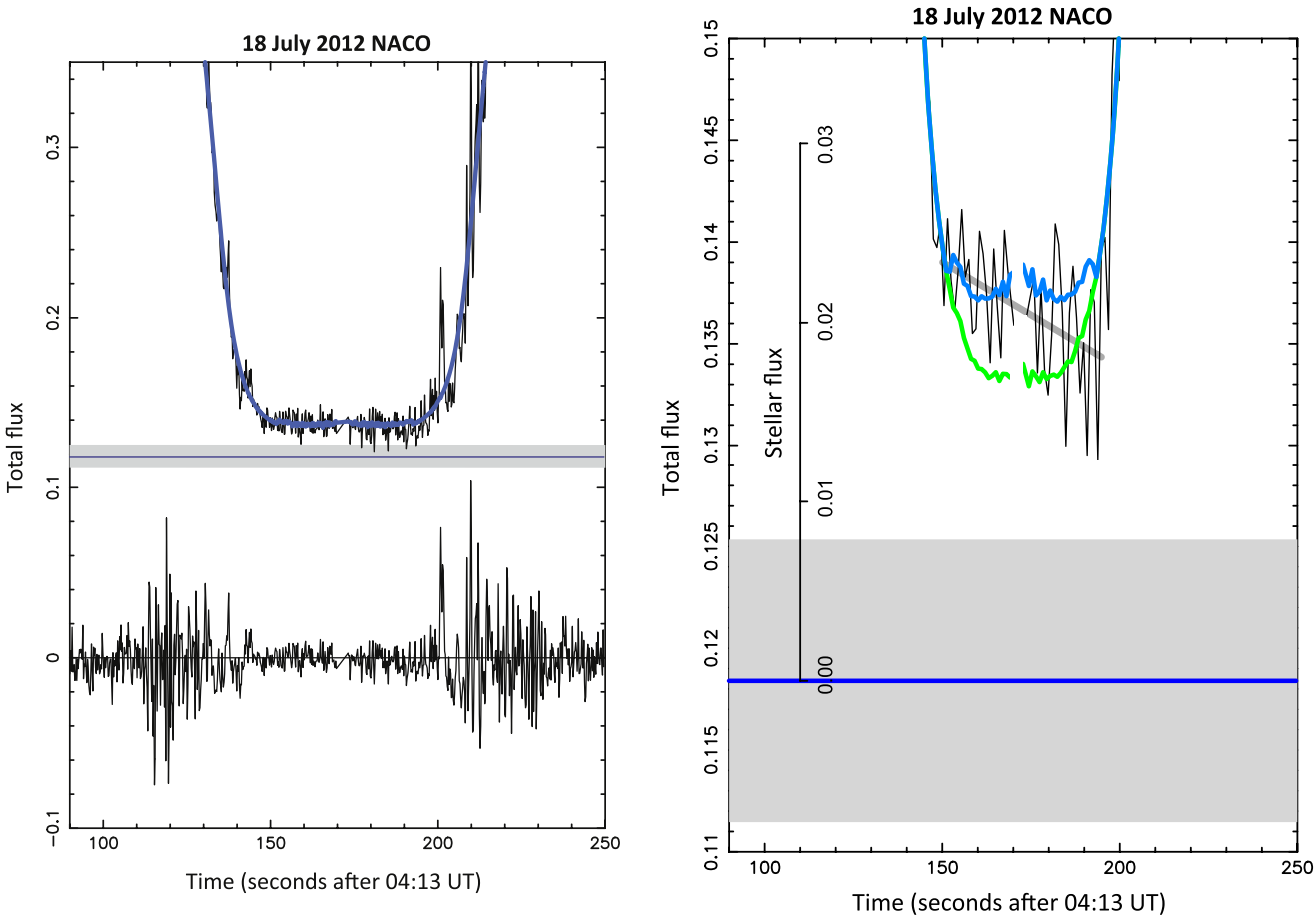

Figure 7. Left: details of the fit to the NACO 2012 July 18 light curve (see also the middle left panel of Figure 3). The horizontal blue line in the gray shaded area indicates the Pluto + Charon contribution to the total observed flux and its 1σ error bar, 0.1184 ± 0.007. The residuals curve at the bottom clearly shows the spike activity at ingress and egress. Right: expanded view of the left panel. The data have been binned over 1 s time intervals to better show the flux decrease during the central phase of the occultation. The flux of the expected *primary* stellar image is plotted in green, while the blue curve is the sum of the primary and secondary images, according to the model (see Figure 2 and the Appendix). Thus, the contribution of the secondary image is the difference between the blue and green curves. Note that the interruption of data acquisition (about 3 s) at mid-occultation, which is necessary for the writing of the data cube before the start of the next data cube. The inclined gray line is a linear fit to the central part of the light curve, which illustrates the ingress/egress asymmetry of the residual stellar flux. The vertical axis inside the box at left indicates the value of the residual, normalized stellar flux. It shows that the stellar flux decreased from about 2.3% to about 1.8% of its full unocculted value during that interval. The systematic error on those values is ±0.8% (corresponding to the shaded area).

(Figure 7). This behavior was already pointed out by Sicardy et al. (2003), based on another high S/N occultation observed in 2002 August. In both cases, the residual stellar flux decreased as the primary stellar image first scanned the summer, permanently lit northern lower atmosphere, and then the winter, low-insolation region (Figure 2). This point is discussed in the last section.

6. MESOSPHERIC NEGATIVE TEMPERATURE GRADIENT

Above the stratopause ($r \sim 1215$ km), the temperature profile exhibits a negative temperature gradient up to $r \sim 1390$ km, with an average value of $dT/dr \sim -0.2$ K km^{-1}. In this ~170 km radius interval, the temperature decreases by some 30 K. This mesospheric gradient is affected very little by the choice of the temperature boundary condition (see Figure 8, panel (d)). While the photometric noise and the boundary condition problem induce rapidly diverging solutions for dT/dr above ~1400 km, the thermal gradient between ~1250 km and ~1360 km is robustly constrained around -0.2 K km^{-1}, with a typical fine-scale scatter of ± 0.05 K km^{-1} that is dominated by Pluto's wave activity, and not by the photometric noise. In this interval, the thermal gradient remains smaller (in absolute value) than the dry adiabatic lapse rate $-g/c_p$ (Figure 8), where g is the acceleration of gravity (Equation (6)) and $c_p = 1.04 \times 10^3$ J K^{-1} kg^{-1} is the specific heat at constant pressure for N_2. Thus, the mesosphere remains convectively stable.

Note that in principle we may choose an extreme temperature boundary condition that provides an isothermal mesosphere, i.e., a thermal profile that is much warmer than the warmer gray profile shown in panel (c) of Figure 8. As commented earlier, however, this replaces one problem with another one, namely that the upper part of our profile is too warm, with seemingly no plausible physical explanation.

The negative mesospheric thermal gradient is further confirmed by the inversions of our best S/N light curves obtained in 2012 July and 2013 May (see Figure 10). This eliminates random, low-frequency sky-transparency variations that may have corrupted the light curves. Moreover, such gradients have also been reported in previous, independent

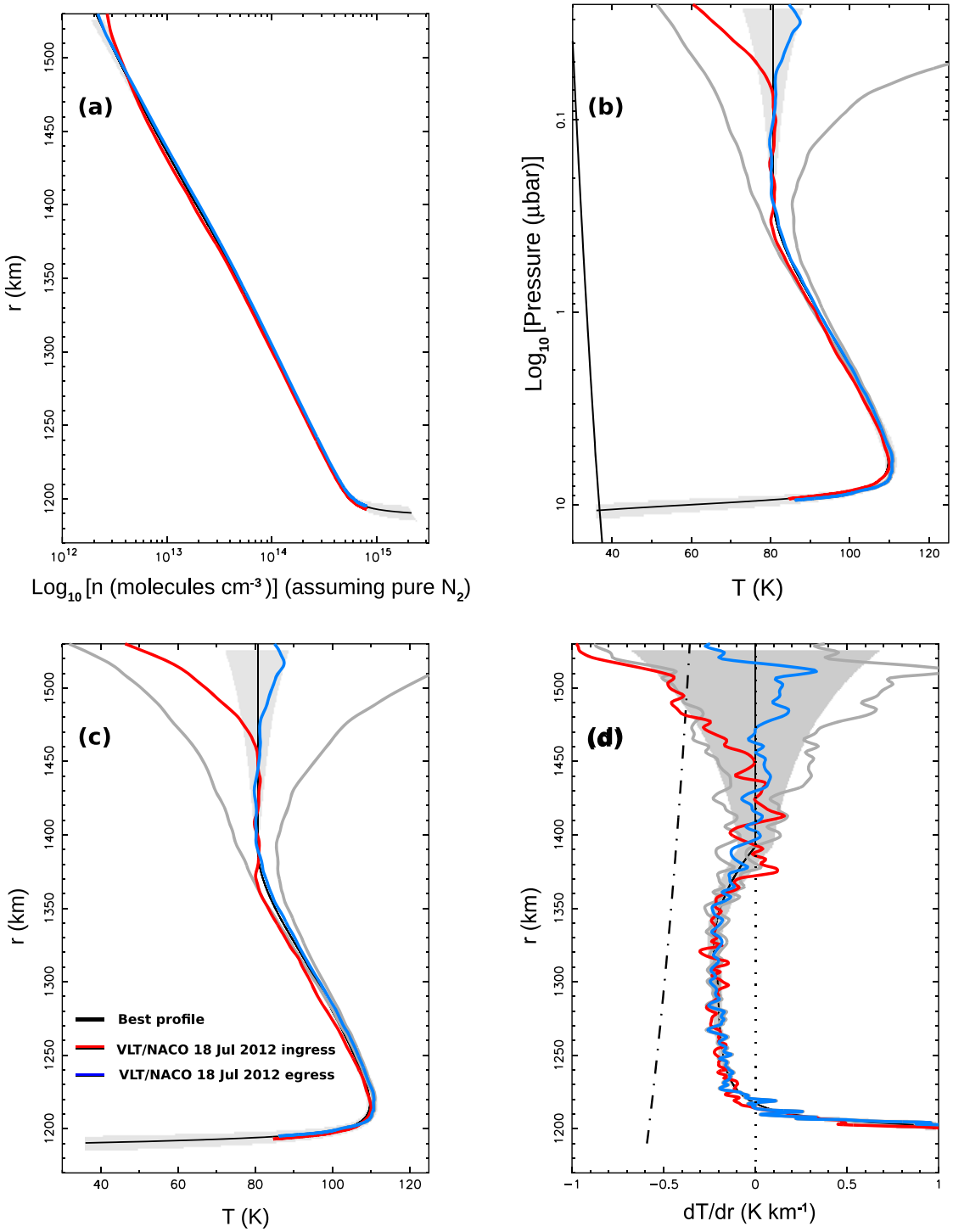

Figure 8. In all of the panels, the black solid line is the model that best fits all of the 2012 July 18 NACO light curves (see Figure 3 and Table 4). The red (resp. blue) lines are the particular profiles obtained from the inversion of the NACO 2012 July 18 light curve at ingress/summer (resp. egress/winter). The shaded areas at the top of the profiles indicate the expected $\pm 1\sigma$ fluctuations caused by the photometric noise (see the text). The shaded areas at the bottom of the profiles are the $\pm 1\sigma$ uncertainty domain caused by the uncertainty on the Pluto + Charon contribution to the 2012 July 18 NACO light curve (see Figure 7). (a) Molecular density vs. radius (assuming a pure N_2 atmosphere); (b) temperature vs. pressure; (c) temperature vs. radius; (d) temperature gradient vs. radius. The two gray temperature profiles in panels (b), (c), and (d) show the effect of different temperature boundary conditions for the egress NACO profile. More precisely, those profiles differ from the nominal one (black lines) by ± 5 K at 1390 km. The oblique solid line at the left of panel (b) is the vapor pressure equilibrium limit for N_2 (Fray & Schmitt 2009). Nitrogen should condense to the left of this line so that its intersection with the temperature profile may define Pluto's surface in the absence of a troposphere (see Figure 9 and the text for details). The dash–dotted line in panel (d) is the dry adiabat for a pure N_2 atmosphere.

Table 4
Pluto Atmospheric Model

	Physical Parameters
Pluto's mass[a]	$GM = 8.703 \times 10^{11}$ m^3 s^{-2}
Nitrogen molecular mass[b]	$\mu = 4.652 \times 10^{-26}$ kg
Nitrogen molecular refractivity[c]	$K = 1.091 \times 10^{-23} + (6.282 \times 10^{-26}/\lambda_{\mu m}^2)$ cm^3 molecule^{-1}
Boltzmann constant	$k = 1.380626 \times 10^{-23}$ J K^{-1}
The Nine Free Parameters of the Best Temperature Profile[d]	
r_1, T_1, $dT/dr\,(r_1)$	1190.4 ± 1 km, 36 K, 16.9 K km^{-1}
r_2, T_2	1217.3 km, 109.7 K
r_3, T_3	1302.4 km, 95.5 K (implying $dT/dr\,(r_3) = -0.206$ K km^{-1})
r_4, T_4	1392.0 km, 80.6 K
$c1$, $c2$	$1.41397736 \times 10^{-3}$, $2.59861886 \times 10^{-3}$
$c3$, $c4$	$-2.19756021 \times 10^{-6}$, $-4.81764971 \times 10^{-7}$
$c5$, $c6$	$8.66619700 \times 10^{-8}$, -3.6213609×10^{4}
$c7$, $c8$	8.2775269×10^{1}, $-6.27372563 \times 10^{-2}$
$c9$	$1.58068760 \times 10^{-5}$
The Three Free Parameters Particular to Each Event[e]	
	2012 July 18 / 2013 May 04
Pressure at $r = 1275$ km, p_{1275}	2.16 ± 0.02 μbar / 2.30 ± 0.01 μbar
Time of closest geocentric approach	04:13:37.24 ± 0.07 UT / 08:22:27.11±0.09 UT
Distance of closest geocentric approach[e]	−404.6 ± 2.7 km / −723.5 ± 2.7 km

Notes.
[a] Tholen et al. (2008).
[b] Assumed to be the only constituent in the ray-tracing code (see the text).
[c] Washburn (1930, p. 11). For both NACO observations of 2012 and 2103, the *H*-band ($\lambda = 1.6$ μm) was used.
[d] Or equivalently, the nine coefficients $c1,\ldots c9$; see the text and Figure 13 for the definition of the various quantities given here.
[e] So that there are twelve free parameters for each date.
[f] Distance of Pluto's center to the star at the closest approach, projected in the sky plane, as seen from the geocenter. A negative value means that Pluto's center went south of the star in the sky plane.

works. For instance Young et al. (2008) derive and discuss a $dT/dr = -0.086 \pm 0.033$ K km^{-1} gradient at $r = 1275$ km from the 2006 June 12 occultation, while Elliot et al. (2007) give -0.17 ± 0.05 K km^{-1} for the same occultation and at the same radius. Gulbis et al. (2015) report a gradient of -0.23 ± 0.05 K km^{-1} in the 1310–1450 km region from the 2011 June 23 occultation, consistent with Person et al. (2013) for that event. Finally, Bosh et al. (2015) derive values of -0.17 ± 0.03 and -0.24 ± 0.01 K km^{-1} around 1280–1300 km for occultations observed on 2012 September 09 and 2013 May 04, respectively.

The origin of this thermal gradient is still debated. Two classes of possible explanations can be proposed: (1) the presence of cooling minor species and (2) yet unmodeled physical mechanisms. They are now examined in detail.

6.1. Possible Cooling by CO or HCN

Radiative-conductive models of Pluto's atmosphere were initially developed by Yelle & Lunine (1989), Hubbard et al. (1988), Lellouch (1994), and Lellouch et al. (2015a) to explain the recently discovered gross characteristics of Pluto's atmosphere: a large lower atmosphere temperature gradient and a warmer (∼100 K) mesosphere. These studies used a simplified description of the heating/cooling properties of Pluto's atmosphere proposed by Yelle & Lunine (1989), with heating in the methane 3.3 μm band and cooling in its 7.6 μm band, both occurring in non-local thermodynamic equilibrium (non-LTE) conditions. Lellouch (1994) first suggested that additional cooling due to LTE CO emission rotational lines was important, based on an estimated abundance of CO in Pluto's atmosphere (10^{-4}–10^{-3}).

These studies were updated with the much more extensive model of Strobel et al. (1996). Notably these authors improved the treatment of solar heating in the CH_4 near-infrared bands by considering the effects of opacity and vibrational (V–V and V–T) energy transfer, and showed the need to include heating from the 2.3 μm band system in addition to the 3.3 μm bands.

As the composition of Pluto's atmosphere, as well as surface (pressure, radius) conditions, were largely unconstrained at that time, Strobel et al. (1996) explored diverse combinations of surface pressure and methane mixing ratios (including non-uniform ones), also including the effect of CO cooling. In general these models were reasonably successful at explaining large near-surface temperature gradients, though (i) fitting 10–20 K km^{-1} gradients near the surface required pushing the models to their limits, e.g., a 3.6% CH_4 mixing ratio confined to the first scale height near the surface and a 3 μbar surface (or tropopause) pressure; and (ii) models tended to overestimate the upper atmosphere temperature (∼130 K instead of 100 K). A general feature of the Strobel et al. (1996) models was their prediction of a mostly isothermal atmosphere at pressures less than ∼2 μbar, though some models exhibited a moderate (0 to −0.1 K km^{-1} negative gradient at 1–2 μbar. As the direct detection of N_2 in Pluto's atmosphere is still missing, they also considered a CO-dominated atmosphere case (e.g., 97% CO + 3% CH_4). This case led, through enhanced CO cooling, to much larger negative temperature gradients in the sub-microbar region and an upper atmosphere temperature of about 55 K.

The availability of new, quantitative, observational constraints on the composition ($CH_4 \sim 0.5\%$, CO ∼ 0.05%) and near-surface structure (surface radius and pressure, tropospheric depth) of Pluto's atmosphere from near-IR observations (Lellouch et al. 2009, 2011) prompted a revival of the Strobel et al. (1996) models (Zalucha et al. 2011a, 2011b; Zhu et al. 2014).

Model updates included new estimates of the vibrational energy transfer based on recent laboratory measurements of collisional relaxation rates (Siddles et al. 1994; Boursier et al. 2003), as well as the introduction of a scheme parameterizing the processes of eddy mixing and convection. With the updated model, Zalucha et al. (2011a) explored the effect of parameter space (CH_4 and CO mixing ratios, surface pressure, and radius) allowed by the recent observations, assuming uniform vertical mixing of CH4 and CO (which was recently demonstrated to be the case for CH_4 in the first 25 km of the atmosphere; Lellouch et al. 2015a). Radiative-convective calculations were then coupled to a model generating synthetic occultation light curves for direct comparison to observations. The study was extended by Zalucha et al. (2011b) to include a putative troposphere.

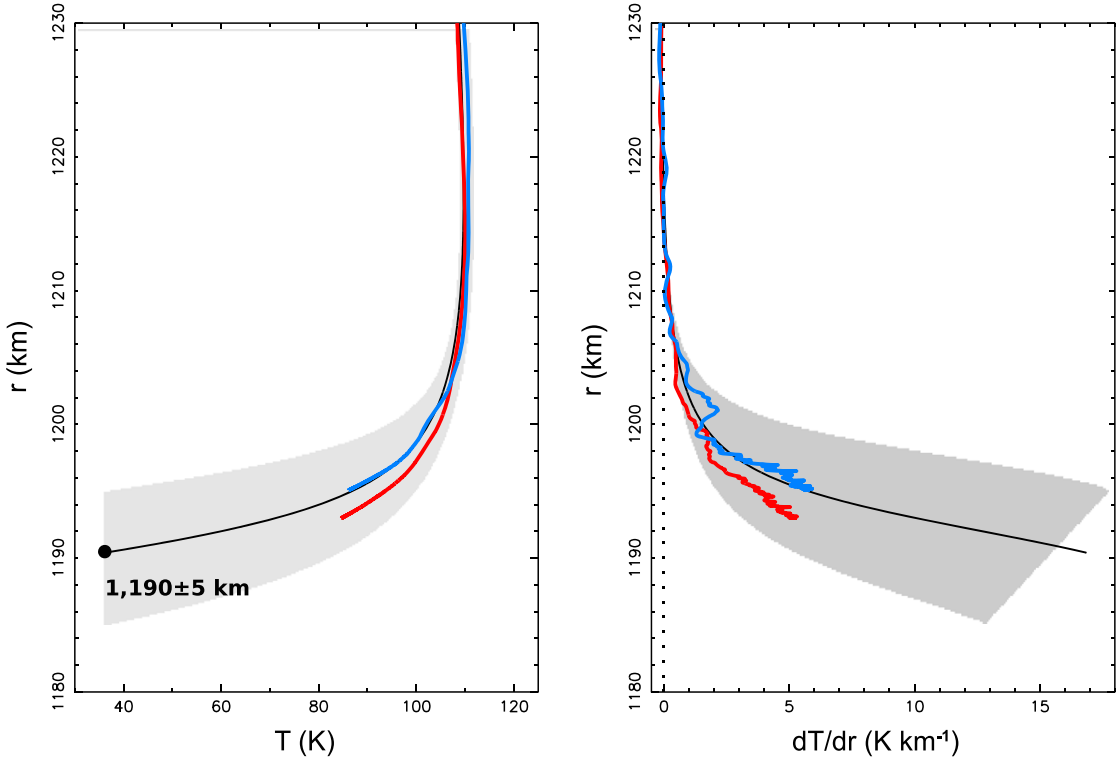

Figure 9. Left: expanded view of the bottom of the temperature profiles shown in Figure 8. The bullet is the intersection with the nitrogen condensation line. The error bar attached to its positions is defined by the radial extension of the shaded uncertainty domain. Right: the corresponding expanded view for the temperature gradient.

In spite of minor changes, the Zalucha et al. (2011a, 2011b) models confirm the essential features of the earlier Strobel et al. (1996) models. The stratopause temperature is still somewhat too high (120–125 K) near the 1215 km radius in Zalucha et al. (2011a). These models generally show only weak negative temperature gradients above this level, typically a ∼5 K decrease over a 300 km range for a CO mixing ratio of 5×10^{-4}, or mild ∼10 K decrease due to atmospheric escape (Zhu et al. 2014). This is in disagreement with the profile reported in the present study, which exhibits a typical 30 K decrease between 1215 and 1390 km and a gradient of $-0.2\,\mathrm{K\,km^{-1}}$, as discussed earlier. Rather, the profile we derive is remarkably similar to that calculated by Zalucha et al. (2011a; their Figure 8) for the case of 40-times enhanced CO mixing ratio (200×10^{-4}) This scenario, however, is at odds with the direct measurement of the CO abundance (Lellouch et al. 2011). This suggests that an additional cooling source is at work.

Through radiation in its intense rotational lines, HCN is the major cooling agent in Titan's upper atmosphere, where its mixing ratio is typically 2×10^{-4} at 1100 km (Vuitton et al. 2007), and where it equilibrates the solar UV heating rates (Yelle 1991). HCN has not yet been detected in Pluto's atmosphere, but its presence is expected from coupled photochemistry in a N_2–CH_4 atmosphere. However, a complete reassessment of the Pluto models is beyond the scope of the present study. Here we only recalculate CO cooling rates and also examine the case of HCN cooling. Photochemical models predictions lead to rather diverse mixing ratios of HCN (10^{-8}–10^{-3} of N_2 (Lara et al. 1997; Summers et al. 1997; Krasnopolsky & Cruikshank 1999), where the difference largely seems to come from the fact that the more "optimistic" models have not accounted for the fact that under cold (<100 K) temperatures, atmospheric condensation of HCN should occur. Here, we nominally consider cases in which the HCN abundance is limited by the saturation law (Fray & Schmitt 2009), but we also run a case with uniformly mixed HCN, as supersaturation may be possible in a clear, tenuous atmosphere such as as Pluto's. Cooling rates at radius r are calculated from the following equation (e.g., for CO):

$$R_{\mathrm{CO}}(r) = 4\pi N_{\mathrm{CO}}(r) \int B_\nu(T(r)) k_\nu E_2(\tau_\nu) d\nu, \qquad (1)$$

where N_{CO} is the local CO number density, T is temperature, k_ν and τ_ν are the absorption coefficients and zenithal opacity at frequency ν, and $E_2(\tau)$ is the second exponential integral. The integral runs over the entire millimeter/submillimeter range (0–200 $\mathrm{cm^{-1}}$), and unlike in Strobel et al. (1996), we include all isotopic variants of CO and HCN, i.e., lines of CO, 13CO, C18O, HCN, H13CN, and HC15N are taken into account when calculating the opacities. Moreover, absorption coefficients are calculated using a Voigt profile, instead of the Doppler approximation. Both aspects lead to a minor but non-negligible increase in the cooling rate at low altitudes. Calculations of the cooling rates are performed for the thermal profile inferred in this work.

Results are shown in Figure 11 for a series of assumed CO and HCN profiles. The CO mixing ratio $q_{\mathrm{CO}} = 5 \times 10^{-4}$ curves show the "nominal" CO cooling. Although Zalucha et al. (2011a, 2011b) do not show their cooling rates, our calculation for CO can be compared to Figure 5(a) of Zhu et al. (2014), showing reasonable agreement. Increasing the q_{CO} by a

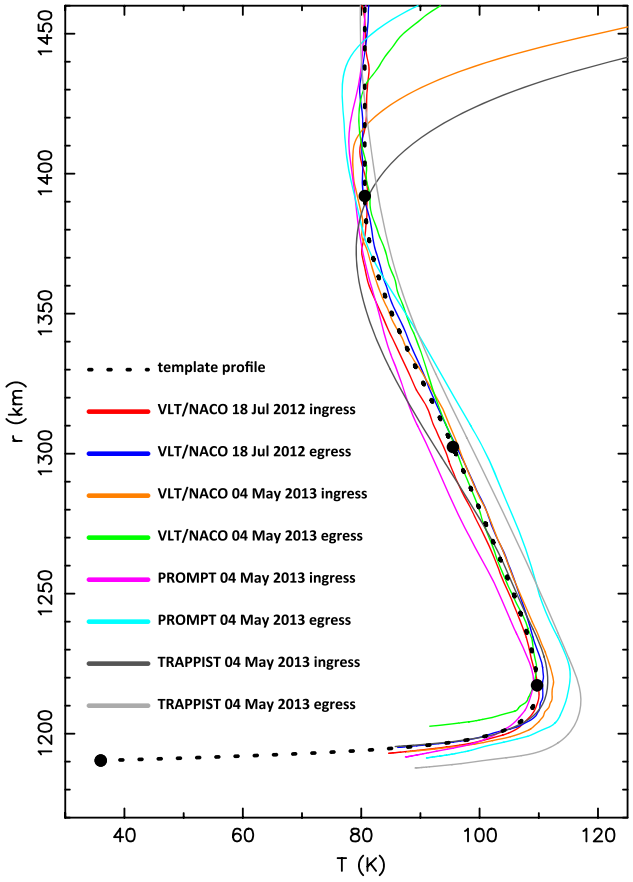

Figure 10. Temperature profiles derived from the inversion of our best occultation light curves obtained on 2012 July 18 and 2013 May 04. The dotted line is our global, best-fitting temperature profile (also shown in Figures 8 and 13).

factor of 40 leads to an increase of the cooling rate, although in much lower proportion due to opacity effects.

Other curves in Figure 11 show the cooling due to HCN for different assumed HCN mixing ratios in the non-saturated part of the atmosphere. For the temperature profile derived in this work, the lower temperatures above 1270 km radius, severely restrict the amount of gaseous HCN if saturation of HCN is accounted for. In fact, HCN appears to be saturated everywhere in the atmosphere, except possibly over the 1210–1270 km range, where the condensation law allows 10^{-7}–10^{-6} HCN mixing ratios. There, the HCN cooling rate may slightly exceed the nominal CO cooling rate (pink versus red curves in the left panel of Figure 11). However, for the HCN cooling rates to approach the "enhanced" CO cooling rates necessary to explain our negative mesospheric temperature gradient (i.e., those for $q_{CO} = 200 \times 10^{-4}$, as considered by Zalucha et al. 2011a), one must assume that HCN is not limited by saturation. Specifically, the blue curve in Figure 11 shows that a uniform HCN mixing ratio of $\sim 5 \times 10^{-5}$ is required.

Although a full reassessment of the radiative models should be undertaken at this point, we conclude from this exercise that there is no obvious "culprit" for a $-0.2\,\mathrm{K\,km^{-1}}$ temperature gradient above the radius of $\sim$ 1220 km. According to the calculations of Zalucha et al. (2011a), CO in amounts consistent with the direct observations of Lellouch et al. (2011) provides unsufficient cooling. We show here that HCN could be an alternative efficient cooling agent, but only if its mixing ration vastly exceeds expectations from the condensation law. Direct measurements/upper limits of HCN from ALMA and perhaps from the *New Horizons* UV spectrometer (ALICE) will shed new light on this issue.[29]

6.2. Alternative Explanations

Coming back a step, the primary result derived from a stellar occultation light curve is the refractivity profile $\nu(r)$, from which a density profile $n(r) = \nu(r)/K$ is obtained, assuming a given gas composition (Equation (7)).

A first idea is to envisage that hazes are present in the mesosphere. Those hazes would absorb part of the stellar flux, in such a way that a basically isothermal mesosphere is thought to host a negative thermal gradient just because of the clear-atmosphere assumption. To test that hypothesis, we have generated synthetic light curves, forcing the mesosphere to be isothermal at $T_{iso} = 95.5$ K above the stratopause (we have also tested other values of T_{iso} between 85 and 110 K, with the same conclusions). Figure 3 shows the resulting residuals for the NACO 2012 July 18 light-curve (labelled "iso." in that figure). They depart from zero well above the noise level, and we can rule out photometric fluctuations caused by absorbing haze layers, since the residuals have both positive and negative values.

That said, two assumptions may be wrong in Equation (5): (1) the atmosphere may be not composed of pure nitrogen N_2, so that the nitrogen molecular mass μ must be replaced by a new value μ', and (2) hypothetical zonal winds may create a centrifugal acceleration, so that the acceleration of gravity g must be replaced by a term g' that includes supplementary terms.

In fact, we can use Equation (5) in a reversed way. More precisely, the refractivity profile $\nu(r)$ is actually an imposed observable (since it is directly derived from the occultation light curve), while we may use a prescribed temperature profile $T'(r)$, taken, for instance, from a theoretical model. With this approach in mind, Equation (5) can be rewritten as

$$\frac{\mu' g'}{\mu g} = -\frac{kT'}{\mu g}\frac{d\,\log(\nu T')}{dr}. \qquad (2)$$

To obtain this equation, we have used $\nu(r) = K \cdot n(r)$, where K is the molecular refractivity (Equation (7)). We assume here that the atmospheric composition varies slowly with radius (i.e., K suffers small variations over one scale height), so that we neglect dK/dr, and finally provide $d\,[\log(\nu)]/dr \sim d\,[\log(n)]/dr$.

Thus, the ratio $\mu' g'/\mu g$ is the factor by which the molecular mass and/or the acceleration of gravity g must be multiplied in order to retrieve a prescribed temperature profile $T'(r)$, given an observed occultation light-curve.

In Figure 12, we consider an example where the prescribed temperature profile $T'(r)$ exhibits a decrease of only 10 K between the stratopause and the mesopause. This is typical of what can be obtained by the combined effects of CO cooling (Zalucha et al. 2011a) and/or an atmospheric escape (Zhu et al. 2014). The right panel of Figure 12 shows the resulting

[29] The detection of HCN in Pluto's atmosphere, using ALMA, was announced by Lellouch et al. (2015b) on 2015 July 30.

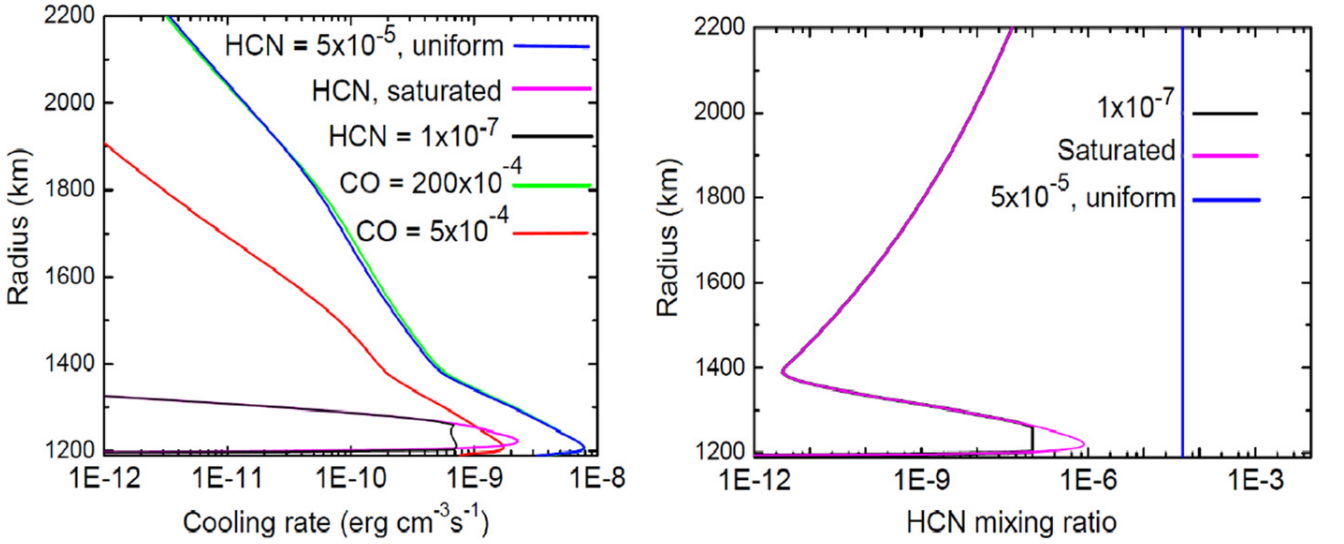

Figure 11. Calculation of cooling rates by CO and HCN. The y-axis is the distance from Pluto's center, with the surface position assumed here at 1,184 km. Left panel: cooling rates assuming the thermal profile from this work. Red and green curves: CO cooling rates for $q_{CO} = 5 \times 10^{-4}$ and 200×10^{-4}, respectively. The other three colored curves show the HCN cooling rate for the corresponding HCN profiles. Right panel: HCN mixing ratios profiles. The black and purple curves make use of the thermal profile from this work. Due to the significantly cold temperatures above ~1300 km, HCN is limited by saturation throughout the atmosphere, except in a limited region at 1210–1270 km for an assumed $q_{HCN} = 10^{-7}$. The blue curve shows the hypothetical case of a uniform (i.e., non-limited by saturation) 5×10^{-5} uniform HCN mixing ratio.

profile for $\mu' g'/\mu g$, restricting ourselves to the mesospheric region.

We first assume here that the atmosphere is composed of pure nitrogen, so that $\mu' = \mu$, and the ratio $\mu' g'/\mu g = g'/g$ is only caused by variations of g'. In the presence of a zonal wind with velocity v, the centrifugal acceleration provides $g' = g - v^2/r$, and from $g = GM/r^2$, a zonal wind of:

$$v = \sqrt{\frac{GM}{r}} \cdot \sqrt{1 - \frac{g'}{g}} \sim 840 \sqrt{1 - \frac{g'}{g}} \text{ m s}^{-1}, \qquad (3)$$

where we have used the value of GM in Table 3 and $r \sim 1250$ km. With the example above, the factor g'/g' reaches a minimum value of about 0.95, yielding $v \sim 190$ m s^{-1}. This is close to supersonic, as the speed of sound for nitrogen N_2 at 100 K is about 200 m s^{-1}. In fact, current general circulation models for Pluto predict zonal winds of less than 10 m s^{-1} at the altitudes considered here (Vangvichith 2013; Zalucha & Michaels 2013). Moreover, we see that above $r \sim 1300$ km, the ratio g'/g becomes larger than unity with the example considered here, which is impossible from Equation (3). Other prescribed profiles $T'(r)$ could be imagined to avoid this problem by displacing the $\mu' g'/\mu g$ profile to the left in Figure 12 (providing smaller values of g'/g), but this would imply even more unrealistic, high zonal winds.

Considering that $g'/g \sim 1$ from the discussion above, the $\mu' g'/\mu g$ profile would represent variations of the atmospheric molecular weight, μ'/μ. In the example of Figure 12, the molecular weight of the atmosphere has to be inferior to that of molecular nitrogen, μ, to mimic the effect of a negative temperature gradient. This could be caused by the presence of a lighter gas, such as neon, which has a molecular weight of $\mu_{Ne} \sim 0.72\mu$. That species has a relatively large solar abundance ($N_e/N \sim 1.5$) and is not condensed at Pluto's atmosphere's temperatures. The minimum value $\mu'/\mu = 0.95$ near 1,230 km (Figure 12) would then require a local neon abundance of about 82%. However, and as before, the ratio μ'/μ would be larger than unity above 1300 km, requiring that another heavier gas (e.g., argon) takes over above 1300 km and drives the molecular mass upward. Such a model is clearly unrealistic though, because mass separation would result in a depletion, not enrichment, of the heavier species in the upper atmosphere.

7. UPPER ATMOSPHERE

Above $r \sim 1400$ km, the results of Figure 8 show that a change of thermal gradient may occur, with a more isothermal upper branch just above the mesosphere. However, the lack of independent constraints on the temperature at that level prevents an unambiguous choice for a particular solution for $T(r)$. In addition, the rapidly increasing contribution of the noise makes any estimation of the thermal gradient above 1450 km (Figure 8, panel (d)) impossible. That said, the lack of obvious mechanisms to drastically warm up or cool down the atmosphere just above 1400 km suggests (but by no means proves) an isothermal branch between 1400 and 1450 km. Under this hypothesis, we estimate a 1σ uncertainty domain of 81 ± 6 K for the temperature of this isothermal branch. (This interval corresponds to an increase of $\Delta\chi^2 = +1$ of the χ^2 function with respect to the best, minimum value χ^2_{min}).

8. DISCUSSION AND CONCLUSIONS

We have analyzed some of the best light curves ever obtained during stellar occultations by Pluto. A combination of well-sampled occultation chords (Figure 2) and high S/N data (Figures 3, 4) has allowed us to constrain the density, temperature, and thermal gradient profiles of Pluto's atmosphere between radii $r \sim 1190$ km (pressure $p \sim 11$ μbar) and $r \sim 1450$ km (pressure $p \sim 0.1$ μbar). Our main results are listed below.

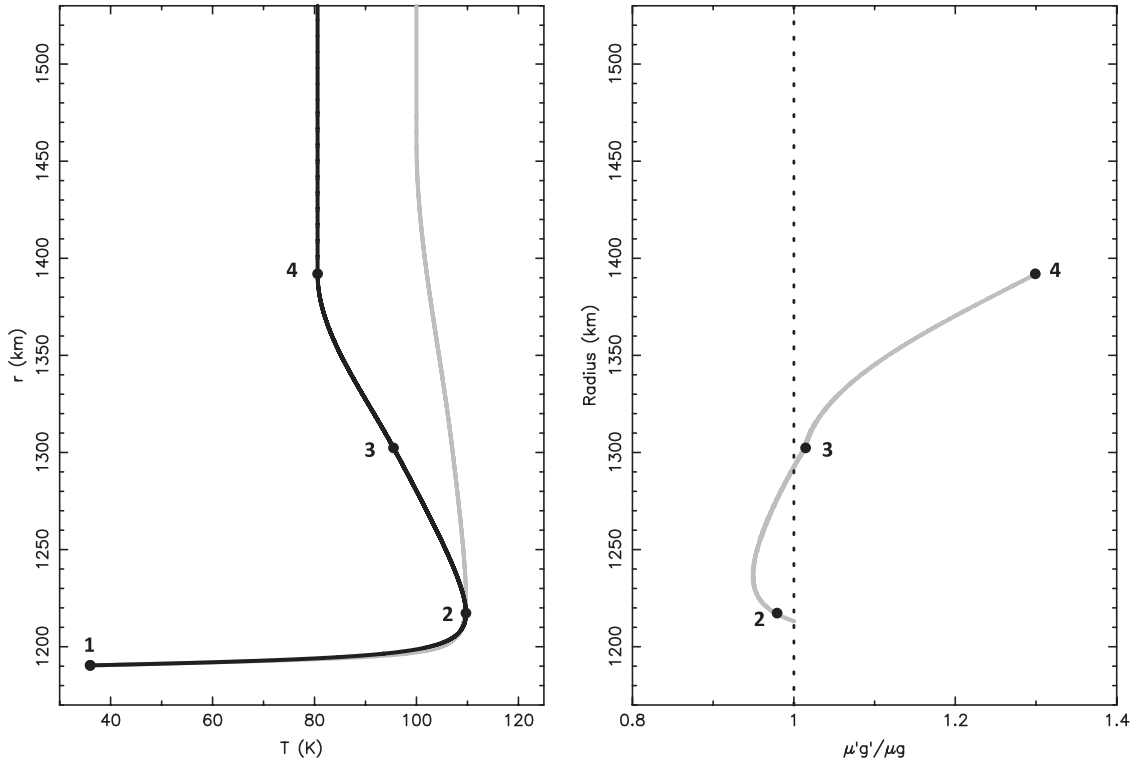

Figure 12. Left panel: solid line: our best temperature profile (see Figure 13). Gray line: an example of a prescribed profile with a milder mesospheric thermal gradient, here a 10 K drop between the stratopause and the mesopause. Right panel: the ratio $\mu' g'/\mu g$, as defined by Equation (2), corresponding to the gray, prescribed profile of the left panel. The points numbered 2–4 respectively correspond to the stratopause, the inflexion point, and the mesopause (see also Figure 13 and the text for details).

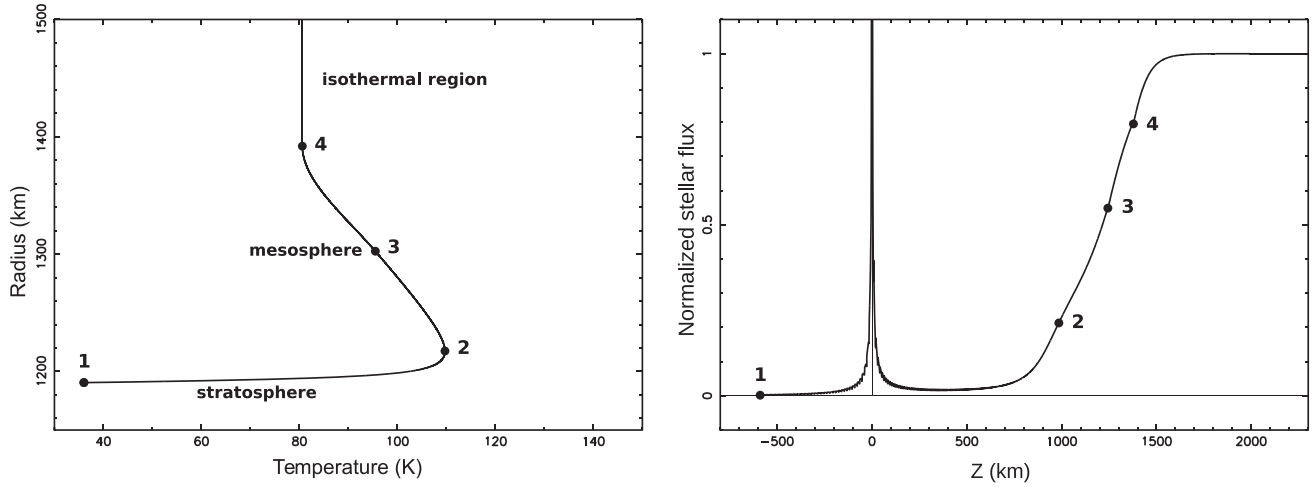

Figure 13. Left: the temperature profile $T(r)$ that best fits our 2012 and 2013 light curves (see also Figures 3 and 4). The parameters used to generate this profile are given in Table 4. Total thickness of the atmosphere: 1100 km; vertical sampling of the model: 0.03 km. Right: the corresponding synthetic flux in the shadow plane for the 2012 July 18 occultation. Here, z is the distance to the shadow center, with the four points corresponding to those of the left panel.

Global Pluto's atmospheric model. We find that a unique thermal model can satisfactorily fit 12 light curves observed in 2012 and 2013 (Figures 3 and 4), assuming a spherically symmetric and clear (no haze) atmosphere. The parameters defining our best model are listed in Table 4 (see also Figure 13), and the various resulting profiles (density, temperature, and thermal gradient) are displayed in Figures 8–10. The absolute vertical scale of our global model has an internal accuracy of about ±1 km (Table 4). However, this error is amplified to ±5 km at the bottom of the profiles (Figure 9), because of the uncertainty on the residual stellar flux (Figure 7) in the central part of the occultation observed by NACO on 2012 July 18.

We quantify in this work the propagation of the photometric noise into the density, temperature, and thermal gradient profiles (Equation (14) and Figure 8). The key parameter that governs the noise propagation is the radius r_0 in the atmosphere, at which the stellar drop caused by differential

refraction is equal to the flux standard deviation. The radius r_0 can be estimated from Equation (13), which includes all of the quantities at work in a stellar occultation: photometric noise, molecular refractivity, atmospheric scale height and radius, and distance to the body. For the NACO light curve, we find $r_0 =$ 1565 km, corresponding to a pressure level of about 14 nbar.

Although a satisfactory fit to all the data used here is provided by a unique model, there are two slight, but significant departures from this global model. They are now discussed in turn.

Pressure increase between 2012 and 2013. In the frame of our model (i.e., assuming a constant temperature profile), we detect a significant 6% pressure increase (at the 6σ level) during the ~9.5 months separating the two events under study. This means that Pluto's atmosphere was still expanding at that time, confirming the work of Olkin et al. (2015), which compiles and analyzes pressure measurements between 1988 and 2013.

Ingress/egress asymmetry of lower temperature profiles. Figure 7 shows that the stellar flux decreased from 2.3% to 1.8% of its unocculted value during the central part of the 2012 July 18 occultation, as observed by NACO from Paranal. This corresponds to the primary stellar image first scanning the summer, permanently lit Pluto northern hemisphere, and then the winter low-insolation southern hemisphere (Figure 2). This confirms a similar trend pointed out by Sicardy et al. (2003) during another high S/N stellar occultation recorded in 2002 August. These authors interpreted this result as a surface boundary layer effect, where the lowermost scale height adjusts itself to the surface temperature variegations, which might explain the behavior displayed in Figure 9.

Another interpretation of this trend is the gradual entrance of the primary stellar image into an absorbing haze layer near Pluto's evening limb, a hypothesis that can be tested during the *New Horizons* flyby in 2015 July.

Pluto's radius and density. The extrapolation of our temperature profiles to the nitrogen saturation line implies that nitrogen may condense at Pluto's radius of $R_P = 1190 \pm 5$ km. However, the few kilometers above Pluto's surface remain *"terra incognita"* as far as stellar occultations are concerned. In particular, the temperature gradients shown in Figure 9 may deviate from the simple extrapolation used here, especially if haze layers affect the retrieved temperature profiles. Although difficult to envisage because of the strong caustics that they cause, a troposphere below 1190 ± 5 km cannot be excluded. Combining high-resolution spectroscopic observations of gaseous methane, combined with constraints from an occultation observed in 2002, Lellouch et al. (2009) conclude that the troposphere depth cannot exceed about 17 km. Consequently (and assuming that the temperature of the deep atmosphere did not change significantly since 2002), our observations constrain Pluto's radius to lie in the range 1168–1195 km. More recently, combining constraints from spectra and a preliminary analysis of the occultation data presented in this work, Lellouch et al. (2015a) concluded that Pluto should have a radius between 1180 and 1188 km, some 2–8 km below the condensation radius of 1190 km that we derive above.

From Pluto's mass of $M_P = 1.304 \pm 0.006 \times 10^{22}$ kg (Tholen et al. 2008), we derive a density $\rho_P = (1.802 \pm 0.007)(R_P/1200\ \mathrm{km})^{-3}\ \mathrm{g\,cm^{-3}}$. Our estimation $R_P = 1190 \pm 5$ km thus implies $\rho_P = 1.85 \pm 0.02\ \mathrm{g\,cm^{-3}}$ in the absence of a troposphere, and a range $\rho_P = 1.83-1.95\ \mathrm{g\,cm^{-3}}$ if a troposphere is allowed. This is larger, but not by much, than Charon's density, $\rho_C = 1.63 \pm 0.05\ \mathrm{g\,cm^{-3}}$ (Ibid.).

The mesospheric negative thermal gradient. Pluto's stratopause occurs near 1215 km (pressure $p = 6.0\ \mu$bar), with a maximum temperature of 110 ± 1 K, where the error bar applies to the best inverted profile (NACO 2012 July 18), and stems from the uncertainty on the Pluto + Charon flux contribution (Figure 8).

Above the stratopause, and up to about 1390 km, our best 2012 and 2013 occultation light curves yield inverted temperature profiles with a negative thermal gradient close to $-0.2\ \mathrm{K\,km^{-1}}$, which amounts to a total decrease of 30 K for the temperature between 1215 and 1390 km (Figures 8, 10).

Explaining this negative gradient by CO cooling requires a mixing ratio (200×10^{-4}) that is too high by a factor of 40 compared to current measurements (Lellouch et al. 2011). Cooling by HCN is also discussed in this paper. It appears to be a possible alternative solution, but only if it remains largely supersaturated in the mesosphere.

Changing the temperature boundary condition may suppress the negative gradient, but at the expense of creating a warm, unexplained thermal profile above 1350 km. We have investigated more exotic solutions, like zonal winds or compositional variations that would "unbend" the retrieved temperature profiles, allowing a more isothemal mesosphere. However, no realistic models could be built upon those alternative assumptions. Again, the *New Horizons* flyby will provide constraints on the temperature boundary conditions and atmospheric composition that will be used to discriminate between the various solutions described here.

We acknowledge support from the French grants "Beyond Neptune" ANR-08-BLAN-0177 and "Beyond Neptune II" ANR-11-IS56-0002.

A. Dias-Oliveira is thankful for the support of the following grants: CAPES (BEX 9110/12-7) FAPERJ/PAPDRJ (E-45/2013). R. Vieira-Martins acknowledges the following grants: CNPq-306885/2013, CAPES/Cofecub-2506/2015, FAPERJ/PAPDRJ-45/2013. TRAPPIST is a project funded by the Belgian Fund for Scientific Research (F.R.S.-FNRS) under grant FRFC 2.5.594.09.F, with the participation of the Swiss National Science Foundation. J. L. Ortiz and N. Morales acknowledge funding from Proyecto de Excelencia de la Junta de Andalucía, J.A. 2012-FQM1776 and from FEDER funds. M. Gillon and E. Jehin are F.R.S.-FNRS Research Associates. C. Opitom acknowledges the support of the F.R.S.-FNRS for her PhD thesis. R. Leiva is supported by the CONICYT PCHA/Doctorado Nacional scholarship. M. Assafin thanks the CNPq (Grants 473002/2013-2 and 308721/2011-0) and FAPERJ (Grant E-26/111.488/2013). J.I.B. Camargo acknowledges CNPq for a PQ2 fellowship (process number 308489/2013-6). A.R. Gomes-Júnior thanks CAPES. We also thank Caisey Harlingten for the use of his 20 inch telescope in San Pedro de Atacama.

APPENDIX A
SYNTHETIC LIGHT CURVES

A.1. Parameterized Temperature Profile

We define a parametric model for Pluto's atmosphere temperature profile, $T(r)$, where r is the radius, i.e., the distance to Pluto's center. The model must be detailed enough to capture

the main features revealed by the inversions (Figures 10 and 13), but still simple enough to allow an easy and meaningful control of $T(r)$ and an assessment of the error bars associated with each parameter. The features we want to describe are: (i) a thin stratosphere just above the surface, with a strong increase of temperature with altitude, (ii) an "elbow" where the temperature reaches its maximum, marking the stratopause, (iii) an intermediate region with a mild negative gradient, and finally (iv), an isothermal upper branch.

These features define three regions, bounded by four points 1,…4 at prescribed radii r_1,…r_4, see Figure 13. More precisely, the profile $T(r)$ is generated as follows:

$$\begin{cases} c1 \cdot r + c2 \cdot T(r) & \\ \quad + c3 \cdot rT(r) + c4 \cdot r^2 & \text{for} \quad r_1 \leqslant r \leqslant r_3 \\ \quad + c5 \cdot T^2(r) = 1 & \text{(hyperbolic branch)} \\ T(r) = c6 + c7 \cdot r & \text{for} \quad r_3 \leqslant r \leqslant r_4 \\ \quad + c8 \cdot r^2 + c9 \cdot r^3 & \text{(polynomial branch)} \\ T(r) = T_{\rm iso} & \text{for} \quad r_4 \leqslant r \ \text{(straight line)}. \end{cases} \tag{4}$$

Note that r_2 does not appear in the equations above, and is defined as the radius where the temperature reaches its maximum (Figure 13). The functional forms chosen here (hyperbolic, polynomial, and straight lines) are *not* based on physical grounds, but rather, are empirical and simple formulae that satisfactorily fit the observed profiles (Figure 8).

The parameters $c1$,…$c9$ are determined to ensure that $T(r)$ is continuous both in temperature and its derivative, dT/dr, at points 1, 3, and 4. Those conditions provide algebraic systems that are solved by a classical Gauss-Jordan method (Press et al. 1992).

In practice: (1) we fix the temperature $T_1 = T(r_1)$ at the bottom of the profile, together with its gradient $(dT/dr)_1$. (2) We fix the value of the maximum of temperature $T_2 = T(r_2)$ at r_2 and the temperature $T_3 = T(r_3)$ at inflexion point 3. We thus have three boundary conditions for T: T_1, T_2, T_3 at r_1, r_2, and r_3, respectively, and two boundary conditions for dT/dr: $(dT/dr)(r_1) = (dT/dr)_1$ and $(dT/dr)(r_2) = 0$, which fixes the five coefficients $c1$,…$c5$. Note in passing that the values of $c1$,…$c5$ then impose the temperature gradient $(dT/dr)_3$ at r_3; (3) We fix the temperature $T_{\rm iso}$ at r_4, the point where the isothermal branch is reached. This provides two boundary conditions in T: T_3 and $T_{\rm iso}$ at r_3 and r_4, respectively, plus two boundary conditions for dT/dr: $(dT/dr)_3$ at r_3 and $(dT/dr)(r_4) = 0$, thus fixing the remaining four coefficients $c6$,…$c9$.

The locations of points 1–4 in the space (T,r) are chosen to best fit the observed profiles (see the main text for details). Once $T(r)$ is defined, the gas number density profile $n(r)$ is obtained by integrating the first order differential equation:

$$\frac{1}{n} \cdot \frac{dn}{dr} = -\left[\frac{\mu g(r)}{kT} + \frac{1}{T} \cdot \frac{dT}{dr}\right], \tag{5}$$

derived from the equation of state for an ideal gas, and the hydrostatic equation. Here,

$$g(r) = \frac{GM}{r^2} \tag{6}$$

is the acceleration of gravity, assuming a spherical, homogeneous planet. The values of μ (Table 4) correspond to molecular nitrogen, assumed to be the unique gas present in the atmosphere. Also listed in Table 4 are the Boltzmann constant k and Pluto's mass parameter GM.

A boundary condition is required to integrate Equation (5), e.g., the pressure p_{1275} at $r = 1275$ km, which fixes the needed boundary condition $n_{1275} = P_{1275}/kT_{1275}$. Finally, the refractivity $\nu(r)$ of the gas (index of refraction minus unity) is given by

$$\nu(r) = K \cdot n(r), \tag{7}$$

where the molecular refracticity is given in Table 3, assuming again pure molecular nitrogen. Once $\nu(r)$ is obtained, we can derive the vertical refractivity gradient $d\nu/dr$ that is used in the ray-tracing code, see below.

The inversions proceed the other way around: the light curves provide $d\nu/dr(r)$ through an abelian integral (Vapillon et al. 1973), then $\nu(r)$, from which $n(r)$ is derived (Equation (7)), followed by the temperature profile, once a boundary condition is given for T (Equation (5)).

A.2. Ray-tracing

For small values of ν (as it is the case here) and under a spherical symmetry assumption, a stellar ray is deviated by $d\omega = (\partial\nu/\partial r) \cdot ds$ (Snell–Descartes law) as it moves along an elementary path ds. In principle, a ray-tracing code should account for the curvature of the stellar ray as it is refracted in the atmosphere. In practice, however, it is enough to assume that the ray has a rectilinear trajectory in the entire atmosphere. In fact, the maximum total deviation ω suffered by the ray is very small for ground-based occultations, more precisely of the order of Pluto's apparent angular radius, ~0.05 arcsec, so that $\omega < \sim 3 \times 10^{-7}$ rad. Most of that deviation occurs in the deepest scale height H traversed at radius r, which represents a traveled length of $l \sim \sqrt{2\pi rH}$ (Baum & Code 1953). Taking typical values of $r \sim 1200$ km and $H < \sim 50$ km, we get $l < \sim 600$ km, i.e., a deviation inside the atmosphere of $\sim\omega \cdot l < 0.2$ m, which is negligible compared to the scales probed by ground-based stellar occultations.

The numerical integration of Equation (5), using a second order scheme, provides $n(r_i)$ at discreet layers of radii r_i, from which the refractivity ν_i and its gradient $(d\nu/dr)(r_i)$ are calculated. The total deviation along the straight line s is then:

$$\omega = \sum_i \Delta\omega_i = \sum_i (d\nu/dr)(r_i) \cdot \Delta s_i, \tag{8}$$

where Δs_i is the path along s traveled inside the layer i. Then, for a closest approach r of a ray to Pluto's center, the corresponding distance z to the shadow center upon arrival on Earth is

$$z = r + \omega(r) \cdot D, \tag{9}$$

where D is Pluto's geocentric distance. The observed stellar flux is then

$$\Phi(z) = f\frac{dr}{dz} = \frac{1}{1 + Dd\omega/dr}, \tag{10}$$

where $f = r/z$ is the focusing factor due to the (assumed circular) limb curvature (see Sicardy et al. 1999).

The thickness Δr_i of the individual refracting layers has been adjusted to 30 m to minimize numerical noise, while keeping computing times reasonably low. Similarly, the sampling for r (the closest distance of the rays to Pluto's center) has been

adjusted so that adjacent rays arrive at separation $\Delta z \approx 1$ km in the shadow plane.

Once the table (r, z, $\Phi(z)$) has been completed, the synthetic flux at a given site and given moment (corresponding to a distance $z_{\rm obs}$ of the observer to the shadow center) is calculated by interpolation. If several stellar images are present, all of the fluxes are summed. In the particular case of a spherically symmetric atmosphere, and for a given distance $z_{\rm obs}$, there is a primary image corresponding to $z = z_{\rm obs}$, and a secondary image corresponding to $z = -z_{\rm obs}$.

The lowest radius r_1 considered in the model (1190.4 km, see Table 4 and Figure 13) is adjusted so that the corresponding flux received in the shadow plane is $\sim 10^{-3}$ of the unocculted stellar flux, negligible compared to the noise level of the best light curves. The upper limit for the atmosphere has been fixed to a radius of about 2300 km. This corresponds to a pressure level of about 0.05 nbar, at which point the stellar drop is several orders of magnitudes less than the noise in our best light curves.

The profile that best fits our light curves is shown in Figure 13. The trajectories of the primary and secondary stellar images as seen from VLT on 2012 July 18 are displayed in Figure 2.

The best fits to the observed light curves are shown in Figures 3 and 4. Their quality is assessed through the so-called χ^2 per degree of freedom:

$$\chi^2_{\rm dof} = \frac{\chi^2}{N-M} = \frac{1}{N-M}\sum_{i=1}^{N}\left(\frac{\Phi_{\rm obs,i} - \Phi_{\rm syn,i}}{\sigma_i}\right)^2, \qquad (11)$$

where $\Phi_{\rm obs,i}$ (resp. $\Phi_{\rm syn,i}$) is the observed (resp. synthetic) stellar flux of the $i^{\rm th}$ data point, σ_i is its associated standard deviation, where the summation is extended to the N data points from all the light curves used in the fit, and M is the number of free parameters of the model. As we have nine coefficients $c_1,\ldots c_9$ to define $T(r)$ (Equation (4)), a boundary condition p_{1275} and two quantities to define Pluto's center, $M = 12$.

APPENDIX B
NOISE PROPAGATION

B.1. Photometric Noise

Here we estimate the effect of photometric noise in an occultation light curve on the retrieved density, temperature, and temperature gradient profiles. We denote δ the fluctuation of a given quantity, and $\sigma = \sqrt{\overline{\delta^2}}$ is its standard deviation, where the bar denotes average values. For estimation purposes, it is enough to assume here (but not in the ray-tracing or inversion procedures) that the atmosphere has locally a constant density scale height H that is small compared to the planet radius. The stellar flux is then given by the Baum and Code (BC) equation (Baum & Code 1953):

$$\frac{1}{\Phi} - 2 + \log\left(\frac{1}{\Phi} - 1\right) = -\frac{z - z_{1/2}}{H}, \qquad (12)$$

where $z_{1/2}$ is the position in the shadow plane at which $\Phi = 1/2$ (half-light level).

We focus on the top of the profiles, corresponding to $\Phi \sim 1$, so that Equation (12) becomes $\Phi(z) \sim 1 - \exp[-(z - z_{1/2})/H]$. Moreover, for $\Phi \sim 1$, the stellar ray deviation ω is small, and we can equate r and z (see Equations (9) and (10)), where $f \sim 1$. In the BC approximation, we have $\omega \sim -\nu\sqrt{2\pi r/H}$, where ν is the refractivity at r. As the atmosphere density profile is basically exponential, $d\omega/dr \sim -\omega/H = \nu\sqrt{2\pi r/H^3}$, so that Equation (10) can be used to estimate the expected refractivity corresponding to a stellar flux Φ, namely $\nu \sim (1 - \Phi)\sqrt{H^3/2\pi r D^2}$.

We denote ν_0 and r_0 the refractivity and corresponding radius where the stellar drop is equal to the standard deviation of the flux, σ_Φ, i.e.,

$$\nu_0 \sim \sigma_\Phi\sqrt{\frac{H^3}{2\pi r D^2}}. \qquad (13)$$

Thus, r_0 is the radius where the stellar drop starts to be barely significant, given the photometric noise. At the upper part of the profiles, we have $H \sim 60$ km. The 2012 July 18 NACO light curve has a photometric standard deviation of $\sigma_\Phi = 0.011$. Using the value of D given in Table 3, we obtain $\nu_0 \sim 1.3 \times 10^{-11}$. Assuming a pure N_2 atmosphere, we obtained the corresponding molecular density $n_0 = \nu_0/K \sim 6 \times 10^{12}$ cm^{-3}, which is reached at radius

$$r_0 \sim 1565 \text{ km}.$$

For $\Phi \sim 1$ (and $f \sim 1$), and using the results above, Equation (10) provides $\Phi \sim 1 - D d\omega/dr = 1 + \sqrt{2\pi r D^2/H}\,(d\nu/dr)$. For a noise-free light curve, we expect $\Phi = 1 - \sigma_\Phi \exp[-(r - r_0)/H]$. In reality, Φ is affected by fluctuations δ_Φ, so the retrieved refractivity gradient is in fact: $d\nu/dr = (\nu_0/H)\cdot[-\exp[-(r - r_0)/H] + \delta_\Phi/\sigma]$. Consequently, the standard deviation associated with each point of the $(d\nu/dr)(r)$ profile (and restricting ourselves to the top of the profile) is:

$$\sigma_{d\nu/dr} \sim \frac{\nu_0}{H}.$$

The profile $(d\nu/dr)(r)$ is the primary result derived from the light curve, and from which all the other profiles are deduced. Once $d\nu/dr$ is known, we have to estimate $\nu(r) = \nu_1 + \int_{r_1}^{r}(d\nu/dr)dr$, where $(r_1, \nu_1 = \nu(r_1))$ is a boundary condition. The integration is performed numerically by taking $\nu(r) = \nu(r_1) + \sum_{i=1}^{N}(d\nu/dr)(r_i)\cdot\Delta r$, where Δr is the spatial sampling of the data (i.e., $\Delta r =$ the star velocity perpendicular to the limb multiplied by the exposure time). Thus, $r_i = r_1 + (i - 1)\Delta r$ and $N = |r - r_1|/\Delta r$. Adding the variances associated with individual $(d\nu/dr)(r_i)$'s, we obtain:

$$\sigma_\nu \sim \sqrt{\frac{|r - r_1|}{H}\frac{\Delta r}{H}}\,\nu_0 \sim \sqrt{\frac{\Delta r}{H}}\,\nu_0,$$

where the second approximation stems from the fact that r_1 is chosen close to r_0 and which we are considering here the few top scale heights of the profiles, so that $|r - r_1|/H \sim \mathcal{O}(1)$. Note that $\sigma_\nu = 0$ for $r = r_1$. This is because (r_1, ν_1) is an arbitrary boundary condition, and as such has no associated error bars.

From $n = \nu/K$, we obtain the standard deviation associated with the density gradient and the density itself: $\sigma_{dn/dr} = \sigma_{d\nu/dr}/K$ and $\sigma_n = \sigma_\nu/K$. Moreover, from Equation (5), and assuming an isothermal upper atmosphere, we obtain $\delta_{dT/dr} = -(T/n)\delta_{dn/dr}$, so that $\sigma_{dT/dr} = (T/n)\sigma_{dn/dr}$. Finally, the temperature profile is obtained from the numerical integration of $T(r) = T_2 + \int_{r_2}^{r}(dT/dr)dr$, where

$(r_2, T_2 = T(r_2))$ is an arbitrary boundary condition. Using the same line of reasoning as for $n(r)$, we obtain σ_T by adding the variances $\sigma^2_{dT/dr}$ of all the points $i = 1 \ldots N$ involved in the integration, where now $N = |r - r_2|/\Delta r$. Combining the results above, we obtain the following standard deviations for $n(r)$, $T(r)$ and $(dT/dr)(r)$:

$$\sigma_n \sim \sqrt{\frac{\Delta r}{H}}\, n_0,$$
$$\sigma_T \sim T\sqrt{\frac{\Delta r}{2\,H}}\,\sqrt{\left|e^{2(r-r_2)/H} - 1\right|}\, e^{(r_2-r_0)/H},$$
$$\sigma_{dT/dr} \sim \frac{T}{H} e^{(r-r_0)/H}. \quad (14)$$

Figure 8 shows the $\pm 1\sigma$ envelopes at the upper parts of the various profiles. We take here $r_2 = 1390$ km, the radius at which we fix a prescribed temperature $T_2 \sim 81$ K. Note again that $\sigma_T = 0$ at $r = r_2$, as (r_2, T_2) is an arbitrary boundary condition. Finally, the envelopes $\pm 1\sigma$ are plotted only down to the half-light level ($r \sim 1290$ km), as the estimations made here apply only for the upper part of the light curve. In any case, below that level, the uncertainties in the profiles are dominated by the uncertainty on the background Pluto + Charon contribution (see below).

B.2. Effect of the Pluto and Charon Flux Contributions

The stellar flux reaches its minimum value in the shadow at typically $z_{\min} \sim (z_{1/2})/2$, i.e., halfway between the half-light level and the shadow center, where the central flash occurs (Figure 13). At the minimum, we have from Equation (12): $\Phi_{\min} \sim H/(z_{1/2} - z_{\min}) \sim 2\,H/z_{1/2}$. Equation (5) then provides

$$H = \left|\frac{n}{dn/dr}\right| = \frac{T}{(\mu g/k) + (dT/dr)} \sim \frac{z_{1/2}}{2}\Phi_{\min}. \quad (15)$$

At the bottom of the temperature profile (stratosphere), $\mu g/k$ and dT/dr are of the same order of magnitude. Consequently, increasing the value of the Pluto + Charon contribution to the light curve decreases the value of Φ (Figure 7), thus increasing the retrieved gradient dT/dr. This is illustrated in Figure 9.

B.3. Effect of Initial Conditions

Once the density profile $n(r)$ is derived from the inversion, Equation (5) yields the temperature profile $T(r)$, provided a boundary condition $T_b = T(r_b)$ is fixed at an arbitrary level r_b. Let us consider two possible solutions $T(r)$ and $(T + \Delta T)(r)$ that differ by $\Delta T(r_b)$ at r_b, then expanding Equation (5) to first order in $(\Delta T/T)(r)$, we obtain:

$$\frac{d}{dr}\left(\frac{\Delta T}{T}\right) \sim \frac{1}{H}\left(\frac{\Delta T}{T}\right),$$

where we have approximated $H \sim kT/\mu g$. Thus, as r increases, the relative difference $\Delta T/T$ diverge exponentially as:

$$\left(\frac{\Delta T}{T}\right)(r) \sim \left(\frac{\Delta T}{T}\right)(r_b) \cdot e^{(r-r_b)/H}. \quad (16)$$

This exponential divergence should not been confused with the one that is provided by Equation (14) for σ_T. The latter tends to zero as the noise tends to zero, while the former is inherent to the nature of Equation (5).

REFERENCES

Assafin, M., Camargo, J. I. B., Vieira Martins, R., et al. 2010, A&A, 515, A32
Assafin, M., Campos, R. P., Vieira Martins, R., et al. 2008, P&SS, 56, 1882
Assafin, M., Vieira-Martins, R., Braga-Ribas, F., et al. 2009, AJ, 137, 4046
Baum, W. A., & Code, A. D. 1953, AJ, 58, 108
Benedetti-Rossi, G., Vieira Martins, R., Camargo, J. I. B., Assafin, M., & Braga-Ribas, F. 2014, A&A, 570, A86
Bosh, A. S., Person, M. J., Levine, S. E., et al. 2015, Icar, 246, 237
Boursier, C., Ménard, J., Doyennette, L., & Menard-Bourcin, F. 2003, JPCA, 107, 5280
Braga-Ribas, F., Sicardy, B., Ortiz, J. L., et al. 2013, ApJ, 773, 26
Brosch, N. 1995, MNRAS, 276, 571
Elliot, J. L., Ates, A., Babcock, B. A., et al. 2003, Natur, 424, 165
Elliot, J. L., Dunham, E. W., Bosh, A. S., et al. 1989, Icar, 77, 148
Elliot, J. L., Person, M. J., Gulbis, A. A. S., et al. 2007, AJ, 134, 1
Fray, N., & Schmitt, B. 2009, P&SS, 57, 2053
French, R. G., Toigo, A. D., Gierasch, P. J., et al. 2015, Icar, 246, 247
Girard, J. H., Kasper, M., Quanz, S. P., et al. 2010, Proc. SPIE, 7736E, 77362N
Gulbis, A. A. S., Emery, J. P., Person, M. J., et al. 2015, Icar, 246, 226
Hansen, C. J., & Paige, D. A. 1996, Icar, 120, 247
Hubbard, W. B., Hunten, D. M., Dieters, S. W., Hill, K. M., & Watson, R. D. 1988, Natur, 336, 452
Jehin, E., Gillon, M., Queloz, D., et al. 2011, Msngr, 145, 2
Krasnopolsky, V. A., & Cruikshank, D. P. 1999, JGR, 104, 21979
Lara, L. M., Ip, W. H., & Rodrigo, R. 1997, Icar, 130, 16
Lellouch, E. 1994, Icar, 108, 255
Lellouch, E., de Bergh, C., Sicardy, B., et al. 2015a, Icar, 246, 268
Lellouch, E., Gurwell, M., Butler, B., et al. 2015b, IAUC, 9273, 1
Lellouch, E., Laureijs, R., Schmitt, B., et al. 2000, Icar, 147, 220
Lellouch, E., Santos-Sanz, P., Lacerda, P., et al. 2013, A&A, 557, A60
Lellouch, E., Sicardy, B., de Bergh, C., et al. 2009, A&A, 495, 17
Lellouch, E., Stansberry, J., Emery, J., Grundy, W., & Cruikshank, D. P. 2011, Icar, 214, 701
Lenzen, R., Hartung, M., Brandner, W., et al. 2003, Proc. SPIE, 4841, 944
Olkin, C. B., Young, L. A., Borncamp, D., et al. 2015, Icar, 246, 220
Olkin, C. B., Young, L. A., French, R. G., et al. 2014, Icar, 239, 15
Ortiz, J. L., Sicardy, B., Braga-Ribas, F., et al. 2012, Natur, 491, 566
Person, M. J., Dunham, E. W., Bosh, A. S., et al. 2013, AJ, 146, 83
Press, W. H., Teukolsky, S. A., Vetterling, W. T., & Flannery, B. P. 1992, Numerical Recipes in C. The Art of Scientific Computing (New York: Cambridge Univ. Press)
Rousset, G., Lacombe, F., Puget, P., et al. 2003, Proc. SPIE, 4839, 140
Sicardy, B., Bellucci, A., Gendron, E., et al. 2006, Natur, 439, 52
Sicardy, B., Ferri, F., Roques, F., et al. 1999, Icar, 142, 357
Sicardy, B., Ortiz, J. L., Assafin, M., et al. 2011, Natur, 478, 493
Sicardy, B., Widemann, T., Lellouch, E., et al. 2003, Natur, 424, 168
Siddles, R., Wilson, G., & Simpson, C. 1994, CPL, 225, 146
Strobel, D. F., Zhu, X., Summers, M. E., & Stevens, M. H. 1996, Icar, 120, 266
Summers, M. E., Strobel, D. F., & Gladstone, G. R. 1997, Chemical Models of Pluto's Atmosphere, ed. S. A. Stern & D. J. Tholen (Tuscon, AZ: Univ. of Arizona Press), 391
Tholen, D. J., Buie, M. W., Grundy, W. M., & Elliott, G. T. 2008, AJ, 135, 777
Vangvichith, M. 2013, Thèse de Doctorat, Ecole Polytechnique
Vapillon, L., Combes, M., & Lecacheux, J. 1973, A&A, 29, 135
Vuitton, V., Yelle, R. V., & McEwan, M. J. 2007, Icar, 191, 722
Washburn, E. W. 1930, International Critical Tables of Numerical Data: Physics, Chemistry and Technology, Vol. 7 (New York: McGraw-Hill)
Yelle, R. V. 1991, AJ, 383, 380
Yelle, R. V., & Lunine, J. I. 1989, Natur, 339, 288
Young, E. F., French, R. G., Young, L. A., et al. 2008, AJ, 136, 1757
Young, L. A. 2013, ApJL, 766, L22
Zacharias, N., Monet, D. G., Levine, S. E., et al. 2004, BAAS, 36, 1418
Zalucha, A. M., Gulbis, A. A. S., Zhu, X., Strobel, D. F., & Elliot, J. L. 2011a, Icar, 211, 804
Zalucha, A. M., & Michaels, T. I. 2013, Icar, 223, 819
Zalucha, A. M., Zhu, X., Gulbis, A. A. S., Strobel, D. F., & Elliot, J. L. 2011b, Icar, 214, 685
Zhu, X., Strobel, D. F., & Erwin, J. T. 2014, Icar, 228, 301

The Astronomical Journal, 154:144 (21pp), 2017 October https://doi.org/10.3847/1538-3881/aa830d

The Structure of Chariklo's Rings from Stellar Occultations

D. Bérard[1], B. Sicardy[1], J. I. B. Camargo[2,3], J. Desmars[1], F. Braga-Ribas[2,3,4], J.-L. Ortiz[5], R. Duffard[5], N. Morales[5], E. Meza[1], R. Leiva[1,6], G. Benedetti-Rossi[2,3], R. Vieira-Martins[2,3,7,8], A.-R. Gomes Júnior[8], M. Assafin[8], F. Colas[7], J.-L. Dauvergne[9], P. Kervella[1,10], J. Lecacheux[1], L. Maquet[7], F. Vachier[7], S. Renner[11], B. Monard[12], A. A. Sickafoose[13,14], H. Breytenbach[13,15], A. Genade[13,15], W. Beisker[16,17], K.-L. Bath[16,17], H.-J. Bode[16,17,54], M. Backes[18], V. D. Ivanov[19,20], E. Jehin[21], M. Gillon[21], J. Manfroid[21], J. Pollock[22], G. Tancredi[23], S. Roland[24], R. Salvo[24], L. Vanzi[25], D. Herald[26,27,28], D. Gault[26,29], S. Kerr[26,30], H. Pavlov[26,27], K. M. Hill[31], J. Bradshaw[27,32], M. A. Barry[26,33], A. Cool[34,35], B. Lade[34,35,36], A. Cole[31], J. Broughton[26], J. Newman[28], R. Horvat[29], D. Maybour[37], D. Giles[29,37], L. Davis[29], R. A. Paton[29], B. Loader[26,27], A. Pennell[26,38], P.-D. Jaquiery[38,39], S. Brillant[20], F. Selman[20], C. Dumas[40], C. Herrera[20], G. Carraro[41], L. Monaco[42], A. Maury[43], A. Peyrot[44], J.-P. Teng-Chuen-Yu[44], A. Richichi[45], P. Irawati[46], C. De Witt[16], P. Schoenau[16], R. Prager[17], C. Colazo[47,48], R. Melia[48], J. Spagnotto[49], A. Blain[50], S. Alonso[51], A. Román[52], P. Santos-Sanz[5], J.-L. Rizos[5], J.-L. Maestre[53], and D. Dunham[27]

[1] LESIA, Observatoire de Paris, PSL Research University, CNRS, Sorbonne Universités, UPMC Univ. Paris 06, Univ. Paris Diderot, Sorbonne Paris Cité, France
[2] Observatório Nacional/MCTIC, R. General José Cristino 77, RJ 20921-400 Rio de Janeiro, Brazil
[3] Laboratório Interinstitucional de e-Astronomia—LIneA, Rua Gal. José Cristino 77, Rio de Janeiro- RJ 20921-400, Brazil
[4] Federal University of Technology- Paraná (UTFPR/DAFIS), Rua Sete de Setembro, 3165, CEP 80230-901, Curitiba, PR, Brazil
[5] Instituto de Astrofísica de Andalucía, CSIC, Apt. 3004, E-18080 Granada, Spain
[6] Instituto de Astrofísica, Facultad de Física, Pontificia Universidad Católica de Chile, Av. Vicuña Mackenna 4860, Santiago, Chile
[7] IMCCE, Observatoire de Paris, PSL Research University, CNRS, Sorbonne Universités, UPMC Univ. Paris 06, 77 av. Denfert-Rochereau, F-75014, Paris, France
[8] Observatório do Valongo/UFRJ, Ladeira Pedro Antonio 43, RJ 20.080-090 Rio de Janeiro, Brazil
[9] Ciel & Espace, Paris, France
[10] Unidad Mixta Internacional Franco-Chilena de Astronomía (CNRS UMI 3386), Departamento de Astronomía, Universidad de Chile, Camino El Observatorio 1515, Las Condes, Santiago, Chile
[11] IMCCE, Observatoire de Paris, CNRS UMR 8028, Université Lille 1, Observatoire de Lille 1 impasse de l'Observatoire, F-59000 Lille, France
[12] Kleinkaroo Observatory, Calitzdorp, St. Helena 1B, P.O. Box 281, 6660 Calitzdorp, Western Cape, South Africa
[13] South African Astronomical Observatory, P.O. Box 9, Observatory, 7935, South Africa
[14] Department of Earth, Atmospheric, and Planetary Sciences, Massachusetts Institute of Technology Cambridge, MA 02139-4307, USA
[15] University of Cape Town, Department of Astronomy, Rondebosch , Cape Town, Western Cape, 7700, South Africa
[16] IOTA/ES, Barthold-Knaust-Strasse 8, D-30459 Hannover, Germany
[17] Internationale Amateursternwarte e. V., IAS, Hakos/Namibia and Bichlerstr. 46, D-81479 München (Munich), Germany
[18] Department of Physics, University of Namibia, 340 Mandume Ndemufayo Ave, P/Bag 13301, Windhoek, Namibia
[19] ESO, Karl-Schwarzschild-Str. 2, D-85748 Garching bei, München, Germany
[20] ESO, Alonso de Cordova 3107, Casilla 19001, Santiago 19, Chile
[21] Institut d'Astrophysique de l'Université de Liège, Allée du 6 Août 17, B-4000 Liège, Belgique
[22] Physics and Astronomy Department, Appalachian State University, Boone, NC 28608, USA
[23] Dpto. Astronomia, Facultat de Ciencias, Uruguay
[24] Observatorio Astronómico Los Molinos, DICYT, MEC, Montevideo, Uruguay
[25] Department of Electrical Engineering and Center of Astro-Engineering, Pontificia Universidad Católica de Chile, Av. Vicuña Mackenna 4860, Santiago, Chile
[26] Occultation Section of the Royal Astronomical Society of New Zealand (RASNZ), Wellington, New Zealand
[27] International Occultation Timing Association (IOTA), P.O. Box 7152, Kent, WA 98042, USA
[28] Canberra Astronomical Society, Canberra, ACT, Australia
[29] Western Sydney Amateur Astronomy Group (WSAAG), Sydney, NSW, Australia
[30] Astronomical Association of Queensland, Queensland, Australia
[31] School of Physical Sciences, University of Tasmania, Private Bag 37, Hobart, TAS 7001, Australia
[32] Samford Valley Observatory, QLD, Australia
[33] Electrical and Information Engineering Department, University of Sydney, Camperdown, NSW 2006, Australia
[34] Defence Science & Technology Group, Edinburgh, South Australia
[35] The Heights Observatory, Modbury Heights, South Australia
[36] Stockport Observatory, Astronomical Society of South Australia, Stockport, SA, Australia
[37] Penrith Observatory, Western Sydney University, Sydney, NSW, Australia
[38] Dunedin Astronomical Society, Dunedin, New Zealand
[39] Royal Astronomical Society of New Zealand (RASNZ), Wellington, New Zealand
[40] TMT International Observatory, 100 West Walnut Street, Suite 300, Pasadena, CA 91124, USA
[41] Dipartimento di Fisica e Astronomia, Universita di Padova, Italy
[42] Departamento de Ciencias Fisicas, Universidad Andres Bello, Fernandez Concha 700, Santiago, Chile
[43] San Pedro de Atacama Celestial Explorations, Casilla 21, San Pedro de Atacama, Chile
[44] Makes Observatory, La Réunion, France
[45] INAF—Osservatorio Astrofisico di Arcetri, Largo E. Fermi 5, I-50125 Firenze, Italy
[46] National Astronomical Research Institute of Thailand, Siriphanich Building, Chiang Mai 50200, Thailand
[47] Ministerio de Educación de la Provincia de Córdoba, Córdoba, Argentina
[48] Observatorio Astronómico, Universidad Nacional de Córdoba, Córdoba, Argentina
[49] Observatorio El Catalejo, Santa Rosa, La Pampa, Argentina
[50] Asociación Argentina Amigos de la Astronomía, Av. Patricias Argentinas 550, Buenos Aires, Argentina
[51] Software Engineering Department, University of Granada, Spain

[52] Sociedad Astronómica Granadina, Granada, Spain
[53] Observatorio Astronómico de Albox, Apt. 63, E-04800 Albox (Almeria), Spain
Received 2017 May 16; revised 2017 July 25; accepted 2017 July 27; published 2017 September 11

Abstract

Two narrow and dense rings (called C1R and C2R) were discovered around the Centaur object (10199) Chariklo during a stellar occultation observed on 2013 June 3. Following this discovery, we planned observations of several occultations by Chariklo's system in order to better characterize the physical properties of the ring and main body. Here, we use 12 successful occulations by Chariklo observed between 2014 and 2016. They provide ring profiles (physical width, opacity, edge structure) and constraints on the radii and pole position. Our new observations are currently consistent with the circular ring solution and pole position, to within the ± 3.3 km formal uncertainty for the ring radii derived by Braga-Ribas et al. The six resolved C1R profiles reveal significant width variations from $\sim$5 to 7.5 km. The width of the fainter ring C2R is less constrained, and may vary between 0.1 and 1 km. The inner and outer edges of C1R are consistent with infinitely sharp boundaries, with typical upper limits of one kilometer for the transition zone between the ring and empty space. No constraint on the sharpness of C2R's edges is available. A 1σ upper limit of $\sim$20 m is derived for the equivalent width of narrow (physical width $<$4 km) rings up to distances of 12,000 km, counted in the ring plane.

Key words: ephemerides – minor planets, asteroids: individual (Chariklo) – occultations – planets and satellites: rings

1. Introduction

The asteroid-like body (10199) Chariklo is a Centaur object orbiting between Saturn and Uranus. It probably moved recently ($\sim$10 Myr ago) from the trans-Neptunian region to its present location and will leave it within a similarly short timescale, due to perturbations by Uranus (Horner et al. 2004). With a radius of 119 ± 5 km, estimated from thermal measurements (Fornasier et al. 2014), it is the largest Centaur known to date, but still remains very modest in size compared to the telluric or giant planets. On 2013 June 3, a ring system was discovered around this small object during a stellar occultation. Two dense and narrow rings, 2013C1R and 2013C2R (C1R and C2R for short), were detected. They are separated by about 15 km and orbit close to 400 km from Chariklo's center (see Braga-Ribas et al. 2014 for details).

Until 2013, rings were only known around the giant planets. This discovery was thus surprising, and is key to better understanding the planetary rings, since they now appear to be more common than previously thought. In particular, the two rings, being dense, narrow, and (at least for C1R) sharp-edged, look like several of the dense ringlets seen around Saturn and Uranus (Elliot et al. 1984; French et al. 1991, 2016). In that context, there was a strong incentive for planning more occultation campaigns, first to unambiguously confirm the existence of Chariklo's rings and second, to obtain more information on their physical properties.

While the discovery occultation of 2013 June 3 provided the general physical parameters of the rings (width, orientation, orbital radius, optical depth, …), several questions are still pending, some of which are addressed in this work: Do the rings have inner structures that give clues about collisional processes? How sharp are their edges? What are the general shapes of C1R and C2R? Do they consist of solidly precessing ellipses like some of Saturn's or Uranus' ringlets? Do they have more complex proper modes with higher azimuthal wave numbers? Are there other fainter rings around Chariklo? What is the shape of the object itself and its role in the ring dynamics? Based on new results, what can we learn about their origin and evolution, which remain elusive (Sicardy et al. 2016)?

This study is made in the context where material has also been detected around the second largest Centaur, Chiron (again using stellar occultations). The nature of this material is still debated, and it could be interpreted as either a ring system (Ortiz et al. 2015) or a dust shell associated with Chiron's cometary activity (Ruprecht et al. 2015). Since Chariklo is presently moving close to the galactic plane, stellar occultations by this body are much more frequent than for Chiron; hence, we have more abundant information about its rings. The spatial resolution achieved during occultations reaches the sub-kilometer level, which is impossible to attain with any of the current classical imaging instruments. That said, the very small angular size subtended by the rings (0.08 arcsec tip to tip, as seen from Earth) has made occultation predictions difficult in the pre-*Gaia* era.

In spite of these difficulties, we were able to observe 13 positive stellar occultations (including the discovery one) between 2013 and 2016, from a total of 42 stations distributed worldwide (in Brazil, Argentina, Australia, Chile, La Réunion Island, Namibia, New Zealand, South Africa, Spain, Thailand, and Uruguay). Here, we focus on the ring detections (a total of 11 chords recorded after the discovery). We also obtained a total of 12 occultation chords by the main body from 2014 to 2016. Their timings are derived here, but their implications concerning Chariklo's size and shape will be presented elsewhere (Leiva et al. 2017). In Section 2, we present our observations and data analysis. In Section 3, we concentrate on the rings structures (width, inner structures, edge sharpness) and geometry (radius and orbital pole). The integral properties of the rings (equivalent width and depth) are derived in Section 4, before concluding remarks are given in Section 5.

2. Observations and Data Analysis

Following the ring discovery of 2013 June 3, we predicted and observed 12 positive stellar occultations by Chariklo and/or its rings between 2014 and 2016. In the following list, we mark in italic the events that led to multichord ring detections (thus providing constraints on the ring orientation, as discussed latter). Four occultations were observed on 2014 February 16 (rings), March 16 (rings), April 29 (rings and body), and June 28 (rings and body). In 2015, only two positive detections were recorded, April 26 (rings) and May 12 (body), while six occultations were

[54] Deceased, 2017 July 16.

The Astronomical Journal, 154:159 (23pp), 2017 October https://doi.org/10.3847/1538-3881/aa8956

Size and Shape of Chariklo from Multi-epoch Stellar Occultations*

R. Leiva[1,2], B. Sicardy[1], J. I. B. Camargo[3,4], J.-L. Ortiz[5], J. Desmars[1], D. Bérard[1], E. Lellouch[6], E. Meza[1], P. Kervella[1,7], C. Snodgrass[8], R. Duffard[5], N. Morales[5], A. R. Gomes-Júnior[9], G. Benedetti-Rossi[3,4], R. Vieira-Martins[3,4,9], F. Braga-Ribas[3,4,10], M. Assafin[9], B. E. Morgado[3], F. Colas[11], C. De Witt[12], A. A. Sickafoose[13,14], H. Breytenbach[13,15], J.-L. Dauvergne[16], P. Schoenau[12], L. Maquet[11], K.-L. Bath[12,17], H.-J. Bode[12,17,25], A. Cool[18,19], B. Lade[18,19,20], S. Kerr[21,22], and D. Herald[21,23,24]

[1] LESIA/Observatoire de Paris, CNRS UMR 8109, Université Pierre et Marie Curie, Université Paris-Diderot, 5 place Jules Janssen, F-92195 Meudon Cédex, France; rnleiva@uc.cl
[2] Instituto de Astrofísica, Facultad de Física, Pontificia Universidad Católica de Chile, Av. Vicuña Mackenna 4860, Santiago, Chile
[3] Observatório Nacional/MCTIC, Rua General José Cristino 77, RJ 20921-400, Rio de Janeiro, Brazil
[4] Laboratório Interinstitucional de e-Astronomia—LIneA, Rua General José Cristino 77, RJ 20921-400, Rio de Janeiro, Brazil
[5] Instituto de Astrofísica de Andalucía, CSIC, Glorieta de la Astronomía s/n, E-18008, Granada, Spain
[6] LESIA, Observatoire de Paris, PSL Research University, CNRS, Sorbonne Universités, UPMC Univ. Paris 06, Univ. Paris Diderot, Sorbonne Paris Cité, 5 place Jules Janssen, F-92195 Meudon, France
[7] Unidad Mixta Internacional Franco-Chilena de Astronomía (CNRS UMI 3386), Departamento de Astronomía, Universidad de Chile, Camino El Observatorio 1515, Las Condes, Santiago, Chile
[8] School of Physical Sciences, The Open University, Milton Keynes, MK7 6AA, UK
[9] Observatório do Valongo/UFRJ, Ladeira Pedro Antonio 43, RJ 20.080-090, Rio de Janeiro, Brazil
[10] Federal University of Technology- Paraná (UTFPR/DAFIS), Rua Sete de Setembro, 3165, CEP 80230-901, Curitiba, PR, Brazil
[11] IMCCE, Observatoire de Paris, PSL Research University, CNRS, Sorbonne Universités, UPMC Univ. Paris 06, 77 Av. Denfert-Rochereau, F-75014, Paris, France
[12] IOTA/ES, Barthold-Knaust-Strasse 8, D-30459 Hannover, Germany
[13] South African Astronomical Observatory, P.O. Box 9, 7935 Observatory, South Africa
[14] Department of Earth, Atmospheric, and Planetary Sciences, Massachusetts Institute of Technology, Cambridge, MA 02139-4307, USA
[15] Department of Astronomy, University of Cape Town, Rondebosch, Cape Town, 7700, South Africa
[16] AFA/Ciel et Espace, 17 Emile Deutsch de la Meurthe, F-75014, Paris, France
[17] Internationale Amateursternwarte e. V. IAS, Hakos/Namibia and Bichler Str. 46, D-81479, Munich, Germany
[18] Defence Science & Technology Group, P.O. Box 1500, Edinburgh SA 5111, Australia
[19] The Heights Observatory, 12 Augustus St, Modbury Heights SA 5092, Australia
[20] Stockport Observatory, Astronomical Society of South Australia, Stockport, SA, Australia
[21] Occultation Section of the Royal Astronomical Society of New Zealand (RASNZ), P.O. Box 3181, Wellington, New Zealand
[22] Astronomical Association of Queensland, 5 Curtis Street, Pimpama QLD 4209, Australia
[23] International Occultation Timing Association (IOTA), P.O. Box 7152, Kent, WA 98042, USA
[24] Canberra Astronomical Society, Canberra, ACT, Australia
Received 2017 July 7; revised 2017 August 28; accepted 2017 August 28; published 2017 September 22

Abstract

We use data from five stellar occultations observed between 2013 and 2016 to constrain Chariklo's size and shape, and the ring reflectivity. We consider four possible models for Chariklo (sphere, Maclaurin spheroid, triaxial ellipsoid, and Jacobi ellipsoid), and we use a Bayesian approach to estimate the corresponding parameters. The spherical model has a radius $R = 129 \pm 3$ km. The Maclaurin model has equatorial and polar radii $a = b = 143^{+3}_{-6}$ km and $c = 96^{+14}_{-4}$ km, respectively, with density 970^{+300}_{-180} kg m^{-3}. The ellipsoidal model has semiaxes $a = 148^{+6}_{-4}$ km, $b = 132^{+6}_{-5}$ km, and $c = 102^{+10}_{-8}$ km. Finally, the Jacobi model has semiaxes $a = 157 \pm 4$ km, $b = 139 \pm 4$ km, and $c = 86 \pm 1$ km, and density 796^{+2}_{-4} kg m^{-3}. Depending on the model, we obtain topographic features of 6–11 km, typical of Saturn icy satellites with similar size and density. We constrain Chariklo's geometric albedo between 3.1% (sphere) and 4.9% (ellipsoid), while the ring I/F reflectivity is less constrained between 0.6% (Jacobi) and 8.9% (sphere). The ellipsoid model explains both the optical light curve and the long-term photometry variation of the system, giving a plausible value for the geometric albedo of the ring particles of 10%–15%. The derived mass of Chariklo of 6–8 $\times$ 10^{18} kg places the rings close to 3:1 resonance between the ring mean motion and Chariklo's rotation period.

Key words: methods: statistical – minor planets, asteroids: individual (Chariklo) – occultations – planets and satellites: rings

1. Introduction

The Centaur object (10199) Chariklo is the only small object of the solar system known thus far to show the unambiguous presence of a ring system. It was discovered during a ground-based stellar occultation in 2013 (Braga-Ribas et al. 2014), and confirmed by several subsequent observations (Bérard et al. 2017).

Meanwhile, the basic physical characteristics of Chariklo remain fragmentary. Chariklo's radius estimations, taken from thermal measurements, vary from 108 to 151 km, with geometric albedo in the range 4%–8% (Jewitt & Kalas 1998; Altenhoff et al. 2001; Sekiguchi et al. 2012; Bauer et al. 2013;

* Based on observations obtained at the Southern Astrophysical Research (SOAR) telescope, which is a joint project of the Ministério da Ciência, Tecnologia, e Inovação (MCTI) da República Federativa do Brasil, the U.S. National Optical Astronomy Observatory (NOAO), the University of North Carolina at Chapel Hill (UNC), and Michigan State University (MSU).
[25] Deceased, 2017 July 16.

LETTER

doi:10.1038/nature24051

The size, shape, density and ring of the dwarf planet Haumea from a stellar occultation

J. L. Ortiz[1], P. Santos-Sanz[1], B. Sicardy[2], G. Benedetti-Rossi[3], D. Bérard[2], N. Morales[1], R. Duffard[1], F. Braga-Ribas[3,4], U. Hopp[5,6], C. Ries[5], V. Nascimbeni[7,8], F. Marzari[9], V. Granata[7,8], A. Pál[10], C. Kiss[10], T. Pribulla[11], R. Komžík[11], K. Hornoch[12], P. Pravec[12], P. Bacci[13], M. Maestripieri[13], L. Nerli[13], L. Mazzei[13], M. Bachini[14,15], F. Martinelli[15], G. Succi[14,15], F. Ciabattari[16], H. Mikuz[17], A. Carbognani[18], B. Gaehrken[19], S. Mottola[20], S. Hellmich[20], F. L. Rommel[4], E. Fernández-Valenzuela[1], A. Campo Bagatin[21,22], S. Cikota[23,24], A. Cikota[25], J. Lecacheux[2], R. Vieira-Martins[3,26,27,28], J. I. B. Camargo[3,27], M. Assafin[28], F. Colas[26], R. Behrend[29], J. Desmars[2], E. Meza[2], A. Alvarez-Candal[3], W. Beisker[30], A. R. Gomes-Junior[28], B. E. Morgado[3], F. Roques[2], F. Vachier[26], J. Berthier[26], T. G. Mueller[6], J. M. Madiedo[31], O. Unsalan[32], E. Sonbas[33], N. Karaman[33], O. Erece[34], D. T. Koseoglu[34], T. Ozisik[34], S. Kalkan[35], Y. Guney[36], M. S. Niaei[37], O. Satir[37], C. Yesilyaprak[37,38], C. Puskullu[39], A. Kabas[39], O. Demircan[39], J. Alikakos[40], V. Charmandaris[40,41], G. Leto[42], J. Ohlert[43,44], J. M. Christille[18], R. Szakáts[10], A. Takácsné Farkas[10], E. Varga-Verebélyi[10], G. Marton[10], A. Marciniak[45], P. Bartczak[45], T. Santana-Ros[45], M. Butkiewicz-Bąk[45], G. Dudziński[45], V. Alí-Lagoa[6], K. Gazeas[46], L. Tzouganatos[46], N. Paschalis[47], V. Tsamis[48], A. Sánchez-Lavega[49], S. Pérez-Hoyos[49], R. Hueso[49], J. C. Guirado[50,51], V. Peris[50] & R. Iglesias-Marzoa[52,53]

Haumea—one of the four known trans-Neptunian dwarf planets—is a very elongated and rapidly rotating body[1–3]. In contrast to other dwarf planets[4–6], its size, shape, albedo and density are not well constrained. The Centaur Chariklo was the first body other than a giant planet known to have a ring system[7], and the Centaur Chiron was later found to possess something similar to Chariklo's rings[8,9]. Here we report observations from multiple Earth-based observatories of Haumea passing in front of a distant star (a multi-chord stellar occultation). Secondary events observed around the main body of Haumea are consistent with the presence of a ring with an opacity of 0.5, width of 70 kilometres and radius of about 2,287 kilometres. The ring is coplanar with both Haumea's equator and the orbit of its satellite Hi'iaka. The radius of the ring places it close to the 3:1 mean-motion resonance with Haumea's spin period—that is, Haumea rotates three times on its axis in the time that a ring particle completes one revolution. The occultation by the main body provides an instantaneous elliptical projected shape with axes of about 1,704 kilometres and 1,138 kilometres. Combined with rotational light curves, the occultation constrains the three-dimensional orientation of Haumea and its triaxial shape, which is inconsistent with a homogeneous body in hydrostatic equilibrium. Haumea's largest axis is at least 2,322 kilometres, larger than previously thought, implying an upper limit for its density of 1,885 kilograms per cubic metre and a geometric albedo of 0.51, both smaller than previous estimates[1,10,11]. In addition, this estimate of the density of Haumea is closer to that of Pluto than are previous estimates, in line with expectations. No global nitrogen- or methane-dominated atmosphere was detected.

Within our programme of physical characterization of trans-Neptunian objects (TNOs), we predicted an occultation of the star URAT1 533−182543 by the dwarf planet (136108) Haumea and arranged observations as explained in Methods. Positive occultation detections were obtained on 21 January 2017, from twelve telescopes at ten different observatories. The instruments and the main features of each station are listed in Table 1.

As detailed in Methods (see also Fig. 1), the light curves (the normalized flux from the star plus Haumea versus time) show deep

[1]Instituto de Astrofísica de Andalucía (CSIC), Glorieta de la Astronomía S/N, 18008-Granada, Spain. [2]LESIA, Observatoire de Paris, PSL Research University, CNRS, Sorbonne Universités, UPMC Universités Paris 06, Universités Paris Diderot, Sorbonne Paris Cité, France. [3]Observatório Nacional/MCTIC, Rua General José Cristino 77, Rio de Janeiro CEP 20921-400, Brazil. [4]Federal University of Technology-Paraná (UTFPR/DAFIS), Rua Sete de Setembro 3165, CEP 80230-901 Curitiba, Brazil. [5]Universitäts-Sternwarte München, München, Scheiner Straße 1, D-81679 München, Germany. [6]Max-Planck-Institut für Extraterrestrische Physik, D-85741 Garching, Germany. [7]Dipartimento di Fisica e Astronomia, 'G. Galilei', Università degli Studi di Padova, Vicolo dell'Osservatorio 3, I-35122 Padova, Italy. [8]INAF—Osservatorio Astronomico di Padova, vicolo dell'Osservatorio 5, I-35122 Padova, Italy. [9]Dipartimento di Fisica, University of Padova, via Marzolo 8, 35131 Padova, Italy. [10]Konkoly Observatory, Research Centre for Astronomy and Earth Sciences, Hungarian Academy of Sciences, Konkoly Thege 15-17, H-1121 Budapest, Hungary. [11]Astronomical Institute, Slovak Academy of Sciences, 059 60 Tatranská Lomnica, Slovakia. [12]Astronomical Institute, Academy of Sciences of the Czech Republic, Fričova 298, 251 65 Ondřejov Czech Republic. [13]Astronomical Observatory San Marcello Pistoiese CARA Project, San Marcello Pistoiese, Pistoia, Italy. [14]Osservatorio astronomico di Tavolaia, Santa Maria a Monte, Italy. [15]Lajatico Astronomical Centre, Via Mulini a Vento 9 Orciatico, cap 56030 Lajatico, Italy. [16]Osservatorio Astronomico di Monte Agliale, Via Cune Motrone, I-55023 Borgo a Mozzano, Italy. [17]Črni Vrh Observatory, Predgriže 29A, 5274 Črni Vrh nad Idrijo, Slovenia. [18]Astronomical Observatory of the Autonomous Region of the Aosta Valley (OAVdA), Lignan 39, 11020 Nus, Italy. [19]Bayerische Volkssternwarte München, Rosenheimer Straße 145h, D-81671 München, Germany. [20]German Aerospace Center (DLR), Institute of Planetary Research, Rutherfordstraße 2, 12489 Berlin, Germany. [21]Departamento de Física, Ingeniería de Sistemas y Teoría de la Señal, Universidad de Alicante, PO Box 99, E-03080 Alicante, Spain. [22]Instituto Universitario de Física Aplicada a las Ciencias y la Tecnología, Universidad de Alicante, PO Box 99, E-03080 Alicante, Spain. [23]University of Zagreb, Faculty of Electrical Engineering and Computing, Department of Applied Physics, Unska 3, 10000 Zagreb, Croatia. [24]Ruđer Bošković Institute, Bijenička cesta 54, 10000 Zagreb, Croatia. [25]European Southern Observatory, Karl-Schwarzschild-Straße 2, 85748 Garching bei München, Germany. [26]IMCCE/Observatoire de Paris, 77 Avenue Denfert Rochereau, 75014 Paris, France. [27]Laboratório Interinstitucional de e-Astronomia-LIneA, Rua General José Cristino 77, Rio de Janeiro CEP 20921-400, Brazil. [28]Observatório do Valongo/UFRJ, Ladeira Pedro Antônio 43, Rio de Janeiro CEP 20080-090, Brazil. [29]Observatoire de Genève, CH1290 Sauverny, Switzerland. [30]International Occultation Timing Association—European Section (IOTA-ES) Bartold-Knausstraße 8, D-30459 Hannover, Germany. [31]Facultad de Ciencias Experimentales, Universidad de Huelva, Avenida de las Fuerzas Armadas, 21071 Huelva, Spain. [32]Ege University, Faculty of Science, Department of Physics, 35100 Izmir, Turkey. [33]University of Adiyaman, Department of Physics, 02040 Adiyaman, Turkey. [34]TUBITAK National Observatory (TUG), Akdeniz University Campus, 07058 Antalya, Turkey. [35]Ondokuz Mayis University Observatory, Space Research Center, 55200 Kurupelit, Turkey. [36]Atatürk University, Science Faculty, Department of Physics, 25240 Erzurum, Turkey. [37]Atatürk University, Astrophysics Research and Application Center (ATASAM), 25240 Erzurum, Turkey. [38]Atatürk University, Science Faculty, Department of Astronomy and Astrophysics, 25240 Erzurum, Turkey. [39]Canakkale Onsekiz Mart University, Astrophysics Research Center (ARC) and Ulupınar Observatory (UPO), Canakkale, Turkey. [40]Institute for Astronomy, Astrophysics, Space Applications and Remote Sensing, National Observatory of Athens, GR-15236 Penteli, Greece. [41]Department of Physics, University of Crete, GR-71003 Heraklion, Greece. [42]INAF—Catania Astrophysical Observatory, Via Santa Sofia 78, I-95123 Catania, Italy. [43]Michael Adrian Observatorium, Astronomie Stiftung Trebur, Fichtenstraße 7, 65468 Trebur, Germany. [44]University of Applied Sciences, Technische Hochschule Mittelhessen, Wilhelm-Leuschner-Straße 13, D-61169 Friedberg, Germany. [45]Astronomical Observatory Institute, Faculty of Physics, A. Mickiewicz University, Słoneczna 36, 60-286 Poznań, Poland. [46]Section of Astrophysics, Astronomy and Mechanics, Department of Physics, National and Kapodistrian University of Athens, GR-15784 Athens, Greece. [47]Nunki Observatory, Skiathos Island 37002, Greece. [48]Ellinogermaniki Agogi Observatory, Dimitriou Panagea street, GR-15351 Athens, Greece. [49]Departamento de Física Aplicada I, Escuela de Ingeniería de Bilbao, Universidad del País Vasco UPV/EHU, Plaza Torres Quevedo 1, 48013 Bilbao, Spain. [50]Observatori Astronòmic de la Universitat de València, Catedrático José Beltrán, 2, 46980 Paterna, Spain. [51]Departament d'Astronomia i Astrofísica, Universitat de València, Calle Dr Moliner 50, E-46100 Burjassot, Spain. [52]Centro de Estudios de Física del Cosmos de Aragón, Plaza de San Juan 1, 2ª planta, 44001 Teruel, Spain. [53]Departamento de Astrofísica, Universidad de La Laguna, Avenida Astrofísico Fco Sánchez, 38200 La Laguna, Spain.

Table 1 | Details of the observations on 21 January 2017

Site	Coordinates	Telescope aperture, filter and observer	Detector/instrument, exposure time and cycle time	Ingress and egress times (UT)
Skalnate Pleso Observatory, Slovakia (S)	49° 11′ 21.8″ N 20° 14′ 02.1″ E 1,826 m	1.3 m No filter R.K.	Moravian G4-9000 10 s 15.5 s	3:08:26.79 ± 0.96 3:10:24.56 ± 0.8
Konkoly Observatory, Hungary (K)	47° 55′ 01.6″ N 19° 53′ 41.5″ E 935 m	1.0 m No filter A.P.	Andor iXon-888 1 s 1.007 s	3:08:20.3 ± 0.2 3:10:17.39 ± 0.07
Konkoly Observatory, Hungary (K)	47° 55′ 01.6″ N 19° 53′ 41.5″ E 935 m	0.6 m No filter A.P.	Apogee Alta U16HC 2 s 2.944 s	3:08:19.5 ± 0.8 3:10:16.4 ± 1.3
Ondrejov Observatory, Czech Republic (O)	49° 54′ 32.6″ N 14° 46′ 53.3″ E 526 m	0.65 m No filter K.H.	Moravian G2-3200 8 s 9.721 s	3:08:29.2 ± 0.8 3:10:12.2 ± 0.8
Crni Vrh Observatory, Slovenia (CV)	45° 56′ 45.0″ N 14° 04′ 15.9″ E 713 m	0.6 m Clear H.M.	Apogee Alta U9000HC 300 s, drifted 315 s	3:07:54 ± 8 3:09:57 ± 10
Wendelstein Observatory, Germany (W)	47° 42′ 13.6″ N 12° 00′ 44.0″ E 1,838 m	2.0 m r′ C.R.	WWFI 10 s 14.536 s	3:08:27.9 ± 2.8 3:09:34.1 ± 0.5
Wendelstein Observatory, Germany (W)	47° 42′ 13.6″ N 12° 00′ 44.0″ E 1,838 m	0.4 m r′ C.R.	SBIG ST10-XME 30 s 53.096 s	3:08:18.8 ± 6 3:09:38.6 ± 6
Bavarian Public Observatory, Munich, Germany (M)	48° 07′ 19.2″ N 11° 36′ 25.2″ E 538 m	0.8 m No filter B.G.	ATIK 314L+ 20 s 20.304 s	3:08:30.0 ± 3.3 3:09:30.0 ± 4.9
Asiago Observatory, Cima Ekar, Italy (As)	45° 50′ 54.9″ N 11° 34′ 08.4″ E 1,376 m	1.82 m No filter V.G.	AFOSC 2 s 5.026 s	3:08:20.17 ± 0.08 3:09:13.27 ± 1.5
San Marcello Pistoiese Observatory, Italy (SMP)	44° 03′ 51.0″ N 10° 48′ 14.0″ E 965 m	0.6 m No filter P. Bacci, M.M., L.N. and L.M.	Apogee Alta U6 10 s 11.877 s	3:08:22.9 ± 0.9 3:08:42.8 ± 0.9
Lajatico Astronomical Centre, Italy (L)	43° 25′ 44.7″ N 10° 43′ 01.2″ E 433 m	0.5 m No filter M.B., F. Martinelli, G.S.	Moravian G3-1000 15 s 16.254 s	3:08:19.9 ± 1.4 3:08:34.3 ± 1.4
Mount Agliale Observatory, Italy (Ag)	43° 59′ 43.1″ N 10° 30′ 53.8″ E 758 m	0.5 m No filter F.C.	FLI proline 4710 15 s 16.724 s	*

The table shows the observing sites from which the most relevant observations were obtained, the main parameters of the observations for each site and the derived disappearance (ingress) and reappearance (egress) times of the star caused by the central body, using the square-well-model fits in Fig. 1. The cycle times are the times between consecutive exposures. At Wendelstein Observatory and Konkoly Observatory, two different telescopes were used; hence there are 12 detections of the occultation from 10 different sites. Weather was clear at all of the stations except at the Bavarian Public Observatory (Munich), where intermitent clouds were present.
*The occultation by the main body of Haumea was not detectable from Mount Agliale; only ring events were detected. See Methods and Extended Data Table 2.

drops caused by Haumea near the predicted time (around 3:09 UT). Because the drops are abrupt, Haumea must lack a global Pluto-like atmosphere. An upper limit on the surface pressure of a nitrogen- or methane-dominated atmosphere is determined to be 15 nbar and 50 nbar, respectively, at the 3σ level.

Square-well fits to the drops provide the times of star disappearance and reappearance at each site. Those times define an occultation chord for each site, and an elliptical fit to the extremities of the chord provides the instantaneous limb of Haumea, with values of $1{,}704 \pm 4$ km and $1{,}138 \pm 26$ km for the major and minor axes of the ellipse (Fig. 2). The position angle of the minor axis is $-76.3° \pm 1.2°$.

In addition to the main occultation, there are brief dimmings before and after the main event. These dips are consistently explained by a narrow and dense ring around Haumea that absorbed about 50% of the incoming stellar flux. This ring has reflectivity similar to those found around the Centaurs Chariklo[7] and Chiron[8,9] and around Uranus[12] and Neptune[13]. From an elliptical fit to the positions of those brief events (projected in the plane of the sky), we obtain an apparent semi-major axis of $a'_{\rm ring} = 2{,}287^{+75}_{-45}$ km and apparent semi-minor axis of $b'_{\rm ring} = 541 \pm 15$ km for the ring (the error here and elsewhere stems from the uncertainty in the timing of the events, see Fig. 3) The position angle of the apparent minor axis of the ring is $P_{\rm ring} = -74.3° \pm 1.3°$, which coincides with that of the fit of Haumea's limb to within error bars, suggesting that the ring lies in Haumea's equatorial plane; see below.

Under the assumption that the ring ellipse seen in Fig. 3 corresponds to the projection of a circular ring, we derive a ring opening angle of $B_{\rm ring} = \arcsin(b'_{\rm ring}/a'_{\rm ring}) = 13.8° \pm 0.5°$ ($B_{\rm ring} = 0°$ corresponds to an edge-on geometry). A ring particle orbiting a triaxial body with semi-axes $a > b > c$ that rotates around the axis c has its average angular momentum H_c along c conserved. In this case, the state of least energy for a collisional, dissipative disk with constant H_c is an equatorial ring. Therefore, Haumea's equator should also be observed under the angle 13.8°. This is consistent with the high amplitude of its rotational light curve, which requires low values of B (ref. 1). The values of $P_{\rm ring}$ and $B_{\rm ring}$ provide two possible solutions for the ring pole, with J2000 equatorial coordinates $(\alpha_{\rm p}, \delta_{\rm p}) = (285.1° \pm 0.5°, -10.6° \pm 1.2°)$ (solution 1) and $(\alpha_{\rm p}, \delta_{\rm p}) = (312.3° \pm 0.3°, -18.6° \pm 1.2°)$ (solution 2). Solution 1 is preferred, because it is consistent with the long-term photometric behaviour of Haumea and because it is coincident, to within error bars, with the orbital pole position of Haumea's main satellite, Hi'iaka, $(\alpha_{\rm p}, \delta_{\rm p}) = (283.0° \pm 0.2°, -10.6° \pm 0.7°)$ (ref. 14). In that context, both the ring and Hi'iaka would lie in Haumea's equatorial plane.

At about 2,287 km from Haumea's centre, the ring is within the Roche limit of a fluid-like satellite, which corresponds to about 4,400 km for a spherical Haumea (using a density of 1,885 kg m^{-3} for the primary and a density of 500 kg m^{-3} for the satellite). When the elongated shape of Haumea is considered, the Roche limit is even further out. Hence, the ring is close enough to Haumea that accretion cannot proceed to form a satellite. The ring is close to the 3:1 spin–orbit resonance with Haumea, a ring particle undergoing one revolution while Haumea completes three rotations. This resonance occurs at $2{,}285 \pm 8$ km (see Methods). More knowledge of the ring orbit and of the internal structure of Haumea (which may be not homogeneous, see below) will be required to show whether this proximity is coincidental or the ring is actually trapped into

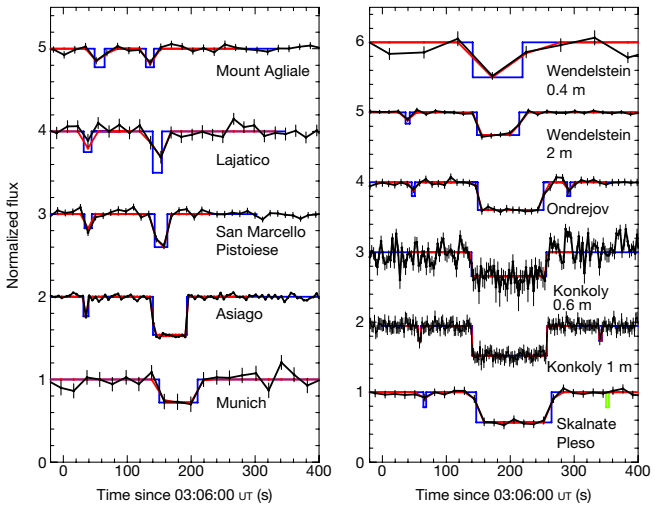

Figure 1 | Light curves of the occultation. Light curves in the form of normalized flux versus time (at mid-exposure) were obtained from the different observatories that recorded the occultation (Table 1). The black points and lines represent the light curves extracted from the observations. The blue lines show the best square-well-model fits to the main body and the ring at Konkoly, with square-well models derived from the assumed ring width and opacity ($W = 70$ km and $p' = 0.5$) at other sites. The red points and lines correspond to the optimal synthetic profile deduced from the square-well model fitted at each data point (see Methods). The rectangular profile in green corresponds to the ring egress event at Skalnate Pleso, which fell in a readout time of the camera (see Fig. 3). The light curves have been shifted in steps of 1 vertically for better viewing. 'Munich' corresponds to the Bavarian Public Observatory. Error bars are 1σ.

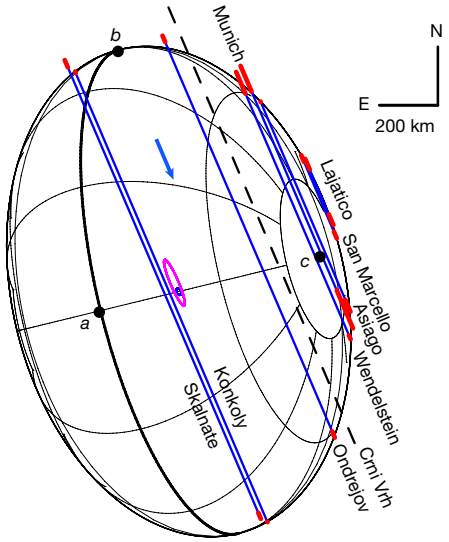

Figure 2 | Haumea's projected shape. The blue lines are the occultation chords of the main body projected onto the sky plane, as seen from nine observing sites (Table 1). The red segments are the uncertainties (1σ level) on the extremites of each chord, as derived from the timing uncertainties in Table 1. We show the chord from Crni Vrh in dashed line because it is considerably uncertain. For the observatories for which two telescopes were used we show only the best chord. Celestial north ('N') and east ('E') are indicated in the upper right corner, together with the scale. The blue arrow shows the motion of the star relative to the body. Haumea's limb (assumed to be elliptical) has been fitted to the chords, accounting for the uncertainties on the extremity of each chord (red segments). The limb has semi-major axis $a' = 852 \pm 2$ km and semi-minor axis $b' = 569 \pm 13$ km, the latter having a position angle $P_{\rm limb} = -76.3° \pm 1.2°$ counted positively from the celestial north to the celestial east. Haumea's equator has been drawn assuming that it is coplanar with the ring, with planetocentric elevation $B_{\rm ring} = 13.7° \pm 0.5°$; see Fig. 3. The pink ellipse indicates the 1σ-level uncertainty domain for the ring centre, and the blue ellipse inside it is the corresponding domain for Haumea's centre. To within error bars, the ring and Haumea's centres (separated by 33 km in the sky plane) cannot be distinguished, indicating that our data are consistent with a circular ring concentric with the dwarf planet. The points labelled '*a*', '*b*' and '*c*' indicate the intersections of the *a*, *b* and *c* semi-axes of the modelled ellipsoid with Haumea's surface.

this resonance, and if the latter, for what reason. However, answering these questions remains out of reach of the present work.

Another important property of Haumea is its geometric albedo ($p_{\rm V}$), which can be determined using its projected area, as derived from the occultation, and its absolute magnitude[15]. We find a geometric albedo $p_{\rm V} = 0.51 \pm 0.02$, which is considerably smaller than the values of 0.7–0.75 and $0.804^{+0.062}_{-0.095}$ derived from the latest combination of Herschel and Spitzer thermal measurements[8,16]. The geometric albedo should be even smaller if the contributions of the satellites and the ring to the absolute magnitude are larger than the 13.5% used here (see Methods).

Because Haumea is thought to have a triaxial ellipsoid shape[1,17,18] with semi-axes $a > b > c$, the occultation alone cannot provide its three-dimensional shape unless we use additional information from the rotational light curve. From measurements performed in the days before and after the occultation, and given that we know Haumea's rotation period with high precision[16], we determined the rotational phase at the occultation time. It turns out that Haumea was at its absolute brightness minimum, which means that the projected area of the body was at its minimum during the occultation.

The magnitude change from minimum to maximum absolute brightness determined from the Hubble Space Telescope is 0.32 mag (using images that separated Haumea and Hi'iaka[7]). Using equation (5) in ref. 19 together with the aspect angle in 2009 (when the observations were taken[7]) and the occultation ellipse parameters, we derive the following values for the semi-axes of the ellipsoid: $a = 1{,}161 \pm 30$ km, $b = 852 \pm 4$ km and $c = 513 \pm 16$ km (see Methods). The resulting density of Haumea, using its known mass[20], is $1{,}885 \pm 80$ kg m^{-3}, and its volume-equivalent diameter is $1{,}595 \pm 11$ km. This diameter is determined under the assumption that the ring does not contribute to the total brightness. For an upper limit of 5% contribution (see Methods), the real amplitude of the rotational light curve increases, and hence the a semi-axis increases too. The volume-equivalent diameter in this case is 1,632 km and the density is 1,757 kg m^{-3}. These two densities are considerably smaller than the lower limit of 2,600 kg m^{-3} based on the figures of hydrostatic equilibrium, or on mass and previous volume determinations[1]. A value in the range 1,885–1,757 kg m^{-3} is far more in line with the density of other large TNOs and in agreement with the trend of increasing density versus size (see, for example, supplementary information in ref. 5, and refs 21 and 22). We also note that the axial ratios derived from the occultation are not consistent with those expected from the hydrostatic equilibrium figures of a homogeneous body[23] for the known rotation rate and the derived density. It has previously been hypothesized[24] that the density of Haumea could be much smaller than the minimum value of 2,600 kg m^{-3} reported previously, if granular physics is used to model the shape of the body instead of the simplifying assumption of fluid behaviour. From figure 4 of ref. 25, we determine an approximate angle of friction of between 10° and 15° for Haumea given the c/a ratio of about 0.4 that we determined here. For reference, the maximum angle of friction of solid rocks on Earth is 45° and that of a fluid is 0°. Also, differentiation and other effects may have an important role in determining the final shape[26].

Chariklo, a body of around 250 km in diameter with a Centaur orbit (between the orbits of Jupiter and Neptune), was the first Solar System object other than the giant planets found to have a ring system[7]. Shortly after that discovery, similar occultation features that resembled those from Chariklo's rings were found on Chiron[8,9], another Centaur. These discoveries directed our attention to Centaurs and phenomenology related to them to explain our unexpected findings. The discovery of

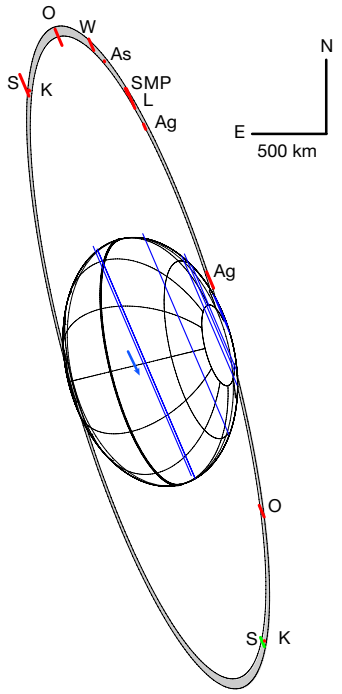

Figure 3 | Haumea's ring geometry. The figure shows a fit to the ring events (red segments), with the other features the same as in Fig. 2. Those segments show the 1σ uncertainty intervals for the midtimes of the secondary events at Mount Agliale (Ag), Lajatico (L), San Marcello Pistoiese (SMP), Asiago (As), Wendelstein (W), Ondrejov (O), Konkoly (K) and Skalnate Pleso (S). No ring event could be detected from the Bavarian Public Observatory (in Munich) because of the low signal-to-noise ratio. The ring egresses at Wendelstein, Asiago, San Marcello Pistoiese and Lajatico are not observed because they are blocked by the main body. At Skalnate Pleso, the ring egress is not detected (despite the high signal-to-noise ratio of the data) either because the ring is not homogeneous or because its egress is lost in the readout time (marked here in green). The latter is the most likely explanation because the readout times of 5.5 s were long compared to the integration time of 10 s. Also, the green segment is very close to the positive Konkoly detection, making the hypothesis of an inhomogeneous ring unlikely. The two ellipses around Haumea delineate a 70-km-wide ring with an apparent opacity of 0.5 (grey area) and semi-major axis of $a_{\rm ring} = 2,287^{+75}_{-45}$ km that best simultaneously fits the secondary events of Fig. 1. The ring fit provides an opening angle $B_{\rm ring} = 13.8° \pm 0.5°$ and a position angle for the apparent minor axis of the ring of $P_{\rm ring} = -74.3° \pm 1.3°$. This is aligned, to within error bars, with Haumea's apparent minor axis $P_{\rm limb} = -76.3° \pm 1.2°$ (Fig. 2). Moreover, the orbital pole position of Hi'iaka[14] implies a sub-observer elevation of $B_{\rm Hi'iaka} = -15.7°$ above the orbit of Hi'iaka on 2017 January 21 and a superior conjunction occurring at a position angle of $P_{\rm Hi'iaka} = -73.6°$. The fact that $|B_{\rm ring}| \approx |B_{\rm Hi'iaka}|$ and $P_{\rm ring} \approx P_{\rm limb} \approx P_{\rm Hi'iaka}$ strongly suggests that the ring and Hi'iaka both orbit in Haumea's equatorial plane.

a ring around Haumea—a much more distant body, in a completely different dynamical class, much larger than Chariklo and Chiron, with satellites and with a very elongated triaxial shape—has numerous implications, such as rings being possibly common also in the trans-Neptunian region from which Centaurs are delivered, and opens the door to new avenues of research.

Online Content Methods, along with any additional Extended Data display items and Source Data, are available in the online version of the paper; references unique to these sections appear only in the online paper.

Received 4 June; accepted 30 August 2017.

1. Rabinowitz, D. L. *et al.* Photometric observations constraining the size, shape, and albedo of 2003 EL61, a rapidly rotating, Pluto-sized object in the Kuiper belt. *Astrophys. J.* **639,** 1238–1251 (2006).
2. Brown, M. E. *et al.* Keck observatory laser guide star adaptive optics discovery and characterization of a satellite to the large Kuiper belt object 2003 EL_{61}. *Astrophys. J.* **632,** L45–L48 (2005).
3. Brown, M. E., Barkume, K. M., Ragozzine, D. & Schaller, E. L. A collisional family of icy objects in the Kuiper belt. *Nature* **446,** 294–296 (2007).
4. Sicardy, B. *et al.* A Pluto-like radius and a high albedo for the dwarf planet Eris from an occultation. *Nature* **478,** 493–496 (2011).
5. Ortiz, J. L. *et al.* Albedo and atmospheric constraints of dwarf planet Makemake from a stellar occultation. *Nature* **491,** 566–569 (2012).
6. Stern, S. A. *et al.* The Pluto system: initial results from its exploration by New Horizons. *Science* **350,** aad1815 (2015).
7. Braga-Ribas, F. *et al.* A ring system detected around the Centaur (10199) Chariklo. *Nature* **508,** 72–75 (2014).
8. Ortiz, J. L. *et al.* Possible ring material around Centaur (2060) Chiron. *Astron. Astrophys.* **576,** A18 (2015).
9. Ruprecht, J. *et al.* 29 November 2011 stellar occultation by 2060 Chiron: symmetric jet-like features. *Icarus* **252,** 271–276 (2015).
10. Lockwood, A. C., Brown, M. E. & Stansberry, J. The size and shape of the oblong dwarf planet Haumea. *Earth Moon Planets* **111,** 127–137 (2014).
11. Fornasier, S. *et al.* TNOs are cool: a survey of the trans-Neptunian region. VIII. Combined Herschel PACS and SPIRE observations of nine bright targets at 70–500 μm. *Astron. Astrophys.* **555,** A15 (2013).
12. Elliot, J. L., Dunham, E. & Mink, D. The rings of Uranus. *Nature* **267,** 328–330 (1977).
13. Hubbard, W. B. *et al.* Occultation detection of a Neptunian ring-like arc. *Nature* **319,** 636–640 (1986).
14. Gourgeot, F. *et al.* Near-infrared spatially resolved spectroscopy of (136108) Haumea's multiple system. *Astron. Astrophys.* **593,** A19 (2016).
15. Rabinowitz, D. L., Schaefer, B. E. & Tourtellotte, S. W. The diverse solar phase curves of distant icy bodies. I. Photometric observations of 18 trans-Neptunian objects, 7 Centaurs, and Nereid. *Astron. J.* **133,** 26–43 (2007).
16. Lellouch, E. *et al.* "TNOs are cool": a survey of the trans-Neptunian region. II. The thermal lightcurve of (136108) Haumea. *Astron. Astrophys.* **518,** L147 (2010).
17. Lacerda, P., Jewitt, D. & Peixinho, N. High-precision photometry of extreme KBO 2003 EL_{61}. *Astron. J.* **135,** 1749–1756 (2008).
18. Thirouin, A. *et al.* Short-term variability of a sample of 29 trans-Neptunian objects and Centaurs. *Astron. Astrophys.* **522,** A93 (2010).
19. Binzel, R. P., Farinella, P., Zappala, V. & Cellino, A. in *Asteroids II* (eds Binzel, R. P. *et al.*) 416–441 (Univ. Arizona Press, 1989).
20. Ragozzine, D. & Brown, M. E. Orbits and masses of the satellites of the dwarf planet Haumea (2003 EL61). *Astron. J.* **137,** 4766–4776 (2009).
21. Carry, B. Density of asteroids. *Planet. Space Sci.* **73,** 98–118 (2012).
22. Stansberry, J. A. *et al.* Physical properties of trans-Neptunian binaries (120347) Salacia-Actaea and (42355) Typhon-Echidna. *Icarus* **219,** 676–688 (2012).
23. Chandrasekhar, S. *Ellipsoidal Figures of Equilibrium* (Dover, 1987).
24. Holsapple, K. A. Spin limits of Solar System bodies: from the small fast-rotators to 2003 EL61. *Icarus* **187,** 500–509 (2007).
25. Holsapple, K. A. Equilibrium configurations of solid cohesionless bodies. *Icarus* **154,** 432–448 (2001).
26. Rambaux, N., Chambat, F., Castillo-Rogez, J. & Baguet D. Equilibrium figures of dwarf planets. In *AAS/Division of Planetary Sciences Meeting* Vol. 48, abstr. 120.15 (American Astronomical Society, 2016).

Acknowledgements These results were based on observations made with the 2-m telescope at Wendelstein Observatory, which is operated by the Universitäts-Sternwarte München, the 1.8-m telescope at Asiago Observatory, operated by Padova Observatory, a member of the National Institute for Astrophysics, the 1.3-m telescope at Skalnate Pleso Observatory, operated by the Astronomical Institute of the Slovak Academy of Science, the 1-m telescope at Konkoly observatory, operated by Astrophysical Institute of the Hungarian Academy of Sciences, the 0.65-m telescope at Ondrejov Observatory, operated by the Astronomical Institute of the Czech Academy of Sciences, the 1.5-m telescope at Sierra Nevada Observatory, operated by the Instituto de Astrofisica de Andalucia-CSIC, the 1.23-m telescope at Calar Alto Observatory, jointly operated by the Max Planck Institute für Astronomie and the IAA-CSIC, the Roque de los Muchachos Observatory 2-m Liverpool telescope, operated by the Astrophysics Research Institute of Liverpool John Moores University, the Roque de los Muchachos Observatory 2.5-m NOT telescope, operated by the Nordic Optical Telescope Scientific Association, the 1-m telescope at Pic du Midi Observatory, operated by the Observatoire Midi Pyrénées, and the La Hita 0.77-m telescope, which is jointly operated by Astrohita and the IAA-CSIC. J.L.O. acknowledges funding from Spanish and Andalusian grants MINECO AYA-2014-56637-C2-1-P and J. A. 2012-FQM1776 as well as FEDER funds. Part of the research leading to these results received funding from the European Union's Horizon 2020 Research and Innovation Programme, under grant agreement no. 687378. B.S. acknowledges support from the French grants 'Beyond Neptune' ANR-08-BLAN-0177 and 'Beyond Neptune II' ANR-11-IS56-0002. Part of the research leading to these results has received funding from the European Research Council under the European Community's H2020 (2014-2020/ERC grant agreement no. 669416 'Lucky Star'). A.P. and R.S. have been supported by the grant LP2012-31 of the Hungarian Academy of Sciences. All of the Hungarian contributors acknowledge the partial support from K-125015 grant of the National Research, Development and Innovation Office (NKFIH). G.B.-R., F.B.-R., F.L.R., R.V.-M., J.I.B.C., M.A., A.R.G.-J. and B.E.M. acknowledge support from CAPES, CNPq and FAPERJ. J.C.G. acknowledges funding from AYA2015-63939-C2-2-P and from the Generalitat Valenciana PROMETEOII/2014/057. K.H. and P.P. were supported by the

project RVO:67985815. The Astronomical Observatory of the Autonomous Region of the Aosta Valley acknowledges a Shoemaker NEO Grant 2013 from The Planetary Society. We acknowledge funds from a 2016 'Research and Education' grant from Fondazione CRT. We also acknowledge the Slovakian project ITMS no. 26220120029.

Author Contributions J.L.O. planned the campaign, analysed data for the prediction, made the prediction, participated in the observations, obtained and analysed data, interpreted the data and wrote the paper. P.S.-S. helped to plan the campaign, analysed data, helped to interpret the data and helped to write the paper. B.S. helped to plan the campaign, analysed data, interpreted data, and wrote part of the paper. G.B.-R. and D.B. helped to plan the campaign, participated in the observations, and analysed and interpreted data. All other authors participated in the planning of the campaign and/or the observations and/or the interpretations. All authors were given the opportunity to review the results and comment on the manuscript.

Author Information Reprints and permissions information is available at www.nature.com/reprints. The authors declare no competing financial interests. Readers are welcome to comment on the online version of the paper. Publisher's note: Springer Nature remains neutral with regard to jurisdictional claims in published maps and institutional affiliations. Correspondence and requests for materials should be addressed to J.L.O. (ortiz@iaa.es).

Reviewer Information *Nature* thanks A. Sickafoose and A. Verbiscer for their contribution to the peer review of this work.

Bibliography

Abe, F., Airey, C., Barnard, E., Baudry, J., Botzler, C., Douchin, D., Freeman, M., Larsen, P., Niemiec, A., Perrott, Y., Philpott, L., Rattenbury, N., Yock, P., 2013. Extending the planetary mass function to Earth mass by microlensing at moderately high magnification. Mon. Not. R. Astron. Soc. 431, 2975–2985.

Aumann, H.H., Walker, R.G., 1987. IRAS observations of the Pluto-Charon system. Astronomical Journal 94, 1088–1091.

Bagenal, F., Horányi, M., McComas, D.J., McNutt, R.L., Elliott, H.A., Hill, M.E., Brown, L.E., Delamere, P.A., Kollmann, P., Krimigis, S.M., Kusterer, M., Lisse, C.M., Mitchell, D.G., Piquette, M., Poppe, A.R., Strobel, D.F., Szalay, J.R., Valek, P., Vandegriff, J., Weidner, S., Zirnstein, E.J., Stern, S.A., Ennico, K., Olkin, C.B., Weaver, H.A., Young, L.A., Gladstone, G.R., Grundy, W.M., McKinnon, W.B., Moore, J.M., Spencer, J.R., Andert, T., Andrews, J., Banks, M., Bauer, B., Bauman, J., Barnouin, O.S., Bedini, P., Beisser, K., Beyer, R.A., Bhaskaran, S., Binzel, R.P., Birath, E., Bird, M., Bogan, D.J., Bowman, A., Bray, V.J., Brozovic, M., Bryan, C., Buckley, M.R., Buie, M.W., Buratti, B.J., Bushman, S.S., Calloway, A., Carcich, B., Cheng, A.F., Conard, S., Conrad, C.A., Cook, J.C., Cruikshank, D.P., Custodio, O.S., Dalle Ore, C.M., Deboy, C., Dischner, Z.J.B., Dumont, P., Earle, A.M., Ercol, J., Ernst, C.M., Finley, T., Flanigan, S.H., Fountain, G., Freeze, M.J., Greathouse, T., Green, J.L., Guo, Y., Hahn, M., Hamilton, D.P., Hamilton, S.A., Hanley, J., Harch, A., Hart, H.M., Hersman, C.B., Hill, A., Hinson, D.P., Holdridge, M.E., Howard, A.D., Howett, C.J.A., Jackman, C., Jacobson, R.A., Jennings, D.E., Kammer, J.A., Kang, H.K., Kaufmann, D.E., Kusnierkiewicz, D., Lauer, T.R., Lee, J.E., Lindstrom, K.L., Linscott, I.R., Lunsford, A.W., Mallder, V.A., Martin, N., Mehoke, D., Mehoke, T., Melin, E.D., Mutchler, M., Nelson, D., Nimmo, F., Nunez, J.I., Ocampo, A., Owen, W.M., Paetzold, M., Page, B., Parker, A.H., Parker, J.W., Pelletier, F., Peterson, J., Pinkine, N., Porter, S.B., Protopapa, S., Redfern, J., Reitsema, H.J., Reuter, D.C., Roberts, J.H., Robbins, S.J., Rogers, G., Rose, D., Runyon, K., Retherford, K.D., Ryschkewitsch, M.G., Schenk, P., Schindhelm, E., Sepan, B., Showalter, M.R., Singer, K.N., Soluri, M., Stanbridge, D., Steffl, A.J., Stryk, T., Summers, M.E., Tapley, M., Taylor, A., Taylor, H., Throop, H.B., Tsang, C.C.C., Tyler, G.L., Umurhan, O.M., Verbiscer, A.J., Versteeg, M.H., Vincent, M., Webbert, R., Weigle, G.E., White, O.L., Whittenburg, K., Williams, B.G., Williams, K., Williams, S., Woods, W.W., Zangari, A.M., 2016. Pluto' interaction with its space environment: Solar wind, energetic particles, and dust. Science 351, aad9045.

Baum, W.A., Code, A.D., 1953. A photometric observation of the occultation of σ ARIETIS by Jupiter. Astron. J. 58, 108–112.

Berard, D., *Étude des anneaux de Chariklo par occultation stellaire* Ph.D. thesis Université Pierre et Marie Curie 2017.

Bérard, D., Sicardy, B., Camargo, J.I.B., Desmars, J., Braga-Ribas, F., Ortiz, J.L., Duffard, R., Morales, N., Meza, E., Leiva, R., Benedetti-Rossi, G., Vieira-Martins, R., Gomes Júnior, A.R., Assafin, M., Colas, F., Dauvergne, J.L., Kervella, P., Lecacheux, J., Maquet, L., Vachier, F., Renner, S., Monard, B., Sickafoose, A.A., Breytenbach, H., Genade, A., Beisker, W., Bath, K.L., Bode, H.J., Backes, M., Ivanov, V.D., Jehin, E., Gillon, M., Manfroid, J., Pollock, J., Tancredi, G., Roland, S., Salvo, R., Vanzi, L., Herald, D., Gault, D., Kerr, S., Pavlov, H., Hill, K.M., Bradshaw, J., Barry, M.A., Cool, A., Lade, B., Cole, A., Broughton, J., Newman, J., Horvat, R., Maybour, D., Giles, D., Davis, L., Paton, R.A., Loader, B., Pennell, A., Jaquiery, P.D., Brillant, S., Selman, F., Dumas, C., Herrera, C., Carraro, G., Monaco, L., Maury, A., Peyrot, A., Teng-Chuen-Yu, J.P., Richichi, A., Irawati, P., De Witt, C., Schoenau, P., Prager, R., Colazo, C., Melia, R., Spagnotto, J., Blain, A., Alonso, S., Román, A., Santos-Sanz, P., Rizos, J.L., Maestre, J.L., Dunham, D., 2017. The Structure of Chariklo's Rings from Stellar Occultations. Astronomical Journal 154, 144.

Bertrand, T., Forget, F., 2016. Observed glacier and volatile distribution on Pluto from atmosphere-topography processes. Nature540, 86–89.

Bertrand, T., Forget, F., Umurhan, O.M., Grundy, W.M., Schmitt, B., Protopapa, S., Zangari, A.M., White, O.L., Schenk, P.M., Singer, K.N., Stern, A., Weaver, H.A., Young, L.A., Ennico, K., Olkin, C.B., 2018. The nitrogen cycles on Pluto over seasonal and astronomical timescales. Icarus 309, 277–296.

Binzel, R., Long-Term Seasonal Variations on Pluto. in: Bulletin of the American Astronomical Society vol. 22 of *baas* 1990 p. 1128.

Binzel, R.P., 1989. Pluto-Charon mutual events. grl 16, 1205–1208.

Bosh, A.S., Person, M.J., Levine, S.E., Zuluaga, C.A., Zangari, A.M., Gulbis, A.A.S., Schaefer, G.H., Dunham, E.W., Babcock, B.A., Davis, A.B., Pasachoff, J.M., Rojo, P., Servajean, E., Förster, F., Oswalt, T., Batcheldor, D., Bell, D., Bird, P., Fey, D., Fulwider, T., Geisert, E., Hastings, D., Keuhler, C., Mizusawa, T., Solenski, P., Watson, B., 2015. The state of Pluto's atmosphere in 2012-2013. Icarus 246, 237–246.

Bouchez, A.H., *Seasonal trends in Titan's atmosphere: Haze, wind, and clouds* Ph.D. thesis California Institute of Technology 2004.

Braga-Ribas, F., Sicardy, B., Ortiz, J.L., Snodgrass, C., Roques, F., Vieira-Martins, R., Camargo, J.I.B., Assafin, M., Duffard, R., Jehin, E., Pollock, J., Leiva, R., Emilio, M., Machado, D.I., Colazo, C., Lellouch, E., Skottfelt, J., Gillon, M., Ligier, N., Maquet, L., Benedetti-Rossi, G., Gomes, A.R., Kervella, P., Monteiro, H., Sfair, R., El Moutamid, M., Tancredi, G., Spagnotto, J., Maury, A., Morales, N., Gil-Hutton, R., Roland, S., Ceretta, A., Gu, S.H., Wang, X.B., Harpsøe, K., Rabus,

M., Manfroid, J., Opitom, C., Vanzi, L., Mehret, L., Lorenzini, L., Schneiter, E.M., Melia, R., Lecacheux, J., Colas, F., Vachier, F., Widemann, T., Almenares, L., Sandness, R.G., Char, F., Perez, V., Lemos, P., Martinez, N., Jørgensen, U.G., Dominik, M., Roig, F., Reichart, D.E., Lacluyze, A.P., Haislip, J.B., Ivarsen, K.M., Moore, J.P., Frank, N.R., Lambas, D.G., 2014. A ring system detected around the Centaur (10199) Chariklo. Nature508, 72–75.

Brosch, N., 1995. The 1985 stellar occultation by Pluto. Mon. Not. R. Astron. Soc. 276, 571–578.

Buie, M.W., Tholen, D.J., Horne, K., 1992. Albedo maps of Pluto and Charon - Initial mutual event results. Icarus 97, 211–227.

Buratti, B.J., Hofgartner, J.D., Hicks, M.D., Weaver, H.A., Stern, S.A., Momary, T., Mosher, J.A., Beyer, R.A., Verbiscer, A.J., Zangari, A.M., Young, L.A., Lisse, C.M., Singer, K., Cheng, A., Grundy, W., Ennico, K., Olkin, C.B., 2017. Global albedos of Pluto and Charon from LORRI New Horizons observations. Icarus 287, 207–217.

Cheng, A.F., Summers, M.E., Gladstone, G.R., Strobel, D.F., Young, L.A., Lavvas, P., Kammer, J.A., Lisse, C.M., Parker, A.H., Young, E.F., Stern, S.A., Weaver, H.A., Olkin, C.B., Ennico, K., 2017. Haze in Pluto's atmosphere. Icarus 290, 112–133.

Christy, J.W., Harrington, R.S., 1978. The satellite of Pluto. Astronomical Journal 83, 1005.

Cruikshank, D.P., Pilcher, C.B., Morrison, D., 1976. Pluto - Evidence for methane frost. Science 194, 835–837.

del Mar, J.Q., Sicardy, B., Giraldo, V.A., Callo, V.R.A., An astronomical observatory for Peru. in: The Role of Astronomy in Society and Culture, (Eds.) D. Valls-Gabaud, A. Boksenberg vol. 260 of *IAU Symposium* 2011 pp. 616–621.

DeMeo, F.E., Dumas, C., de Bergh, C., Protopapa, S., Cruikshank, D.P., Geballe, T.R., Alvarez-Candal, A., Merlin, F., Barucci, M.A., 2010. A search for ethane on Pluto and Triton. Icarus 208, 412–424.

Desmars, J., Camargo, J.I.B., Braga-Ribas, F., Vieira-Martins, R., Assafin, M., Vachier, F., Colas, F., Ortiz, J.L., Duffard, R., Morales, N., Sicardy, B., Gomes-Júnior, A.R., Benedetti-Rossi, G., 2015. Orbit determination of trans-Neptunian objects and Centaurs for the prediction of stellar occultations. Astron. Astrophys. 584, A96.

Dias-Oliveira, A., Sicardy, B., Lellouch, E., Vieira-Martins, R., Assafin, M., Camargo, J.I.B., Braga-Ribas, F., Gomes-Júnior, A.R., Benedetti-Rossi, G., Colas, F., Decock, A., Doressoundiram, A., Dumas, C., Emilio, M., Fabrega Polleri, J., Gil-Hutton, R., Gillon, M., Girard, J.H., Hau, G.K.T., Ivanov, V.D., Jehin, E., Lecacheux, J., Leiva, R., Lopez-Sisterna, C., Mancini, L., Manfroid, J., Maury, A., Meza, E., Morales, N., Nagy, L., Opitom, C., Ortiz, J.L., Pollock, J., Roques, F., Snodgrass, C., Soulier, J.F., Thirouin, A., Vanzi, L., Widemann, T., Reichart, D.E., LaCluyze, A.P., Haislip, J.B., Ivarsen, K.M., Dominik, M., Jørgensen, U., Skottfelt, J., 2015.

Pluto's Atmosphere from Stellar Occultations in 2012 and 2013. Astrophys. J. 811, 53.

Duncombe, R.L., Seidelmann, P.K., 1980. A history of the determination of Pluto's mass. Icarus 44, 12–18.

Elliot, J.L., 1979. Stellar occultation studies of the solar system. Ann. Rev. Astron. Astropys. 17, 445–475.

Elliot, J.L., Ates, A., Babcock, B.A., Bosh, A.S., Buie, M.W., Clancy, K.B., Dunham, E.W., Eikenberry, S.S., Hall, D.T., Kern, S.D., Leggett, S.K., Levine, S.E., Moon, D.S., Olkin, C.B., Osip, D.J., Pasachoff, J.M., Penprase, B.E., Person, M.J., Qu, S., Rayner, J.T., Roberts, L.C., Salyk, C.V., Souza, S.P., Stone, R.C., Taylor, B.W., Tholen, D.J., Thomas-Osip, J.E., Ticehurst, D.R., Wasserman, L.H., 2003. The recent expansion of Pluto's atmosphere. Nature 424, 165–168.

Elliot, J.L., Dunham, E.W., Bosh, A.S., Slivan, S.M., Young, L.A., Wasserman, L.H., Millis, R.L., 1989. Pluto's atmosphere. Icarus 77, 148–170.

Elliot, J.L., French, R.G., Dunham, E., Gierasch, P.J., Veverka, J., Church, C., Sagan, C., 1977. Occultation of Epsilon Geminorum by Mars. II - The structure and extinction of the Martian upper atmosphere. Astrophys. J. 217, 661–679.

Elliot, J.L., Olkin, C.B., 1996. Probing Planetary Atmospheres with Stellar Occultations. Ann. Rev. Earth and Plan. Sci. 24, 89–124.

Fabry, L., 1929. Le rôle des Atmosphères dans les Occultations par les planètes. Journal des Observateurs 12, 102.

Fjeldbo, G., Kliore, A.J., Eshleman, V.R., 1971. The Neutral Atmosphere of Venus as Studied with the Mariner V Radio Occultation Experiments. Astron. J. 76, 123.

Forget, F., Bertrand, T., Vangvichith, M., Leconte, J., Millour, E., Lellouch, E., 2017. A post-new horizons global climate model of Pluto including the N2, CH4 and CO cycles. Icarus 287, 54 – 71.

Fray, N., Schmitt, B., 2009. Sublimation of ices of astrophysical interest: A bibliographic review. Plan. Sp. S. 57, 2053–2080.

French, R.G., Toigo, A.D., Gierasch, P.J., Hansen, C.J., Young, L.A., Sicardy, B., Dias-Oliveira, A., Guzewich, S.D., 2015. Seasonal variations in Pluto's atmospheric tides. Icarus 246, 247–267.

Gaia Collaboration, Brown, A.G.A., Vallenari, A., Prusti, T., de Bruijne, J.H.J., Mignard, F., Drimmel, R., Babusiaux, C., Bailer-Jones, C.A.L., Bastian, U., et al., 2016. Gaia Data Release 1. Summary of the astrometric, photometric, and survey properties. Astron. Astrophys. 595, A2.

Gaia Collaboration, Brown, A.G.A., Vallenari, A., Prusti, T., de Bruijne, J.H.J., Babusiaux, C., Bailer-Jones, C.A.L., 2018. Gaia Data Release 2. Summary of the contents and survey properties. ArXiv e-prints.

Gladstone, G.R., Stern, S.A., Ennico, K., Olkin, C.B., Weaver, H.A., Young, L.A., Summers, M.E., Strobel, D.F., Hinson, D.P., Kammer, J.A., Parker, A.H., Steffl, A.J., Linscott, I.R., Parker, J.W., Cheng, A.F., Slater, D.C., Versteeg, M.H., Greathouse, T.K., Retherford, K.D., Throop, H., Cunningham, N.J., Woods, W.W., Singer, K.N., Tsang, C.C.C., Schindhelm, E., Lisse, C.M., Wong, M.L., Yung, Y.L., Zhu, X., Curdt, W., Lavvas, P., Young, E.F., Tyler, G.L., Bagenal, F., Grundy, W.M., McKinnon, W.B., Moore, J.M., Spencer, J.R., Andert, T., Andrews, J., Banks, M., Bauer, B., Bauman, J., Barnouin, O.S., Bedini, P., Beisser, K., Beyer, R.A., Bhaskaran, S., Binzel, R.P., Birath, E., Bird, M., Bogan, D.J., Bowman, A., Bray, V.J., Brozovic, M., Bryan, C., Buckley, M.R., Buie, M.W., Buratti, B.J., Bushman, S.S., Calloway, A., Carcich, B., Conard, S., Conrad, C.A., Cook, J.C., Cruikshank, D.P., Custodio, O.S., Ore, C.M.D., Deboy, C., Dischner, Z.J.B., Dumont, P., Earle, A.M., Elliott, H.A., Ercol, J., Ernst, C.M., Finley, T., Flanigan, S.H., Fountain, G., Freeze, M.J., Green, J.L., Guo, Y., Hahn, M., Hamilton, D.P., Hamilton, S.A., Hanley, J., Harch, A., Hart, H.M., Hersman, C.B., Hill, A., Hill, M.E., Holdridge, M.E., Horanyi, M., Howard, A.D., Howett, C.J.A., Jackman, C., Jacobson, R.A., Jennings, D.E., Kang, H.K., Kaufmann, D.E., Kollmann, P., Krimigis, S.M., Kusnierkiewicz, D., Lauer, T.R., Lee, J.E., Lindstrom, K.L., Lunsford, A.W., Mallder, V.A., Martin, N., McComas, D.J., McNutt, R.L., Mehoke, D., Mehoke, T., Melin, E.D., Mutchler, M., Nelson, D., Nimmo, F., Nunez, J.I., Ocampo, A., Owen, W.M., Paetzold, M., Page, B., Pelletier, F., Peterson, J., Pinkine, N., Piquette, M., Porter, S.B., Protopapa, S., Redfern, J., Reitsema, H.J., Reuter, D.C., Roberts, J.H., Robbins, S.J., Rogers, G., Rose, D., Runyon, K., Ryschkewitsch, M.G., Schenk, P., Sepan, B., Showalter, M.R., Soluri, M., Stanbridge, D., Stryk, T., Szalay, J.R., Tapley, M., Taylor, A., Taylor, H., Umurhan, O.M., Verbiscer, A.J., Versteeg, M.H., Vincent, M., Webbert, R., Weidner, S., Weigle, G.E., White, O.L., Whittenburg, K., Williams, B.G., Williams, K., Williams, S., Zangari, A.M., Zirnstein, E., 2016. The atmosphere of Pluto as observed by New Horizons. Science 351, aad8866.

Grundy, W.M., Binzel, R.P., Buratti, B.J., Cook, J.C., Cruikshank, D.P., Dalle Ore, C.M., Earle, A.M., Ennico, K., Howett, C.J.A., Lunsford, A.W., Olkin, C.B., Parker, A.H., Philippe, S., Protopapa, S., Quirico, E., Reuter, D.C., Schmitt, B., Singer, K.N., Verbiscer, A.J., Beyer, R.A., Buie, M.W., Cheng, A.F., Jennings, D.E., Linscott, I.R., Parker, J.W., Schenk, P.M., Spencer, J.R., Stansberry, J.A., Stern, S.A., Throop, H.B., Tsang, C.C.C., Weaver, H.A., Weigle, G.E., Young, L.A., 2016. Surface compositions across Pluto and Charon. Science 351, aad9189.

Gulbis, A.A.S., Elliot, J.L., Person, M.J., Adams, E.R., Babcock, B.A., Emilio, M., Gangestad, J.W., Kern, S.D., Kramer, E.A., Osip, D.J., Pasachoff, J.M., Souza, S.P., Tuvikene, T., 2006. Charon's radius and atmospheric constraints from observations of a stellar occultation. Nature439, 48–51.

Hansen, C., Paige, D., Young, L., 2015. Pluto's climate modeled with new observational constraints. Icarus 246, 183 – 191.

Hansen, C.J., Paige, D.A., 1996. Seasonal Nitrogen Cycles on Pluto. Icarus 120, 247–265.

Hanuš, J., Viikinkoski, M., Marchis, F., Ďurech, J., Kaasalainen, M., Delbo', M., Herald, D., Frappa, E., Hayamizu, T., Kerr, S., Preston, S., Timerson, B., Dunham, D., Talbot, J., 2017. Volumes and bulk densities of forty asteroids from ADAM shape modeling. Astron. Astrophys. 601, A114.

Hinson, D.P., Linscott, I.R., Young, L.A., Tyler, G.L., Stern, S.A., Beyer, R.A., Bird, M.K., Ennico, K., Gladstone, G.R., Olkin, C.B., Pätzold, M., Schenk, P.M., Strobel, D.F., Summers, M.E., Weaver, H.A., Woods, W.W., 2017. Radio occultation measurements of Pluto's neutral atmosphere with New Horizons. Icarus 290, 96–111.

Hubbard, W.B., Hunten, D.M., Dieters, S.W., Hill, K.M., Watson, R.D., 1988. Occultation evidence for an atmosphere on Pluto. Nature336, 452–454.

Hubbard, W.B., McCarthy, D.W., Kulesa, C.A., Benecchi, S.D., Person, M.J., Elliot, J.L., Gulbis, A.A.S., 2009. Buoyancy waves in Pluto's high atmosphere: Implications for stellar occultations. Icarus 204, 284–289.

Jewitt, D.C., 1994. Heat from Pluto. Astronomical Journal 107, 372–378.

Kervella, P., Thévenin, F., Di Folco, E., Ségransan, D., 2004. The angular sizes of dwarf stars and subgiants. Surface brightness relations calibrated by interferometry. Astron. Astrophys. 426, 297–307.

Leiva, R., *Stellar occultations by Trans-Neptunian Objects and Centaurs Application to Chariklo and its ring system* Ph.D. thesis Université Pierre et Marie Curie, Pontificia Universidad Católica de Chile 2017.

Leiva, R., Sicardy, B., Camargo, J.I.B., Ortiz, J.L., Desmars, J., Bérard, D., Lellouch, E., Meza, E., Kervella, P., Snodgrass, C., Duffard, R., Morales, N., Gomes-Júnior, A.R., Benedetti-Rossi, G., Vieira-Martins, R., Braga-Ribas, F., Assafin, M., Morgado, B.E., Colas, F., De Witt, C., Sickafoose, A.A., Breytenbach, H., Dauvergne, J.L., Schoenau, P., Maquet, L., Bath, K.L., Bode, H.J., Cool, A., Lade, B., Kerr, S., Herald, D., 2017. Size and Shape of Chariklo from Multi-epoch Stellar Occultations. Astronomical Journal 154, 159.

Lellouch, E., de Bergh, C., Sicardy, B., Forget, F., Vangvichith, M., Käufl, H.U., 2015. Exploring the spatial, temporal, and vertical distribution of methane in Pluto's atmosphere. Icarus 246, 268–278.

Lellouch, E., de Bergh, C., Sicardy, B., Käufl, H.U., Smette, A., 2011. High resolution spectroscopy of Pluto's atmosphere: detection of the 2.3 μm CH_4 bands and evidence for carbon monoxide. Astron. Astrophys. 530, L4.

Lellouch, E., Gurwell, M., Butler, B., Fouchet, T., Lavvas, P., Strobel, D.F., Sicardy, B., Moullet, A., Moreno, R., Bockelée-Morvan, D., Biver, N., Young, L., Lis, D., Stansberry, J., Stern, A., Weaver, H., Young, E., Zhu, X., Boissier, J., 2017. Detection of CO and HCN in Pluto's atmosphere with ALMA. Icarus 286, 289–307.

Lellouch, E., Laureijs, R., Schmitt, B., Quirico, E., de Bergh, C., Crovisier, J., Coustenis, A., 2000. Pluto's Non-isothermal Surface. Icarus 147, 220–250.

Lellouch, E., Santos-Sanz, P., Fornasier, S., Lim, T., Stansberry, J., Vilenius, E., Kiss, C., Müller, T., Marton, G., Protopapa, S., Panuzzo, P., Moreno, R., 2016. The long-wavelength thermal emission of the Pluto-Charon system from Herschel observations. Evidence for emissivity effects. Astron. Astrophys. 588, A2.

Lellouch, E., Sicardy, B., de Bergh, C., Käufl, H.U., Kassi, S., Campargue, A., 2009. Pluto's lower atmosphere structure and methane abundance from high-resolution spectroscopy and stellar occultations. Astron. Astrophys. 495, L17–L21.

Marcialis, R.L., 1988. A two-spot albedo model for the surface of Pluto. Astronomical Journal 95, 941–947.

McKinnon, W.B., Nimmo, F., Wong, T., Schenk, P.M., White, O.L., Roberts, J.H., Moore, J.M., Spencer, J.R., Howard, A.D., Umurhan, O.M., Stern, S.A., Weaver, H.A., Olkin, C.B., Young, L.A., Smith, K.E., Beyer, R., Buie, M., Buratti, B., Cheng, A., Cruikshank, D., Dalle Ore, C., Gladstone, R., Grundy, W., Lauer, T., Linscott, I., Parker, J., Porter, S., Reitsema, H., Reuter, D., Robbins, S., Showalter, M., Singer, K., Strobel, D., Summers, M., Tyler, L., Banks, M., Barnouin, O., Bray, V., Carcich, B., Chaikin, A., Chavez, C., Conrad, C., Hamilton, D., Howett, C., Hofgartner, J., Kammer, J., Lisse, C., Marcotte, A., Parker, A., Retherford, K., Saina, M., Runyon, K., Schindhelm, E., Stansberry, J., Steffl, A., Stryk, T., Throop, H., Tsang, C., Verbiscer, A., Winters, H., Zangari, A., New Horizons Geology, G.a.I.T.T., 2016. Convection in a volatile nitrogen-ice-rich layer drives Pluto's geological vigour. Nature 534, 82–85.

Meza, E., Ricra, J., Pereyra, A., OA-UNI: an Astronomical Observatory at the Peruvian Andes. in: Abstract Book - Special Session - The International Year of Astronomy - IAU's XXVII General Assembly, Rio de Janeiro 2009 p. 407.

Moore, J.M., McKinnon, W.B., Spencer, J.R., Howard, A.D., Schenk, P.M., Beyer, R.A., Nimmo, F., Singer, K.N., Umurhan, O.M., White, O.L., Stern, S.A., Ennico, K., Olkin, C.B., Weaver, H.A., Young, L.A., Binzel, R.P., Buie, M.W., Buratti, B.J., Cheng, A.F., Cruikshank, D.P., Grundy, W.M., Linscott, I.R., Reitsema, H.J., Reuter, D.C., Showalter, M.R., Bray, V.J., Chavez, C.L., Howett, C.J.A., Lauer, T.R., Lisse, C.M., Parker, A.H., Porter, S.B., Robbins, S.J., Runyon, K., Stryk, T., Throop, H.B., Tsang, C.C.C., Verbiscer, A.J., Zangari, A.M., Chaikin, A.L., Wilhelms, D.E., Bagenal, F., Gladstone, G.R., Andert, T., Andrews, J., Banks, M., Bauer, B., Bauman, J., Barnouin, O.S., Bedini, P., Beisser, K., Bhaskaran, S., Birath, E., Bird, M., Bogan, D.J., Bowman, A., Brozovic, M., Bryan, C., Buckley, M.R., Bushman, S.S., Calloway, A., Carcich, B., Conard, S., Conrad, C.A., Cook, J.C., Custodio, O.S., Ore, C.M.D., Deboy, C., Dischner, Z.J.B., Dumont, P., Earle, A.M., Elliott, H.A., Ercol, J., Ernst, C.M., Finley, T., Flanigan, S.H., Fountain, G., Freeze, M.J., Greathouse, T., Green, J.L., Guo, Y., Hahn, M., Hamilton, D.P., Hamilton, S.A., Hanley, J., Harch, A., Hart, H.M., Hersman, C.B., Hill, A., Hill, M.E., Hinson, D.P., Holdridge, M.E., Horanyi, M., Jackman, C., Jacobson, R.A., Jennings, D.E., Kammer, J.A., Kang, H.K., Kaufmann, D.E., Kollmann, P., Krimigis, S.M., Kusnierkiewicz, D., Lee, J.E., Lindstrom, K.L., Lunsford, A.W., Mallder, V.A., Martin, N., McComas, D.J., McNutt, R.L., Mehoke, D., Mehoke, T., Melin,

E.D., Mutchler, M., Nelson, D., Nunez, J.I., Ocampo, A., Owen, W.M., Paetzold, M., Page, B., Parker, J.W., Pelletier, F., Peterson, J., Pinkine, N., Piquette, M., Protopapa, S., Redfern, J., Roberts, J.H., Rogers, G., Rose, D., Retherford, K.D., Ryschkewitsch, M.G., Schindhelm, E., Sepan, B., Soluri, M., Stanbridge, D., Steffl, A.J., Strobel, D.F., Summers, M.E., Szalay, J.R., Tapley, M., Taylor, A., Taylor, H., Tyler, G.L., Versteeg, M.H., Vincent, M., Webbert, R., Weidner, S., Weigle, G.E., Whittenburg, K., Williams, B.G., Williams, K., Williams, S., Woods, W.W., Zirnstein, E., 2016. The geology of Pluto and Charon through the eyes of New Horizons. Science 351, 1284–1293.

Nimmo, F., Umurhan, O., Lisse, C.M., Bierson, C.J., Lauer, T.R., Buie, M.W., Throop, H.B., Kammer, J.A., Roberts, J.H., McKinnon, W.B., Zangari, A.M., Moore, J.M., Stern, S.A., Young, L.A., Weaver, H.A., Olkin, C.B., Ennico, K., 2017. Mean radius and shape of Pluto and Charon from New Horizons images. Icarus 287, 12–29.

Olkin, C.B., Ennico, K., Spencer, J., 2017. The Pluto system after the New Horizons flyby. Nature Astronomy 1, 663–670.

Olkin, C.B., Young, L.A., Borncamp, D., Pickles, A., Sicardy, B., Assafin, M., Bianco, F.B., Buie, M.W., de Oliveira, A.D., Gillon, M., French, R.G., Ramos Gomes, A., Jehin, E., Morales, N., Opitom, C., Ortiz, J.L., Maury, A., Norbury, M., Braga-Ribas, F., Smith, R., Wasserman, L.H., Young, E.F., Zacharias, M., Zacharias, N., 2015. Evidence that Pluto's atmosphere does not collapse from occultations including the 2013 May 04 event. Icarus 246, 220–225.

Olkin, C.B., Young, L.A., French, R.G., Young, E.F., Buie, M.W., Howell, R.R., Regester, J., Ruhland, C.R., Natusch, T., Ramm, D.J., 2014. Pluto's atmospheric structure from the July 2007 stellar occultation. Icarus 239, 15–22.

Ortiz, J.L., Santos-Sanz, P., Sicardy, B., Benedetti-Rossi, G., Bérard, D., Morales, N., Duffard, R., Braga-Ribas, F., Hopp, U., Ries, C., Nascimbeni, V., Marzari, F., Granata, V., Pál, A., Kiss, C., Pribulla, T., Komžík, R., Hornoch, K., Pravec, P., Bacci, P., Maestripieri, M., Nerli, L., Mazzei, L., Bachini, M., Martinelli, F., Succi, G., Ciabattari, F., Mikuz, H., Carbognani, A., Gaehrken, B., Mottola, S., Hellmich, S., Rommel, F.L., Fernández-Valenzuela, E., Campo Bagatin, A., Cikota, S., Cikota, A., Lecacheux, J., Vieira-Martins, R., Camargo, J.I.B., Assafin, M., Colas, F., Behrend, R., Desmars, J., Meza, E., Alvarez-Candal, A., Beisker, W., Gomes-Junior, A.R., Morgado, B.E., Roques, F., Vachier, F., Berthier, J., Mueller, T.G., Madiedo, J.M., Unsalan, O., Sonbas, E., Karaman, N., Erece, O., Koseoglu, D.T., Ozisik, T., Kalkan, S., Guney, Y., Niaei, M.S., Satir, O., Yesilyaprak, C., Puskullu, C., Kabas, A., Demircan, O., Alikakos, J., Charmandaris, V., Leto, G., Ohlert, J., Christille, J.M., Szakáts, R., Takácsné Farkas, A., Varga-Verebélyi, E., Marton, G., Marciniak, A., Bartczak, P., Santana-Ros, T., Butkiewicz-Bąk, M., Dudziński, G., Alí-Lagoa, V., Gazeas, K., Tzouganatos, L., Paschalis, N., Tsamis, V., Sánchez-Lavega, A., Pérez-Hoyos, S., Hueso, R., Guirado, J.C., Peris, V., Iglesias-Marzoa, R., 2017. The size, shape, density and ring of the dwarf planet Haumea from a stellar occultation. Nature550, 219–223.

Owen, T., Geballe, T., de Bergh, C., Young, L., Elliot, J., Cruikshank, D., Schmitt, B., Brown, R.H., Green, J., 1992. Pluto. iauc 5532.

Pasachoff, J.M., Babcock, B.A., Durst, R.F., Seeger, C.H., Levine, S.E., Bosh, A.S., Person, M.J., Sickafoose, A.A., Zuluaga, C.A., Kosiarek, M.R., Abe, F., Nagakane, M., Suzuki, D., Tristram, P.J., Arredondo, A., 2017. Pluto occultation on 2015 June 29 UTC with central flash and atmospheric spikes just before the New Horizons flyby. Icarus 296, 305–314.

Pasachoff, J.M., Person, M.J., Bosh, A.S., Sickafoose, A.A., Zuluaga, C., Kosiarek, M.R., Levine, S.E., Osip, D.J., Schiff, A., Seeger, C.H., Babcock, B.A., Rojo, P., Servajean, E., 2016. Trio of stellar occultations by pluto one year prior to *new horizons*' arrival. The Astronomical Journal 151, 97.

Pereyra, A., Tello, J., Meza, E., Cori, W., Ricra, J., Isela Zevallos, M., 2015. UNI Astronomical Observatory - OAUNI: First light. ArXiv e-prints.

Person, M.J., Elliot, J.L., Gulbis, A.A.S., Zuluaga, C.A., Babcock, B.A., McKay, A.J., Pasachoff, J.M., Souza, S.P., Hubbard, W.B., Kulesa, C.A., McCarthy, D.W., Benecchi, S.D., Levine, S.E., Bosh, A.S., Ryan, E.V., Ryan, W.H., Meyer, A., Wolf, J., Hill, J., 2008. Waves in Pluto's Upper Atmosphere. Astronomical Journal 136, 1510–1518.

Phinney, R.A., Anderson, D.L., 1968. On the radio occultation method for studying planetary atmospheres. J. Geophys. Res. 73, 1819.

Press, W.H., Teukolsky, S.A., Vetterling, W.T., Flannery, B.P., *Numerical Recipes in C., The Art of Scientific Computing,* New York: Cambridge Univ. Press, 1992 .

Schenk, P., Beyer, R., Moore, J., McKinnon, W., Spencer, J., Stern, S., Olkin, C., Ennico, K., Weaver, H., High-Resolution Topography of Pluto and Charon: Getting Down to Details. in: Lunar and Planetary Science Conference vol. 49 of *Lunar and Planetary Science Conference* 2018 p. 2300.

Schmitt, B., Philippe, S., Grundy, W., Reuter, D., Côte, R., Quirico, E., Protopapa, S., Young, L., Binzel, R., Cook, J., Cruikshank, D., Ore, C.D., Earle, A., Ennico, K., Howett, C., Jennings, D., Linscott, I., Lunsford, A., Olkin, C., Parker, A., Parker, J., Singer, K., Spencer, J., Stansberry, J., Stern, S., Tsang, C., Verbiscer, A., Weaver, H., 2017. Physical state and distribution of materials at the surface of Pluto from New Horizons LEISA imaging spectrometer. Icarus 287, 229 – 260.

Shepard, M.K., Timerson, B., Scheeres, D.J., Benner, L.A.M., Giorgini, J.D., Howell, E.S., Magri, C., Nolan, M.C., Springmann, A., Taylor, P.A., Virkki, A., 2018. A revised shape model of asteroid (216) Kleopatra. Icarus 311, 197–209.

Showalter, M.R., Hamilton, D.P., 2015. Resonant interactions and chaotic rotation of Pluto's small moons. Nature522, 45–49.

Showalter, M.R., Hamilton, D.P., Stern, S.A., Weaver, H.A., Steffl, A.J., Young, L.A., 2011. New Satellite of (134340) Pluto: S/2011 (134340) 1. iauc 9221.

Showalter, M.R., Weaver, H.A., Stern, S.A., Steffl, A.J., Buie, M.W., Merline, W.J., Mutchler, M.J., Soummer, R., Throop, H.B., 2012. New Satellite of (134340) Pluto: S/2012 (134340) 1. iauc 9253.

Sicardy, B., Colas, F., Widemann, T., Bellucci, A., Beisker, W., Kretlow, M., Ferri, F., Lacour, S., Lecacheux, J., Lellouch, E., Pau, S., Renner, S., Roques, F., Fienga, A., Etienne, C., Martinez, C., Glass, I.S., Baba, D., Nagayama, T., Nagata, T., Itting-Enke, S., Bath, K.L., Bode, H.J., Bode, F., Lüdemann, H., Lüdemann, J., Neubauer, D., Tegtmeier, A., Tegtmeier, C., Thomé, B., Hund, F., deWitt, C., Fraser, B., Jansen, A., Jones, T., Schoenau, P., Turk, C., Meintjies, P., Hernandez, M., Fiel, D., Frappa, E., Peyrot, A., Teng, J.P., Vignand, M., Hesler, G., Payet, T., Howell, R.R., Kidger, M., Ortiz, J.L., Naranjo, O., Rosenzweig, P., Rapaport, M., 2006. The two Titan stellar occultations of 14 November 2003. J. Geophys. Res. (Planets) 111, E11S91.

Sicardy, B., Ferri, F., Roques, F., Lecacheux, J., Pau, S., Brosch, N., Nevo, Y., Hubbard, W.B., Reitsema, H.J., Blanco, C., Carreira, E., Beisker, W., Bittner, C., Bode, H.J., Bruns, M., Denzau, H., Nezel, M., Riedel, E., Struckmann, H., Appleby, G., Forrest, R.W., Nicolson, I.K.M., Hollis, A.J., Miles, R., 1999. The Structure of Titan's Stratosphere from the 28 Sgr Occultation. Icarus 142, 357–390.

Sicardy, B., Talbot, J., Meza, E., Camargo, J.I.B., Desmars, J., Gault, D., Herald, D., Kerr, S., Pavlov, H., Braga-Ribas, F., Assafin, M., Benedetti-Rossi, G., Dias-Oliveira, A., Gomes-Júnior, A.R., Vieira-Martins, R., Bérard, D., Kervella, P., Lecacheux, J., Lellouch, E., Beisker, W., Dunham, D., Jelínek, M., Duffard, R., Ortiz, J.L., Castro-Tirado, A.J., Cunniffe, R., Querel, R., Yock, P.C., Cole, A.A., Giles, A.B., Hill, K.M., Beaulieu, J.P., Harnisch, M., Jansen, R., Pennell, A., Todd, S., Allen, W.H., Graham, P.B., Loader, B., McKay, G., Milner, J., Parker, S., Barry, M.A., Bradshaw, J., Broughton, J., Davis, L., Devillepoix, H., Drummond, J., Field, L., Forbes, M., Giles, D., Glassey, R., Groom, R., Hooper, D., Horvat, R., Hudson, G., Idaczyk, R., Jenke, D., Lade, B., Newman, J., Nosworthy, P., Purcell, P., Skilton, P.F., Streamer, M., Unwin, M., Watanabe, H., White, G.L., Watson, D., 2016. Pluto's Atmosphere from the 2015 June 29 Ground-based Stellar Occultation at the Time of the New Horizons Flyby. Astrophys. J., Lett. 819, L38.

Sicardy, B., Widemann, T., Lellouch, E., Veillet, C., Cuillandre, J.C., Colas, F., Roques, F., Beisker, W., Kretlow, M., Lagrange, A.M., Gendron, E., Lacombe, F., Lecacheux, J., Birnbaum, C., Fienga, A., Leyrat, C., Maury, A., Raynaud, E., Renner, S., Schultheis, M., Brooks, K., Delsanti, A., Hainaut, O.R., Gilmozzi, R., Lidman, C., Spyromilio, J., Rapaport, M., Rosenzweig, P., Naranjo, O., Porras, L., Díaz, F., Calderón, H., Carrillo, S., Carvajal, A., Recalde, E., Cavero, L.G., Montalvo, C., Barría, D., Campos, R., Duffard, R., Levato, H., 2003. Large changes in Pluto's atmosphere as revealed by recent stellar occultations. Nature 424, 168–170.

Stansberry, J.A., Lunine, J.I., Hubbard, W.B., Yelle, R.V., Hunten, D.M., 1994. Mirages and the nature of Pluto's atmosphere. Icarus 111, 503–513.

Stansberry, J.A., Spencer, J.R., Schmitt, B., Benchkoura, A.I., Yelle, R.V., Lunine,

J.I., 1996. A model for the overabundance of methane in the atmospheres of Pluto and Triton. planss 44, 1051–1063.

Stern, S.A., Bagenal, F., Ennico, K., Gladstone, G.R., Grundy, W.M., McKinnon, W.B., Moore, J.M., Olkin, C.B., Spencer, J.R., Weaver, H.A., Young, L.A., Andert, T., Andrews, J., Banks, M., Bauer, B., Bauman, J., Barnouin, O.S., Bedini, P., Beisser, K., Beyer, R.A., Bhaskaran, S., Binzel, R.P., Birath, E., Bird, M., Bogan, D.J., Bowman, A., Bray, V.J., Brozovic, M., Bryan, C., Buckley, M.R., Buie, M.W., Buratti, B.J., Bushman, S.S., Calloway, A., Carcich, B., Cheng, A.F., Conard, S., Conrad, C.A., Cook, J.C., Cruikshank, D.P., Custodio, O.S., Dalle Ore, C.M., Deboy, C., Dischner, Z.J.B., Dumont, P., Earle, A.M., Elliott, H.A., Ercol, J., Ernst, C.M., Finley, T., Flanigan, S.H., Fountain, G., Freeze, M.J., Greathouse, T., Green, J.L., Guo, Y., Hahn, M., Hamilton, D.P., Hamilton, S.A., Hanley, J., Harch, A., Hart, H.M., Hersman, C.B., Hill, A., Hill, M.E., Hinson, D.P., Holdridge, M.E., Horanyi, M., Howard, A.D., Howett, C.J.A., Jackman, C., Jacobson, R.A., Jennings, D.E., Kammer, J.A., Kang, H.K., Kaufmann, D.E., Kollmann, P., Krimigis, S.M., Kusnierkiewicz, D., Lauer, T.R., Lee, J.E., Lindstrom, K.L., Linscott, I.R., Lisse, C.M., Lunsford, A.W., Mallder, V.A., Martin, N., McComas, D.J., McNutt, R.L., Mehoke, D., Mehoke, T., Melin, E.D., Mutchler, M., Nelson, D., Nimmo, F., Nunez, J.I., Ocampo, A., Owen, W.M., Paetzold, M., Page, B., Parker, A.H., Parker, J.W., Pelletier, F., Peterson, J., Pinkine, N., Piquette, M., Porter, S.B., Protopapa, S., Redfern, J., Reitsema, H.J., Reuter, D.C., Roberts, J.H., Robbins, S.J., Rogers, G., Rose, D., Runyon, K., Retherford, K.D., Ryschkewitsch, M.G., Schenk, P., Schindhelm, E., Sepan, B., Showalter, M.R., Singer, K.N., Soluri, M., Stanbridge, D., Steffl, A.J., Strobel, D.F., Stryk, T., Summers, M.E., Szalay, J.R., Tapley, M., Taylor, A., Taylor, H., Throop, H.B., Tsang, C.C.C., Tyler, G.L., Umurhan, O.M., Verbiscer, A.J., Versteeg, M.H., Vincent, M., Webbert, R., Weidner, S., Weigle, G.E., White, O.L., Whittenburg, K., Williams, B.G., Williams, K., Williams, S., Woods, W.W., Zangari, A.M., Zirnstein, E., 2015. The Pluto system: Initial results from its exploration by New Horizons. Science 350, aad1815.

Stern, S.A., Mitton, J., *Pluto and Charon: Ice Worlds on the Ragged Edge of the Solar System, Second Edition* 2005.

Stern, S.A., Trafton, L.M., Gladstone, G.R., 1988. Why is Pluto bright? Implications of the albedo and lightcurve behavior of Pluto. Icarus 75, 485–498.

Stern, S.A., Weintraub, D.A., Festou, M.C., 1993. Evidence for a Low Surface Temperature on Pluto from Millimeter-Wave Thermal Emission Measurements. Science 261, 1713–1716.

Strobel, D.F., Zhu, X., Summers, M.E., Stevens, M.H., 1996. On the Vertical Thermal Structure of Pluto's Atmosphere. Icarus 120, 266–289.

Sykes, M.V., Cutri, R.M., Lebofsky, L.A., Binzel, R.P., 1987. IRAS serendipitous survey observations of Pluto and Charon. Science 237, 1336–1340.

Tholen, D.J., Buie, M.W., 1988. Circumstances for Pluto-Charon mutual events in 1989. Astronomical Journal 96, 1977–1982.

Toigo, A.D., Gierasch, P.J., Sicardy, B., Lellouch, E., 2010. Thermal tides on Pluto. Icarus 208, 402–411.

Tryka, K.A., Brown, R.H., Chruikshank, D.P., Owen, T.C., Geballe, T.R., de Bergh, C., 1994. Temperature of nitrogen ice on Pluto and its implications for flux measurements. Icarus 112, 513–527.

Tyler, G.L., Linscott, I.R., Bird, M.K., Hinson, D.P., Strobel, D.F., Pätzold, M., Summers, M.E., Sivaramakrishnan, K., 2008. The New Horizons Radio Science Experiment (REX). Space Sci. Rev. 140, 217–259.

Urban, S.E., Seidelmann, P.K., *Explanatory supplement to the astronomical almanac* University Science Books 2013.

van Belle, G.T., 1999. Predicting Stellar Angular Sizes. Pub. Astron. Soc. Pac. 111, 1515–1523.

Vapillon, L., Combes, M., Lecacheux, J., 1973. The beta Scorpii occultation by Jupiter. II. The temperature and density profiles of the Jupiter upper atmosphere.. Astron. Astrophys. 29, 135–149.

Walker, M.F., Hardie, R., 1955. A Photometric determination of the rotational period of Pluto. Publi. of the Astron. Soc. of the Pacific67.

Washburn, E.W., *International Critical Tables of Numerical Data: Physics, Chemistry and Technology.* Vol. 7, p. 11. McGraw-Hill, New York, 1930.

Weaver, H.A., Buie, M.W., Buratti, B.J., Grundy, W.M., Lauer, T.R., Olkin, C.B., Parker, A.H., Porter, S.B., Showalter, M.R., Spencer, J.R., Stern, S.A., Verbiscer, A.J., McKinnon, W.B., Moore, J.M., Robbins, S.J., Schenk, P., Singer, K.N., Barnouin, O.S., Cheng, A.F., Ernst, C.M., Lisse, C.M., Jennings, D.E., Lunsford, A.W., Reuter, D.C., Hamilton, D.P., Kaufmann, D.E., Ennico, K., Young, L.A., Beyer, R.A., Binzel, R.P., Bray, V.J., Chaikin, A.L., Cook, J.C., Cruikshank, D.P., Dalle Ore, C.M., Earle, A.M., Gladstone, G.R., Howett, C.J.A., Linscott, I.R., Nimmo, F., Parker, J.W., Philippe, S., Protopapa, S., Reitsema, H.J., Schmitt, B., Stryk, T., Summers, M.E., Tsang, C.C.C., Throop, H.H.B., White, O.L., Zangari, A.M., 2016. The small satellites of Pluto as observed by New Horizons. Science 351, aae0030.

Weaver, H.A., Stern, S.A., Mutchler, M.J., Steffl, A.J., Buie, M.W., Merline, W.J., Spencer, J.R., Young, E.F., Young, L.A., 2006. Discovery of two new satellites of Pluto. Nature439, 943–945.

Yelle, R.V., Elliot, J.L., *Atmospheric Structure and Composition: Pluto and Charon* 1997 p. 347 p. 347.

Yelle, R.V., Lunine, J.I., 1989. Evidence for a molecule heavier than methane in the atmosphere of Pluto. Nature339, 288–290.

Young, E.F., Binzel, R.P., 1993. Comparative mapping of Pluto's sub-Charon hemisphere - Three least squares models based on mutual event lightcurves. Icarus 102, 134–149.

Young, E.F., French, R.G., Young, L.A., Ruhland, C.R., Buie, M.W., Olkin, C.B., Regester, J., Shoemaker, K., Blow, G., Broughton, J., Christie, G., Gault, D., Lade, B., Natusch, T., 2008. Vertical structure in pluto's atmosphere from the 2006 june 12 stellar occultation. The Astronomical Journal 136, 1757–1769.

Young, L.A., 2012. Volatile transport on inhomogeneous surfaces: I - Analytic expressions, with application to Pluto's day. Icarus 221, 80–88.

Young, L.A., 2013. Pluto's Seasons: New Predictions for New Horizons. Astrophysical Journal, Letters766, L22.

Young, L.A., Elliot, J.L., Tokunaga, A., de Bergh, C., Owen, T., 1997. Detection of Gaseous Methane on Pluto. Icarus 127, 258–262.

Young, L.A., Kammer, J.A., Steffl, A.J., Gladstone, G.R., Summers, M.E., Strobel, D.F., Hinson, D.P., Stern, S.A., Weaver, H.A., Olkin, C.B., Ennico, K., McComas, D.J., Cheng, A.F., Gao, P., Lavvas, P., Linscott, I.R., Wong, M.L., Yung, Y.L., Cunningham, N., Davis, M., Parker, J.W., Schindhelm, E., Siegmund, O.H.W., Stone, J., Retherford, K., Versteeg, M., 2018. Structure and composition of Pluto's atmosphere from the New Horizons solar ultraviolet occultation. Icarus 300, 174–199.

Young, L.A., Stern, S.A., Weaver, H.A., Bagenal, F., Binzel, R.P., Buratti, B., Cheng, A.F., Cruikshank, D., Gladstone, G.R., Grundy, W.M., Hinson, D.P., Horanyi, M., Jennings, D.E., Linscott, I.R., McComas, D.J., McKinnon, W.B., McNutt, R., Moore, J.M., Murchie, S., Olkin, C.B., Porco, C.C., Reitsema, H., Reuter, D.C., Spencer, J.R., Slater, D.C., Strobel, D., Summers, M.E., Tyler, G.L., 2008. New Horizons: Anticipated Scientific Investigations at the Pluto System. Space Sci. Rev. 140, 93–127.

Zhang, X., Strobel, D.F., Imanaka, H., 2017. Haze heats Pluto's atmosphere yet explains its cold temperature. Nature551, 352–355.